Loughborough
University

Thesis Access Form

Copy No…………...…………………….**Location**……………………………………….…………...…

Author…………...……………………………………………………………………….…..……

Title…………………………………………………………………………………………………..

Status of access OPEN / RESTRICTED / CONFIDENTIAL

Moratorium Period:…………………………………years, ending………../…………200…………………….

Conditions of access approved by (CAPITALS):………………………………………………………

Supervisor (Signature)……………………………………..…………………………...

Department of………………………………………………………...…………………………

Author's Declaration: *I agree the following conditions:*

Open access work shall be made available (in the University and externally) and reproduced as necessary at the discretion of the University Librarian or Head of Department. It may also be digitised by the British Library and made freely available on the Internet to registered users of the EThOS service subject to the EThOS supply agreements.

*The statement itself shall apply to **ALL** copies including electronic copies:*

This copy has been supplied on the understanding that it is copyright material and that no quotation from the thesis may be published without proper acknowledgement.

Restricted/confidential work: All access and any photocopying shall be strictly subject to written permission from the University Head of Department and any external sponsor, if any.

Author's signature……………………………………….Date……………………………...…………..……...

users declaration: for signature during any Moratorium period (Not Open work): *I undertake to uphold the above conditions:*			
Date	Name (CAPITALS)	Signature	Address

Characterisation and Modification of Optoelectronic
Substrate Surfaces for Enhanced Adhesive Flow
Control

A Doctoral Thesis

By
Owain Williams

Submitted in partial fulfillment of the requirements
for the award of
PhD of Loughborough University

July 2010

Certificate of Originality

This is to certify that I am responsible for the work submitted in this thesis, that the original work is my own except as specified in acknowledgements, footnotes or references, and that neither the thesis or the original work contained therein has been submitted to this or any other institution for a higher degree.

…………………………………………Signed

…………………………………………Date

Abstract

Optoelectronics manufacturers are under continuous pressure for miniaturisation of optoelectronic modules. One route to further miniaturisation is to reduce the spacing between the optical and optoelectronic components in the optical path adhesively mounted to ceramic carriers. Flow control of the adhesives over the ceramic surface is then imperative. Uncontrolled wetting can lead to an excessive adhesive footprint which interferes in the application of other adhesives for subsequent components. However, insufficient wetting can lead to low strength bonds vulnerable to thermal fatigue and shear failure. The goal of the work was to minimise the potential for uncontrolled wetting while maintaining unmodified bond properties. In addition positional stability of adhered parts on cure and in-service must not be detrimentally affected.

Epoxy bleed and fillet size issues were experienced in the assembly processes of Oclaro plc. They approached Loughborough University and proposed a project be created to tackle these issues. This project was proposed by Oclaro plc and was funded by Oclaro and the EPSRC.

The first step in the practical investigation was to characterise the surface properties of alumina and aluminium nitride ceramic plates variously processed by commercial suppliers. The surface conditions included lapped, polished, etched and as-fired. Initial characterisation was performed by XPS, contact angle, SEM and surface texture analysis, amongst others. Commercially available conductive and thermally conductive adhesives were applied to the ceramics and their wetting behaviour linked to the surface properties observed.

Once the primary factors which affect wetting were identified the investigation focussed upon modification of these parameters to optimise wetting and adhesion. Chemical and physical modifications were studied, including adventitious carbon adsorption, laser micromachining and self assembled monolayer application. Each showed promising results but the use of self assembled monolayers stood out as a good candidate for a solution to the problem, which could be incorporated into the assembly line of Oclaro's operations.

Contents

Nomenclature

OEM	Optoelectronics Manufacturer
SEM	Scanning Electron Microscopy
WLI	White Light Interferometry
AFM	Atomic Force Microscopy
TESP	Tapping Etched Silicon Probe
XPS	X-ray Photoelectron Spectroscopy
AlN	Aluminium Nitride
SAM	Self Assembled Monolayer
CTE	Coefficient of Thermal Expansion
OTS	Octadecyltrichlorosilane
XRD	X-ray Diffraction
DI	Deionised
HCl	Hydrochloric Acid
FCOOH	Fluorinated Carboxylic Acid
KOH	Potassium Hydroxide
MSDS	Material Safety Data Sheet
BN	Boron Nitride
KrF	Krypton Fluoride

Table of Figures

Table of Tables

1 Introduction

Optoelectronics is a field of electronics which deals with the use of light within electronic devices. The optoelectronic devices employ electrical-to-optical or optical-to-electrical transducers in their operation for such applications as fibre optic communications.

There is strong commercial pressure to reduce the overall cost and size of optoelectronic modules[1], or include additional functionality within existing footprints, without compromising the yield against the already demanding performance requirements. One way of achieving this is through improvements in package design and processes. Typically, a telecoms, i.e. high data rate, high precision, laser package consists of a hermetically sealed composite Kovar/ ceramic / copper tungsten "gold box", containing the semiconductor laser, other optical components and lenses, electronic driver and monitoring components, and thermoelectric cooler. These components are mounted on ceramic substrates using adhesives. The package is coupled to a fibre optic tail through a lens or an optical window in the package. A typical module is illustrated in Figure 1-1.
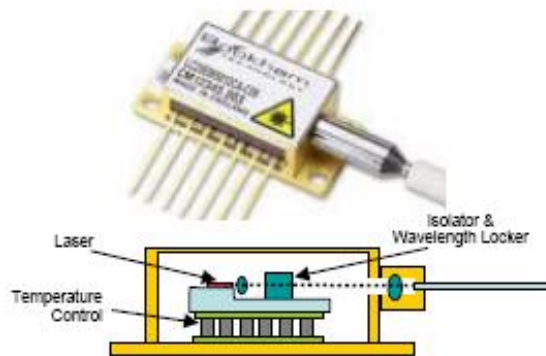
Figure 1-1 10Gbps optical transmitter in a 14 pin butterfly package

The two major functional drivers in the package design, and assembly process are the requirement to maintain the laser at a constant temperature for wavelength stability, and the requirement to achieve high coupling efficiency of the laser output into the optical fibre.

The constant temperature requirement leads to the choice of AlN as the substrate for its good thermal conductivity and close expansion match to the InP-based laser chip, together with its rigidity, processability and electrically isolative properties. Additionally, good thermal interfaces are required between the laser, thermoelectric coolers and the AlN substrate, leading to the use of filled adhesives for bonding these components.

The specification for high coupling efficiency places demands on the precision of the assembly of the optical components and the adhesive used to hold them in place. The laser spot size is around 1 micron and the alignment between the laser and a coupling lens typically has to be held at sub-micron accuracy. Since passive placement techniques are increasingly difficult to control below 10 micron accuracy[2], a compensatory active alignment process is usually needed for the optical components. Having been placed and aligned the optical components are tacked in place by a UV cure of the adhesive. Modules are later baked in batches to complete the cure. There must be minimal movement of the part on curing. Long term stability of the adhesive is also important to maintain the coupling efficiency over the operating lifetime of the module of 20 years or more.

Potential improvements to the packaging centre around the behaviour of the adhesives on the ceramic substrates, particularly those used during the alignment procedure. Because the beam path optimisation procedure is sequential, with one optical component being placed, aligned and the adhesive UV tacked before the next component is placed, the spacing between components is in part constrained to be larger than is optically necessary by the size of the adhesive fillets around each component. The fillet size in turn is determined by the amount of adhesive dispensed and by the wetting interaction between the adhesive and the ceramic. The fillet size of an adhesive bond is depicted in Figure 1-2.
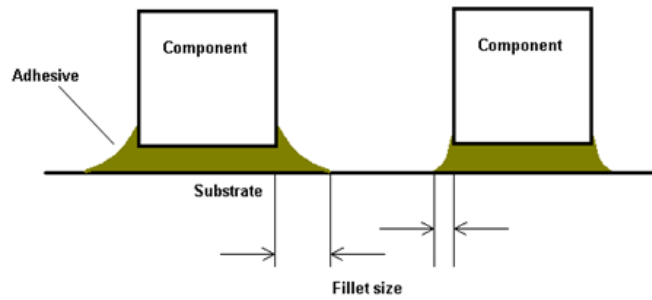
Figure 1-2 Fillet size and its dependence on the contact angle between adhesive and ceramic, low contact angle and large fillet (left), high contact angle and small fillet (right)

A second adhesive-flow related problem is epoxy bleed, where a component of the adhesive bleeds across the surface of the substrate causing a contamination problem. This phenomenon is shown in Figure 1-3 where bleed can occur randomly on apparently identical substrates. At present some control of adhesive flow is achieved by mechanical cutting of trenches into the surface of the ceramic. This is an extra process step which adds cost to the package components.

Figure 1-3 Epoxy bleed from thermally conductive boron nitride loaded epoxy, pronounced (left) and acceptable (right).

Figure 1-4 shows a breakdown of the assembly processes for an optoelectronic module and their associated costs. The diagram does not take into account the yield due to adhesive spreading or the cost of redesign to accommodate the potential spreading. The diagram was produced by Oclaro plc who were the industrial partner in this research.
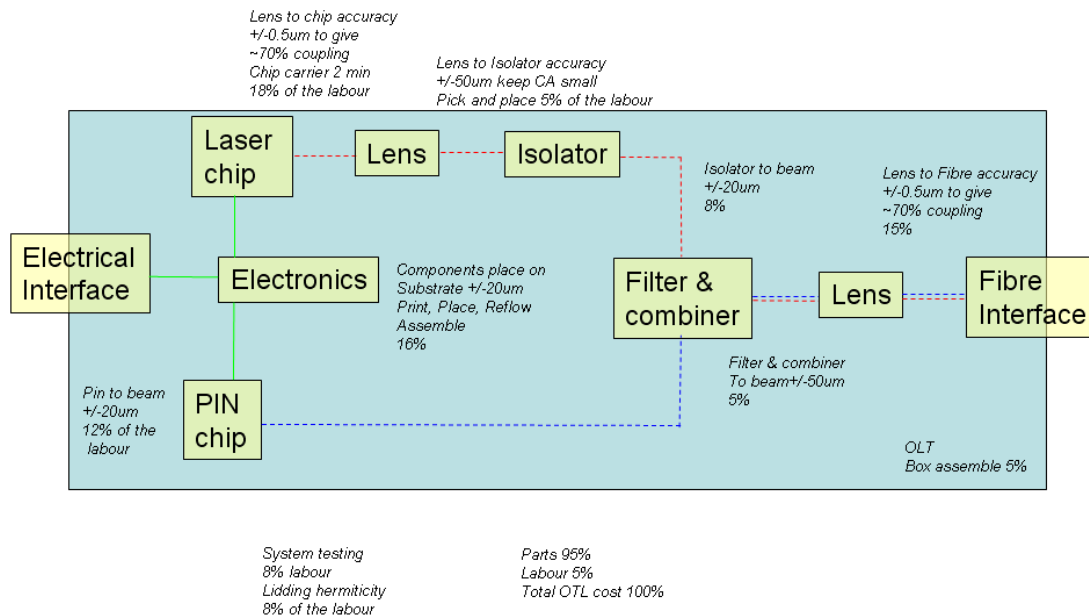
Figure 1-4 The assembly process and associated cost for a typical optoelectronic module (courtesy of P Firth,Oclaro plc)

The aim of this work is to find methods to control epoxy bleed and fillet size which are implementable in the existing large scale manufacturing optoelectronics assembly line. The cost of any methods must not significantly increase the manufacturing costs of the modules and will preferably offer a cost reduction by increasing yields and removing design limitations. Other considerations for potential solutions are:

- Solutions should be an isolated process not requiring changes to the entire assembly line

- Solutions should not affect subsequent processes i.e. active alignment

- Solutions must not affect the functionality of the modules

The first step in the investigation was to identify those factors which affect the epoxy bleed and fillet size, and ascertain which ones can be controlled and which can only be quantified. In *Section 5.2 Surface Parameter Effects on Epoxy Bleed* epoxy bleed has been linked to substrate composition and contamination which directly affect surface energy[3-4]. The available literature, which is reviewed in *Section 2 Literature Review*, also suggests substrate surface roughness and texture could influence the behaviour of liquids on surfaces[5]. The literature thus shows the potential for solutions to be found from a surface engineering approach. In this work both physical modifications

and chemical modifications were investigated for potential solutions. Investigations by other researchers into the development of bleed free adhesive formulations has been performed[6-7] and this is reviewed in *Section 2 Literature Review*. However, this approach could lead to a number of issues surrounding adhesives used for optoelectronics in that they are extensively characterised and tested at great cost before being marketed. Modifications to adhesives would have implications throughout the assembly line. This approach therefore fails to meet the conditions above and so is not investigated in any great depth in this work. It was considered preferable to undertake a surface engineering approach to finding discrete solutions.

Following the review of the literature and the initial experimental characterisation of the adhesives and adherends to identify the key parameters of interest, a number of surface engineering approaches were taken to identify potential solutions to the adhesive control problem. The characterisations of as-received substrates had identified variations in chemical species on surfaces which had ostensibly undergone the same processing. The presence of these species directly affected the occurrence of epoxy bleed and so they were investigated in the work described in *Section 5.3 Identification and Removal of Contamination* to identify their source and potential for controlling them. The implications of this contamination for module integrity are explored with both physical measurements of bond strength in *Section 5.1 Characterisation of Surfaces and Adhesives* and by a more theoretical approach in *Section 5.4 Application of Wenzel and Cassie Theory to Experimental Data*, by the application of theories described in the literature review. It was found that epoxy bleed could be controlled if there was sufficient build up of organic contaminants from environmental sources. However, this was seen to take an extended period of time making the practicality as a solution debateable.

The conclusions drawn from the data gathered for *Sections 5.1-5.4* justified the development of a capability for direct engineering of the substrate surfaces. The identification of surface energy as a key parameter affecting the behaviour of adhesives on surfaces lead to the consideration of chemical modification methods producing stable surface energies, namely the

26

application of self assembled monolayers (SAMs). The application and behaviour of these monolayers was the subject of much investigation described in *Section 5.5 Self Assembled Monolayers*. The application of different types of SAMs was extensively studied and their effectiveness was found to be linked to the chemical bond by which they were joined to the substrate. A method for chemical surface energy homogenisation of heterogeneous metal/ceramic surfaces through the multiple stage application of SAMs was also developed and is the subject of a patent application[8].

The experimental observation that roughness also affects the flow of the adhesives, contrary to some literature reports, lead to the investigation of physical surface engineering for the production of artefacts on the substrate surfaces with the aim of controlling adhesives. The resistance of the ceramic materials to heat, chemicals and abrasives left few potential methods for creating the desired features, however laser micromachining showed to be very promising and is described in *Section 5.6 Laser Micromachining*. Various methods of material removal via lasers were explored and characterised for their capabilities. This work also lead to the identification of potential applications for laser micromachining beyond control of epoxy bleed and fillet size in the field of optoelectronics manufacturing. The feasibility of further methods for the control of adhesives on ceramics, i.e. photolithographic patterning of SAMs, were also considered briefly as reported in *Section 5.5 Self Assembled Monolayers*.

Each of the solutions developed and the results of the extensive testing conducted was presented to the industrial sponsor (Oclaro plc) for assessment of suitability for implementation into the optoelectronics assembly line. As a result of their assessment Oclaro funded a currently pending US patent application[8] covering the technique for SAM coating of heterogeneous surfaces, which is reproduced in *Section 9.2 Appendix 2 – Patent Application*.

---

[1] Hall, J.; Edge, C.; Randle, F.; Pope, S.; Fraser, J.; Loosley, J.; Kimber, E.M.; Firth, P "Integrated tunable transmitters for 10Gb/s long-haul DWDM applications" 53rd Electronic Components and Technology Conference, 2003 Page(s):796 – 800

[2] Lo, J.C.C.; Lee, S.W.R.; Lee, S.H.K.; Wu, J.S.; Yuen, M.M.F. Modified passive alignment of optical fibers with low viscosity epoxy flow running in V-grooves, Electronic Components and Technology Conference, 2004. Proceedings. 54th Volume 1, Issue , 1-4 June 2004 Page(s): 830 - 834

[3] Hsiung, J.C. Pearson, R.A. Lloyd, T.B. "A surface energy approach for analyzing die attach adhesive resin bleed" Journal of adhesion science and technology 2003 Vol. 17 Issue no. 1 pp 1-14

[4] Burmeister, M. "Elimination of epoxy resin bleed through thin film plasma deposition" Proceedings of SPIE--the international society for optical engineering 2003 Vol. 5288 pp 780-785

[5] Surface analysis and pretreatment of plastics and metals / edited by D.M. Brewis. -- London : Applied Science, 1982

[6] Neff, B.; Huneke, J.; Nguyen, M.; Liu, P.; Herrington, T.; Gupta, S.K. No-bleed die attach adhesives, Advanced Packaging Materials: Processes, Properties and Interfaces, 2005. Volume , Issue , 16-18 March 2005 Page(s): 79 - 81

[7] Law, W.l. Erfe, E. Vaquilar, A. Khor, L. Thong, K. Yong, N, Ng, P.N. Wafer Backside Coating of Electrically Conductive Die Attach Adhesives for Small IC Packaging, Electronic Packaging and Technology Conference 2009

[8] USPTO application no 61/266,611; Filed 04 December 2009. Surface treatments and coatings to reduce adhesive spread, Inventors: O. Williams, C.Liu, D.P.Webb, P.Firth. Assignee: Oclaro Technology plc

2 Literature Review

2.1 Optoelectronics Background

The optoelectronics industry has been a multi billion dollar industry since the mid 90s[1] and is continuing to grow. It is an area of extensive applications ranging from telecommunications and electromagnetic sensing to personal products such as home computers. The sector of the optoelectronics industry of interest in this work is primarily telecommunications, and in particular the optoelectronic modules used for fibre optic transmission and signal reception. The issues surrounding the current manufacturing methods of these optoelectronic modules are described in the *Introduction* of this work. The layout of the modules and assembly processes used are considered below.

2.1.1 The Optoelectronic Module Assembly Processes

The optoelectronic module assembly process includes such processes as: surface adhesive mounting, wire bonding, active alignment, solder paste application, reflow, adhesive full curing, adhesive snapping (UV tacking), die bonding and others. It also includes various intermediate steps, such as plasma cleaning, which tend to be specific to the particular manufacturer and dependent upon their specific methods.
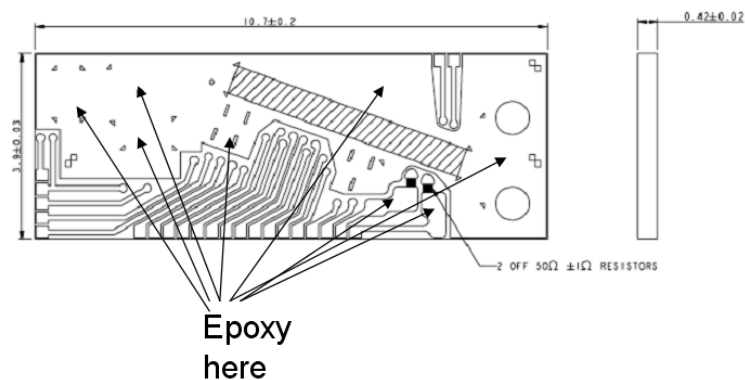
Figure 2.1-1 A typical optoelectronic carrier sled with metallisation pattern and areas for epoxy application highlighted (image courtesy of P. Firth, Oclaro).

Figure 2.1-1 shows a typical optoelectronic assembly substrate metallised according to the pattern shown in the figure. The application positions for epoxy adhesives are shown.

In terms of epoxy adhesives a number of different epoxies are applied. In this study a thermally conductive boron nitride filled adhesive and an electrically conductive silver flake filled adhesive are used. However, others such as optical adhesives may be used in the assembly process[2]. Assembly of optical and other components with adhesives is a multiple stage process including a number of cure schedules in between. In active alignment processes adhesives are UV snapped (partially cured into tack properties to secure parts) before being cured into their final positions. Other adhesive or solder processes include the bonding of the laser diode to a heat sink and then to the ceramic carrier. Die attach techniques are used to achieve this[2].

Once the ceramic carrier or sled is fully assembled it is then inserted into a Kovar box which allows interconnection with exterior drive circuits and fibre optics. The ceramic carrier and Kovar box are baked at 150°C for 12 hours to remove any residual moisture and contaminants, before being hermetically sealed. This completes the assembly of the optoelectronic module which is then ready to be interconnected to exterior electronics and other optoelectronic assemblies.

2.1.2 Optoelectronic Components and Materials

Optoelectronic materials are chosen for their properties supporting the required functionality of the component. Disregarding materials used for optical components (lenses, mirrors, beamsplitters and various others) which are not relevant to this work, materials used for assembly may fall into the categories of semiconductors, solders, adhesives, submounts, heatsinks and enclosures. For this work the categories of interest are submounts and adhesives. Submount materials currently in use are mainly aluminium oxide, and aluminium nitride. Both are used for their similarity to the CTE of silicon and reasonably good thermal conductivity (for ceramics). Where thermal conduction is of special importance aluminium nitride is used, and where thermal conduction is not imperative and cost is an issue, aluminium oxide is used which is cheaper than aluminium nitride.

Boron nitride filled epoxies are used for their thermal conduction and electrical insulation combined with thermal stability and small shrinkage percentage.

Silver filled epoxies are used where good electrical conduction and/or good thermal conduction is required. The epoxy phenol novolac is used in the formulation of the silver filled epoxy for enhanced thermal stability.

2.1.3 Surface Mounting of Components

For the surface mounting of components with adhesives it is first necessary to apply the adhesive to the adherend material. This can be done in a number of ways such as stencil printing, pin transfer and syringing[3]. Stencil printing is similar to the solder paste application process whereby paste is pushed through a stencil and coats the areas adhesive is required. Pin transfer is a method which relies on the properties of the adhesive, such as surface tension and viscosity, for reliable application. A single pin, or an array of pins arranged in the pattern of the areas adhesive spots are needed can be used. The process relies upon the greater affinity the adhesive has for the adherend than the metallic pin, and gravity and the adhesive surface tension for consistent adhesive volumes[4]. Syringing of adhesives is the commonly used process with the most accuracy and reproducibility. Adhesives are forced though a hollow needle by a drive circuit which applies a precise pressure for a precise time to achieve a desired volume of adhesive. A syringe system can be typically programmed to dispense adhesives in the desired areas, to the movement accuracy of its X-Y table.

2.1.3.1 Active Alignment

Active alignment is a feedback driven process in which optical components are moved whilst laser light is applied to them and an output signal is measured, until the maximum light coupling efficiency is achieved. Active alignment is the process within optoelectronics assembly which has prevented the development of a fully automated assembly procedure[5] and is therefore responsible for a considerable labour cost in the assembly process. Alignment of a laser beam with an optical component is defined with respect to the centre of the Gaussian power distribution of the laser beam[6]. It is a slow process which can contribute over 60% of the total labour cost in the assembly process. See Figure 1-4 for a fuller breakdown of labour costs. When used in conjunction with surface mount adhesives, components are

placed on pre-dispensed adhesive spots, active aligned and then UV snapped to hold the component in place until the adhesive is thermally cured. This process is undertaken for all components requiring high coupling efficiency and positional accuracy on the micron scale.

2.1.3.2 Passive Alignment

Passive alignment is the geometric positioning of objects which have multiple degrees of freedom by features in an assembly which remove some of these degrees of freedom. It is attractive by comparison with active alignment as it is an automatic alignment process which is the result of careful design, and not labour intensive. However, it is has only recently been used to achieve alignment of submicron accuracy in the lab[7] for optical fibres, which have fewer degrees of freedom to begin with. Thus it is desirable to replace active with passive alignment where possible in optoelectronics assembly due to the labour and time saving it would offer.

2.2 Material Properties

2.2.1 Ceramics

The ceramic materials of interest in this study are alumina and aluminium nitride. Material parameters of the samples are shown in Table 2.2-1 below[8].

	Aluminum Oxide	Aluminium Nitide
Formulae	Al_2O_3	AlN
Knoop Hardness	2100	1225
Specific Gravity	4	3.26
Specific Heat kJ/kgK @20°C	0.82	1.7
Service Temperature °C	1650	1100
Thermal Conductivity W/K/m @20°C	36	185
Resistivity Ohm m 20°C	10^16	10^11
Thermal Expansion x10-6 m/k	9.5	5.6
Modulus GPa @20°C	370-407	345
Tensile Strength GPa @20°C	1400-2100	6900
Stability	Resistant to all but HFl	Reacts with water

Table 2.2-1 Properties of pure α aluminium oxide and aluminium nitride ceramics.

2.2.1.1 Preparation of Ceramics for Analysis

Ceramic preparation guidelines were found in the literature in an article by Elssner et al[9]. All material preparation for this investigation was performed to these guidelines.

2.2.2 Adhesives

Two commercial epoxy adhesives were used in this study. Each were prepared by EPO-TEK®, an adhesive manufacturing firm. EPO-TEK® H20E is a silver loaded electrically conductive epoxy. It is designed specifically for conductive bonds in optoelectronic applications. EPO-TEK® 930-4 is a boron-nitride fibre loaded thermally conductive epoxy. It is designed with high heat dissipation and electrical insulation properties for applications requiring high thermal conductivity and operating temperatures. Table 2.2-2 below shows important properties of the adhesives[10,11].

	H20E	930-4
Glass Transition Temp °C	>80	>90
Viscosity cPs	2200-3200	10500-15500
Thermal Expansion Below Tg °C x10-6	31	27
Thermal Expansion Above Tg °C x10-6	120	136
Lap Shear Stress MPa	10.34	>13.29
Die Shear Stress MPa	>23.44	>35.16
Degradation Temp °C	410	425
Thermal Conductivity W/mK	2	1.67
Resistivity Ohm-cm	<0.0004	>2x1013
Continuous Operating Temp °C	200	200
Pot Life /days	4	1
Cure time 175°C	45 seconds	---
Cure time 150°C	5 minutes	10 minutes
Cure time 120°C	15 minutes	---
Cure Time 100°C	---	4 hours

Table 2.2-2 Properties of the commercial adhesives, EPO-TEK 930-4 and H20E investigated in this work

2.2.3 Optoelectronic Interconnection Metallisations

Optoelectronic metallisations used in the optoelectronic assemblies of interest consist of layers of titanium, platinum and gold or titanium, palladium and gold. Gold is used as the top and thickest layer (1-5µm) metallisation whilst titanium is used for its adhesion to the ceramics. The metallisations are applied via electroplating.

2.3 Theories of Adhesion

The theories of adhesion are attempts to model interactions between an adhesive and an adherend[12]. As would be expected, different systems show different interactions, both physical and chemical. The set of theories of adhesion are not all relevant to every adhesive/adherend system[13]. However, all adhesive/adherend systems show evidence consistent with at least one of the current accepted theories.

2.3.1 Mechanical Interlocking Theory

Mechanical interlocking is the presence of an adhesive material in the surface texture of the adherend. Upon application the adhesive flows into any pores, holes and surface features. Once the adhesive hardens the adherends are held together mechanically by the adhesive being unable to leave the areas it flowed into when in its liquid state, without energy absorbing deformations[14]. For interlocking to occur the adhesive must displace any air remaining between itself and the adherend. Therefore the surface energy of the adherend must be sufficiently high for adhesive attraction, and the surface tension of the adhesive must be sufficiently low so wetting is not impeded[15].

This theory supposes the adherend surface to be non-uniform or rough. All surfaces have these characteristics to a varying degree. The roughness of a surface is generally considered beneficial to an adhesive bond due to the inherent increase in surface area[12]. Increasing the adherend surface area will increase the contact area between the adhesive and adherend, providing the surface energies are sufficient for wetting to occur. If intermolecular or interfacial attraction form the basis for adhesion in the system then an increase in surface area will result in an increase in the total surface interaction energy.

2.3.2 Diffusion Theory

Diffusion is the passage of one substance into an adjacent one, resulting in a mixture. Diffusion can apply to only part of a long chain molecule such as a polymer. In the context of an adhesive this means diffusion across the adhesive/adherend interface and can result in single molecules lying on both

sides of the interface. This mechanism is thought to occur only when the materials are mutually soluble, for example with two polymers. It is therefore unlikely a ceramic and a polymer will exhibit this adhesion mechanism.

2.3.3 Electrostatic Theory

The electrostatic theory states that[12]: the work of adhesion W_a between adherend and adhesive is

$$Wa = \frac{\delta^2 h}{2\varepsilon}$$

Equation 2.3-1

Where Wa is the work of adhesion, δ the surface charge density, h the distance between the surfaces and ε the dielectric constant of the medium.

The electrostatic contribution to the bond strength is thought to be very small except for specific cases unrelated to this work.

2.3.4 Adsorption Theory

This theorises that the bond strength arises from intermolecular forces such as van der Waals forces[12]. Intimate molecular contact is required for these forces to occur as the interaction range of van der Waals forces is approximately 0.4nm. For the occurrence of the necessary contact good wetting of the adhesive on the adherend is paramount. Any air bubbles or unfilled regions of the adherend topography can lead to both decrease of contact area and residual stresses at the small air bubbles[15], both of which would result in a weaker bond.

2.3.5 Chemical Bonding Theory

This is the formation of covalent bonds across the adhesive/adherend interface[13]. For this to occur the adhesive and adherend must be mutually chemically reactive to produce the covalent bonds. Further to the necessity of reactivity, intimate contact between the adhesive and adherend is required.

The presence of a hydroxyl group proves beneficial for formation of covalent bonds, and is often found in abundance in epoxies.

Surfaces and adhesives are frequently not mutually reactive. Coupling agents and adhesion promoters are available to act as an intermediate layer between non-reactive adhesive and adherend. These work by forming covalent bonds with both materials[12,16].

2.3.6 Work of Adhesion

The work of adhesion is defined as the energy input required to form two new surfaces at an interface between two adhered materials[12,17]. If cohesive failure occurs, i.e. failure through a material, rather than at an interface, then the work of cohesion is described by:

$$W_C = 2\gamma$$

Equation 2.3-2

Where W_c is the work of cohesion and γ is the surface free energy of the material.

I.e.; the work that is required to create two new surfaces with surface energy γ. When dealing with a system where more than one material is present, such as an adhesive on an adherend, the work of adhesion is determined by the work to create the two new surfaces less the energy recovered by destroying the interface. Equation 2.3-2 above thus becomes the Dupré equation:

$$W_A = \gamma_1 + \gamma_2 - \gamma_{12}$$

Equation 2.3-3

Where W_A is the work of adhesion, γ_1 and γ_2 are the respective surface energies of the materials and γ_{12} is the interfacial energy.
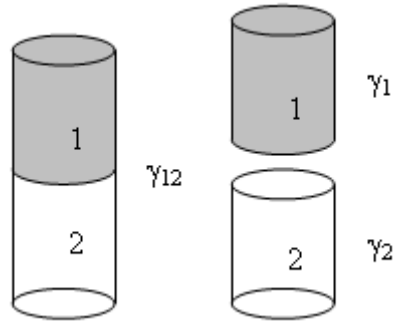
Figure 2.3-1 Depiction of the work of adhesion.

Figure 2.3-1 shows the energy expended upon failure of an adhesive should be the sum of the surface energies of the adhesive and adherend materials less the energy of the interface.

The work of adhesion theory is a simplification which neglects to include energy absorbtion due to deformation of the materials. Ahagon and Gent related practical adhesion to the theoretical work of adhesion[12] by the inclusion of a term describing energy dissipations in a bond:

$$W_{Actual} = W_A + f(W_A)\zeta$$

Equation 2.3-4

Where ζ represents the viscoelastic properties of the adhesive and consequently represents energy absorption of the joint. If the adhesive and adherend materials are brittle then the bond failure energy is equivalent to the work of adhesion. If the adhesive or adherend exhibits deformation before failure a further energy component is introduced.

Equation 2.3-3 above can also be written in terms of state interfaces[18]:

$$W_A = \gamma_{lv} + \gamma_{sv} - \gamma_{sl}$$

Equation 2.3-5

Where γ_{lv} is the liquid-vapour interfacial tension, γ_{sv} is the solid-vapour interfacial tension and γ_{sl} is the solid-liquid interfacial tension.

Young linked the contact angle of a liquid to the interfacial tensions:

$$\gamma_{lv} \cos\theta + \gamma_{sl} = \gamma_{sv}$$

Equation 2.3-6

Where γ_{lv} is the liquid/gas interfacial tension, γ_{sl} the solid/liquid interfacial tension, γ_{sv} the solid/gas interfacial tension and θ is the contact angle at the solid/liquid/gas interface.

The Young equation, Equation 2.3-6, can be substituted into the modified Dupré equation to form an expression incorporating easily measured parameters[18]:

$$W_A = \gamma_{lv}\left(1 + \cos\theta\right)$$

Equation 2.3-7

Where θ is the equilibrium contact angle the liquid forms on the solid and γ_{lv} is the liquid-vapour surface tension.

Fowkes suggested that the surface energy of a solid or liquid is the sum of the effects of dispersion forces, polar interactions and hydrogen bonding[19]:

$$\gamma = \gamma^d + \gamma^p + \gamma^h$$

Equation 2.3-8

Whereby the total work of adhesion becomes:

$$W_A = W_A^d + W_A^p + W_A^h$$

Equation 2.3-9

Owens and Wendt then suggested the hydrogen bonding interaction could be considered together with polar interactions[19] . This simplifies Equation 2.3-8 and Equation 2.3-9 to the polar and dispersion terms only, as the hydrogen bond term is considered together with the polar term.

Fowkes theorised the dispersive forces in a system are more prevalent and therefore account for the larger fraction of the work of adhesion. He included the assumption that the rest of the work of adhesion was due entirely to acid-base, and not polar interactions[20].

$$W_A = 2\left(\gamma_A^d \gamma_B^d\right)^{1/2} + W_{ab}$$

Equation 2.3-10

Where W_{ab} is the work of adhesion due to acid base interactions.

By considering the polar and dispersive terms for the surface free energy, Owens and Wendt suggested the work of adhesion could be calculated from:

$$W_A = 2\left(\gamma_A^d \gamma_B^d\right)^{1/2} + 2\left(\gamma_A^p \gamma_B^p\right)^{1/2}$$

Equation 2.3-11

Where the components of the surface energy are calculated using the theory of fractional polarity[19].

The above relationships suggest that the maximum possible work of adhesion occurs when the contact angle of the system tends towards zero (for a partially wetting liquid). For this to occur the surface energy of the adherend and the surface tension of the adhesive must be compatible for a contact angle of zero. This means the attraction of the adhesive molecules to the adherend is greater than the mutual attraction of the adhesive molecules.

2.4 Wetting, Contact angle and Surface energy

2.4.1 Contact Angle

Epoxy adhesives are applied to the adherend surfaces in their liquid state. Therefore the system can be described using interfacial tensions at the three interfaces formed between the liquid adhesive, the solid adherend and the gaseous atmosphere. The relationship of interfacial tensions at the different interfaces can be determined by considering the balance of surface forces at the line of contact of the three planes shown in Figure 2.4-1 below. The balance is expressed by the Young equation[21], Equation 2.3-6. This can be arranged with respect to contact angle, which as defined in Figure 2.4-1:

$$\cos\theta = \frac{\gamma_{sv} - \gamma_{sl}}{\gamma_{lv}}$$

Equation 2.4-1
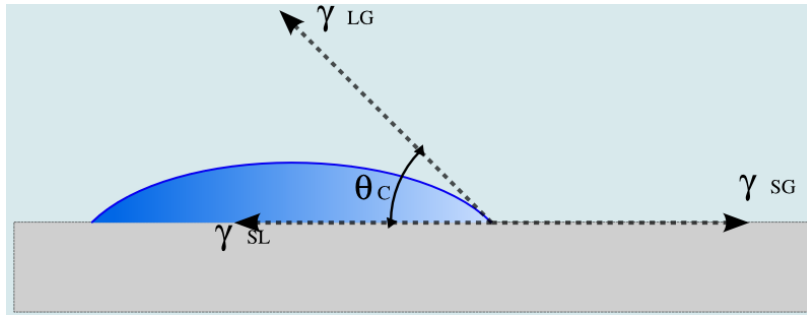
Figure 2.4-1 The force balance of interfacial tensions of a liquid drop on a solid surface.

For cases such as the one described in[22] where the liquid wets the surface completely (contact angle of zero), the above equations Equation 2.3-6 and Equation 2.4-1 are not useful and it is more convenient to consider wetting.

2.4.2 Surface Energy

Surface energy can be defined as the quantification of the energy required to disrupt the intermolecular bonds of a material in order to create a new surface[18]. This is evident when considering that material in bulk form must be more energetically favourable than surfaces. If this were not so then material in bulk form would not be stable. Therefore there must be an associated energy input for the formation of a surface.

As described in Equation 2.3-2 the surface energy of a material can be described as half the work of cohesion, or as explained above half the energy required to form two new surfaces. This equation applies under the conditions that the material is pure, defect free, and the surfaces are created in a vacuum[21].

The surface energy of a material is relevant to this investigation when considered in terms of contact angle and wetting.

2.4.3 The Effect of Surface Roughness

The above theories make the assumption that the surface is homogeneous and smooth. Surface roughness as a quantifiable parameter was first introduced to contact angle theory by Bikerman[23] and was later refined by Wenzel. Surface roughness effects on the contact angle can be considered using the Wenzel equation[24,25]:

$$\cos\theta_r = r\cos\theta_{true}$$

40

Equation 2.4-2

Where the roughness factor r is defined as the ratio of the true surface area to the apparent area. θ_r is the apparent contact angle formed on the rough surface and θ_{true} is the contact angle which would be formed on the same material if it were flat and homogeneous.

The true surface area is the resultant area created by all of the deviations from the theoretical flat surface[26].

Equation 2.4-2 shows that if θ_{true} is less than 90° the apparent contact angle will be decreased by the effects of roughness. However if θ_{true} is more than 90° then the roughness has the effect of increasing the apparent contact angle[27].

When considering Equation 2.4-2 at the microscopic level the apparent contact angle θ_r on a rough surface is[26]:

$$\theta_r = \theta_{true} \pm \alpha$$

Equation 2.4-3

Where α is the slope of the roughness profile of the surface at the point of contact between the solid and liquid phases.

Figure 2.4-2 below shows the formation of a droplet on an idealised rough surface and the associated effect of the roughness profile.

Equation 2.4-3 above and Figure 2.4-2 are of disputable usefulness in practice. The roughness profiles of most surfaces are invisible without a microscope[28]. Profiles created by common manufacturing methods are usually on the micrometre scale. To view an image like Figure 2.8-1 in practice would require looking at the cross section of a liquid droplet with a microscope. This would be necessary to measure the angle α at any point on the interface. It is highly unlikely that the angle α would remain constant around the interface unless the surface had a radial surface pattern.
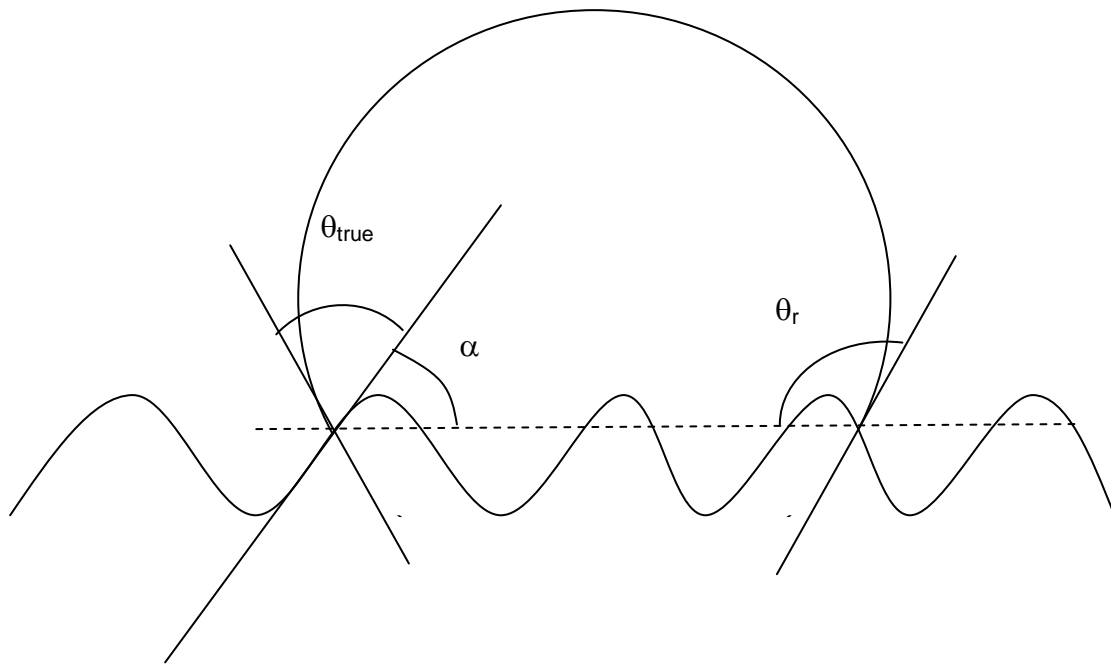
Figure 2.4-2 The microscopic effect of roughness upon contact angle.

Some mechanical machining methods such as milling do produce a repeatable pattern over the surface such like the one in Figure 2.4-2[29]. However, if this is considered in three dimensions one would see that Figure 2.4-2 be present at the situation of one infinitesimally small slice.

Johnson and Dettre considered this situation further and investigated a model to predict the behaviour of a liquid on an idealised rough surface[30]. This was supported with experimental data[31]. Although a number of assumptions were made in the work, i.e. surface is a constant sinusoid shape and there is no effect of gravity, they found a correlation between their theory and the experimental work. The investigation extended to contact angle hysteresis and composite surfaces. The models are too lengthy to be described in this thesis and so are given here only as references. Another model was proposed by Ruckenstein and Berim[32], and a simplified one by Tamai and Aratani[33]. Both models require a large number of assumptions, mostly involving the representation of a rough surface, which do not represent well the random granular nature of ceramic surfaces. Therefore the Wenzel equation is the only model used in this work to describe the effects of roughness on wetting.

2.4.4 Heterogeneity

The subject of heterogeneity is studied in *Section 5.4 Application of Wenzel and Cassie Theory to Experimental Data*.

2.4.5 Wetting

Wetting can be considered in terms of partial wetting and complete wetting. Complete wetting means that the contact angle between solid and liquid tends toward zero so that no stable droplet is formed but the droplet spreads over the surface. When $\theta \rightarrow 0$ the Young equation, Equation 2.3-6, ceases to be applicable and the free energy change for the production of the solid/liquid interface is given the name spreading coefficient S_{ls}, as shown in Equation 2.4-4:

$$S_{ls} = \gamma_{sv} - \gamma_{sl} - \gamma_{lv}$$

Equation 2.4-4

However, this definition is again based on a number of assumptions including that the surface has no roughness. A more practical version of Equation 2.4-4 was derived by Hunstberger[34] in which the Wenzel ratio r as defined in *Section 2.4.3 The Effect of Surface Roughness* is included:

$$\Delta G_{sl} = -\gamma_{lv}(1+r)\cos\theta$$

Equation 2.4-5

Where G is the free energy of formation of the solid/liquid interface, r is the Wenzel ratio and theta is the true contact angle.

This Equation 2.4-5 shows that for any system in equilibrium with negligible roughness any liquid applied will wet the surface (form intimate contact between liquid/solid), but also that a rough surface will be wetted if the true surface contact angle of the liquid is below 90°.

Figure 2.4-3 below shows a wetted and a non wetted or composite surface.
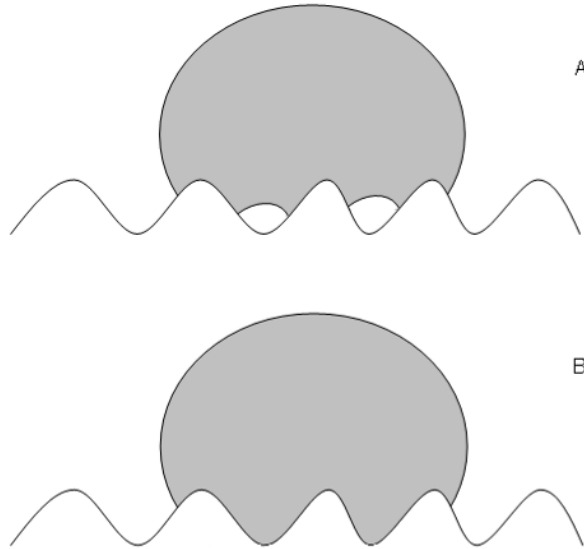
Figure 2.4-3 A – a non-wetted composite surface, B – a wetted rough surface.

The above Equation 2.4-5 makes the assumption that the surface is pure and free from contamination.

When a liquid is unable to penetrate the roughness profile the surface is known as a composite surface[26]. When this occurs Equation 2.3-6 becomes Equation 2.4-6[26,35]:

$$\cos\theta = \Omega_{sl}\cos\theta_1 - \Omega_{lv}$$

Equation 2.4-6

Where Ω_{sl} is the solid liquid interface area and Ω_{lv} is the liquid vapour interface area. Equation 2.4-6 above reduces to Equation 2.3-6 when $\Omega_{sv} = 0$.

This is believed to occur if the true contact angle is sufficiently high to prevent wetting into the surface texture. As described by the Young equation, Equation 2.3-6, the contact angle is determined by the surface energies. Therefore the extent of penetration into surface texture is determined by the surface energies, which are represented by the contact angle. It has also been observed that increasing the roughness of a surface can change a non-composite surface into a composite surface[31].

Wetting is also affected by the direction of the surface texture. Furrows in the surface can cause wetting along their axis whilst random roughness creates a

uniform effect. When the furrows are considered the excessive wetting along their axis can be described as capillary action:

$$\Delta P = \frac{2(\gamma_{sv} - \gamma_{sl})}{R}$$

Equation 2.4-7

Where ΔP is the pressure drop along the furrow, and R is the average radii.

However, if the true contact angle of the system is equal to zero then:

$$\Delta P = \frac{2\gamma_{lv}}{R}$$

Equation 2.4-8

This suggests that to obtain a large ΔP and so excessive wetting, γ_{sl} should be as small as possible, which is consistent with experimental work[22].

2.4.6 Wetting and Spreading in Relation to Adhesion

A requirement for good adhesion is intimate contact between adhesive and adherend. This is supported by the discussion of composite surfaces and the work of adhesion.

All the theories of droplet formation presented above agree that a solid/liquid interface is formed when a liquid lies on a surface, and that the energy change on formation of this interface is determined by the properties of both the liquid and the solid[36].

Huntsberger[34] proposed that the short time an adhesive spends as a liquid on the surface, and its high viscosity, promote creation of a composite bond, as insufficient time is given for penetration. An equation derived from a model for the dynamics of adhesive penetration into the roughness profile of a surface with respect to time, which incorporates viscosity is[19]:

$$t = \frac{2\eta}{\gamma \cos\theta} \bullet \frac{x^2}{r}$$

Equation 2.4-9

Where η is the surface tension of the adhesive, γ is the surface energy of the adherend, θ is the true contact angle, t is the time for complete penetration, x is the distance moved and r is the radius of the capillary.

This is of disputable usefulness in calculating penetration time for a real surface due to the assumption that the cavities to be penetrated are cylindrical and of constant radius. Such surfaces would have to be specifically manufactured for such a structure and would be considered porous. The ceramics used in this study are >99% dense, so no such porosity would be present in the surface structure.

2.4.7 Estimation of Surface Energy Through Contact Angle Measurements

The use of contact angles to measure surface energy is not a direct measurement method. The term surface energy estimation is used for the mathematical manipulation of the contact angles which yield the surface energies of the solid. In this work the method according to Owens and Wendt[37] is considered along with the method according to Wu[38]. Both of these methods yield dispersive and polar components of surface energy. The difference between the two methods is that the Owens Wendt method uses the geometric mean of the surface tensions to yield results, where Wu uses the harmonic mean of the surface tensions. The equations and calculations surface energies according to these two methods are considered in *Section 9.3 Appendix 3 – Evaluation of Surface Energy Estimation Methods*.

2.4.8 Three Phase Contact Line

Contrary to the assumptions in the theories presented above on the effect of roughness on wetting, and of those leading to the Young equation itself, Starov et al[21] consider that there is no abrupt interface between the solid and the liquid, but instead a gradual transition zone between the liquid droplet and a thin film of liquid which forms on the solid surface.
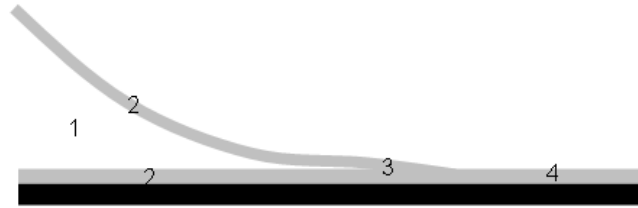
Figure 2.4-4 The three phase contact line in Starov et al's theory

Figure 2.4-4 above shows Starov's theorised three phase contact line where the numbers represent:

1. Bulk liquid

2. Boundary layers of the liquid-air and solid-air interfaces

3. Boundary layer overlap region

4. Flat thin equilibrium film

The motivation for the theory is that wetting is in fact a non-equilibrium condition. Starov's work suggests that the length scale of this phenomenon is much smaller than the scale of epoxy bleed and so it is unlikely that this theory can be applied to this work.

The supposition of a three phase contact line would make the Young equation, Equation 2.3-6, thermodynamically invalid. This is an area under dispute in the literature, with work both supporting the validity of the Young equation[39] and disputing it[21]. For this work, as with many other studies, the Young equation will be considered valid.

2.4.9 Calculating and Interpreting the Wetting Envelope

The wetting envelope is a plot which describes a given surface. It is a contour line which represents the properties of all liquids which will give rise to a specified contact angle on the surface. It is calculated by reversing the Owens Wendt method. First the Owens Wendt equation:

$$\gamma_{sl} = \gamma_s + \gamma_l - 2\left(\sqrt{\gamma_s^D \cdot \gamma_l^D} + \sqrt{\gamma_s^P \cdot \gamma_l^P}\right)$$

Equation 2.4-10

47

Was combined with the Young equation, Equation 2.3-1, and the consideration that for complete wetting cosθ=1, to get:

$$\gamma_l^D + \gamma_l^P = \left(\sqrt{\gamma_s^D \cdot \gamma_l^D} + \sqrt{\gamma_s^P \cdot \gamma_l^P} \right)$$

Equation 2.4-11

In a wetting envelope plot the polar and dispersive components of the test liquid surface tension form the two axes of a coordinate system. Any particular liquid is then a coordinate on the plot, and the wetting parameter W of the liquid is the geometric quantity:

$$W = \sqrt{\left(\gamma_l^D\right)^2 + \left(\gamma_l^P\right)^2}$$

Equation 2.4-12

With an associated angle phi given by:

$$W \cos \phi = \gamma_l^D$$

Equation 2.4-13

and

$$W \sin \phi = \gamma_l^P$$

Equation 2.4-14

Inserting Equation 2.4-13 and Equation 2.4-14 into Equation 2.4-11 gives:

$$W \cos \phi + W \sin \phi = \left(\sqrt{W \cos \phi \cdot \gamma_s^D} + \sqrt{W \sin \phi \cdot \gamma_s^P} \right)$$

Equation 2.4-15

Resolving for W as a function of ϕ, Equation 2.4-15 can be evaluated over a range of ϕ from 0 to 90° using:

$$W(\phi) = \frac{\sqrt{W \cos \phi \cdot \gamma_s^D} + \sqrt{W \sin \phi \cdot \gamma_s^P}}{\cos \phi + \sin \phi}$$

Equation 2.4-16

This allows plotting an isoline of constant, zero contact angle on the wetting envelope plot, as seen in Figure 2.4-5 for low density polyethylene. The wetting envelope can also be plotted for any particular non-zero contact

angle. For example Figure 2.4-5 also shows the transition point to poor wetting, 90°.

To plot a contact angle other than zero the W parameter must be multiplied by

$$\frac{2}{1+\cos\theta}$$, where θ is the desired wetting envelope contact angle.
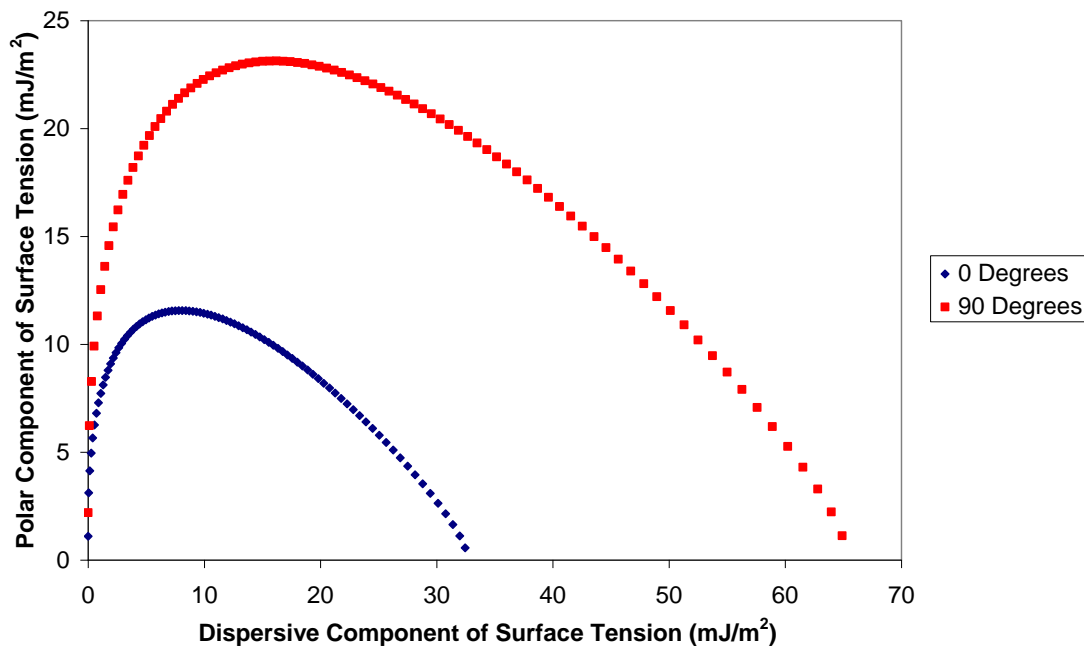
Figure 2.4-5 The 0°and 90° wetting envelopes for low density polyethylene.

Wetting envelopes can be useful for visually identifying regimes of behaviour of liquids on a particular surface. An example is the regime for expected formation of composite bonds, where air pockets are included at the interface, as this is believed to happen above a liquid contact angle of 90°. As the plot gives information on the effects of both the polar and dispersive components of the surface tension of the liquids, it can be applied in choice of adhesive and surface treatment to optimise adhesion.

2.5 Adsorption

Adsorption is the adhesion of molecules of gas, liquid, or dissolved solids to a surface which is a consequence of surface energy. Throughout the bulk of a material all of the bonding requirements of the constituent atoms are satisfied by other atoms of the material. However, atoms on the surface of the material are exposed and not fully surrounded by other atoms of the bulk material,

therefore they can attract adsorbates. The mechanism of the adhesion between the adsorbent and adsorbate depends on the properties of the surfaces and adsorbates present, but the adsorption process can be considered physisorption – the interactions of weak van der Waals forces, or chemisorption - the formation of covalent bonds between the adsorbent and adsorbate. In the situation considered in this chapter, physisorption is the likely mechanism for adsorption of adventitious carbon molecules bearing few functional groups onto the ceramic surfaces, however it is possible that chemisorption take place should the surface be exposed to fatty acids[40].

The process of adsorption is frequently described through isotherms, the derivations of which differ in the assumptions they apply to the description of the adsorption process. The process is usually described as the amount of adsorbate adsorbed onto the adsorbent as a function of the adsorbate concentration or partial pressure.

The first reported application of an expression to predict adsorption was exclusively for the adsorption of gaseous adsorbates[41]

$$\frac{x}{m} = k P^{\frac{1}{n}}$$

Equation 2.5-1

Where x is the quantity adsorbed, m is the mass of adsorbent, k and n are experimentally derived constants for a specific adsorbent/adsorbate combination at a specific temperature and P is the partial pressure of the adsorbate.

In the case of this work this expression is of limited practicality unless extensive experimentation is first undergone to identify the adsorbates, their partial pressures, and quantify values of k and n. There is some usefulness to the expression, however, in offering details on the effects of concentration upon the amount of adsorbate adsorbed.

The Langmuir isotherm (meaning the process occurs at constant temperature) was proposed in 1916 and, like the expression above, related the adsorption

of molecules, at constant temperature, onto a solid surface to concentration of the adsorbate in a liquid, or partial pressure of an adsorbate in a gas[42]:

$$\frac{\delta\theta}{\delta t} = k_a c(1-\theta)$$

Equation 2.5-2

Where k_a is the rate constant, c is the concentration, t is time and θ is the fractional coverage. The Langmuir model extends to desorption also:

$$\frac{\delta\theta}{\delta t} = k_d \theta$$

Equation 2.5-3

Where kd is the rate constant of desorption.

When equilibrium is reached i.e. the adsorption rate is equivalent to the desorption rate, the surface coverage is given by Langmuir to be[43]:

$$\theta = \frac{KP}{1+KP}$$

Equation 2.5-4

Where θ is the coverage of the surface as a fraction, P is the partial pressure in the gas phase and K is the Langmuir adsorption constant which is equal to k_a/k_d.

The assumptions of the work by Langmuir are:

- Multilayers do not form, only monolayers, i.e.; layers of adsorbate are not adsorbed onto existing layers of adsorbate.

- The surface is a series of receptive sites which are identical and can absorb only one atom

- The adsorption of molecules is completely independent on the status of neighbouring sites, i.e.; adsorbed molecules do not affect adsorption of further molecules

It was proposed by Brunauer, Emmet and Teller that multilayers do form – that adsorbates do adsorb onto adsorbed adsorbates. This model, known at BET, is a modification of Langmuir's mechanism to incorporate the formation of multilayers[44]:

$$\frac{x}{v(1-x)} = \frac{1}{v_{mon}c} + \frac{x(c-1)}{v_{mon}c}$$

Equation 2.5-5

Where x is the pressure divided by the vapour pressure, v is the volume of adsorbed adsorbate, v_{mon} is the volume of the amount of adsorbate necessary for complete coverage of the surface to create a monolayer and c is the equilibrium constant from the Langmuir isotherm multiplied by the vapour pressure of the adsorbate.

In terms of application, the assumptions of the different models make them suitable for different situations. The Langmuir isotherm, due to the assumptions requiring one atom per receptive site and formation of only monolayers, is suited to chemisorption where the adsorbate reacts with the adsorbent. Contrarily BET is suited to predicting the behaviour of a physisorption situation where van der Waals forces are the predominant mechanism for adsorption and will ultimately lead to the formation of multilayers.

Although the two well established theories are very relevant to this area of work, their direct application is not possible due to the number of unknowns in the situation being studied. A large amount of experimental work would be required to quantify the parameters used in the above expressions.

2.6 Epoxy Bleed

Epoxy bleed is the separation of adhesive components and their undesired spread across the substrate surface. This phenomena causes problems with contamination of components and interference with adjacent bonds. The degree of bleed has been linked to substrate composition, contamination and surface energy[45,46], whilst the available literature also suggests substrate

surface roughness and texture could have an effect[34,46]. Adhesives which exhibit no bleed have been developed[47], however, their details are not available for use in this work. Adhesives for optical applications where the bleed problem will not interfere with optical components due to their transparency have also been developed[48]. However they are not designed to be electrically or thermally conductive.

Controlling epoxy bleed through substrate surface energy has had most attention in the literature, usually through the introduction of low energy organic coatings through vacuum baking[49]. Theoretical investigations have also been performed to find the most influential factors affecting resin bleed, which concluded surface energy and atom density were predominantly responsible[50].

The studies centred around the premise that high surface energy causes resin bleed concluded that the problem can be solved by the introduction of low energy organic films[45,49]. Although a slight reduction in bond strength was realised, the bonds were still within acceptable breaking shear stress limits. However, attention was not given to the film effects on bond resistance to thermal fatigue or bond conductivity. The presented solutions to the resin bleed phenomenon also required addition of process steps to the production line.

Although the problem of resin bleed can be solved by the introduction of thin films, this is not an adequate solution due to the specialist equipment required. The literature suggests surface energy can be influenced in more ways than just the introduction of contaminants, of which the overall impact is not documented. The literature related to this issue shows there is much room for further investigation into this topic.

In *Section 2.4.8 Three Phase Contact Line*, the hypothesis that a thin film is formed at the edge of a sessile drop was presented. The film formation could be related to the phenomenon epoxy bleed. However, evidence suggests that the bleed material is preferentially made up of components of the epoxy systems and not the complete system[45]. This suggests that the excessive

wetting of the bleed material is due to its lower surface tension than the adhesive bulk.

2.7 Fillet Size

To date the author has been unable to find any literature relating to the control of fillet size of adhesives for miniturisation of microelectronics or optoelectronics. However, fillet size is frequently of interest for structural adhesives, where fillet design can heavily influence the stress distribution and strength of bonds[51].

The fillet size and shape is the result of the relationship between the adherend, adhesive and adhered component. The contact angle of a fluid on a solid surface is directly related to the properties of the fluid and surface. It therefore stands to reason that the fillet shape will be related to the contact angle of the adhesive on the surface, and will only be affected by the properties of the component should the volume of adhesive be small enough that a fluid surface of complex shape is formed. The Lamella contact angle method relies on such an effect where the fillet size is a function of the wetting properties of the surface[52].

2.8 Surface Engineering

Epoxy bleed is affected by surface properties and fillet size can be equally as sensitive. This section introduces some of the methods of surface preparation used in the work. The surface preparations are considered under two variants, physical and chemical. Each technique is discussed only briefly as surface preparation is a large subject in itself[53]. Further information can be found in the references.

2.8.1 Physical

2.8.1.1 Laser Machining

This method has been used to reduce wetting over substrates. It could be considered a form of micromachining for material is physically removed from the surface. A detailed review of specific laser machining literature can be found in *Section 5.6.2 Background*.

2.8.1.2 Conventional Machining

Traditional machining methods can be implemented to produce a desired surface finish on many materials. The machining parameters can be set to produce a specific R_a value[29]. However, conventional machining processes when applied to hard ceramic materials such as aluminium oxide, suffer extreme tool wear. Diamond impregnated resin is frequently used to cut or machine aluminium oxide and is used in current optoelectronic assembly methods to machine grooves and multiple levels in ceramic substrates. This is a costly method and has an associated yield, and so it is an undesirable part of the materials preparation and assembly process.

Polishing methods are also used for aluminium oxide and aluminium nitride substrates, but these also can be lengthy[54] and increase the cost of materials.

2.8.1.3 Chemical Etching

Etching can be used to add microscopic texture to a surface, it can reveal the crystal structure or create porosity. It can also be used as a method of cleaning a surface by removing any impurities and loose particles. Surface heterogeneity and texture have both been related to adhesion and wetting in previous sections.

Chemical etching could be employed to create complex surface features on the ceramic materials. Etching of aluminium oxide is challenging, but, along with aluminium nitride, can reportedly be achieved at a sufficient rate with concentrated potassium hydroxide[55,56]. Other etching methods for the ceramics include etching with molten salts, which was not practical to use in this work.

2.8.1.4 Surface micromachining

A number of forms of surface micromachining exist[57]. There are chemical based methods which can form a shaped surface[29] either by removal or deposition of material. Using these methods features could be produced on the ceramic surfaces to physically block adhesive bleed. These methods are

currently finding their way into optoelectronics manufacture for formation of surface features[58].

2.8.2 Chemical

2.8.2.1 Self Assembled Monolayers

Self assembled monolayers are single molecule thick coatings which form spontaneously on a suitable surface. They have been seen previously to reduce the surface energy of high energy surfaces to low levels[14,59]. SAMs have been successfully ink-jet printed[60] making accurate application and patterning possible. Patterning a defined region of low energy areas could be used to contain epoxy bleed.

A self assembled monolayer (SAM) is an organised, single molecule thick layer of amphiphilic (having a hydrophilic end and a hydrophobic end in the same molecule) molecules in which the functional head group of the molecule shows an affinity for a desired substrate material and reacts spontaneously to form a stable bond upon introduction of a suitable substrate to a suitable monolayer system. SAM molecules also have a tail with a functional group, Figure 2.8-1, at the opposite end of the molecule, which can be chosen based on the desired resultant properties of the surface following treatment.

The application of a SAM occurs in two stages[61], an initial fast adsorption stage whereby the SAM molecules bond to the surface with some randomness. This can happen in a number of minutes and can result in a SAM of about 80% of its final density. The second stage is a slow ordering of the molecules through the interaction of the chains via van der Waals forces, and the constraint of the SAM/surface covalent bond which forms a specific angle to the surface dependent on the system.
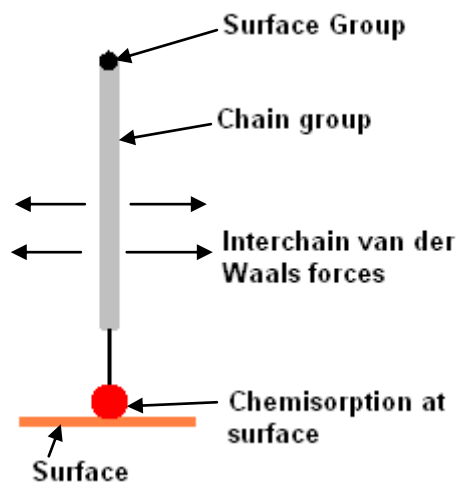
Figure 2.8-1 Structure and organisation of a SAM molecule on a suitable surface

The stability of a self assembled monolayer is defined by the strength of the covalent bond to the coated surface. For alkanethiols on metal surfaces this can be as high as 100kJ/mol, and for fatty acids on aluminium oxide ~38.5kJ/mol[62]. An ordered monolayer is favoured by the SAM systems due to the ordering resulting in a reduction of the free energy of the new surface, meaning that a crystalline or semicrystalline structure is thermodynamically more stable than a disordered one.

It has been suggested that the formation of self assembled monolayers on surfaces can be thought of as a surface-site filling mechanism where the adsorption and desorption of molecules work against each other. It has been proposed that since the solution concentration is much higher than the surface concentration, the adsorption of molecules on the surface is the rate determining step. An expression for the surface coverage rate can then be written as:

$$\frac{\delta\theta}{\delta t} = \frac{k_a}{N_0}c(1-\theta) - \frac{k_d}{N_0}\theta$$

Equation 2.8-1

Where θ is the amount of surface coverage as a fraction, t is the time for adsorption and k_a and k_d are the adsorption and desorption rate constants, N_0 is the surface adsorbate concentration at total coverage and c is the concentration of the solution containing the adsorbate.

Integration of Equation 2.8-1 with respect to the initial condition that the surface coverage is 0 at time equal to zero yields:

$$\theta = \frac{k_a c}{k_a c + k_d} \left\{ 1 - \exp\left(-\frac{k_a}{N_0} \left[c + \frac{k_d}{k_a} \right] t \right) \right\}$$

Equation 2.8-2

Which reduces to the Langmuir adsorption isotherm at equilibrium[16]:

$$\theta_{eq} = \frac{k_a c}{k_a c + k_d} = \frac{c}{c + k}$$

Equation 2.8-3

Where:

$$k = \frac{k_d}{k_a} \propto e^{\frac{\Delta G_a^0}{RT}}$$

Equation 2.8-4

Where ΔG^0_a is the free energy of adsorption at infinite dilution.

The above is valid for systems where interchain reactions can be neglected from the initial deposition adsorption.

In addition to the use of SAMs for a reduction in the surface energy of a substrate, SAMs in the form of silanes are frequently documented for their use as adhesion promoters[15,63]. Correct selection of a silane material will allow the formation of a self assembled monolayer on the adherend surface, which also bonds covalently to the adhesive, creating a strong bond by adding a further adhesion mechanism. Sufficient wetting and suitable surface texture are also required for these to be used at their optimum conditions. Silane based adhesion promotion monolayers could be useful if adhesion is detrimentally affected by any other surface preparation procedures investigated in this work. Silane adhesion promoters have been proven to improve adhesion to alumina[63].

2.8.2.2 Cleaning

A number of methods exist for the removal of free particles and contamination from material surfaces and can be considered chemical modifications:

- Plasma treatment[64,65]

- Ozone cleaning[66]

- Flame treatment[53]

These methods have been shown to improve adhesion, but also to favour epoxy bleed. Of these methods plasma treatment showed the greatest practicality due to it being used currently in optoelectronic assembly processes[*]. Its effectiveness and use for cleaning the particular samples in this study is considered in *Section 5.3 Identification and Removal of Contamination*.

2.9 Surface Texture Measurement

The measurement and definition of surface texture is a large subject in itself[28,29,67] and so what follows is a brief summary of information relevant to this work.

The measurement of surface texture is an attempt to quantify small deviations from a perfect surface[29]. No real manufactured part is perfect, but the degree of perfection is a useful measurement as it can affect the performance of parts. The connection between surface texture and adhesion strength, surface energy and wetting has been discussed in this work as well as many other publications[68,69]. The relationship of surface texture to adhesion is documented not only in adhesion literature, but also surface texture literature[25,29].

There are many ways to define surface texture, as well as many methods to measure it. Some parameters and measurement methods of interest are given below.

---

[*] Communication from Paul Firth of Oclaro plc.

2.9.1 Contact Measurement Methods

Contact methods of surface texture analysis incorporate a stylus which is drawn across a surface while remaining (in theory) in contact with the sample surface. The vertical movement of the stylus is plotted against the constant horizontal movement, resulting in a two dimensional profile which is a direct representation of the peaks and troughs of the surface. Major issues determining the accuracy and resolution of the system are[29,70]:

- Tip dimensions

- Tip shape

- Contact force

- Stylus dynamics and damping

- Material characteristics

The tip shape and dimensions limit the surface features detectable by the stylus. Its radii and point angle limit the steepness and radius of surface features detectable. The contact force and material characteristics can affect the stylus's effect on the sample. A large force on a soft sample could cause deformation of the surface and erroneous results. Contact force and dynamics can affect the method's sensitivity to sharp changes in surface texture If the stylus leaves the surface or "bounces" at any point the results will not represent the surface. Just as if the stylus deforms when it meets sharp changes, the surface will not be truly represented[71].

There are many limitations and considerations to be taken into account when using this method of measurement, including that the output consists only of two dimensional profiles.

Machines for contact measurement vary in size, ranging from portable hand held equipment to lab based equipment. As would be expected the lab based equipment produces superior resolution and accuracy.

A number of advanced surface analysis machines also exist, such as Atomic Force Microscopy (AFM). This utilises an extremely fine stylus with a tip radii in the region of 15nm. Combined with certain software variables such as contact force, AFM overcomes many of the described limitations. This has

given rise to AFM having higher resolution and accuracy than many other stylus methods, but at the cost of measurement length which is limited[70].

2.9.2 Non-Contact Measurement Methods

Non contact measurement methods utilise reflected light off sample surfaces to judge the height of the reflection point above a theoretical base line. Although specific machines measure the distance in different ways (optical followers, optical triangulation) the general principles remain the same throughout the technology[70].

Non-contact is frequently chosen over contact methods for the following reasons:

- Delicate surfaces

- Ductile surfaces

- Wide ranging topography

- Higher resolution, accuracy and precision

- Aerial measurements

Some surfaces are not suited to optical measurement. The method relies on reflection of the light to the sensor. Should the nature of the material or surface be such that light is not reflected to the sensor then the measurement could be erroneous. Steep sided features are one texture which can cause problems.

It should also be noted that all of the above methods are incapable of detecting overhangs and porosity, and any other features which might be shielded by material above it in the profile.

Porosity is another quality[72] which is difficult to measure on ceramics. Given that the density of typically prepared ceramics is close to 100% (see review of literature on ceramics production earlier in this chapter), it can be concluded that measurement of the porosity is unnecessary. However, surface porosity created by manufacturing methods or etching could still be present in the

samples used in this study. In fact SEM inspection of sample fracture sections showed no evidence of porosity, just of multi-crystalline micro-structure.

Surface Texture Parameters

Many parameters for surface texture representation exist[73], ranging from direct measurements such as the maximum peak to trough height R_t, to more statistical representations such as the widely used R_a value – the arithmetic mean of the modulus deviation from the derived centre line. These exist in both two dimensional and three dimensional forms.

The parameters used in this body of work were R_a and R_t, whilst the ratio of actual to apparent surface area as defined by Wenzel[24] was also considered. The definition of R_a is as follows:

$$Ra = \frac{1}{N} \sum_{i=1}^{N} |Zi|$$

Equation 2.9-1

Where N is the number of samples points and Z is the distance from the mean line.

The A/A_0 parameter described by Wenzel is equivalent to the S_{dr} areal roughness parameter[74]:

$$S_{dr} = \frac{\left(\sum_{k=0}^{M-2} \sum_{l=0}^{N-2} A_{kl} \right) - (M-1)(N-1)\delta x \delta y}{(M-1)(N-1)\delta x \delta y} \, 100\%$$

Equation 2.9-2

Where:

$$A_{kl} = \frac{1}{4} \left(\sqrt{\delta y^2 + (z(x_k,y_l) - z(x_k,y_{l+1}))^2} + \sqrt{\delta y^2 + (z(x_{k+1},y_l) - z(x_{k+1},y_{l+1}))^2} \right).$$
$$\left(\sqrt{\delta x^2 + (z(x_k,y_l) - z(x_{k+1},y_l))^2} + \sqrt{\delta x^2 + (z(x_k,y_{l+1}) - z(x_{k+1},y_{l+1}))^2} \right)$$

Equation 2.9-3.

2.10 References

62

[1] Messenger, HW Multibillion-dollar optoelectronics market makes the mark, , Laser Focus World VL 33 IS 12 1997 0740-2511

[2] Mickelson, A.R. Optoelectronic packaging / New York ; Chichester : Wiley, 1997

[3] Prasad, R. P. Surface mount technology : principles and practice. London : Chapman & Hall, 1997

[4] Solberg, V. Design guidelines for surface mount and fine pitch technology / New York ; London : McGraw-Hill, c1996

[5] Jang, S. Optoelectronics module manufacturing and its prospects/barriers for assembly automation, Lasers and Electro-Optics Society 2000 Annual Meeting. 858 - 859 vol.2

[6] Guo, J. Heyler, R. Fast active alignment in photonics device packaging, Electronic Components and Technology Conference, 2004 813 - 817 Vol.1.

[7] Lee, S.R. Lo, C. Passive Alignment of Optical Fibers in V-grooves with Low Viscosity Epoxy Flow, Springer US, 2007

[8] Daniels, C. A. Carole, A. Ceramics : structure and properties / Washington, D.C. : Abyss Books, 2002.

[9] Elssner, G. Ceramics and ceramic composites : materialographic preparation / N.Y. : Elsevier, 1999.

[10] http://www.epotek.com/SSCDocs/datasheets/H20E.PDF Supplied with adhesive order and accessed 17-02-10

[11] http://www.epotek.com/SSCDocs/datasheets/930-4.PDF Supplied with adhesive order and accessed 17-02-10

[12] Petrie, E. M. Handbook of adhesives and sealants / New York ; London : McGraw-Hill, 2007.

[13] Kinloch, A. J. 1946- Adhesion and adhesives : science and technology / London : Chapman and Hall, 1987

[14] Petrie, E. M. Epoxy adhesive formulations / New York ; London : McGraw-Hill, 2006.

[15] Lee, L. H. 1924- Fundamentals of adhesion / New York ; London : Plenum Press, 1991

[16] Ulman, A. 1946- An introduction to ultrathin organic films : from Langmuir-Blodgett to self-assembly / London : Academic, 1991

[17] DeMejo, L. P. Fundamentals of adhesion and interfaces / Amsterdam : Gordon and Breach Science, 1999.

[18] Zisman, W.A. Contact angle, wettability and adhesion : the Kendall Award Symposium honoring William A. Zisman, sponsored by the Division of Colloid and Surface Chemistry at the 144th Meeting of the American Chemical Society, Los Angeles, 1963 / Washington : American Chemical Society, 1964

[19] Brewis, D. M. Industrial adhesion problems / New York : Wiley, 1985

[20] Pocius, A. V. Adhesion and adhesives technology : an introduction / Cinncinati, Ohio : Hanser Gardner, 2002

[21] Starov, V. M. Manuel, G. Wetting and spreading dynamics / Boca Raton, Fla. ; London : CRC/Taylor & Francis, 2007.

[22] Ebbens, S. Hutt, D.A. Liu, C. Williams, O. Surface Micro-patterning with Self-assembled Monolayers Selectively Deposited on Copper Substrates by Ink-jet Printing. ECTC '07 Year: 2007 , Page(s): 1362 - 1367

[23] Bikerman, J. J. Surface Roughness and Contact Angle. J. Phys. Chem., 54, 5, 653 - 658, 1950, 10.1021/j150479a008

[24] Wenzel, R.N. Surface roughness and contact angle. Journal of Physical Chemistry 1949;53(9):1466–7,

[25] Packham, D. E. 1939- Handbook of adhesion / Chichester : John Wiley, c2005.

[26] Brewis, D.M. Surface analysis and pretreatment of plastics and metals. -- London : Applied Science, 1982

[27] Somorjai, G.A. Principles of surface chemistry, Englewood Cliffs, New Jersey, Prentice-hall, Inc, 1972

[28] Exploring surface texture : a fundamental guide to the measurement of surface finish. Leicester, England : Taylor Hobson Ltd., 2003.

[29] Whitehouse, D. J. Handbook of surface metrology / Bristol : Institute of Physics Publishing, 1994

[30] Johnson, R.E. Dettre, R.H. Advances in chemistry series. No.43, 112 1963

[31] Dettre, R.H. Johnson, R.E. Advances in chemistry series. No.43, 136 1963

[32] Berim, G.O. Ruckenstein, E. Microscopic Interpretation of the Dependence of the Contact Angle on Roughness Langmuir, 21, 17, 7743 - 7751, 2005, 10.1021/la050676d

[33] Tamai, Y. Aratani, K. Experimental study of the relation between contact angle and surface roughness J. Phys. Chem., 76, 22, 3267 - 3271, 1972, 10.1021/j100666a026

[34] Huntsberger, J.R. "interfacial energies, contact angles, and adhesion" adhesives age 0001-821X 1978 Vol 21 issue 12

[35] Adamson, A.W. Physical Chemistry of Surfaces, fifth edition, Chichester, West Sussex, John Wiley & Sons inc, 1990

[36] Henrich, B. Cupelli, C. Moseler, M. Santer, M. An adhesive DPD wall model for dynamic wetting. December 2007 Volume: 80 Start Page: 60004 EPL

[37] Owens, D.K. Wendt, R.C. Estimation of the surface free energy of polymers, Journal of Applied Polymer Science, Volume 13, Issue 8, 1969, Pages 1741-1747.

[38] Wu, S. Brzozowski, K.J. Surface free energy and polarity of organic pigments, Journal of Colloid and Interface Science, Volume 37, Issue 4, December 1971, Pages 686-690,

[39] Whyman, Bormashenko, E. Stein, T. The rigorous derivation of Young, Cassie-Baxter and Wenzel equations and the analysis of the contact angle hysteresis phenomenon, Chemical Physics Letters, Volume 450, Issues 4-6, 4 January 2008, Pages 355-359

[40] Ulman, A. 1946- Characterization of organic thin films / Boston, Mass. ; London : Butterworth-Heinemann, c1995

[41] Freundlich, H. Ueber die Adsorption in Losungen. - 1906 - Leipzig

[42] Langmuir, I. The constitution and fundamental properties of solids and liquids. part i. solids. J. Am. Chem. Soc. 38, 2221-95 1916

[43] Hamley, I.W. Introduction to soft matter : synthetic and biological self-assembling materials / Chichester : Wiley, 2007.

[44] Brunauer, S. Emmett, P.H. Teller, E. Adsorption of Gases in Multimolecular Layers, Journal of the American Chemical Society 1938 60 (2), 309-319

[45] Hsiung, J.C. Pearson, R.A. Lloyd, T.B. A surface energy approach for analyzing die attach adhesive resin bleed Journal of adhesion science and technology 2003Vol. 17Issue no. 1pp 1-14

[46] Burmeister, M. Elimination of epoxy resin bleed through thin film plasma deposition Proceedings of SPIE--the international society for optical engineering 2003Vol. 5288pp 780-785

[47] Neff, B. Huneke, J. Nguyen, M. Liu, P. Herrington, T. Gupta, S.K., No-bleed die attach adhesives, Advanced Packaging Materials: Processes, Properties and Interfaces, 2005. Proceedings. International Symposium on , vol., no., pp. 79-81, 16-18 March 2005

[48] Murata, N. Adhesives for optical devices. Electronic Components and Technology Conference, 1998. 48th IEEE , vol., no., pp.1178-1185, 25-28 May 1998

[49] Ireland, J. Epoxy bleedout in ceramic chip carriers. International Journal of Hybrid Micro-electronics, Vol.5, No 1, 1982.

[50] Iwamoto, N. Pedigo, J. Property trend analysis and simulations of adhesive formulation effects in the microelectronics packaging industry using molecular modelling. Electronic Components and Technology Conference, 1998. 48th IEEE , vol., no., pp.1241-1246, 25-28 May 1998

[51] Adams, R.D. Comyn, J. Wake, W.C. Structural Adhesive Joints in Engineering, London : Chapman & Hall, 1997

[52] http://www.kruss.de/en/theory/measurements/surface-tension/plate-method.html accessed 31-03-10.

[53] Wegman, R.F. Surface preparation techniques for adhesive bonding / Park Ridge, N.J., U.S.A. : Noyes Publications, c1989

[54] Kara, H. Roberts, S.G. Polishing behaviour and surface quality of alumina and alumina/silicon carbide nanocomposites. J. Am. Ceram. Soc. 83 5 (2000), pp. 1219–1225

[55] Williams, K.R. Kishan, G. Matthew, W. Etch rates for micromachining processing - Part 2. 6, California : IEEE, 2003, Jounal of microelectromechanical systems, Vol. 12, pp. 761-777.

[56] Cimalla, I. Foerster, C.H. Cimalla, V. Lebedev, V. Cengher, D. Ambacher, O. Wet chemical etching of AlN in KOH solution. Physica status solidi. Volume 3 NO: 6 PG: 1767-1770 2006

[57] Johnstone, R.W. Parameswaran, M. An introduction to surface-micromachining / Norwell, Mass. ; London : Kluwer Academic, 2004.

[58] Han, H. Boudreau, R.A. Bowen, T. Tan, S. Reed, M.L., Micromachined structures for optoelectronics packaging. Lasers and Electro-Optics Society Annual Meeting, 1995. 8th Annual Meeting Conference Proceedings, Volume 1., IEEE , vol.1, no., pp.232-233 vol.1, 30-31 Oct 1995

[59] Xia, Y. et al Microcontact Printing of Alkanethiols on Copper and Its Application in Microfabrication 1996

[60] Ebbens, S. Hutt, D.A. Liu, C. Investigation of ink-jet printing of self-assembled monolayers for copper circuit patterning, EPTC '06 pg 46 – 52.

[61] Love et al. Self-Assembled Monolayers of Thiolates on Metals as a Form of Nanotechnology. Chem. Rev. 105: 1103–1170, 2005.

[62] Ulman, A, 1946- Characterization of organic thin films /   Boston, Mass. ;   London : Butterworth-Heinemann,   c1995

[63] Tanoglu M. McKnight S.H. Palmese G.R. Gillespie J.W. Use of silane coupling agents to enhance the performance of adhesively bonded alumina to resin hybrid composites International Journal of Adhesion and Adhesives, Volume 18, Number 6, December 1998 , pp. 431-434(4)

[64] Herzog, T Kohler, M. Wolter, K.-J., Improvement of the adhesion of new memory packages by surface engineering. Electronic Components and Technology Conference, 2004. Proceedings. 54th , vol.1, no., pp. 1136-1141 Vol.1, 1-4 June 2004

[65] Laniog, B. N. Ramos, H. J. Wada, M. Mena, M. G. Flauta, R. E. Surface Modification of Epoxy Resin Based PCB Substrates using Argon and Oxygen Plasmas. Electronic Materials and Packaging, 2006. EMAP 2006. International Conference on , vol., no., pp.1-6, 11-14 Dec. 2006

[66] Remy, M.J. In-line ozone cleaning for plated ceramic substrates. Electronic Components and Technology Conference, 2002. Proceedings. 52nd , vol., no., pp. 263-267, 2002

[67] BS ISO 1302:1992, "Technical drawings – Method of indicating surface texture".

[68] Chen, Y. He, B. Lee, J. Patankar, N.A. Anisotropy in the wetting of rough surfaces, Journal of Colloid and Interface ScienceVolume 281, Issue 2, , 15 January 2005, Pages 458-464.

[69] Oliver, J.P. Huh, C. Mason, S.G. An experimental study of some effects of solid surface roughness on wetting, Colloids and SurfacesVolume 1, Issue 1, , January 1980, Pages 79-104.

[70] Smith, G.T. 1947-   Industrial metrology :   surfaces and roundness /   London :   Springer, 2001

[71] BS EN ISO 4288:1998 Geometric product specification (GPS) – Surface texture: Profile method – Rules and procedures for the assessment of surface texture.

[72] Gregg, S. J. Sing, K. S. W. Adsorption, surface area and porosity /   London :   Academic Press,   1982

[73] BS EN ISO 4287:2000 "Geometric product specification (GPS) – Surface texture: Profile method – Terms, definitions and surface texture parameters.

[74] ISO 25178 -2 Geometrical product specifications (GPS) -- Surface texture: Areal -- Part 2: Terms, definitions and surface texture parameters, Under development as of 2010

3 Methodology

3.1 Industrial Perspective

The epoxy bleed phenomenon has caused issues in both the assembly and design stage of the industrial partner Oclaro's operations for manufacture of optoelectronic modules. Process yields below 100%, caused by the uncontrolled flow of adhesives, has lead to redesign of sled layouts which must make provision for this occurrence. In the continual drive towards miniaturisation, this design requirement has become one of the limiting factors to package shrinkage. Optical components are frequently assembled at pitches which are greater than optically necessary, due to the unpredictability of the adhesives used for surface mounting.

The material which spreads from the edge of an adhesive droplet can interfere with subsequent bonding sites, wire bonding pads and optical components. Reworking and removal of this material is made challenging by the chemical and thermal stability of a cured epoxy and excellent adhesion to the ceramics and metallisations used as substrate materials. These properties make the epoxies a favourable choice for surface mounting components, as well as creating issues when their behaviour is unpredictable.

The industrial nature of the problem put limitations upon the solutions which were to be explored in this work, i.e.; solutions must be implementable in the existing large scale optoelectronics assembly line. The cost of any methods must not significantly increase the manufacturing costs of the modules and will preferably offer a cost reduction by increasing yields and removing design limitations. Consequently, any proposed solution, to be industrially viable, should affect the current module design and assembly process as little as possible. This constrains solutions to methods which do not require excessive time, expensive equipment or a complex set of chemical treatments.

The ceramic sleds used in Oclaro's assembly line, which are similar to those used by other manufacturers, are either AlN or Al_2O_3 ceramics with conductive metallisation patterns with a tolerance of ~0.0125mm. The top

layer of the metallisation is usually gold. It is when components are surface mounted to these substrates that the epoxy bleed phenomenon causes issues. For this reason, solutions suited to substrates such as the one shown in Figure 3.1-1 are the focus of this work.
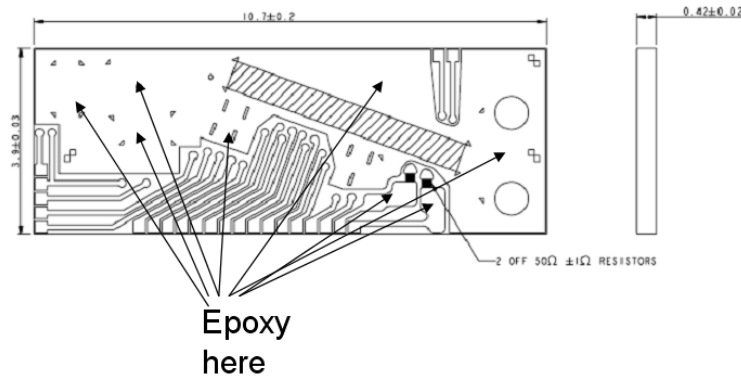
Figure 3.1-1 A typical optoelectronic carrier sled with metallisation pattern and areas for epoxy application highlighted. Image supplied by, Oclaro plc.

It can be seen from Figure 3.1-1 that epoxies are applied to both metallisation areas as well as ceramic areas. This means that any complete solutions developed must be applicable to heterogeneous surfaces formed of gold, and AlN or Al_2O_3.

3.2 Proposed Experimental Areas and Justification

The available literature on the subject of epoxy bleed was found to be limited and frequently contradictory. It was not clear if the disagreement upon the effects of surface parameters was due to poor investigative techniques, or the varying effects due to different substrate materials. Because of this the experimentation in this work began with extensive characterisation of industrially used ceramic materials so the effects of the parameters on adhesion could be studied.
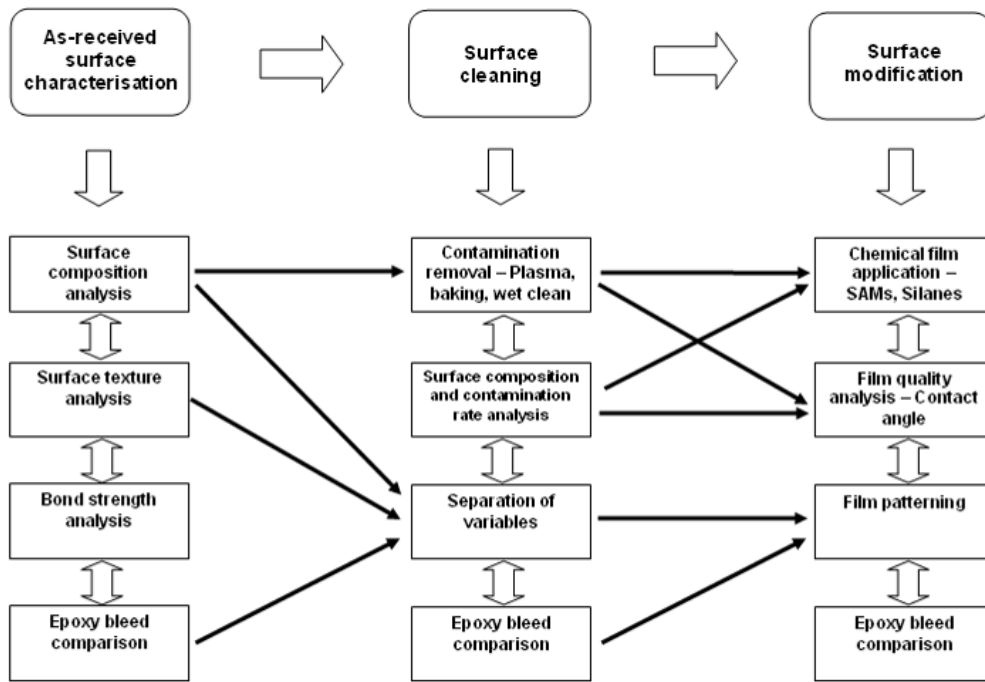
Figure 3.2-1 The proposed approach to characterisation and modification works. Where solid arrows represent follow through experimental results which would affect subsequent methods. (diagram produced May 2008).

Figure 3.2-1 shows the approach to characterisation work as initially conceived and the way in which the work linked to interpretation and justification for future methods. The first proposed modification method is also included on the diagram, self assembled monolayer application.

3.2.1 As-Received Surface Characterisation

The literature suggested that the reasons for the occurrence of epoxy bleed were not fully understood. A series of physical and chemical characterisation methods were employed to develop an understanding of the state of the substrate materials in the condition in which they would enter the production line. The characterisation approach was based upon determining the substrate surface properties which theory and literature suggested could affect the wetting behaviour of adhesives. The methods used were: XPS for chemical characterisation of the surfaces, contact angle for data on the wetting properties of the surfaces, surface metrology to determine the surface textures of the surfaces and tensile testing to ascertain the adhesion strength of joints formed by industrially used adhesives with the substrate materials. The results of each of the analyses were compared to epoxy bleed distance, as measured with SEM, to determine the surface properties which exacerbate

the bleed. Figure 3.2-1 shows how the results of these analyses were used for the next steps of the work which focussed upon surface cleaning.

Oclaro plc, the industrial sponsor and optoelectronic module manufacturer, uses a variety of different substrates in the manufacture of their modules for a variety of reasons. The surface properties of these substrates on receipt at the factory, such as roughness and chemical composition, vary considerably. Representative samples were supplied for the preliminary study and are shown in Table 3.2-1.

Sample	Preparation	Material	SJ-400 Ra (μm)
1	Polished and light etch	AlN	0.06
2	Polished and heavy etch	AlN	0.08
3	Polished	AlN	0.04
4	Fired	AlN	0.17
5	Fired	AlN	0.61
6	Fired	AlN	0.85
7	Lapped	AlN	0.75
8	Fired	Al_2O_3	0.05
9	Polished	Al_2O_3	0.02
10	Lapped	Al_2O_3	0.45

Table 3.2-1 As received materials and information supplied with them.

Samples were supplied in both aluminium nitride and aluminium oxide as they are both used as optoelectronic substrates. Aluminium nitride is the higher cost material but is used when good thermal conductivity is essential. The variety of surface preparations supplied were selected to allow study of the range of adhesive behaviour witnessed on the production line. Polished surfaces were supplied because Oclaro's experience is that polished surfaces resist bleed more frequently than preparations yielding a higher surface roughness. It should be noted that polishing is a time consuming process which adds undesirable cost to substrate materials, so is avoided where possible and the problem of epoxy bleed is addressed through design of the layout of adhesives and sensitive components. Different as-fired materials were supplied due to their different inherent roughnesses (which was found to be due to the different grain sizes of the constituent ceramic powders).

Ceramics purchased by Oclaro for manufacturing are specified only geometrically, and no compositional constraints are applied to the materials other than bulk purity which does not guarantee the surface composition. For

this reason, and considering the link of epoxy bleed to surface composition reported in the literature, chemical compositional analysis of the as-received surfaces was considered imperative.

3.2.2 Surface Cleaning

Surface cleaning was adopted to homogenise chemical surface properties. Plasma cleaning was the method chosen for this study. The areas that surface cleaning is applicable to are shown in Figure 3.2-1. By removing variation between samples by equalising surface properties across sample sets, the study of the individual effect of each surface property variable on spreading of adhesive materials was made possible. This in turn facilitated study of surface modification techniques to find a solution to the industrial problem. A second sample set was introduced to the experimental method in this section of work. These samples were purchased as as-fired tiles and were laser diced and cleaned in the lab, this allowed the homogenisation of roughness and surface chemistry. The lab-prepared sample set removed the unknown factors which were present with the commercially prepared samples. After the initial characterisation of surfaces and separation of variables as shown in Figure 3.2-1, the second sample set was used for all experimentation where roughness was not a variable.

3.2.3 Surface Modification

Once the characterisation work of as-received substrates had been completed methods of modification were considered and are summarised in Figure 3.2-2.
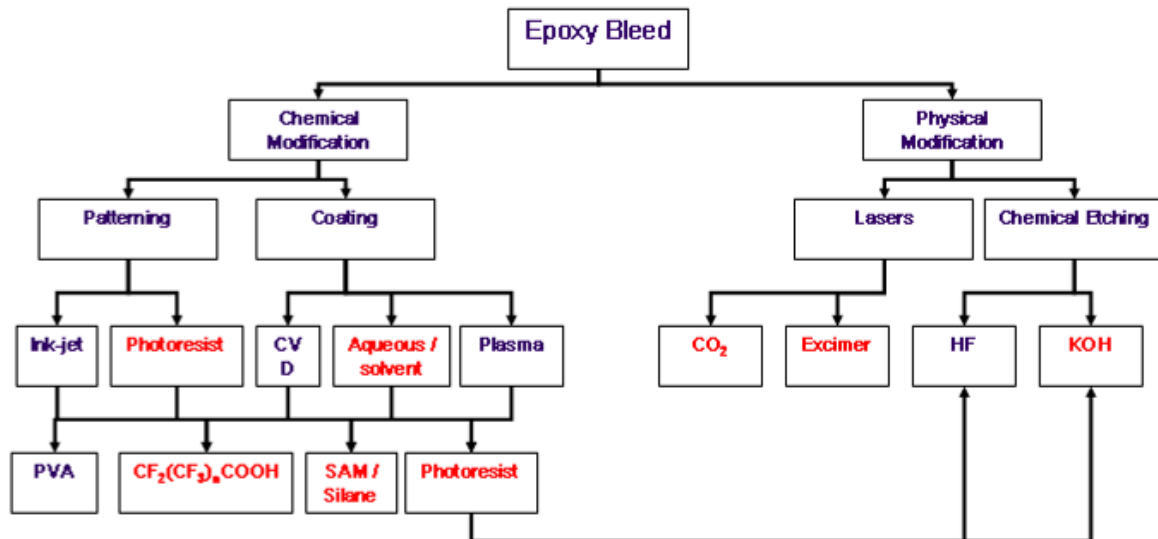
Figure 3.2-2 Possible techniques for surface modification as found from an extensive literature search, where those in red are areas which were selected for further study, and those in blue were deemed impractical. (Diagram produced October 2008)

Figure 3.2-2 shows the initial breakdown of potential chemical and physical modification methods which according to the literature, preliminary trials, and theory could potentially solve the epoxy bleed issue. Some areas were eliminated from the work programme, such as plasma deposition, due to expensive equipment being required, and some such as ink-jet printing due to the impracticality of implementing the method into a production line, in contravention to the desired characteristics of a solution as set out in *Section 1 Introduction*. The potential modification methods were classified into physical modifications and chemical modifications. The physical modifications focus on changing the structure/topology of the ceramic substrates to create either physical barriers to bleed material flow, or to drain it away harmlessly. The chemical modifications considered were aimed at modifying the surface energy of the high energy substrates to inhibit uncontrollable spreading of adhesive.

3.3 Formulation of a Home Made Adhesive

The effects of filler material on the performance of an adhesive can be quite complex[1] and the ingredients which go into an epoxy adhesive formulation are usually a commercial secret. However, some results in this work, such as the failure surface of the silver filled epoxy being through the silver flake/epoxy interface, and that a reaction occurs between the adhesive curing agents and

71

self assembled monolayers, are clearly directly linked to the ingredients of the adhesives. It was therefore important to have an adhesive, the constituents of which were known, so adequate information was available to interpret results. To achieve this a home made adhesive was formulated based on the epoxy polymer constituent and curing agent of the EPO-TEK 930-4 boron nitride filled epoxy. This adhesive was used extensively during this work in addition to the commercial ones. The formulation of this adhesive can be found in *Section 5.1 Characterisation of Surfaces and Adhesives*.

3.4 References

[1] Petrie, Edward M.   Epoxy adhesive formulations /   New York ;   London :   McGraw-Hill, 2006.

4 Experimental Procedures

4.1 Ceramic Sample Preparation

For this study two batches of ceramic were used. The first was industry prepared optoelectronic quality aluminium oxide and aluminium nitride ceramic substrates, and the second unprocessed ceramic tiles. For the industry prepared samples, because the as-received properties of the substrates were the features of interest, no post-receipt processing was undertaken to prepare the samples for analysis. The industrially prepared ceramic substrates had undergone the following preparations prior to delivery[2]:

Firing → Mechanical/Chemical surface preparation → Diamond saw dicing →
Aqueous washing → Firing → Packing

The final firing step has the purpose of cleaning the ceramic surfaces by the evaporation of contamination which has formed in the previous processing steps. The packaging used for storage of prepared ceramic substrates was polycarbonate waffle packs containing lint free paper and an anti static polyethylene sheet.

More extensive preparations were required for the unprocessed as-fired ceramic tiles. These were supplied as 75mm x 75mm x 1mm tiles with an as-fired granular surface texture. The preparation method upon delivery and before experimentation was:

CO_2 laser dicing → 2 min rinse in DI water → 5 min ultrasonics → 1 min
solvent rinse → 10 min drying → Plasma cleaning → Packaging

CO_2 laser dicing was performed to cut the tiles to 14mm x 5mm sized substrates. The method was determined experimentally to offer maximum yield and minimum heat-induced material changes. The laser parameters used are given in Table 4.1-1.

---

[2] Information supplied by Paul Firth of Oclaro plc and Andrew Walker of LEW Techniques (ceramic material supplier).

Variable	Al_2O_3	AlN
Pulse Width (µs)	500	500
Pulse Period (µs)	50	75
Spot Size (µm)	300	300
Feedrate (mm/s)	300	300
Runs	45	20

Table 4.1-1 Laser parameters used for dicing ceramic tiles.

The parameters used were sufficient to cut half way through the thickness of the ceramic tiles. The tiles were then snapped along the score lines into small substrates. The ceramics were not cut through completely due to the desire to not affect the adhesion surface. Snapping the ceramics ensured that only the reverse side of the substrates contained laser affected areas.

Following laser processing it was necessary to remove redeposited and loosely attached melted material to ensure that the surfaces were uniform and free from detritus which could affect highly surface sensitive experimentation. The first cleaning step was performed with an aggressive jet of DI water to remove larger pieces of loose material. The ceramics were then drained, placed into clean DI water, and subjected to ultrasound for five minutes for the purpose of removing further loosely attached material and also fragile melted areas. Following this step the ceramics were washed again with DI water to thoroughly remove the particle loaded ultrasonic liquid. The final liquid clean was a solvent clean used to ensure fast drying and to stop contamination from water impurities due to the liquid evaporation. Propan-2-ol solvent was used for its immiscibility with water and volatility. The solvent was sprayed onto the ceramic substrates and agitated, then the ceramics were removed and placed in a 60°C air flow to dry.

Plasma cleaning was used frequently throughout these investigations. Unless otherwise stated it was performed with an Oxford Instruments *Plasmalab* with the following parameters:

Variable	Setting
Frequency (MHz)	13.56
Pressure (torr)	0.05
Gas	O_2
Flow rate (s^{-1}ccm)	100
Power (W)	300
Time (s)	60

Table 4.1-2 Plasma treatment parameters for general substrate cleaning

Following the initial plasma clean the samples were sealed in tin foil pouches and were used for experimentation within twenty four hours to ensure retention of cleanliness.

4.2 Copper Surface Preparations

The copper used for experimentation was in the form of 2mm sheet prior to processing. Processing involved cutting, cleaning, mounting, mechanical surface preparations, chemical surface preparations and coating.

4.2.1 Cutting

The copper sheet was cut into suitably sized samples with a high speed cutting disc. Samples were deburred with sand paper and thoroughly cleaned to remove any remaining debris.

4.2.2 Mounting

Where it was necessary for samples to be flat, e.g. for contact angle experimentation, copper samples were mounted in carbon loaded conductive phenolic polymer under 20kN of pressure at 150°C for 8 minutes. The top surface of the copper was exposed, flush with the top of the mounting; whilst the bottom was completely contained within the mounting material, thus the mounting material compensated any irregularities in the copper producing flat, surfaces for experimentation.

4.2.3 Mechanical Surface Preparations

Some mounted samples were mechanically treated to enable study of the effect of roughness. The mechanical surface preparation was carried out using the following order of sand paper grit sizes:

240 → 400 → 600 → 800 → 1200 → 6μm cloth → 1μm cloth

Each treatment was performed for 2 minutes, or until scratches were uniform and consistent with the current grit type. Samples which were prepared to an intermediate finish were abraded by following the sequence until the desired finish was reached. Samples were washed thoroughly with deionised water throughout the preparations and frequently inspected with a microscope to ensure quality. Following mechanical preparations samples were etched with HCl, as described below, for the removal of oxides and hydroxides which formed on the surfaces.

4.2.4 Copper Oxide Removal

Oxides, hydroxides and carbonates form spontaneously on copper surfaces exposed to air or water. The surface preparations the copper underwent were not performed in the absence of water and air and so it was necessary to remove the oxides to avoid their affecting the subsequent surface sensitive experimentation.

Dilute hydrochloric acid was used as an oxide removal etchant. The electrochemical series suggests hydrochloric acid will react only slowly with copper at high enough concentrations and temperature. Due to the higher reactivity of hydrogen, the oxygen in both oxides of copper is displaced and removed by the hydrogen ions. When hydrochloric acid is added to water it undergoes the following dissociation[1]:

$$HCl_{(g)} + H_2O_{(l)} \rightarrow H_3O^+_{(aq)} \; Cl^-_{(aq)}$$
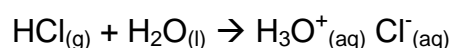
This takes place for up to 90% of all molecules, creating an acid of low pH.

Upon exposure of an oxidised copper surface consisting of copper (II) oxide, copper (I) oxide, copper (II) hydroxide and copper carbonate to hydrochloric acid the following reactions are exploited for the conversion of insoluble oxides and carbonates to water soluble chlorides, allowing the removal of the solid impurities:

First for copper (II) oxide:
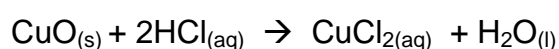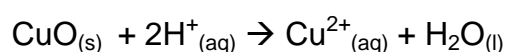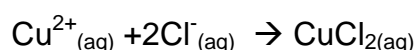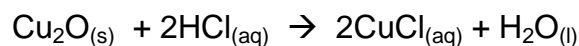
$$CuO_{(s)} + 2HCl_{(aq)} \rightarrow CuCl_{2(aq)} + H_2O_{(l)}$$

This can be broken into:

$$CuO_{(s)} + 2H^+_{(aq)} \rightarrow Cu^{2+}_{(aq)} + H_2O_{(l)}$$

Followed by:

$$Cu^{2+}_{(aq)} + 2Cl^{-}_{(aq)} \rightarrow CuCl_{2(aq)}$$

And for copper (I) oxide:

$$Cu_2O_{(s)} + 2HCl_{(aq)} \rightarrow 2CuCl_{(aq)} + H_2O_{(l)}$$

This can be broken into:

$$Cu_2O_{(s)} + 2H^{+}_{(aq)} \rightarrow H_2O_{(l)} + 2Cu^{2+}_{(aq)}$$

Followed by:

$$2Cu^{+}_{(aq)} + 2Cl^{-}_{(aq)} \rightarrow 2CuCl_{(aq)}$$

For copper carbonate:

$$2HCl_{(aq)} + CuCO_{3(s)} \rightarrow CuCl_{2(aq)} + H_2O_{(l)} + CO_{2(g)}$$

Which can be broken into:

$$CuCO_{3(s)} + 2H^{+}_{(aq)} \rightarrow Cu^{2+}_{(aq)} + H_2O_{(l)} + CO_{2(g)}$$

And then:

$$Cu^{2+}_{(aq)} + 2Cl^{-}_{(aq)} \rightarrow CuCl_{2(aq)}$$
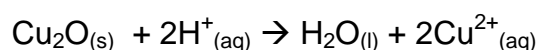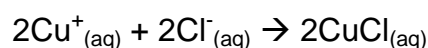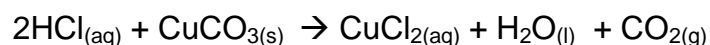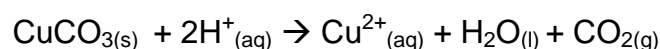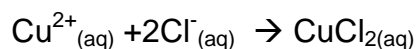
The above reactions show the effectiveness of a HCl etch for the removal of copper oxides and carbonates. The suitability of HCl as an oxide removal etchant is enhanced by its non reactivity with copper metal. This ensures that the dilute HCl etch solution will not affect the underlying copper surface, but will only produce an oxide free surface as desired.

Dilute HCl ~ 10% was prepared from concentrated HCl solution and deionised water. Copper samples were placed into the HCl solution for twenty minutes to ensure complete removal of surface species. Following this reagent grade propan-2-ol was used to thoroughly wash the samples, and a brief air dry was used to evaporate the remaining propan-2-ol. Samples were used immediately after drying to minimise the reformation of the oxides.

4.2.5 Ferric Chloride Etching

Iron(III)chloride is used in industry as a fast copper etchant[2]. Etching a metallic surface quickly can produce a granular type surface texture, which was desirable for some experiments where surface texture was important. The ability to produce a surface texture similar to that of the granular ceramics was imperative for experimentation, and the degree of similarity achieved was verified with AFM surface texture profiling, reported in *Section 5.5.7 Effects of SAMs on Electrical Conductivity*.

Iron(III)chloride when mixed with water produces an exothermic reaction following the scheme shown here:

$$FeCl_{3(s)} \rightarrow Fe^{3+}_{(aq)} + 3Cl^{-}_{(aq)}$$

$$H_2O_{(l)} \rightarrow H^{+}_{(aq)} + OH^{-}_{(aq)}$$

$$Fe^{3+}_{(aq)} + 3OH^{-}_{(aq)} \rightarrow Fe(OH)_{3(aq)}$$
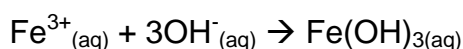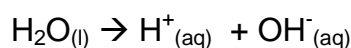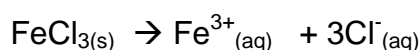
The iron then oxidises the copper:

$$FeCl_{3(aq)} + Cu_{(s)} \rightarrow FeCl_{2(aq)} + CuCl_{(aq)}$$

Or:

$$Fe^{3+}_{(aq)} + Cu_{(s)} \rightarrow Fe^{2+}_{(aq)} + Cu^{+}_{(aq)}$$

And then:

$$Cu^{+}_{(aq)} + Cl^{-}_{(aq)} \rightarrow CuCl_{(aq)}$$
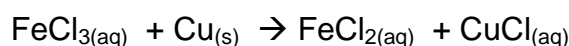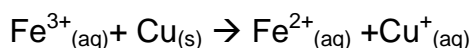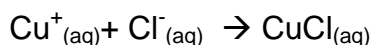
And then oxidises it again:

$$FeCl_{3(aq)} + CuCl_{(aq)} \rightarrow FeCl_{2(aq)} + CuCl_{2(aq)}$$

Or

$$Fe^{3+}_{(aq)} + Cu^{+}_{(aq)} \rightarrow Fe^{2+} + Cu^{2+}$$

And then:

$$Cu^{2+}_{(aq)} + 2Cl^{-}_{(aq)} \rightarrow CuCl_{2(aq)}$$
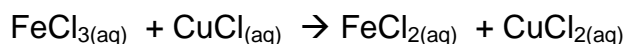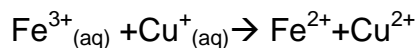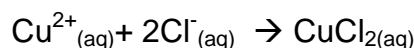
The above reactions show that a finite amount of etching can be done with a given amount of iron (III) chloride. It also shows that the products of the reactions are water soluble chlorides of iron and copper meaning that no

etching residue is left on the etched copper surface. This is imperative for experiments where clean copper surfaces are needed.

For aggressive etching of copper a 1M solution of iron (III) chloride was prepared.

1. 100ml of deionised water was measured into a beaker.

2. 16.2g of iron (III) chloride powder was measured into another beaker.

3. The iron (III) chloride powder was added slowly to the water stirring constantly.

4. The mixture was stirred continuously until all iron(III)chloride was dissolved.

5. Copper samples were added to the solution with the surface to be experimented on facing away from the beaker sides.

6. Samples were left for 10 minutes (which was determined experimentally to produce the desired roughness).

7. Samples were washed thoroughly with deionised water after etching.

8. A dilute HCl etch was used afterwards to ensure the surfaces were chemically identical to the surfaces which underwent a HCl etch only.

After the above preparations the copper was ready for either experimentation or for coating with SAMs (*Section 4.7*).

4.3 X-ray Photoelectron Spectroscopy

X-ray photoelectron spectroscopy (XPS) was used extensively for elemental and compound analysis of surfaces. The method is very surface sensitive (due to the ~10nm escape depth of photoelectrons) and so was ideal for isolating and analysing the surface conditions which affect surface energy, wetting and contact angle. Two sets of XPS apparatus were used for experiments, a VG ESCALAB Mk I with an Al X-ray source and 3-10mm^2 analysis area and a Kratos AXIS ULTRA with an Al X-ray source and a 300x700µm or a 110x110µm analysis area. The procedures followed for XPS were closely tied to the particular experiment and results, and so are not described here.

The Kratos AXIS ULTRA had a mono-chromated Al kα X-ray source (1486.6eV) operated at 3mA emission current and 12kV anode potential. The ULTRA was used in fixed analyser transmission mode, with pass energy of 80eV for wide scans and pass energy 20eV for high resolution scans.

The magnetic immersion lens system allowed the area of analysis to be defined by apertures, a 'slot' aperture of 300x700 μm was used for wide scans and a 110μm aperture was be used for high resolution scans. As the analysis areas were small and changes over a length were of interest, the 110μm aperture was used for high resolution scans of O, C, N, Al and B and Ag where applicable. Wide scans for the output of relative elemental percentages were performed with both the slot aperture and the 110μm aperture and compared. The take off angle for the photoelectron analyser was 90 degrees and acceptance angle of 30 degrees in magnetic lens mode.

As the samples were non-conducting a charge neutraliser filament above the sample surface was used to give a flux of low energy electrons providing uniform charge neutralisation.

The analysis was typically performed with a chamber pressure of 1 x 10^{-8} torr

Element	Electron	Binding Energy (eV)
C	1s	285
O	1s	531
Al	2p	74
B	1s	191
N	1s	398
F	1s	686
Si	2s	153
Ag	3d	368
Na	1s	1072
Ca	2p	347

Table 4.3-1 Elemental binding energies for elements present on samples analysed, to 1eV[3].

Elemental peaks were identified using the data in Table 4.3-1 which was populated from the literature. The wide scans were charge corrected to the main C1s peak at 285.00eV and then quantified to compare the amounts of each element present, using appropriate sensitivity factors for the XPS apparatus used[4]. Components were fitted under the peaks to give chemical bonding information. The interpretation of these peaks was performed with the aid of an extensive literature search of previous XPS analyses of organic and inorganic samples.

The probable reaction products formed during the curing stage of the adhesive application were identified by consideration of the known chemistry of epoxy systems. The peak positions expected in high resolution XPS spectra associated with the bond types in the products were then also identified from the literature. Table 4.3-2 shows the possible bond types along with their binding energy positions. The positions of nearby elemental peaks is also given to aid identification.

Carbon Bond Type	BE	Oxygen Bond Type	BE	Nitrogen Bond Type	BE
C1s	285.00	O1s	531.00	N1s	398.4
C-O-C	286.45	C-O-C	532.64		
N-C	285.94			N-C	400
N=C	285.96			N=C	400.17
Epoxide	287.02	Epoxide	533.13		
C-OH	286.55	C-OH	532.89		
O-C-O	287.93	O-C-O	533.15		
				BN	398.4
				Pyridine	401.5

Table 4.3-2 Possible present bond types with their respective binding energies where BE is binding energy in electron volts (eV) with reference to the C1s peak at 285.00eV[3,5,6,7,8,9].

Accuracy

The accuracy of elemental relative compositions evaluated from XPS data was determined by the use of the correct relative sensitivity factors, signal to noise ratio, peak fitting accuracy and the sensitivity of the XPS apparatus. For the VG ESCALAB Mk I the quoted detection limit was 1%, with the total accuracy ~±3%. For the Kratos AXIS ULTRA the detection limit was 0.1% with total accuracy of ~±1%. . When peak fitting for bond type analysis on high resolution scans was performed the accuracy of the VG ESCALAB Mk I was within ~±5% and the Kratos AXIS ULTRA ~±3%. However, the accuracy of all XPS quantifications is dependant on correct interpretation of spectral peaks

4.4 Contact Angle

Contact angle testing was performed as a means of estimating surface energy and wetting of liquids on as-received and modified surfaces. For consistent results to be gained a preparation, storage and testing method was developed to limit the influence of unpredictable factors such as adsorption of

contaminants from the environment. All samples were stored in tin foil pouches (unless effect of storage media was the control variable being tested) before testing and were always tested within twenty four hours of sample preparation unless otherwise stated in specific experiments. Samples were probed for surface energy estimation using water and diiodomethane test liquids with a Dataphysics OCA20 contact angle goniometer. Contact angles were measured for three different droplet volumes in at least two different areas on each sample for each liquid using Dataphysics proprietary image capture and analysis software in its semi-automated mode, with the droplets applied from motorised syringes controlled by the software. More measurements were done if the sample size allowed it. At least two samples of each preparation were tested and mean results were taken when the measurements were not grossly dissimilar. Where they were this is noted.

Surface energy estimation calculations were performed with the Owens et al method and compared with the Wu method. Various other theories/methods were also applied to the contact angle data, which work is described in *Section 9.3 Appendix 3 – Evaluation of Surface Energy Estimation Methods*.

Where dynamic wetting of adhesives was being investigated the functionality of the equipment data capture and control software was exploited to track the change in contact angle over time. Here the contact angle was measured with the software as with static drops at intervals of thirty seconds until wetting had ceased or slowed to negligibility. For these experiments, due to their viscosity, the liquids could not be applied automatically by the motor driven syringes and so were applied by hand. Extreme care was taken so that uniform droplets were formed. The liquids and surfaces used for this experimentation is described in detail along with the results in *Section 5.5.5.5 Adhesive Wetting on SAM Coated Ceramics*.

Accuracy

The measurement of a contact angle by image analysis software has an inherent accuracy with contributions from the image analysis method and the resolution of the live video feed. Contact angles in this work are therefore quoted with a measurement accuracy of ±1°. A further source of inaccuracy is

the averaging of contact angles from both the left and right of the droplet. Averaging is standard procedure for contact angle measurements which improves accuracy and consistency providing sufficient measurements are taken and drops are of sufficient volume. The homogeneity of the surfaces measured in this study resulted in excellent reproducibility and consistency among measurements. In this work the error in averaged contact angles for a given surface is taken to be ±5° of which ±1° can be attributed to actual measurement error. The propagation of this estimated error through to the estimate of error in surface energy was different depending on the liquid it applied to and the contact angles they formed. For this reason a global value for the estimated error in surface energy cannot be given. Instead the estimated error in the contact angles should be sufficiently representative.

4.5 Surface Metrology

Atomic force microscopy (AFM) was used extensively for the physical characterisation of surfaces. It was chosen over other surface metrology methods due to the repeatability of the results and versatility of the output data. The microscope used for analysis was a Veeco Instruments DI3100 instrument. Imaging was carried out in tapping mode using TESP (tapping etched silicon probes) probes over an area of 10µm x 10µm. 256 data points were measured for each pass of 256 lines. This gave 65536 data points outputted by the software, with a spacing of 0.04µm in both the y and x directions. Each pass was repeated in the return direction automatically by the software. Parameters such as the tip pressure on the surface were adjusted manually to ensure good tracking between the outward and return runs of the tip.

The data was a map of height data points which were joined together with triangles to form an approximation of the surface with an algorithm inside the software. From this data a number of manipulations could be made to summarise the surface texture in different ways. These included areal (S) and linear (R) surface texture parameters, bearing ratio curves, and three

dimensional representations of the surface topography. More details of these parameters can be found in the literature review.

Measurements were taken in three different areas of each sample and each data set was considered together with the others, either by averaging the results or to characterise the variation across the surfaces.

4.6 FCOOH Coating

Fluorinated carboxylic acids (FCOOH acids) were found to bond to hydroxylated aluminium oxide surfaces and form a self assembled monolayer (SAM). It was possible to bond these species to both aluminium oxide and aluminium nitride due to the tendency of aluminium nitride to form a stable aluminium oxide layer a number of nanometres thick on its surface, see *Section 5.1 Characterisation of Surfaces and Adhesives.* These were experimented with extensively for their effectiveness in reducing the surface energy of substrates. The application method was as follows:

1. The ceramics were prepared using the method outlined in *Section 4.1.*

2. The required mass of the selected fluorinated carboxylic acid having the formula $CF_3(CF_2)_nCOOH$ was weighed out to 0.001g accuracy.

3. The acid was dissolved in deionised water with the aid of ultrasonics, typically at 60°C to make an approximately 0.01M solution.

4. Al_2O_3 and/or AlN specimens were immersed in the solution. The exposure was at approximately 60°C for one hour.

5. The ceramics were removed from the treatment solution and washed thoroughly with deionised water.

6. The coated samples were dried in a room temperature air flow for 5 minutes.

The mass of SAM substance required to give the selected molarity was calculated with the molar mass constant:

$$M_u = 1x10^{-3} kg/mol = 1g/mol$$

And the concentration expression:

$$c = \frac{n}{V}$$

Where the molar concentration c is equal to the number of moles n in solution divided by the volume of liquid V.

For 10ml of solution the above expressions yielded the masses listed in Table 4.6-1, for the different FCOOH substances used.

Substance	Formula	Molecular Weight	Mass in g for 0.01M solution
Perfluoropropionic acid	CF_3CF_2COOH	164.03	0.0164
Perfluorooctanoic acid	$CF_3(CF_2)_6COOH$	414.07	0.0414
Perfluorododecanoic acid	$CF_3(CF_2)_{10}COOH$	614.10	0.0614
Perfluorooctadecanoic acid	$CF_3(CF_2)_{16}COOH$	914.14	0.0914

Table 4.6-1 Mass requirements for 10ml FCOOH solutions

Following coating all samples were stored in tin foil pouches to maintain cleanliness, before experimentation took place. Other SAMs identified which would be suitable for ceramic surface coating have the formula $CA_3(CB_2)_nCOOH$, where A and B are hydrogen, chlorine or fluorine, and n is an integer from 1-21. However, not all members of this family may dissolve satisfactorily in water and so it were not investigated.

4.7 Thiol Coating

Organosulphides, especially alkanethiols, have been found to bond to clean, pure FCC structure metallic surfaces and form a self assembled monolayer. Metals they are known to bond to include gold and copper, gold being extensively used in optoelectronics for interconnections and metallisation. SAM substances exhibiting bonding are those with the chemical formulas HS-R or R-S-S-A where R and A are alkyl or aryl chains which could be partially or totally fluorinated or chlorinated. The hydrocarbon chains terminate in a

methyl, ethylene, fluorinated methyl or chlorinated methyl tail group. In the current work alkanethiols were experimented with extensively to determine their effectiveness in reducing the surface energy of optoelectronic metallisations. Copper was used in experimentation as a cheap model for gold, which is generally the metallisation found in optoelectronic modules. An additional justification for the use of copper as a proxy material is that there is interest in the industry in switching to copper to reduce costs. The application method was as follows:

1. The organosulphide was dissolved into propan-2-ol, or another suitable solvent, typically a hydroxylic solvent for a concentration of 0.01M at room temperature.

2. Surfaces were prepared for the acceptance of the SAM as described in *Section 1.2.*

3. The metal surface was immersed in the coating solution. The surface was exposed to the solution for a period of approximately one hour at room temperature.

4. The metal was removed from the treatment solution and washed thoroughly with fresh solvent (typically propan-2-ol).

5. Samples were dried in a room temperature air flow for 5 minutes.

6. Samples were stored in tin foil pouches to maintain cleanliness before experimentation.

The mass of SAM substance used and the particular SAMs experimented with are shown in Table 4.7-1 below.

Substance	Molecular Formula	Molecular Weight	Mass for 0.01M solution
1-Pentanethiol	$CH_3(CH_2)_3CH_2SH$	104.21	0.0104
1-Dodecanethiol	$CH_3(CH_2)_{10}CH_2SH$	202.40	0.0202
1-Octadecanethiol	$CH_3(CH_2)_{16}CH_2SH$	286.56	0.0287

Table 4.7-1 Thiol substances used for experimentation and the calculated masses in grams required to make solutions of 0.01M.

4.8 Silane Coating

Silanes were used for their ability to coat the ceramic substrates with a self assembled monolayer, with each molecule attaching itself with a strong covalent bond. As with the fluorinated carboxylic acid, the silane is capable of bonding to both the aluminium oxide and aluminium oxide substrates. SAM substances suited to this were those with a silane group and general formula R-SiA$_3$ where A can be hydrogen, chlorine or fluorine and R is a linear or branched alkyl or aryl chain of length 1-21 carbon atoms which may be partially or totally chlorinated or fluorinated.

The silanes were applied using the following method.

1. A solution of silane was prepared to a concentration of 0.01M, in cyclohexane. The silanes were in the liquid phase so were dispensed into a beaker using a pipette and the mixture stirred.

2. The Al$_2$O$_3$ or AlN ceramic was immersed in the solution. The exposure was at approximately 20°C for one hour. The vessel was sealed to ensure the volatile cyclohexane did not evaporate.

3. The ceramics were removed from their treatment solution and were washed thoroughly with cyclohexane. The coated substrates were then exposed to ultrasound for two minutes whilst in clean cyclohexane to remove any SAM molecules not directly attached to the surface.

4. Ceramics were removed from the cyclohexane and left to dry in a room temperature air flow for five minutes.

5. Samples were stored in new tin foil pouches immediately after preparation, to await experimentation.

Silanes used for experimentation were octadecyltrichlorosilane (CH$_3$(CH$_2$)$_{17}$SiCl$_3$) and hexyltrichlorosilane (C$_6$H$_{13}$SiCl$_3$), both of which were liquid at room temperature. Due to their volatility and sensitivity to water the substances were handled in a fume cupboard only, and so could not be accurately weighed on a balance. It was therefore ensured that an excess of SAM substance was used to make a solution of at least 0.01M. The ultrasonic

step was inserted to ensure that this higher concentration did not leave excessive silane on the ceramic surfaces, i.e. that anything which was not covalently bonded was removed.

4.9 Electrical Testing

It is important that any organic coatings (i.e SAMs) applied to ceramic or metallic surfaces on optoelectronic substrates should not affect the bond properties of electrically and thermally conductive adhesives that are subsequently applied. Experiments were therefore devised to verify that there is no effect. In addition to the effect of the SAM on adhesion, a conjectured effect of the surface texture of the adherend surface was of interest. It was thought that a rougher surface may result in a reduced number of surface to filler particle point contacts, and hence a reduced electrical or thermal joint conductance. A four point probe test was used to measure electrical conductivity through a joint formed between two SAM coated copper strips and the conductive adhesive used in this work, as shown in Figure 4.9-1 below.
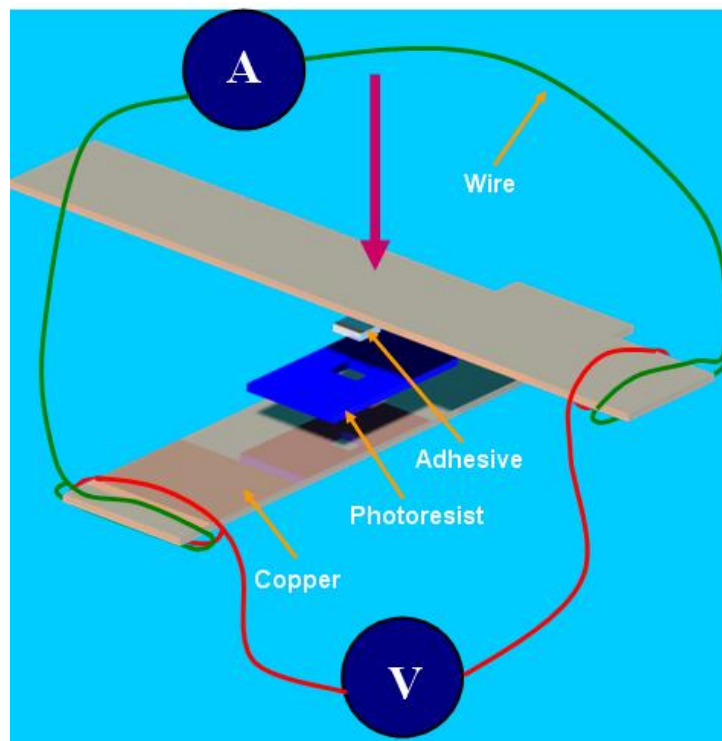
Figure 4.9-1 Arrangement of parts and sensors for the four point probe test of adhesive bonds.

To ensure that a consistent area of adhesive was applied, structured photoresist was applied to one of the copper test pieces. The pattern consisted of sufficient area of photoresist to isolate the two copper test pieces from each other, with a $4mm^2$ recess in the middle of the photoresist into which electrically conductive adhesive could be filled. The arrangement ensured the copper strips were completely isolated from each other and the only conductive path was through the adhesive. It also ensured that the bond thickness was consistent, being equal to the thickness of the photoresist which was ~30µm. The method for the application of photoresist was:

1. Multiple copper strips were super glued onto acetate, aligned to a grid which was printed on paper and showed through the acetate

2. Dry film photoresist was cut to size and taped over the samples

3. The photoresist was laminated onto the samples using a dry film laminator set to a temperature of 115°C

4. The mask artwork was aligned with the coated samples using the grid showing through the acetate and held in place by a vacuum

5. The photoresist was exposed to ultraviolet light for 8 seconds

6. The photoresist's protective outer coating was removed

7. The samples were passed through 1% potassium carbonate to develop the photoresist (i.e.; to remove all areas exposed to the ultraviolet light)

8. Samples were washed and dried ready for further processing.

The experimental protocols for preparation of the copper strips and four point probe specimen assembly used were:

1. 2mm thick sheet copper was cut into 7.5mm x 40mm strips

2. Strips were de-burred using wet and dry paper

3. Those to be polished were prepared using the method outlined in *section 4.2*

4. Those to be etched were treated with the ferric chloride method described in *section 4.2*

5. Half of the samples were coated with photoresist using the method described previously

6. All samples were etched with HCl in accordance to the method in *section 4.2*

7. Samples were washed with propan-1-ol and were dried in a room temperature air flow for two minutes

8. Electrically conductive adhesive was applied in the photoresist recesses using a doctor blade method with a scalpel blade to ensure the volume of adhesive was equal to the volume of the photoresist recess

9. Copper of the same surface preparation was placed on top of the square of adhesive, perpendicular to the orientation of the copper bearing the adhesive

10. Light pressure was applied to the bond until the top piece of copper was tacked to the bottom

11. Samples were cured in an oven at 150°C for 30 minutes

12. Samples were removed from the oven and left to cool

13. As shown in Figure 4.9-1 wires were mechanically attached to the exposed legs of the four point probe specimen

14. A micro ohmmeter with built in ammeter and voltmeter measured the voltage across and current through the adhesive bond and outputted the electrical resistance in ohms.

The experiment was conducted with polished uncoated, etched uncoated, polished and SAM coated, and etched and SAM coated copper.

4.10 Adhesive Preparation and Curing

Where the cure conditions of epoxies were not themselves the subject of experimentation, the manufacturer's instructions were followed for adhesive preparation[10,11]. Adhesives were mixed as and when required and were always used within one hour of preparation. The liquid components were weighed out into the correct ratios using a balance accurate to 0.0001g. Once

weighed they were thoroughly mixed together for 5 minutes to ensure good distribution of epoxy and curing agent. Occasionally it was necessary to cure the adhesives at a different temperature to those given by the manufacturers. In these cases the cure times were adjusted as follows. Exponential curves were fitted to plots of the manufacturers' cure conditions for the electrically conductive and thermally conductive adhesives. These are shown in Figure 4.10-1 and Figure 4.10-2.

$$y = 34521e^{-0.0536x}$$
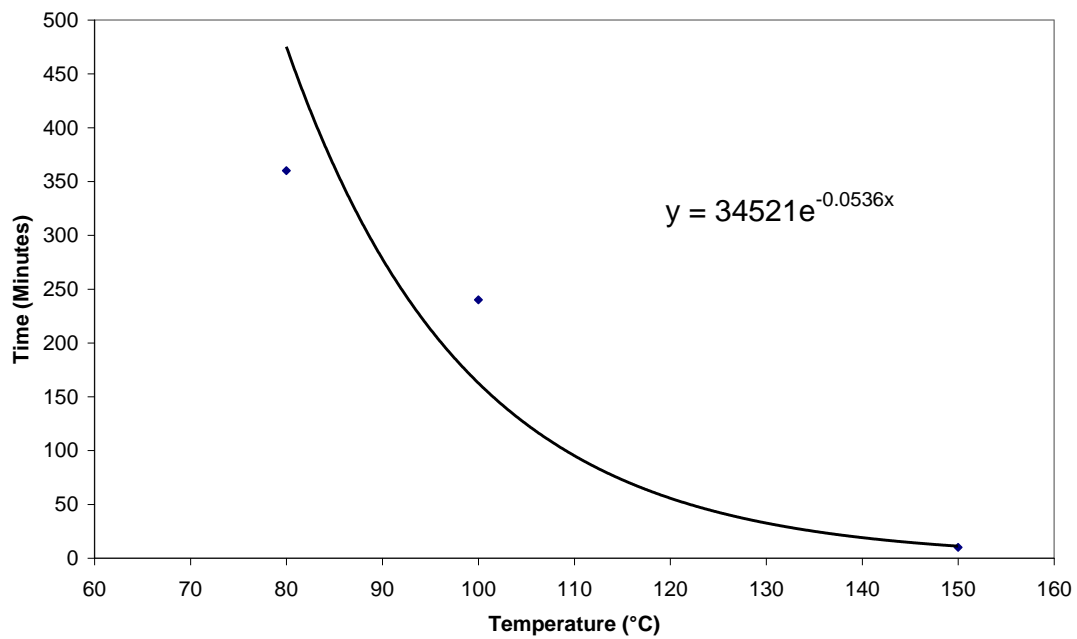
Figure 4.10-1 Cure schedule for 930-4 thermally conductive boron nitride loaded epoxy

$$y = 4915.4e^{-0.0485x}$$
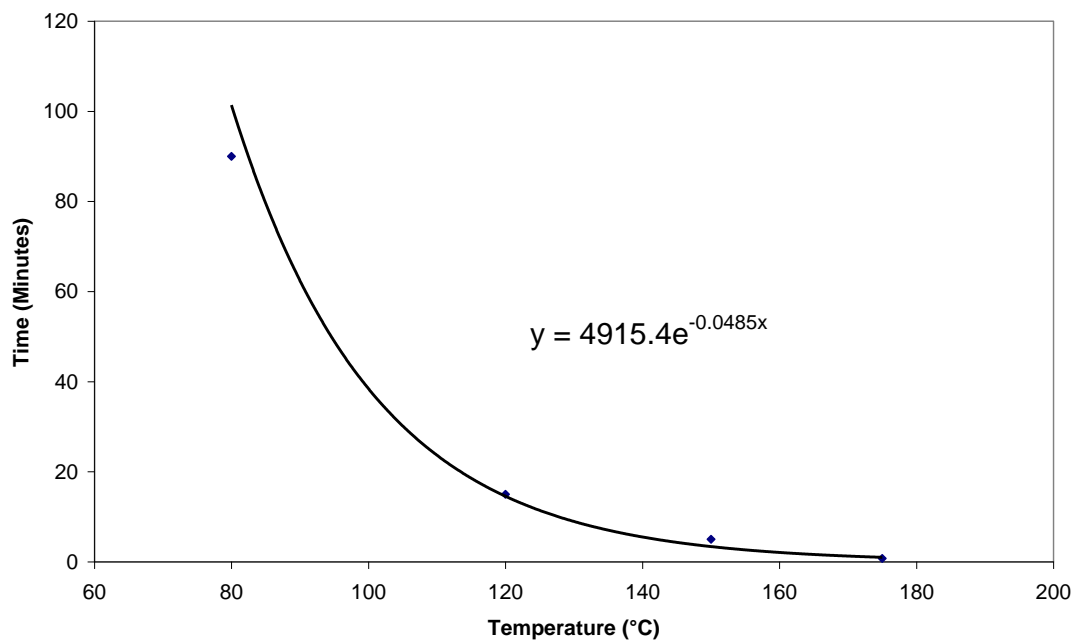
Figure 4.10-2 Cure schedule for H20E electrically conductive silver flake loaded epoxy

Where specific cure time for an intermediate temperature was required the equations of the exponential fitted curves were used to calculate the correct time. Adhesives were cured using an oven with feedback governed temperature control, controlled to ±1.5°C around the specified cure temperature. The oven was preheated for over 30 minutes prior to being used to cure adhesives and was only used once the temperature was stable. The time taken for samples to reach the cure temperature after being placed in the oven was not considered.

Specific application methods and uses for the adhesives are explored more in the results section of this work.

For some experimentation a "home-made" unfilled epoxy adhesive was used to exclude the influence of phenomena due to the presence of fillers. The chemicals shown below were used in the formulation of the home made adhesive. The materials were chosen due to the epoxy and curing agent being used in the silver flake filled epoxy (H20E) used in this study.
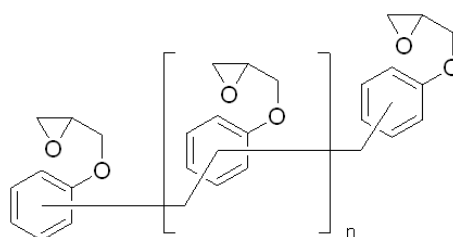
Figure 4.10-3 Poly[(phenyl glycidyl ether)-co-formaldehyde], the epoxy constituent.
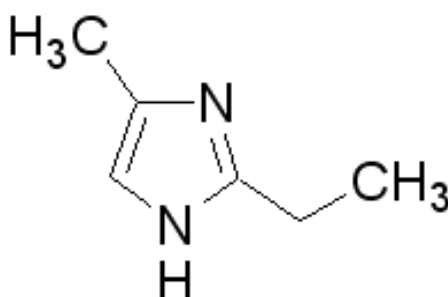
Figure 4.10-4 2-Ethyl-4-methylimidazole, the curing agent
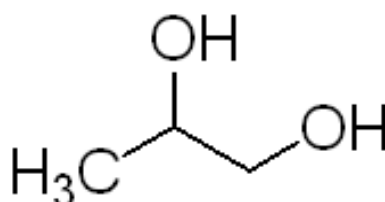
Figure 4.10-5 1,2-Propanediol, solvent used to dissolve the solid curing agent

The solvent and curing agent were first combined in a 1:1 weight ratio and stirred until the curing agent was completely dissolved. If necessary the solvent was heated to 35°C to promote dissolution. The curing component and epoxy component were then mixed in a 6.6:100 ratio. Subsequently the home made adhesive was mixed and used by the same methods as the commercial adhesives.

4.11 Tensile Testing

Tensile test pieces were prepared with ceramic samples in a single lap joint configuration using the commercial silver filled H20E and boron nitride loaded 930-4 adhesives and unfilled epoxy home made adhesive. Tensile testing was used extensively throughout this work to identify the effects of such parameters as contamination, roughness and surface energy on the adhesive strength of bonds. It was found not practical to employ the adhesive lap shear testing[12] method defined by industry standards due to the limitation in volumes of adhesives and size of ceramic pieces available for this work. Therefore a bespoke test was developed. Ceramic lap shear specimens were prepared using a jig milled from aluminium alloy billet shown in Figure 4.11-1.
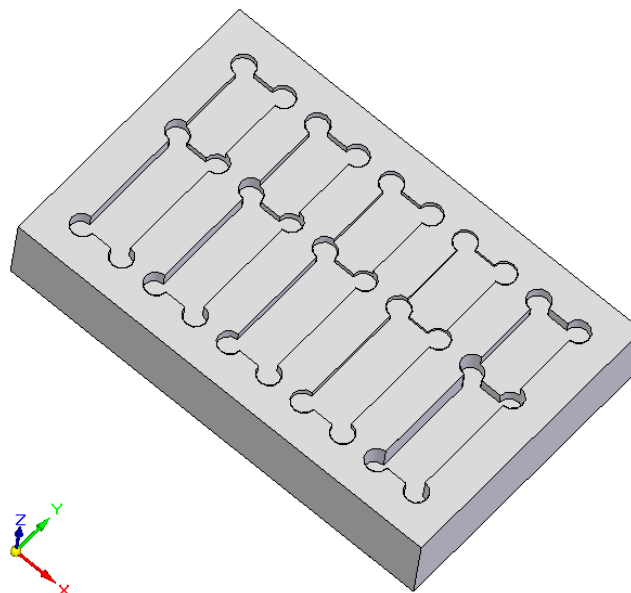
Figure 4.11-1 Lap shear joint jig for ceramic pieces with 5mm overlap. Note that the different recess depths allow use with different thicknesses of samples.

Preliminary experimentation with micrometer driven gas syringes highlighted the difficulty of using this method to repeatedly apply small volumes of

adhesives. It was therefore mutually agreed with the industrial sponsor that a dip and place approach with a needle was valid and sufficiently repeatable for experimentation. The adhesives were therefore applied using a cylindrical needle 0.56mm in diameter. It was found that the volume of adhesive applied by dipping was reasonably consistent, as the amount loaded onto the needle was governed by the wetting properties of the needle and adhesive. Variation in the applied volume was accounted for by measurement of the final bond area on fracture surfaces.

The adhesive joints between ceramic parts were tested to the point of failure under shear loading using the compression function of micro tensile test equipment. The compression was controlled at a constant rate of 0.001mm/s whilst the applied load and extension were recorded. The joint fracture surfaces were examined by scanning electron microscopy (SEM) and profiled with a Talysurf CLS 2000 to determine the failure mode. The joint areas for shear stress calculation were taken from the diameters of the fracture surfaces on the SEM images. The joint diameters were measured using the SEM image processing software but it was found necessary to apply a correction factor obtained from a measurement of a reference artefact to the values obtained. The reason for this was that the measurement facility in the SEM software was not calibrated. Figure 4.11-2 shows the method adopted for the measurement and correction of the diameter of the failed adhesive spots. The correction factor was taken to be the ratio of the measured sled width to its known width (5.5mm). The measured adhesive spot diameter was then multiplied by this ratio to get a corrected diameter. This corrected diameter was then used to calculate the area of the failed spot and thus the shear force at failure.
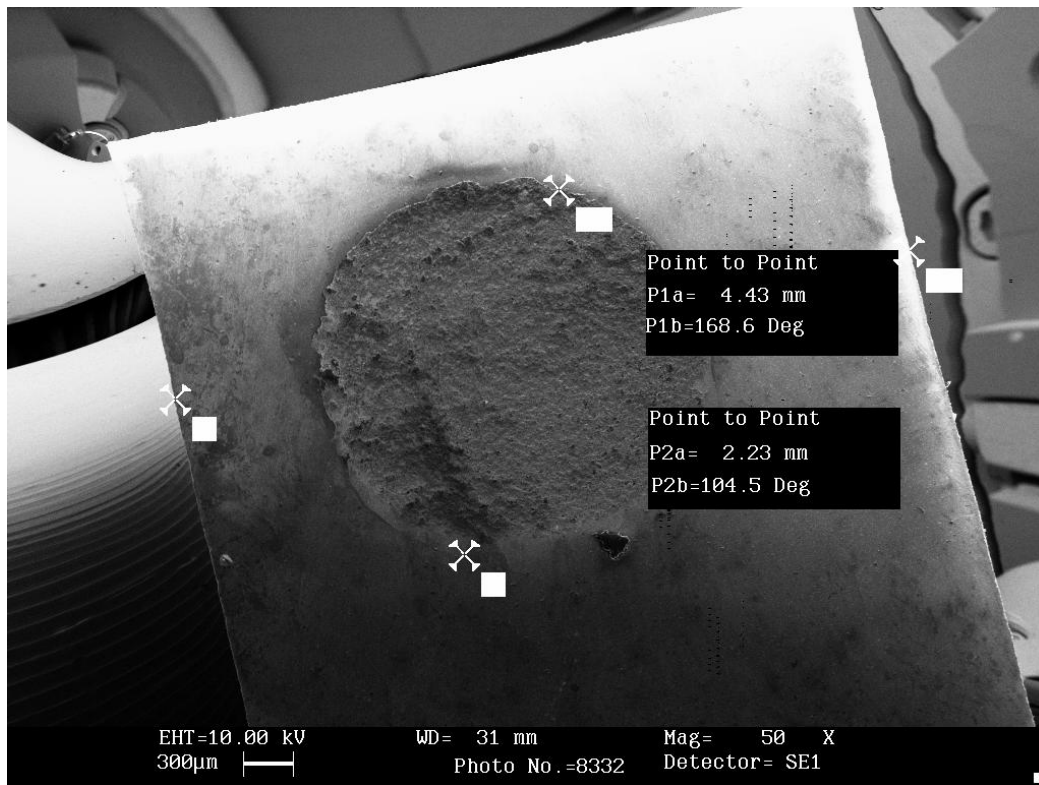
Figure 4.11-2 SEM image showing the measurement method and correction factor derivation for assessment of adhesive joint areas from fracture surfaces.

Copper lap joints were prepared and tested in tensile mode due to the different reaction of the softer and more ductile copper to the application of the load. Copper was cut to 15mm x 80mm x 2mm pieces and a 15mm x 15mm piece of copper was adhered and cured to the end of the copper test pieces to reduce the turning moment on the lap joints in the tensile test. Parts were then subjected to any necessary surface preparations in accordance to the methods described previously. Following treatment pieces were placed on an alignment grid before having 20mm of the end coated in a thin layer of the adhesive. The mating piece to complete the lap joint was placed using the grid as a guide to give 15mm of overlap and a joint area of approximately 15mm x 15mm. No pressure was applied to the parts during cure as the interactions between adhesive and adherend was usually of interest, and any excessive pressure could have directly affected the bond line.

Copper lap joints were tested under extension at 0.4mm/m until failure. The failure mode was judged by the distribution of adhesive following testing. Further analysis was not necessary due to the larger size of the samples

making visual inspection sufficient. Applied load and extension were also recorded and plotted.

4.12 Thermal Cycling

In an optoelectronic module assemblies are subjected to temperature cycles during service. Consequently the resistance of adhesive joints to this and any detrimental effects on the bond strength was of interest. To assess such effects thermal cycling of lap joints was performed with both commercial adhesives and most of the commercially prepared samples. Bonds were subjected to thermal cycling from -40°C to +80°C, with a twenty minute transition and ten minute dwell time, for two days. The thermal cycling curve is shown in Figure 4.12-1 below. Samples underwent lap shear testing immediately following cycling.
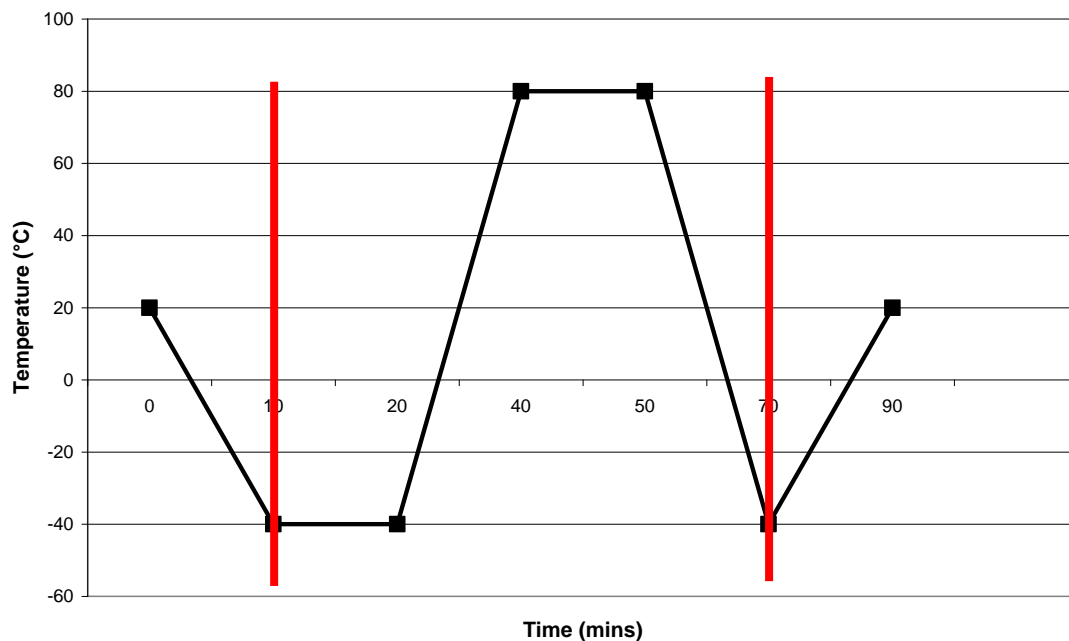
Figure 4.12-1 Graph showing the thermal cycling curve. The vertical lines represent the start and end of the repeat loop.

4.13 Epoxy Bleed Measurements

The epoxy bleed distance was measured using SEM. It was taken to be the distance from the edge of the adhesive spot to the edge of the bleed along a

line normal to the tangent to the edge of the adhesive spot. A correction to the distances measured was applied as described in *Section 4.11 Tensile Testing above*.

[1] Ucko, D.A, Basics for chemistry, London, England: academic press, Inc. Ltd. 1982

[2] Greenwood, N.N, Earnshaw, N. Chemistry of the Elements, 2nd ed., Oxford: Butterworth-Heinemann. 1997

[3] Briggs, D. 1948- Practical surface analysis /   Chichester :   Wiley,   1990

[4] http://www.kratos.com/PolyJISO/index.html

[5] Briggs, D. (David), 1948-   Surface analysis of polymers by XPS and static SIMS / Cambridge :   Cambridge University Press,   1998.

[6] Zhang, B. Wei, B. Sullivan, D. Gotts, H.E. A systematic study of a-CNx overcoat film for proximity recording. IEEE Trans. Magn. 33 (1997), pp. 3109–3111

[7] Zhu, Q. Money, S.L. Russell, A.E. Thomas, K.M. Determination of the Fate of Nitrogen Functionality in Carbonaceous Materials during Pyrolysis and Combustion Using X-ray Absorption Near Edge Structure Spectroscopy. Langmuir 1997, 13, 2149-2157

[8] Bhattacharyya, A. Roy, R. Sen, S.K. Sen, S. Chakraborty, A.K. Bhattacharyya, T.K. X-ray photoelectron spectroscopic studies of conducting polyaniline, poly bisphenol A carbonate and electrochemically synthesized composite of the two, Vacuum, Volume 49, Issue 4, April 1998, Pages 253-256

[9] Awaja, F. Pigram, P.J. Surface molecular characterisation of different epoxy resin composites subjected to UV accelerated degradation using XPS and ToF-SIMS, Polymer Degradation and Stability, Volume 94, Issue 4, April 2009, Pages 651-658, ISSN 0141-3910, DOI: 10.1016/j.polymdegradstab.2009.01.001.

[10] http://www.epotek.com/SSCDocs/datasheets/H20E.PDF Supplied with adhesive order and accessed 17-02-10

[11] http://www.epotek.com/SSCDocs/datasheets/930-4.PDF Supplied with adhesive order and accessed 17-02-10

[12] ISO 4587:2003 Adhesives -- Determination of tensile lap-shear strength of rigid-to-rigid bonded assemblies

5 Experimental Results

5.1 Characterisation of Surfaces and Adhesives

5.1.1 Introduction

The aim of this research was to address process problems experienced in an optoelectronics manufacturing line. Therefore an initial programme of materials surface characterisation was conducted on commercially sourced ceramic sleds and adhesives used in optoelectronic manufacture, in the as-received state, in order to aid understanding of the materials and bond system. The surfaces of commercially sourced aluminium oxide and aluminium nitride ceramic sleds were analysed in terms of their physical and chemical properties. The composition of commercially sourced adhesives were also investigated to the greatest extent possible, however, problems arose with the chemical analysis due to the secrecy of the adhesive formulation.

5.1.2 Background Information

The literature suggests that the phenomenon of epoxy bleed is a condition caused by the combined effects of the properties of the adherend and the properties of the adhesive used in the bond system[1,2]. However, the literature was found to be contradictive or incomplete when considering which specific adhesive and adherend properties were responsible for causing epoxy bleed. The biggest discrepancy in the literature was the effect of surface roughness on epoxy bleed, a factor long known to have implications in the wetting of surfaces[3]. Conclusions of experimental work performed by other researches stated that there was no correlation between surface roughness and the appearance of epoxy bleed[2], this appeared to be in contravention of established theories[4]. As described in *Section 2 Literature Review*, surface energy, surface roughness and surface composition can all have direct effects upon each other and the adhesive strength of the adhesive to the adherend.

For the epoxies and bleed material to be analysed it was necessary to identify the possible bond types in the substances so the XPS data could be interpreted. For this to be done the reactions between the epoxies and curing agents needed to be known, for the home made adhesive and the boron nitride filled adhesive this was possible, as the epoxies and curing agents were known, however, for the silver filled epoxy only the epoxy type was known, the curing agent was not. The home made epoxy was the only adhesive of which all of the ingredients were known, numerous additives are probably present in the commercial adhesives, unfortunately their ingredients are kept a secret by the manufacturers. The epoxy/polymer constituents of the adhesive systems made up 93% of the home made adhesive, 35-55% of the boron nitride 930-4 adhesive and 30-50% of the silver flake filled H20E adhesive. This component is the adhesive component, the carrier for the filler material and that which gives the system its function.

The epoxy materials are defined by the epoxide group shown in Figure 5.1-1 below.
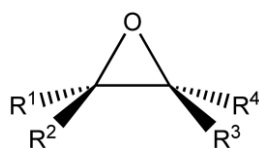
Figure 5.1-1 Epoxide group consisting of an oxygen atom bonded to 2 carbon atoms which are bonded to each other and 2 other unspecified groups.

This epoxide group is highly strained due to its atomic orientation and bond angles, this makes is susceptible to nucleophilic ring opening and bond formation and subsequent polymerisation if suitable reagents are present.
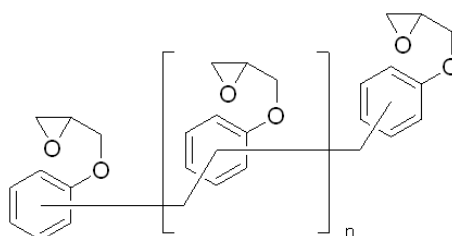
Figure 5.1-2 Poly[(phenyl glycidyl ether)-co-formaldehyde], the epoxy/polymer constituent in the home made epoxy and commercial boron nitride filled epoxy.
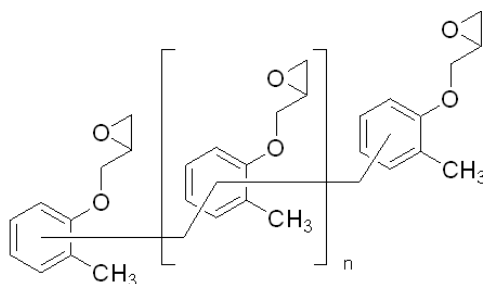
Figure 5.1-3 Poly[(*o*-cresyl glycidyl ether)-*co*-formaldehyde], the epoxy/polymer constituent in the silver flake filled epoxy.

Figure 5.1-2 and Figure 5.1-3 show the polymerised phenolic monomers of bisphenol f (DGEBF) and cresol novolac respectively, each showing the characteristic epoxide bond at their zenith. Figure 5.1-2 shows the polymer/epoxy constituent of the commercial and boron nitride filled adhesives, which differs from the epoxy used for the silver filled epoxy, Figure 5.1-3, by a methyl group on carbon 2 in the aromatic ring. Each of the monomers is joined by CH_2 groups, with the remaining 2 carbon atom bonds joined to the aromatic rings of the monomers.
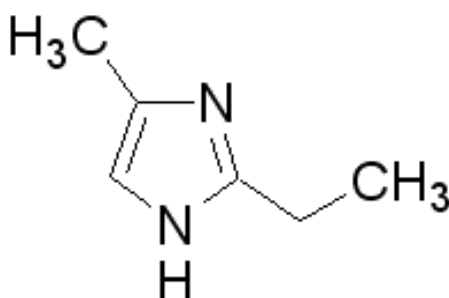
Figure 5.1-4 2-Ethyl-4-methylimidazole, the curing agent used in the boron nitride filled and home made epoxies.

Figure 5.1-4 is the curing agent used to crosslink the polymer chains to form a thermosetting polymer, imidazoles are frequently used as curing agents and react nucleophilically to form part of the resulting thermoset network[1]. The curing agent for the silver filled H20E epoxy, as mentioned, was unknown.
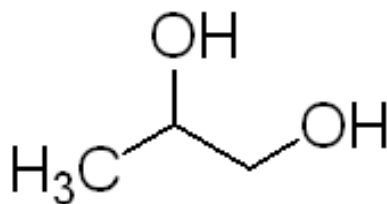
Figure 5.1-5 1,2-Propanediol, solvent used to dissolve the solid curing agent for the home made epoxy.

Figure 5.1-5 shows 1,2-Propanediol, a known solvent for 2-ethyl-4-methylimidazole[5] which is solid at room temperature.

Figure 5.1-2 and Figure 5.1-4 show the basic building blocks of the epoxies which were analysed with XPS, before the analysis could be fully interpreted the way in which the basic blocks react together to make the thermosetting polymer had to be identified.
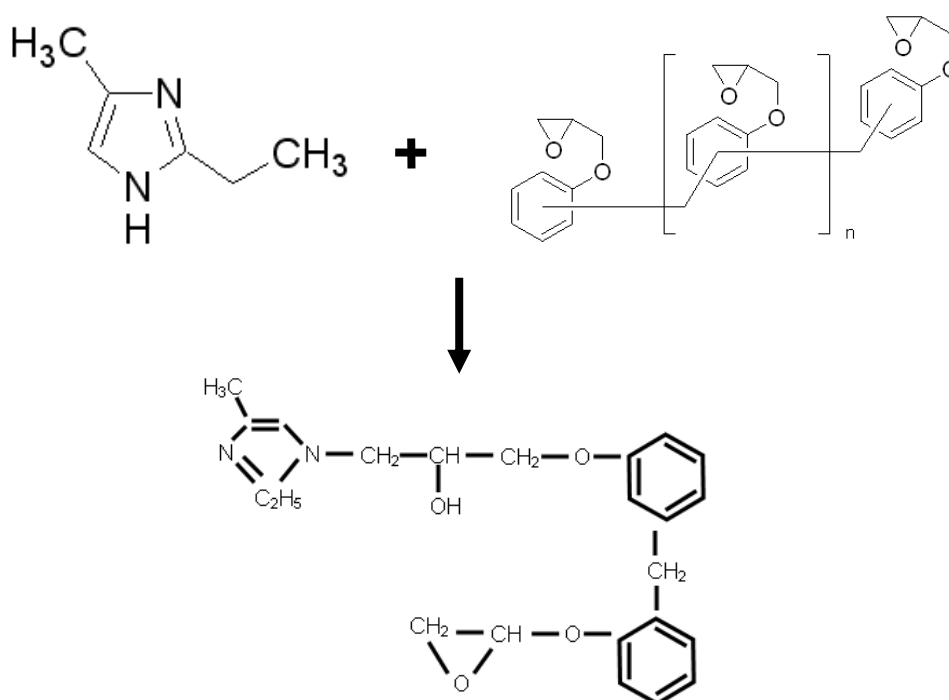
Figure 5.1-6 Probable initial reaction of the curing agent with the polymer[6].

Figure 5.1-6 shows the probable reaction between a simplified polymer chain and the 2-ethyl-4-methylimidazole curing agent, the nitrogen at ring position 3 donates its hydrogen atom to the broken epoxide bond to satisfy the oxidised oxygen, the free bond in the carbon of the epoxide bond then reacts with the nitrogen at ring position 3 to form a strong covalent C-N bond.
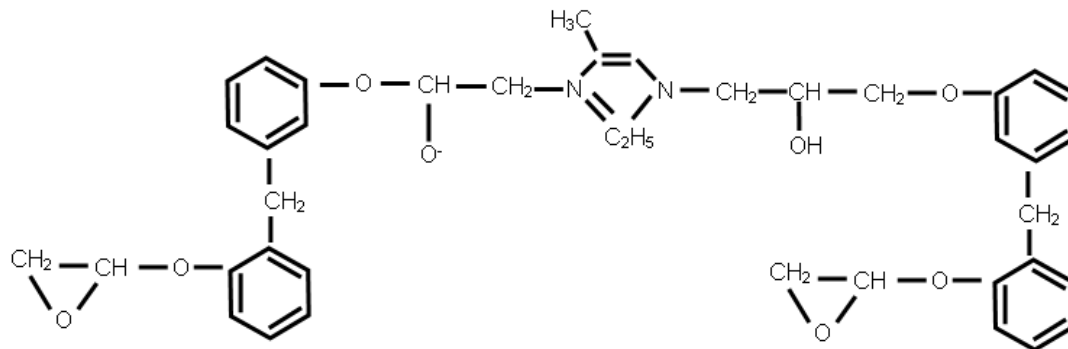
Figure 5.1-7 Reaction of the product in **Figure 5.1-6** with further polymer molecules.

Figure 5.1-7 shows the further cross linking due to the reaction of the nitrogen at ring position 1 with a further broken epoxide bond, here the nitrogen is saturated with 4 bonds.
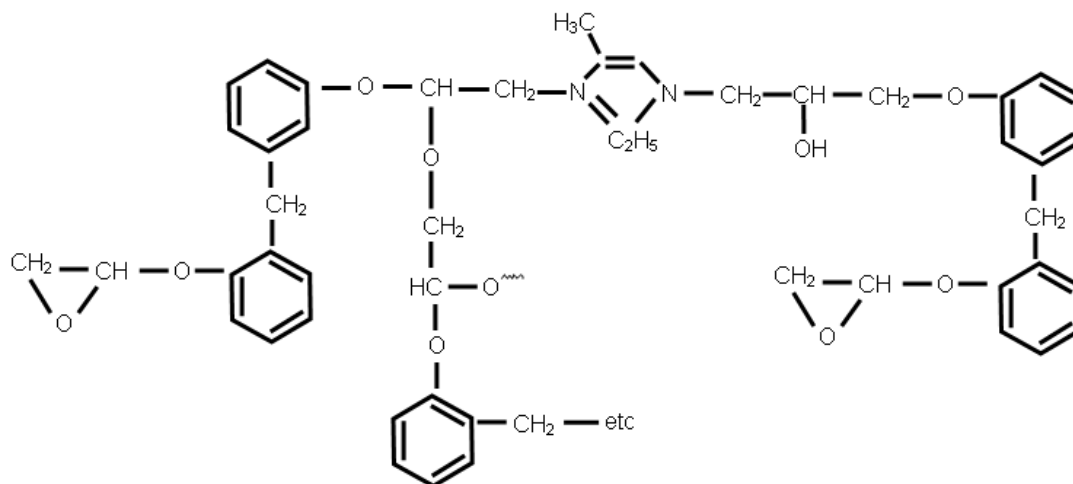
Figure 5.1-8 Cross linking reaction between polymer chains.

Figure 5.1-8 shows the esterification of the product of the reaction between the curing agent and the polymer chains by further polymer epoxide groups.

5.1.3 Methodology

All ceramic materials were supplied by LEW Techniques and all adhesives were supplied by Epo-Tek. The ceramics were supplied with different surface preparations to give an adequate cross section of conditions which are used in industry. Table 5.1-1 below shows the samples supplied along with the details they were supplied with.

Sample	Preparation	Material	SJ-400 R_a (μm)
1	Polished and light etch	AlN	0.06
2	Polished and heavy etch	AlN	0.08
3	Polished	AlN	0.04
4	Fired	AlN	0.17
5	Fired	AlN	0.61
6	Fired	AlN	0.85
7	Lapped	AlN	0.75
10	Fired	Al_2O_3	0.05
11	Polished	Al_2O_3	0.02
12	Lapped	Al_2O_3	0.45

Table 5.1-1 Information received with commercial ceramic samples, where SJ-400 R_a is the R_a value as measured with a portable, stylus surface texture measuring machine in micrometres.

The commercially sourced adhesives of interest were Epo-Tek H20E, a silver loaded electrically conductive adhesive, and Epo-Tek 930-4 a boron nitride loaded thermally conductive and electrically insulative adhesive. These adhesives were recommended by Oclaro plc as they are used for the assembly of their optoelectronic products. Properties of the adhesives can be found in the literature review section of this work.

When considering the wetting of a liquid droplet on a surface there are a number of properties independent to the liquid which can have a dramatic effect on the interaction between the two materials. Table 5.1-1 shows the wide range of surface conditions the unchanging adhesives are used upon. Established theories of adhesion predict that the primary adhesion mechanism between the materials used would be the thermodynamic attraction of the materials to one another, due to the high surface free energy of the adherend and the low surface tension of an epoxy. Mechanical interlocking would also contribute some adhesion strength to this bond system, unless a composite bond was formed. The production of a composite bond is one with more than one state interface, usually due to the inclusion of gas bubbles. Liquid/gas and solid/gas interfaces would form if the gas bubbles remained between the adhesive and adherend, creating a series of interfaces[7] inside the bond itself. This means that the formation of a composite surface can be predicted using the general rule that a system with a contact angle above 90° will produce a composite surface and one with an intrinsic contact angle below this figure will create a bond with a single

solid/liquid interface. This occurs above 90° because at this point the liquid has more attraction to itself than to the surface, and so wetting forces into the roughness profile are not sufficient to displace trapped air. For this affect to be apparent the surface must also exhibit high enough roughness for the gas to remain in the profile[8], and not be displaced just by the force arising from the mass of the adhesive. The 90° contact angle figure is used with consideration to the roughness of the surface, it has been observed that an increase of roughness can promote the production of a composite surface[9], so the contact angle of a solid/liquid system with no roughness would not adequately predict the interface condition of a rough surface.

The adhesive/adherend system of interest here is further complicated by a number of factors. Classical wetting analysis assumes thermodynamic equilibrium. In reality, high viscosity of a liquid can retard its penetration into a roughness profile, creating a transient composite surface behaviour. The fillers of the adhesive could be of a size such that they will not enter into the roughness profile. Temperatures can have an affect on surface energy, contact angle and viscosity. The curing of the adhesives could produce a change of properties with temperature and time, this would certainly occur with the viscosity as the adhesives polymerise and cure.

To predict the undesirable formation of composite bonds the surface tension of the adhesives needed to be known along with the roughnesses, surface energies and chemical compositions. The surface tension of a liquid can be calculated using the pendant drop method[10] which was calculated using Dataphysics software and a contact angle goniometer. However, the adhesives of interest are a mixture of liquid components with a suspension of solid particles, therefore the surface tension of the system can be measured only, and not the properties of the individual components. This is especially problematic when considering epoxy bleed, which will be explored in a future chapter.

The experimental work undertaken focussed upon the characterisation of the ceramic surfaces and adhesive chemistry. The first step taken was an in depth roughness analysis of the surfaces of various preparations. Both contact (AFM, Surftest) and a non-contact method WLI (White Light

Interferometry) were employed and compared to find the most suitable one. It was deemed necessary to explore a number of measurement methods due to the different limitations of each, these limitations are discussed in more depth in the literature review section of this work. WLI and AFM were used to measure the surface in terms of roughness, and to produce 3D images to give further information on the morphology. An array of different roughness parameters could be derived and compared to wetting, contact angle and shear strength, allowing the correct parameter(s) to be chosen for the best indication of adhesion strength. Scanning electron microscopy (SEM) was used to show qualitatively, at micron scale, the effect of processing on the morphology of the surfaces and to relate this later to the shear test results, contact angles and surface roughness measurements.

Chemical analysis was performed to identify any contamination presence and to allow the affects of it to be quantified, only the top few atomic layers of a surface (assuming no absorption) determine the adhesion interactions in a bond system so it was necessary for only the top, and not the bulk of the material, to be analysed. This was done using XPS by the methods described in *Section 4.3 X-ray Photoelectron Spectroscopy*.

The wetting behaviour of a system is governed by the properties of the surface, the liquid in contact and the vapour. The commercial nature of the adhesives meant that their surface tensions was unknown and so had to be measured, this was done with the pendant drop method.

5.1.4 Results and Discussion

5.1.4.1 Ceramic Sample Surface Chemical Characterisation

Surface chemical characterisation of the sleds was carried out by XPS, while the wetting characteristics were determined by contact angle measurement. The XPS elemental quantifications from broad scans are listed in Table 5.1-2. The major constituents of the AlN surface signal after aluminium and nitrogen were primarily carbon and oxygen, suggesting the presence of organic molecules, probably atmospheric or other contamination. High energy, clean surfaces such as the ceramics studied have a tendency to adsorb organic films upon exposure to air[3], the composition of which is determined by the

atmosphere the surfaces are subjected to. The spectra of the Al_2O_3 indicated the presence of trace amounts of group 1 and 2 metals (calcium, sodium, magnesium) along with up to 14% silicon. The silicon is present on the surface regardless of surface preparation method, while the "as fired" samples exhibit a comparable surface composition of trace elements to those which have undergone further processing. It is difficult to determine the origin of these elements due to the commercial nature of the samples. The magnitude of the signal from the group 1 and 2 metals is closely related to the purity of the samples as reported by the suppliers; those which were over 99% pure have only trace amounts of these elements present, whilst those 96% pure showed presence of up to 3%. The correlation with purity and insensitivity to surface treatment suggests that the trace elements form part of the material composition.

Figure 5.1-9 shows a plot of surface carbon percentage against r, showing that there is evidently no correlation. The two very high carbon percentage data points are for the etched AlN sleds, suggesting that either the chemical etch provides a clean high energy surface for the adsorption of higher levels of organic contamination, or that it leaves behind residues on the substrate surface after drying. There is also no evident correlation between the surface energy calculated from the contact angle measurements and r, as can be seen in Figure 5.1-10. The very high energy AlN surface (72 mJ/m^2) in Figure 5.1-10 is the lapped sample (number 7). The surface carbon content of this sample is not particularly low at 21.1%, so the low contact angles seen may be due to the high roughness (r of 1.63).

The lack of correlation between the surface energy calculated by wetting measurements and surface roughness is surprising in view of the well known effects of roughness on contact angles[11]. However, there is a clear correlation between surface energy and surface carbon visible in Figure 5.1-9, with surface energy decreasing with increasing carbon content for both AlN and Al_2O_3, apart from the anomalous result for sample 7 already noted, as seen in other work[2]. Since in principle both roughness and surface contamination affect wetting, it would therefore appear that the variation in carbon content is large enough to mask any effect of roughness on the contact angles in Figure

5.1-10 apart from the very rough lapped AlN (sample 7), while the roughness variation is not large enough to disturb the trend seen with carbon percentage in Figure 5.1-11, again excepting sample 7. It is worth noting that the R_a value given by the supplier of 0.75 µm for sample 7 was not the highest in the sample set, while the value of r determined by AFM was the highest by some margin (next highest sample 5, r 1.35, R_a 0.61µm; highest R_a value sample 6 at 0.85 µm but r only 1.23). Wenzel's parameter r is therefore a better predictor of wetting than R_a with this sample set.

Sample	Relative atomic percentage							
	Al	O	N	C	Si	Mg	Ca	Na
1	23.5	37.0	4.0	35.6	0.0	0.0	0.0	0.0
2	28.6	25.3	13.7	32.5	0.0	0.0	0.0	0.0
3	31.7	39.2	9.0	20.1	0.0	0.0	0.0	0.0
4	28.9	42.4	6.2	22.6	0.0	0.0	0.0	0.0
5	30.4	42.5	5.5	21.6	0.0	0.0	0.0	0.0
6	33.4	44.6	5.2	16.8	0.0	0.0	0.0	0.0
7	30.1	42.8	6.0	21.1	0.0	0.0	0.0	0.0
8	23.1	44.0	0.0	18.2	12.3	0.9	0.5	1.0
9	28.0	40.2	0.0	21.2	8.8	1.2	0.0	0.6
10	20.1	39.4	0.0	21.0	14.2	3.2	2.2	0.0

Table 5.1-2 Relative atomic percentages of the elements present on the ceramic substrates, measured using XPS.
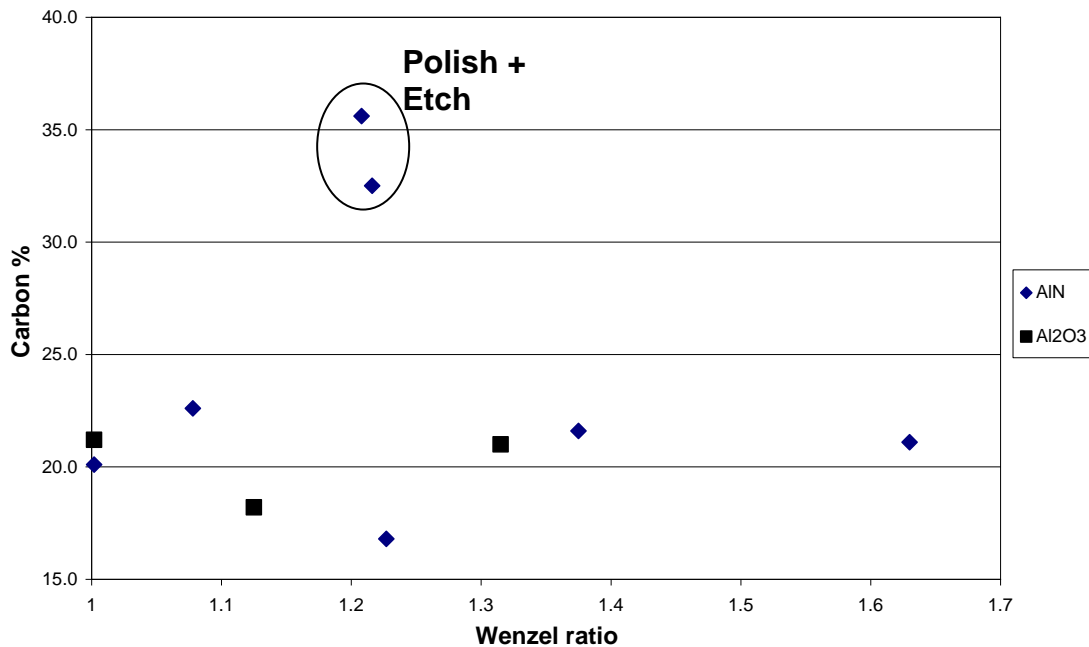
Figure 5.1-9 Comparison of Wenzel ratio to relative carbon percentage as measured with XPS. Circle highlights the samples which underwent mechanical polishing and chemical etching (1 and 2).
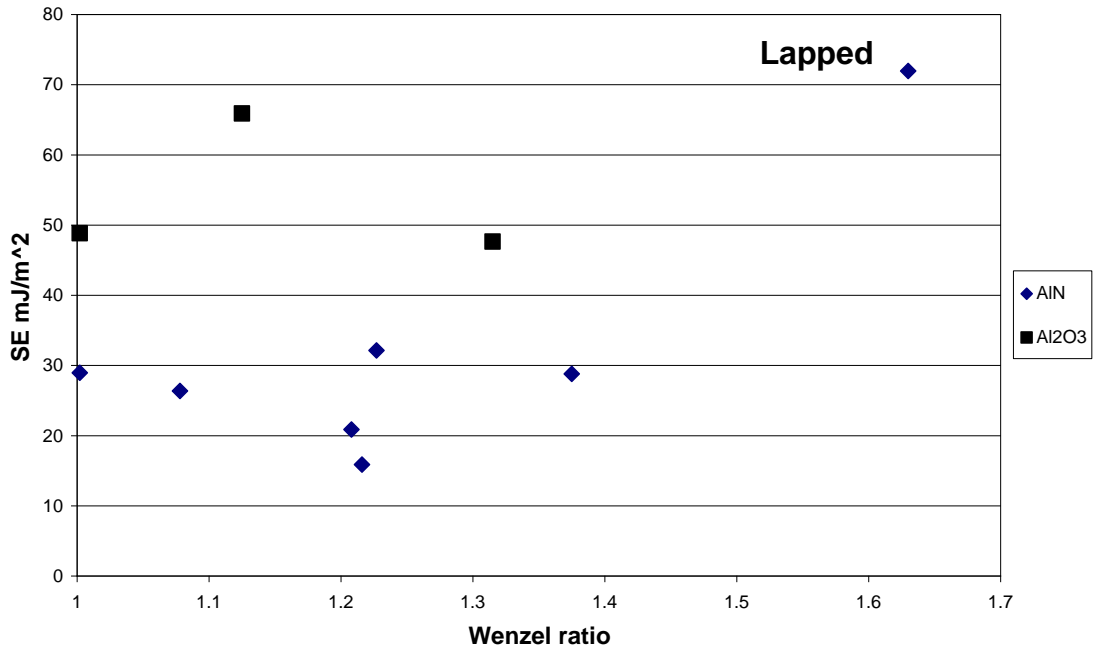
Figure 5.1-10 Plot of apparent surface energy (according to Owens-Wendt) against the Wenzel ratio.
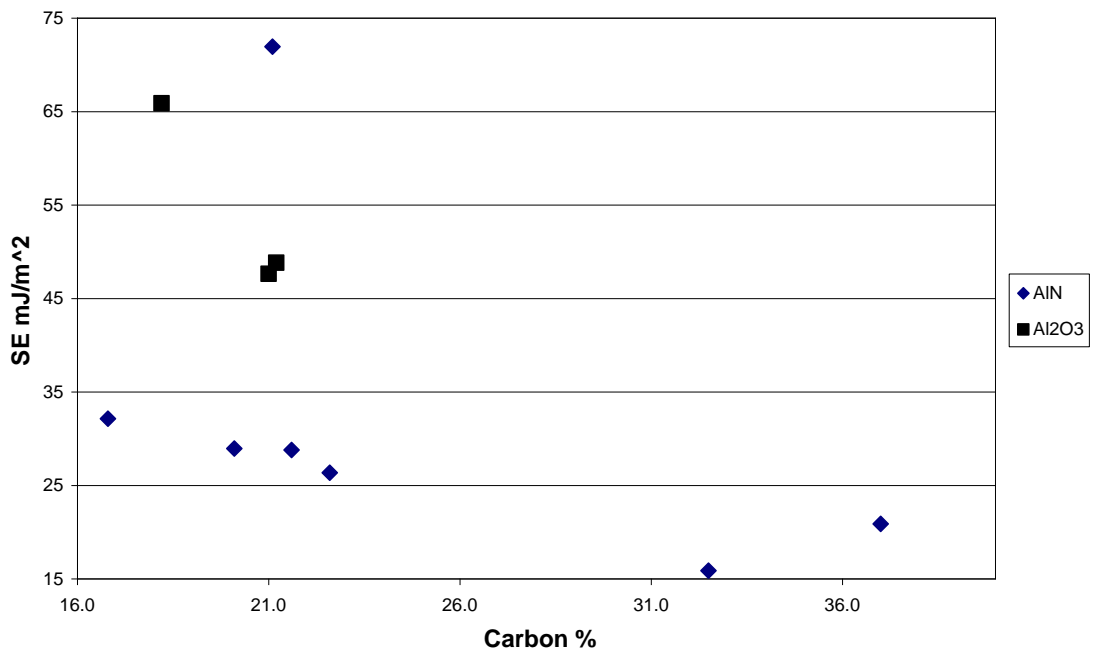
Figure 5.1-11 Plot of surface energy (according to Owens-Wendt) against relative atomic carbon percentage as by XPS.

5.1.4.2 AFM Surface Texture Characterisation

The industrial surface preparation methods used to modify the surfaces of the samples used for this study fall under two categories, chemical preparations and mechanical preparations. As-fired, lapped, polished and chemically etched surface preparations were all used for this characterisation work, just

as they are all used in industry. The methods used to treat the samples are described in more detail in the literature review section of this work.

The heavy and light etches used to treat samples 1 and 2 (Table 5.1-1) were both potassium hydroxide (KOH). The main material removal mechanism of this method is via defect and grain boundary attack[12], however, KOH does attack AlN crystals from certain directions[13].

As-fired ceramics have undergone no further processing to their surfaces following manufacture. Lapping and polishing of surfaces involves their abrasion via shear forces arising from contact from a spinning disc parallel to the plane of the surface, addition of slurries, a suspension of ultra hard materials in a lubricant, and the grit size of the abrasive discs defines the final roughness of the surface.

Given the knowledge of the material removal methods gained from the literature it was deemed important to assess the conditions of the surfaces in their as-received state. AFM was used to investigate the surface topology and assess the affects of the processing on the commercial samples. Consideration was given to the feature sizes and physical damage to the surfaces, both of which could affect the strength of an adhesive bond to the surface. Figure 5.1-12 to Figure 5.1-22 shown below show the results of the AFM investigation of the surfaces. Note that the z-axis (heights) scale differs between figures. The R_a values quoted are from Table 5.1-1.
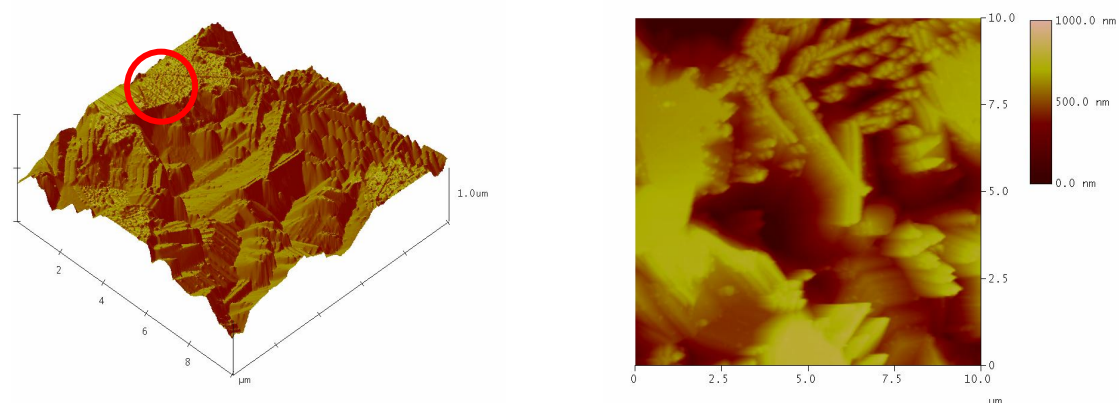
Figure 5.1-12 3d morphology representation (left) and 2d representation of 3d morphology (right) of sample 1(AlN, polish + light etch, R_a 0.06µm). Circle highlights flat area due to mechanical polishing.
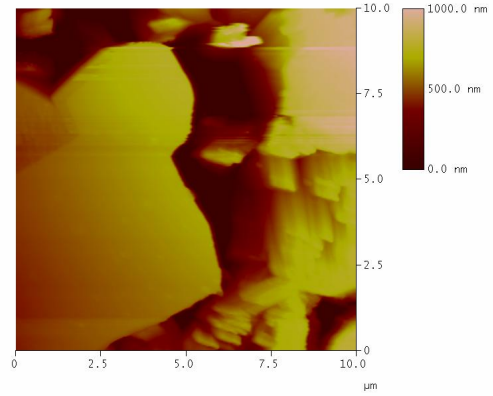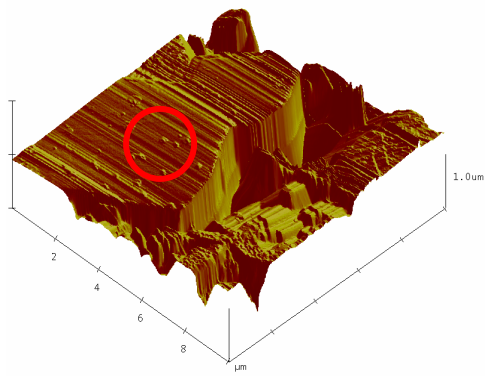
Figure 5.1-13 3d morphology representation (left) and 2d representation of 3d morphology (right) of sample 2 (AlN, polish plus heavy etch, R_a 0.08μm) Circle highlights flat area due to mechanical polishing.
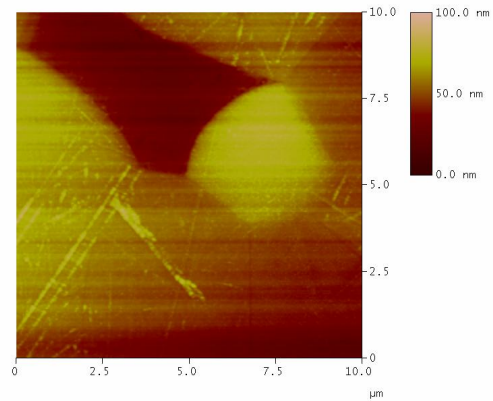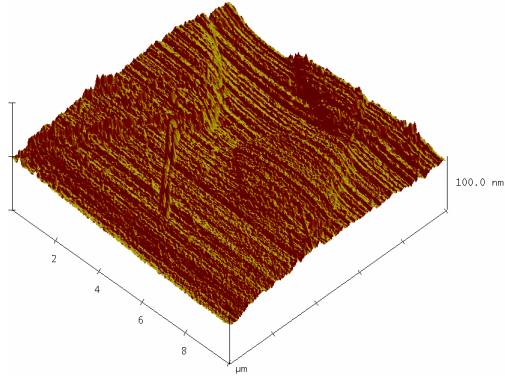
Figure 5.1-14 3d morphology representation (left) and 2d representation of 3d morphology (right) of sample 3 (AlN, polish only, R_a 0.04μm).
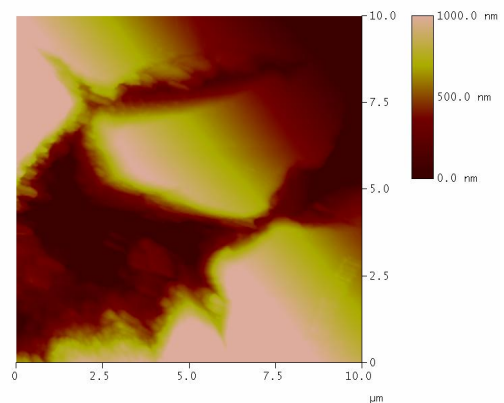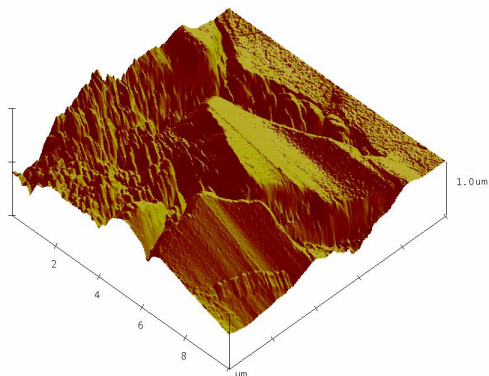
Figure 5.1-15 3d morphology representation (left) and 2d representation of 3d morphology (right) of sample 3 in an area which appears as a hole in the surface (AlN, polish only, R_a 0.04μm).
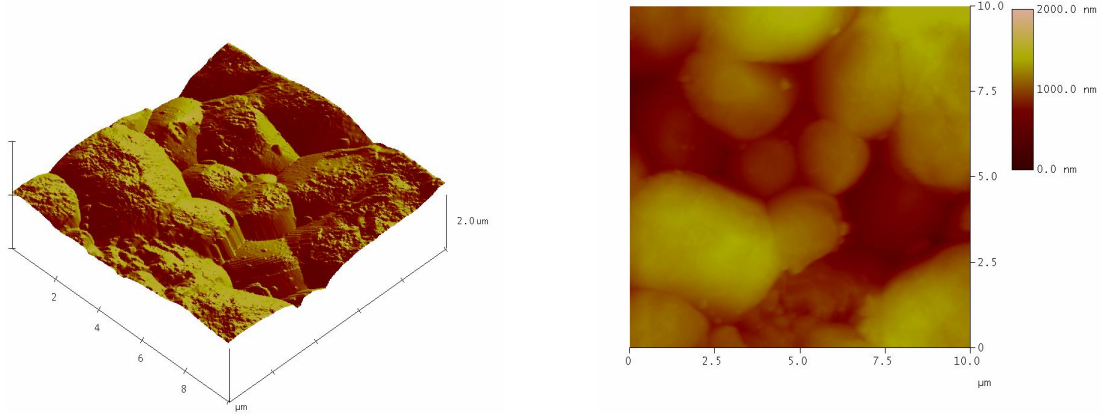
Figure 5.1-16 3d morphology representation (left) and 2d representation of 3d morphology (right) of sample 4 (AlN, as-fired, R_a 0.17μm).
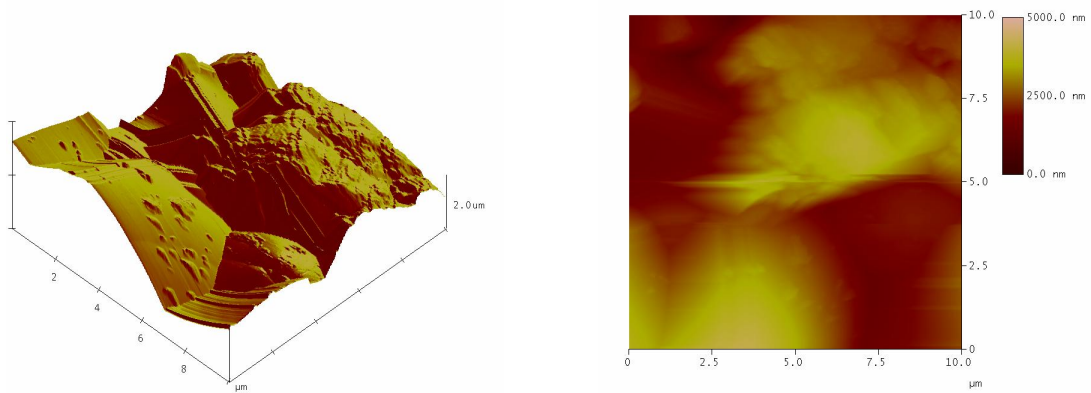
Figure 5.1-17 3d morphology representation (left) and 2d representation of 3d morphology (right) of sample 5 (AlN, as-fired, R_a 0.61μm)
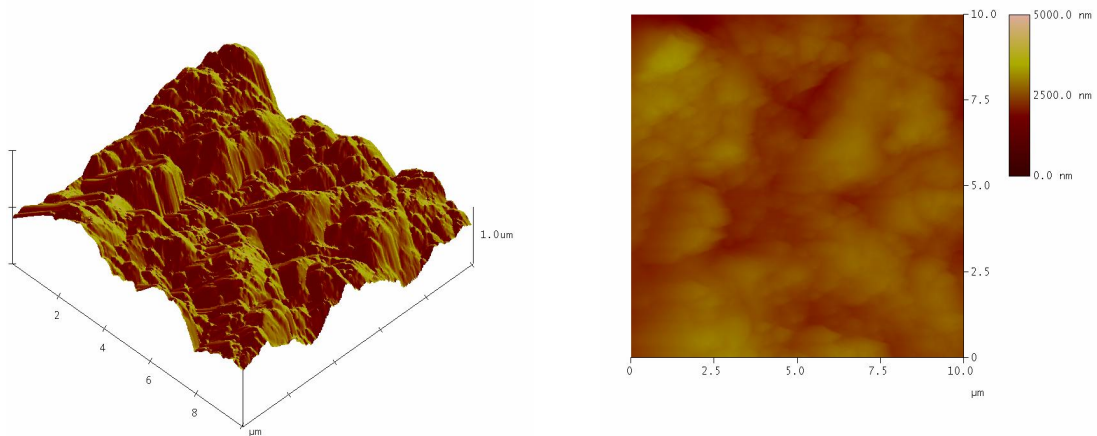
Figure 5.1-18 3d morphology representation (left) and 2d representation of 3d morphology (right) of sample 6 (AlN, as-fired, R_a 0.85μm)
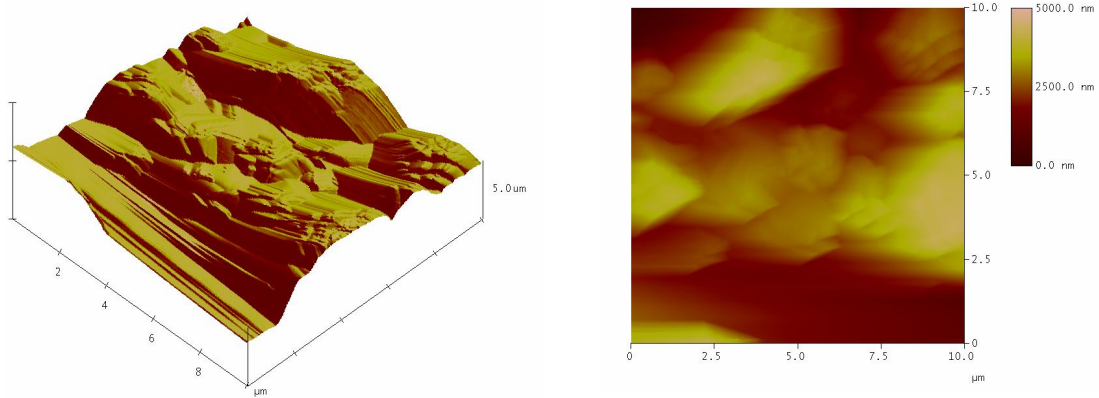
Figure 5.1-19 3d morphology representation (left) and 2d representation of 3d morphology (right) of sample 7 (AlN, lapped, R_a 0.75µm)
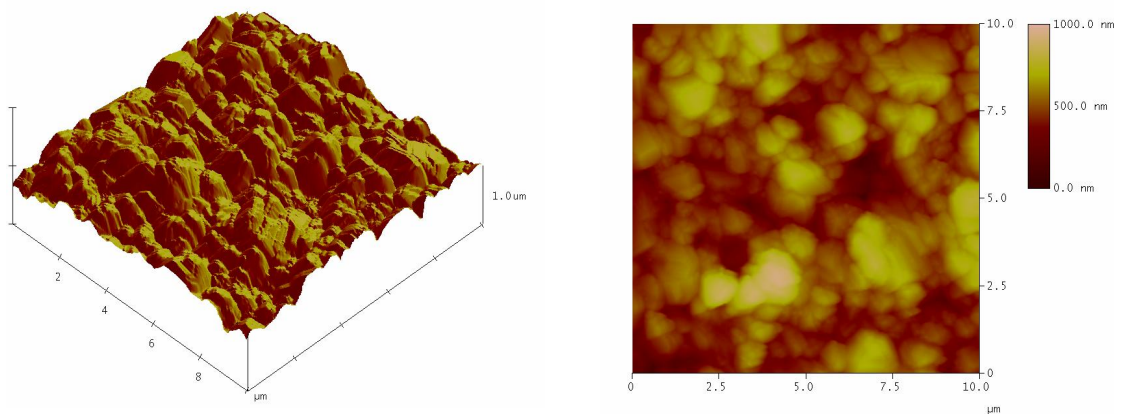
Figure 5.1-20 3d morphology representation (left) and 2d representation of 3d morphology (right) of sample 8 (Al_2O_3, as-fired, R_a 0.05µm)
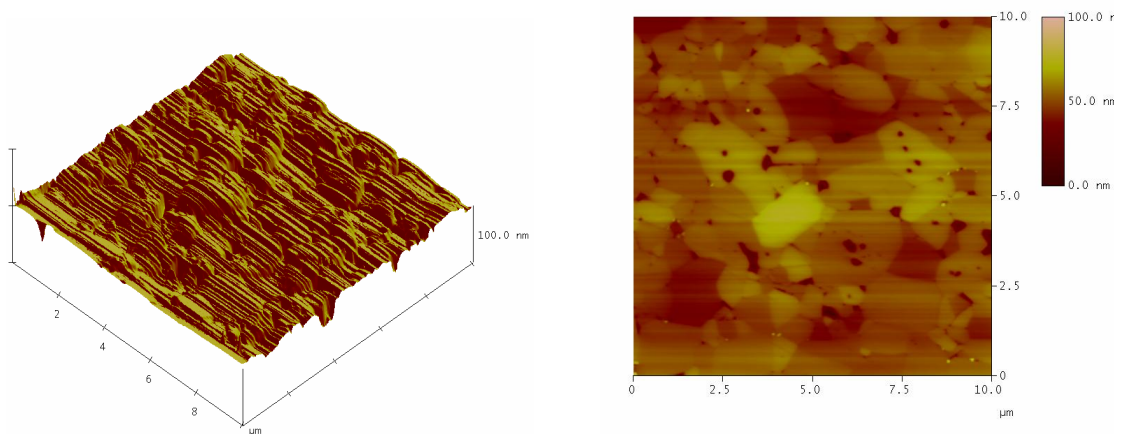
Figure 5.1-21 3d morphology representation (left) and 2d representation of 3d morphology (right) of sample 9 (Al_2O_3, polished, R_a 0.02µm).
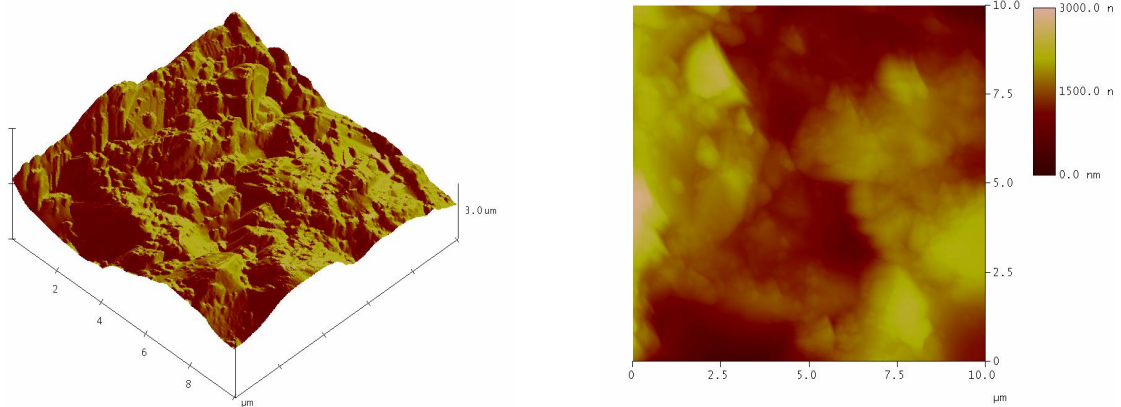
Figure 5.1-22 3d morphology representation (left) and 2d representation of 3d morphology (right) of sample 10 (Al_2O_3, lapped, R_a 0.45µm)

It can be seen in Figure 5.1-12 and Figure 5.1-13 that the effect of the etching is a slight roughening of the surface as whole crystals are removed leaving defects. Samples 1 and 2, both of which underwent chemical etching show recesses in an otherwise smooth polished surface (shown in the circles). However, if sample 3 is considered along with this it can be seen in Figure 5.1-14 that polishing also has the affect of removing whole crystals from the surfaces. Figure 5.1-14 shows the uniform polished surface of sample 3 whilst Figure 5.1-15 shows a different area of the same sample where either the mechanical polishing procedure has torn out whole grains along their boundaries which is the weakest part of the material. It is also possible that the mechanical polishing has removed the peaks of the roughness profile, leaving the deepest valleys one of which is shown in Figure 5.1-13. This shows a potential combined material removal mechanism for polishing, shear failure of grains and removal of grains at the grain boundary. Further analysis via SEM confirmed these findings with the appearance of a pitted, but otherwise smooth surface, Figure 5.1-23.
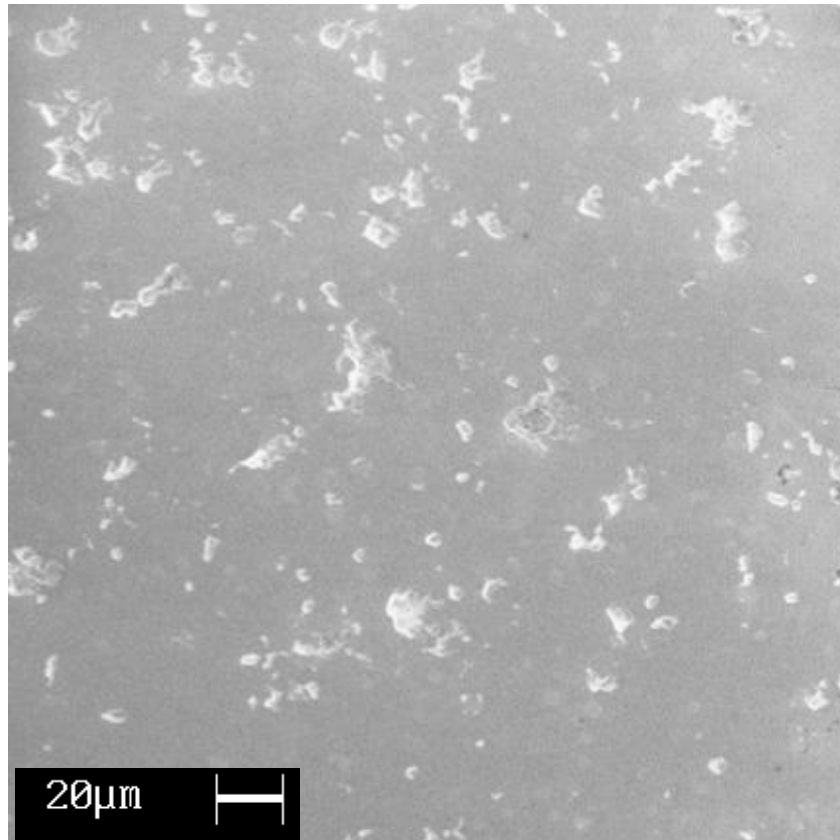
Figure 5.1-23 500x SEM image of sample 3 surface.

It was found that the effect of the etching was to increase the size of these recesses in the sample surfaces, increasing the mean roughness of the samples.

Samples 4,5,6 and 8 were all received in the condition of as-fired. Interestingly all samples showed very different surface conditions, even though the same processing had been used in their manufacture. The above Figure 5.1-16 to Figure 5.1-19 show markedly different grain sizes of the ceramics ranging from 2-3μm for samples 4 and 5 to 5+ micrometres for sample 6 and less than one micron for sample 8. These ceramics were produced by different manufacturers, each of whom have opted to produce ceramics with different grain sizes, this is something which is easily controlled in the manufacture of ceramics, as described in the literature review section of this work. The effects of the different grain sizes are plainly a large array of surface topographies. Surface topography could become an important factor in this work if bonds formed to surfaces fail at the ceramic/adhesive interface.

Lapping is a method performed similarly to polishing, which are performed with a similar method to the one described in *Section 4.2.3 Mechanical Surface Preparations*. Polishing and lapping are performed with discs of different grit sizes, lapping without the presence of a polishing slurry. The material removal method of lapping is predominantly by the removal of whole grains, this is an aggressive process which usually has the effect of roughening the surface. However, greater geometric accuracy can be gained using this process, with properties such as flatness being readily controllable. The effect of lapping on the samples analysed in this work appears to be a large amount of damage to the surfaces, samples 7 and 10 shown in Figure 5.1-19 and Figure 5.1-22 above give examples the effects of lapping, each shows a large z axis variability on a ceramic with large grains. The result of this is a surface of high roughness. Lapping can be implemented to produce surfaces of incredibly smooth surface finish and low roughness, however for these samples it appears that the manufacturer has purposefully created a rough surface through the use of a coarse abrasive.

Considerations to be taken from these results are the effects of the roughness on the wetting and surface energy of the surfaces, as well as the weakening of the surfaces through the mechanical forces subjected to them.

The AFM surface maps show the effects of processing on the surface morphologies of the Al_2O_3 substrates. Figure 5.1-20 shows the as-fired surface where the separate crystals are clearly visible as grains of various sizes. Figure 5.1-21 shows the polished surface as both a 3D rendering and 2D height plot. In the height plot, the crystals and their boundaries can be clearly seen, but in the 3D rendering the grooves in the surface caused by the polishing abrasive are much more apparent than the crystals themselves. Figure 5.1-21 also indicates different hardnesses of the material across the surface, this could have implications with the cohesion strength of the ceramic. Unfortunately the scale of these features is such that their hardness is not measureable, even with nanoindentation. Material from between the crystals has been removed to a greater depth than the crystals have been abraded, suggesting heterogeneous material hardnesses.

5.1.4.3 Surface Texture Parameter Measurement

From Table 5.1-1 it can be seen that as fired samples (4-6 and 8) show a large range of roughness (0.05 μm ≤ R_a ≤ 0.85 μm), probably due to variation in the grain size of the ceramic in the green state prior to sintering. The granular texture of the as fired surfaces can be seen in the 3D AFM plot in Figure 5.1-20 for sample 8 (A_2O_3 as-fired, R_a 0.05 μm). The large variation in as-fired surface textures is one reason for a manufacturer to specify a mechanical or mechanical chemical surface preparation to the sleds to reduce manufacturing variations due to surface texture variation. To attempt to determine whether R_a gives sufficient information to allow this source of manufacturing variation to be controlled, white light interferometry and an AFM were also used to characterise the surface textures. The AFM gives the additional capability of producing a value for the Wenzel roughness ratio r. A comparison of R_a measured by the different methods plotted versus r is given in Figure 5.1-24.
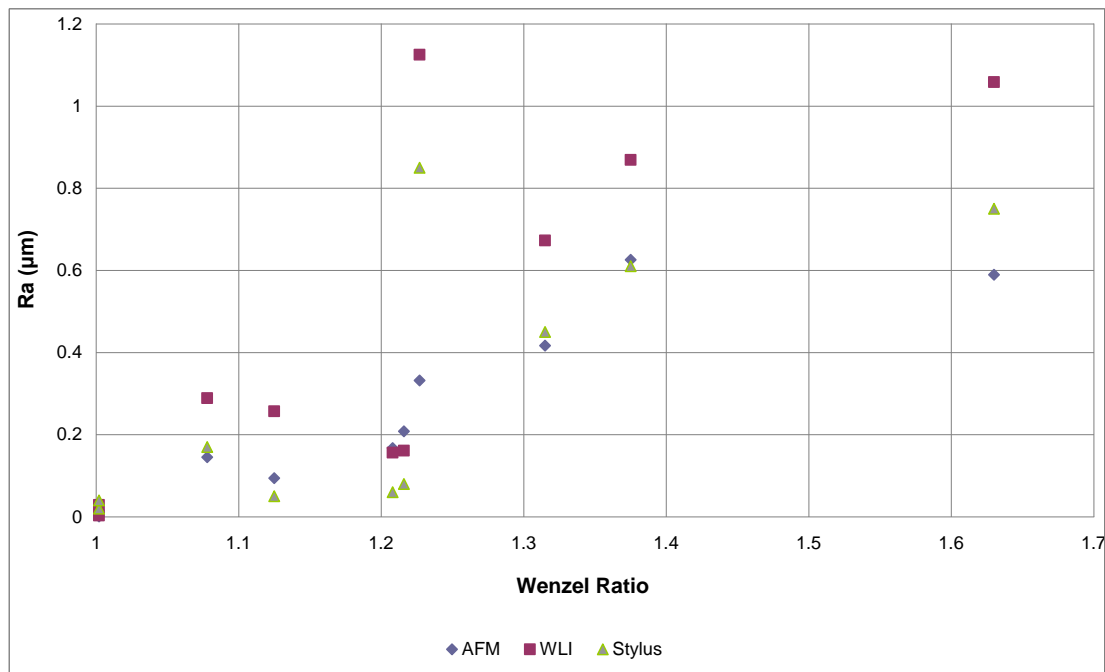
Figure 5.1-24 Comparison of R_a roughness values produced by AFM, WLI and stylus profiling to the Wenzel ratio produced by AFM.

On average (mean of the ratios) R_a by WLI is twice that by AFM. This is probably due to measurement artefacts in the WLI data. The 3D surface plots show multiple steep sided fissures which are not visible in AFM. The artefacts

are probably caused by multiple reflections from the surface features which increase the length of the light path. Evidence for this suggestion is provided by the high frequency of the occurrence of the fissures in the profiles and their equal depth. In addition there is a high frequency of missing data in the profiles, Figure 5.1-25, probably due to the incident light angles being such that the light is not returned to the sensor. These issues have been documented in the literature[14]

The mean ratio of R_a by the stylus instrument (Surftest SJ-400) to that by AFM is around 1.3 (single anomalous data point at very low R_a ignored, stylus: AFM value of 25 at r=1.002). Since both methods are surface contact the closer correlation is unsurprising. However, there are reasons to prefer the AFM measurements. In Figure 5.1-24 it can be seen that R_a by any method is not strongly correlated with r until R_a>0.2 μm. This shows that the AFM is picking up structure relevant to wetting in the surface texture at low R_a that is not reflected by that index. The major limitation of the AFM for assessing surface texture application is its inability to analyse large areas, and so properties such as flatness cannot be determined. However, for adhesive flow micro and nanoscale roughness is likely to be more important. Other reasons for preferring the AFM are that profiles are measured along an outwards and a return stroke along the same line of travel. This gives added reliability to the measurements because the tracking of the two directions can be compared. The AFM used in tapping mode allows precise control of the pressure the tip exerts on the surface.

A potential reason for the anomalous R_a ratio obtained with the stylus instrument at low roughness (stylus: AFM value of 25 at r=1.002) is the nature of the situations in which the measurement methods are performed. The AFM is insulated against vibration and air flow whilst the portable stylus instrument has no means of filtering background vibration and atmospheric effects. The vulnerability of the stylus instrument to vibration could define its measurement limit, the point at which the effect of the surface upon the stylus is exceeded by the effect of noise.

An interesting result obtained with the AFM can be seen in Figure 5.1-21 for a polished Al_2O_3 surface (sample 9), which shows a 2D height plot. Despite the

polishing a grain structure is still apparent. This is probably due to different hardnesses of the material across the surface. Intergranular material and grains with different crystalline orientations have been removed differing extents. This implies sharp height boundaries which may provide good keying features for adhesive joint formation. The R_a and R_t values for the stylus, non-contact and AFM roughness measuring methods are given in Table 5.1-3.
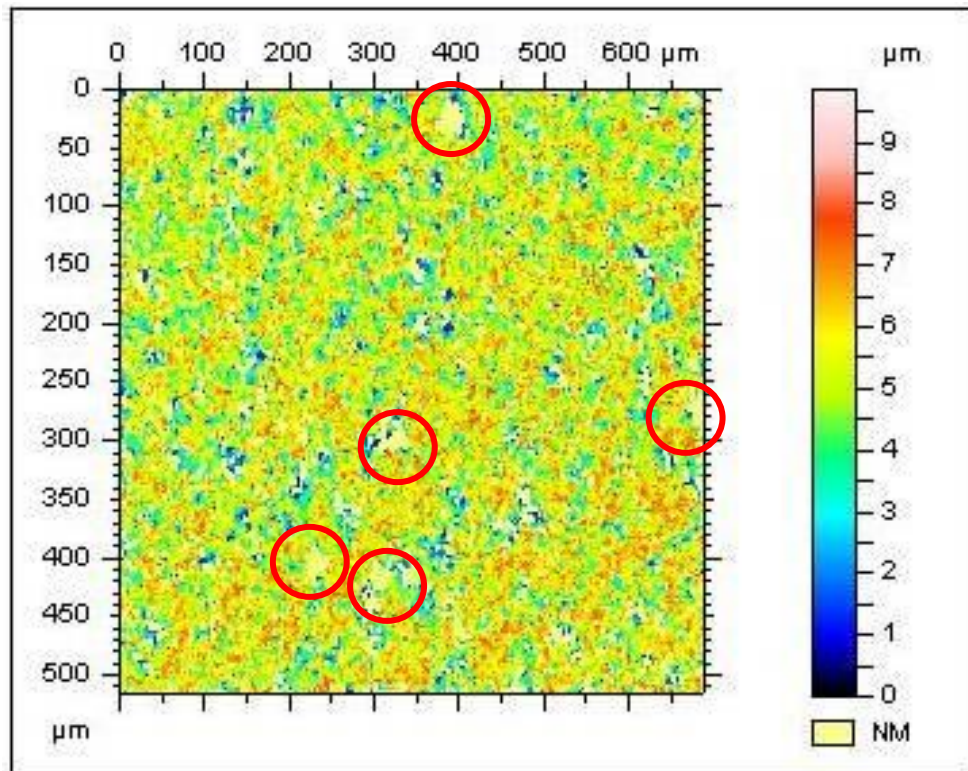
Figure 5.1-25 WLI z axis contour plot of sample 7 with large areas of missing data highlighted. Areas where there is an interface between a dark blue area (0µm) and white area (10µm) indicate 10µm vertical faces on the surface which were not seen with SEM or AFM and so were concluded to be due to the inadequacies of the WLI method.

Sample	Ra_1	Rt_1	Ra_2	Rt_2	Ra_3	Rt_3	r
1	0.156	5.8	0.06	1.3	0.1673	1.025	1.208
2	0.161	5.66	0.08	2.7	0.208	1.672	1.216
3	0.029	5.19	0.04	1.9	0.0107	0.098	1.002
4	0.289	7.55	0.17	2.1	0.1452	1.079	1.078
5	0.869	7.55	0.61	4.9	0.6257	4.117	1.375
6	1.125	9.79	0.85	7.2	0.3321	2.522	1.227
7	1.0584	9.85	0.75	8.2	0.58951	4.46	1.63
8	0.257	8.36	0.05	0.5	0.0942	0.791	1.125
9	0.0029	0.05	0.02	0.4	0.0008	0.084	1.002
10	0.673	7.26	0.45	4.0	0.4165	2.772	1.315

Table 5.1-3 Measured surface texture parameters, subscript 1 denotes WLI, 2 Mitotoyo Surftest SJ-400 with a 5µm tip radius, 3 AFM in tapping mode with a 15nm tip radius. r is the

Wenzel roughness factor, as measured with the AFM. All roughness parameter units are μm, r is unitless.

5.1.4.4 Adhesive Characterisation

Using the pendant drop method the surface tensions of the two adhesive systems were measured, and are shown in Table 5.1-4   below. The measurements are a representation of the aggregate effects of all of the adhesive components.

Adhesive	Surface Tension mJ/m^2
930-4	52.43
H20E	47.81

Table 5.1-4 Mean surface tensions of the epoxy adhesives as calculated using the pendant drop method, measurements have an estimated error of ±2mJ/m^2.

The data in the above table is higher than expected for an epoxy adhesive. However other work[15] has shown that a filler material can have the influence of increasing the surface tension of a filled polymer.

It was deemed important to identify the size of the filler material particles in the adhesives, this was attempted with SEM. The particle size of the 930-4 boron nitride filled adhesive was given on the data sheet as ≤20μm, this was taken to be accurate due to the strict limitations imparted on the manufacture of the adhesive. The size of the silver flakes in the H20E adhesive was not given, images were taken to verify their sizes, Figure 5.1-26 below shows the silver flakes in an adhesive spot. The flakes were found to have maximum dimensions of 15μm, a figure much above the feature sizes found by AFM investigation, *Section 5.1.4.2 AFM Surface Texture Characterisation*. The implications of this will be explored in later chapters.
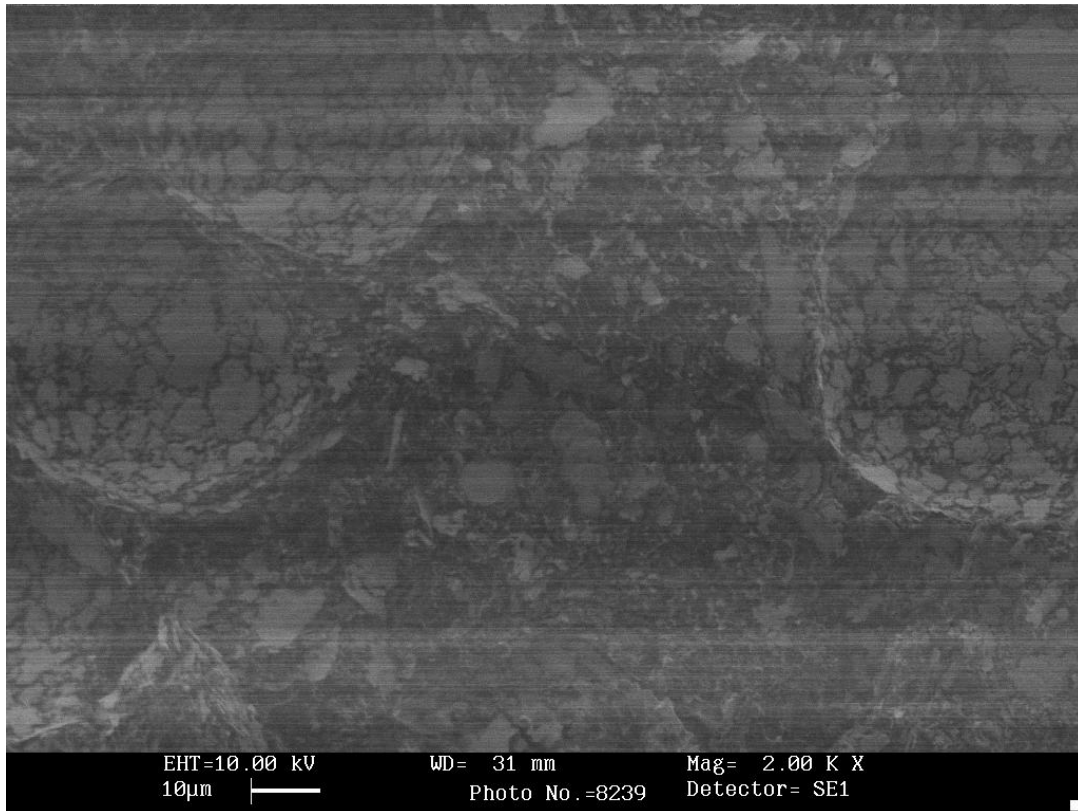
Figure 5.1-26 SEM image of the silver flakes in the H20E adhesive.

5.1.4.5 Analysis of Adhesives and Epoxy Bleed With XPS

XPS analysis was employed for the analysis of the commercial adhesives, homemade adhesive and their respective bleed materials. The aim of this analysis was to determine the chemical properties of the material which had bled from the bulk adhesive and how it differed from the adhesive itself.
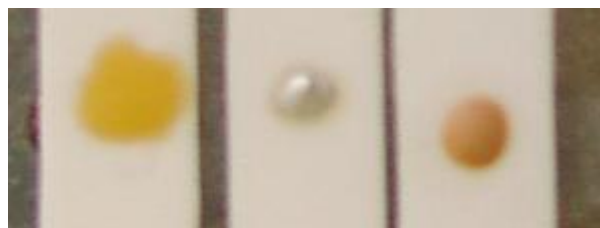
Figure 5.1-27 Adhesive samples on aluminium oxide analysed with XPS, home made adhesive (left) silver filled H20E adhesive (middle) boron nitride filled 930-4 adhesive (right) each with characteristic halo of bleed material.

Figure 5.1-27 shows the samples which were analysed, the analysis method was to align the aperture with the bare ceramic close to the sample and analyse every 300µm from the outer edge towards the centre of the spot, the bleed material spread sufficiently to guarantee that it would be caught in at

120

least one of the analysis areas. For each area a wide scan and high resolution scan for each element found to be present from the wide scan, was performed. Analyses were made with the Kratos AXIS ULTRA as described in *Section 4.3 X-ray Photoelectron Spectroscopy*.
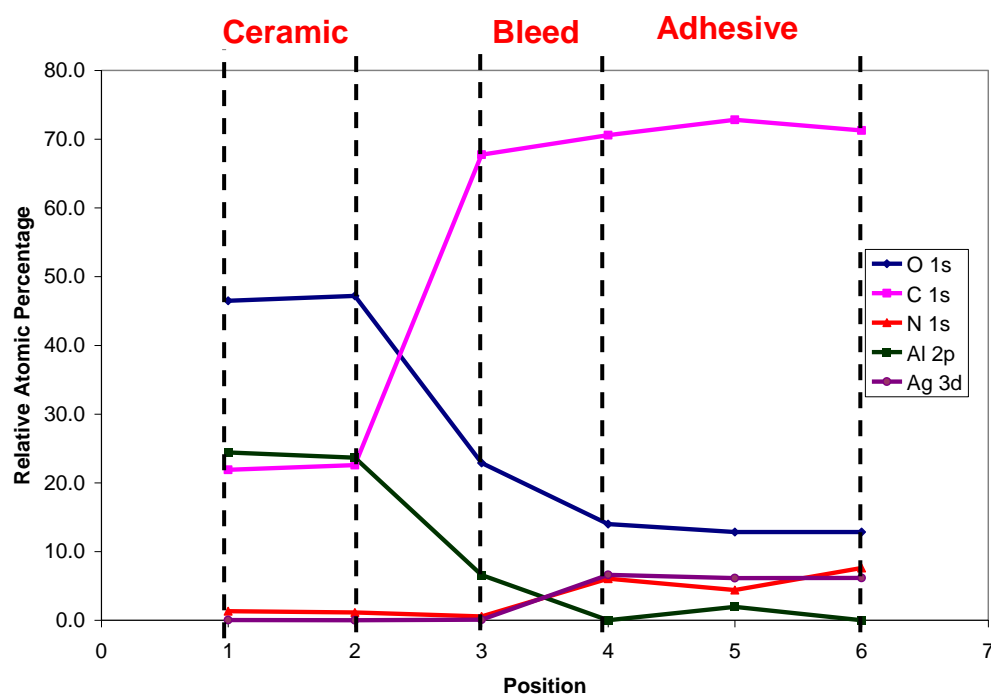
Figure 5.1-28 Relative atomic percentage plot for oxygen, carbon, nitrogen, aluminium and silver from aluminium oxide sled (positions 1 and 2) epoxy bleed (position 3) and bulk H20E adhesive (positions 4, 5 and 6)

Figure 5.1-28 shows the results of the series of wide scan XPS spectra across the surface of the ceramic carrying the silver filled adhesive, the bleed from the adhesive and the bulk adhesive also. The graph shows the data in terms of relative elemental composition. It can be seen that the composition of the surface of the aluminium oxide substrate consisted primarily of oxygen (46.5%), aluminium (24.4%) and carbon (21.9%), which is typical of as-received materials. The similarity in composition between positions 1 and 2 show the uniformity of the composition of the surface and contaminants adsorbed onto it. Tracing the relative percentage of the aluminum shows that the presence is significantly reduced (6.6% from 21.9%) once the bleed area is reached, this suggests that the thickness of the bleed material is sufficient to reduce the aluminium signal, suggesting multiple layers of molecules and

not monolayers. Once the analysis is fully within the bounds of the intended analysis area of the bleed and bulk adhesive the signal from the aluminium is almost zero, this is to be expected due to the highly surface sensitive nature of XPS. The nitrogen data shows that the curing agent used for the silver filled adhesive probably has a high presence of nitrogen such as the 2-ethyl-4-methylimidazole. The nitrogen is present in higher quantities as the bulk adhesive is reached, at position 3 it is clear that the analysis area is almost entirely within the bleed material (due to lower aluminium, 6.6% and oxygen, 22.9% and significant increase in carbon 67.7%), however the nitrogen signal is very low (0.6%) compared to the bulk adhesive value of 7.6%, suggesting a lack of curing agent. This result could begin to suggest the mechanism for bleed to occur during the curing process, the bleed material could be polymer which has not been crosslinked into the thermoset network, possibly due to its lower molecular weight. The molecular weight of the epoxy polymers has been linked to epoxy bleed in previous work[16]. It can be noted from Figure 5.1-28 that the filler material is not present in the bleed material. Figure 5.1-29 shows the series of high resolution scans and a plot of the silver signal from the high resolution scans. The emergence of the silver signal conforms to the proximity to the bulk adhesive, it is clear in image (a) that no silver is present and considering this with Figure 5.1-28 it can be surmised that this area is within the bleed material, but the action of the bleed has not taken filler material with it. Two peaks are present in the silver area, these are representative of the $3d_3$ (at 374eV) and $3d_5$ (at 368eV) electrons which have undergone interaction with the X-rays[3] and produced a signal. The maximum silver contribution to the total composition of the bulk adhesive according to the XPS analyses is 6.6%, when the analysis area is fully within the bulk material. It is known from the MSDS of the two components of the silver adhesive that the silver flakes make up 60-83% by weight of the epoxy when the two components are combined in the right fractions. The reason for the lower XPS silver signal than the known composition of the adhesive material is that the carrier epoxy wets the silver flakes, giving them a surface of cured epoxy resin and not uniform silver. XPS data is also given in atomic percentage, so the high density of silver and comparatively low density of

epoxy also accounts for the difference in silver content by weight and observed atomic percentage.
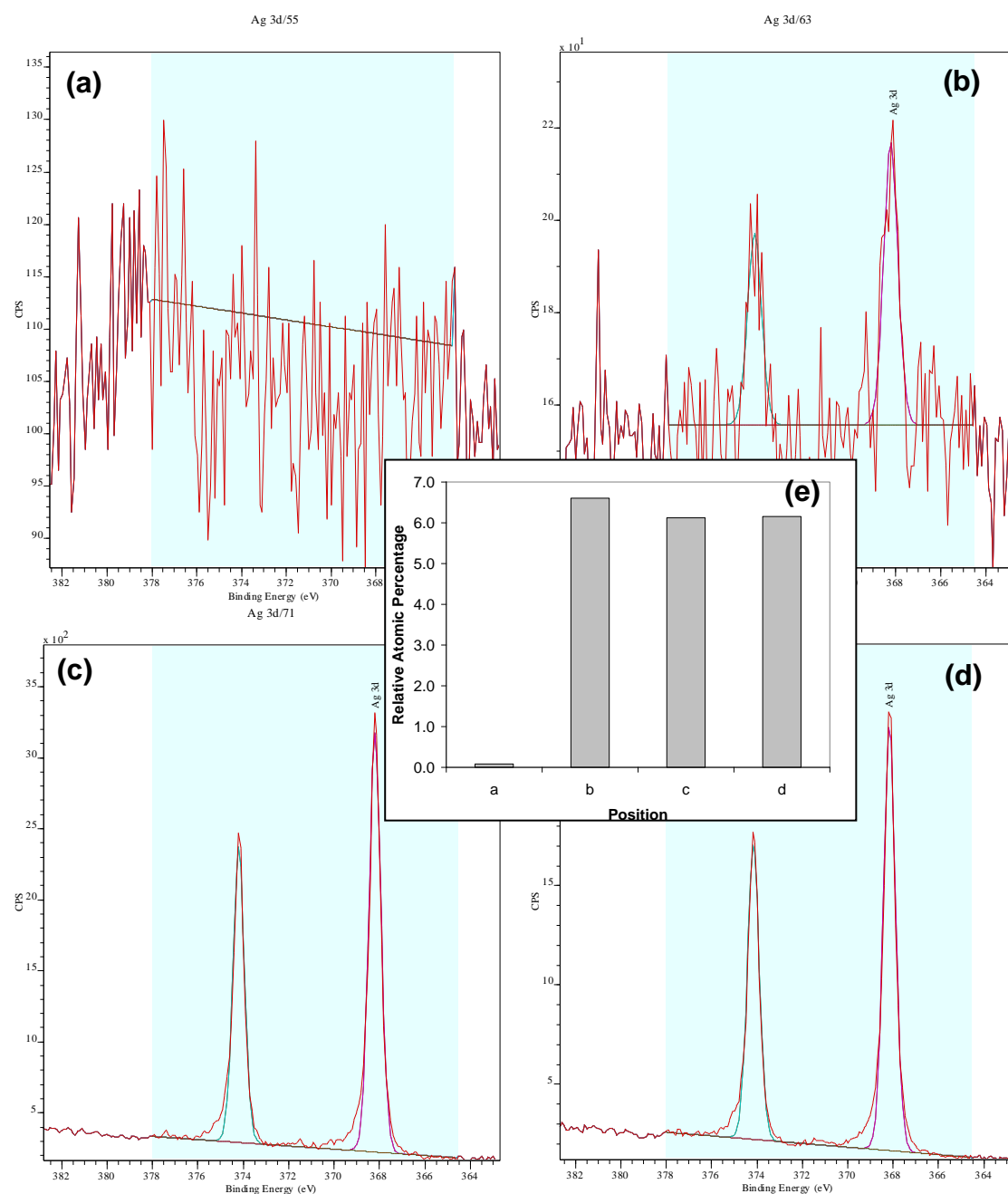
Figure 5.1-29 XPS high resolution spectra of silver for H20E adhesive, of epoxy bleed (a) and bulk adhesive (b), (c) and (d). Plot of relative atomic percentages from wide scans. (e).

The bond types present across the different areas of analysis were analysed, it was found with the oxygen that the peaks change as the analysis passes from ceramic to bleed area to bulk adhesive suggesting different bond types. On the ceramic material the majority of the oxygen signal (82-83%) is from the O1s signal and Al_2O_3 bond signal, which both appear in the same binding

energy areas. Considering the oxygen high resolution scan with the carbon high resolution scan the second oxygen peak found on the ceramic surfaced can be identified as a C-O-C bond giving a peak for carbon at 286.4eV and 532.4eV for oxygen. This is attributable to organic contaminants adsorbed onto the surface. All analyses from the ceramic materials show the same two peaks which can be seen in Figure 5.1-30 (a). This shows consistency over different samples as well homogeneity over individual samples. Once the bleed material is reached the oxygen peaks corresponding to Al_2O_3 and C-O-C are reduced dramatically with the C-O-C peak absent entirely, Figure 5.1-30(b). Instead, a new peak is seen at 533.13eV which is attributable to an epoxide group. The new peak contributes 60.27% to the total oxygen presence, with the remaining peak still consistent with the O1s position. For the high resolution carbon spectra a peak is present at 287.0eV which confirms the high presence of epoxide groups. The remaining groups for the carbon peak area are difficult to identify due to their respective oxygen peaks being very close to the epoxide peak, possibly making them indistinguishable. An example of this is the carbon peak at 286.3eV which could indicate the presence of C-OH groups from the 1,2-propanediol, however, the corresponding oxygen peak has been seen to appear as high as 533.09eV[5] and could be indistinguishable from the epoxide peak at 533.13eV. Once the bulk adhesive is reached the majority (85-90%) of the signal is seen to be from epoxide groups, Figure 5.1-30 (c).
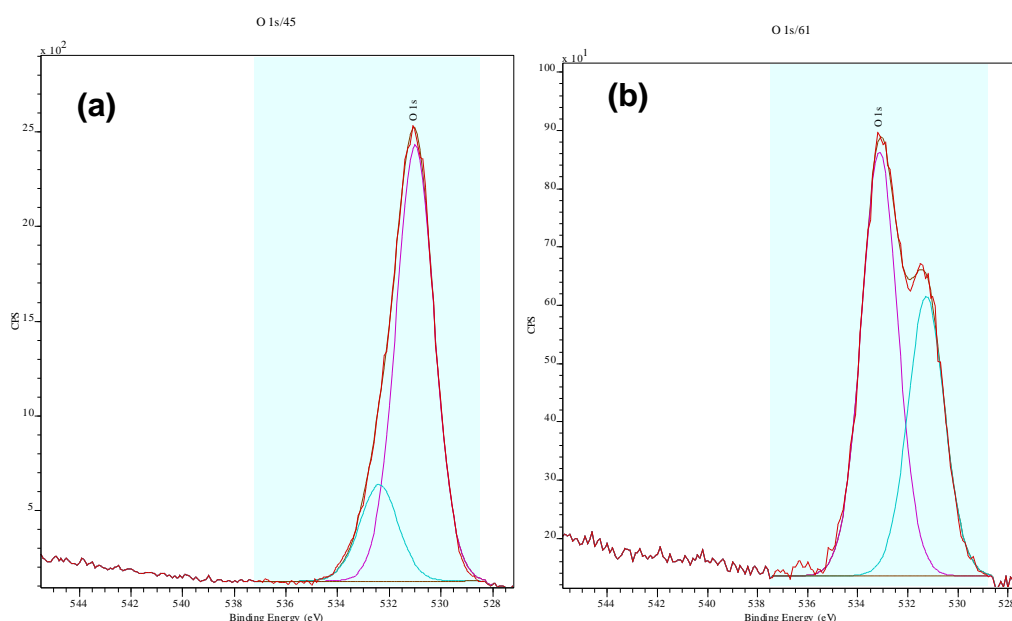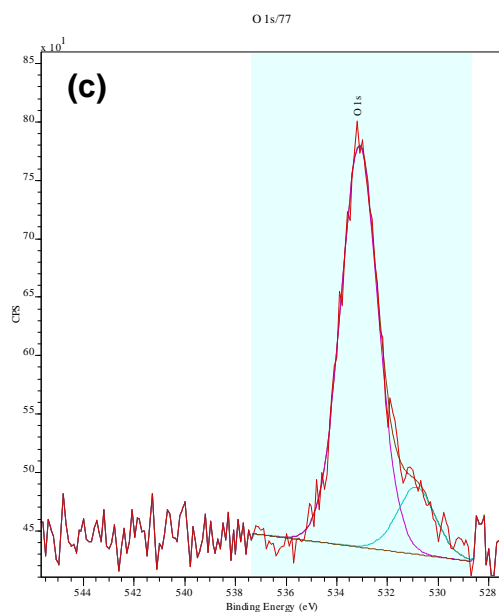
Figure 5.1-30 High resolution XPS spectra of oxygen binding energy area. (a) on ceramic material (b) on silver filled epoxy bleed material (c) on silver filled epoxy bulk material.

For the analysis of the bulk adhesive region the ratio of bond types is different to the bleed material as well as the original surface condition. The O1s peak is reduced from 40% of the total signal in the bleed material to ~12% in the bulk material, the remainder (60%) of oxygen bond types is again made up of epoxide groups at 533.13eV. The amount of nitrogen increases also, to a maximum of 7.6% of the total composition. As the curing agent was unknown, it was concluded that it contained a high degree of nitrogen and that this was the source of the signal, more could not be concluded from the data due to the high number of possible curing agents used in the composition[17]. Three peaks were seen, Figure 5.1-31, in the high resolution nitrogen spectra at 398.4eV, 400.17eV and 401.5eV, these were attributable to N1s, C-N/C=N and pyridine respectively, again suggesting similarity of the curing agent to those used in the other epoxies studied.
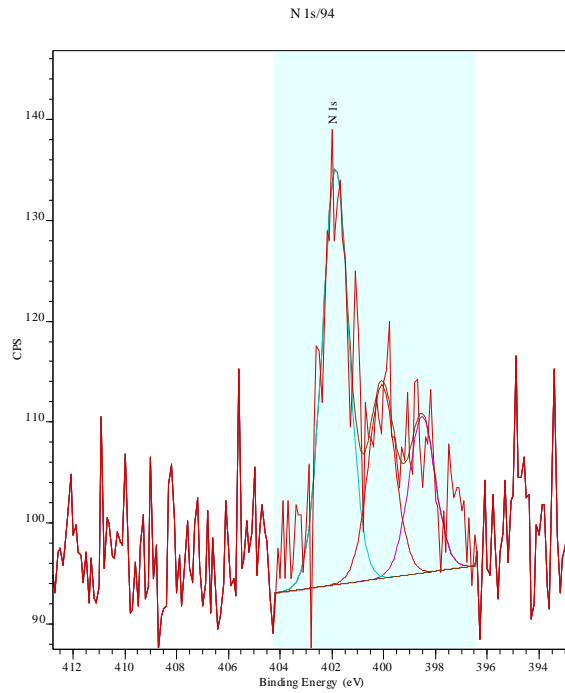
Figure 5.1-31 High resolution nitrogen spectra showing 3 distinct peaks attributable to N1s C-N/C=N and pyridine (nitrogen included in an aromatic ring).
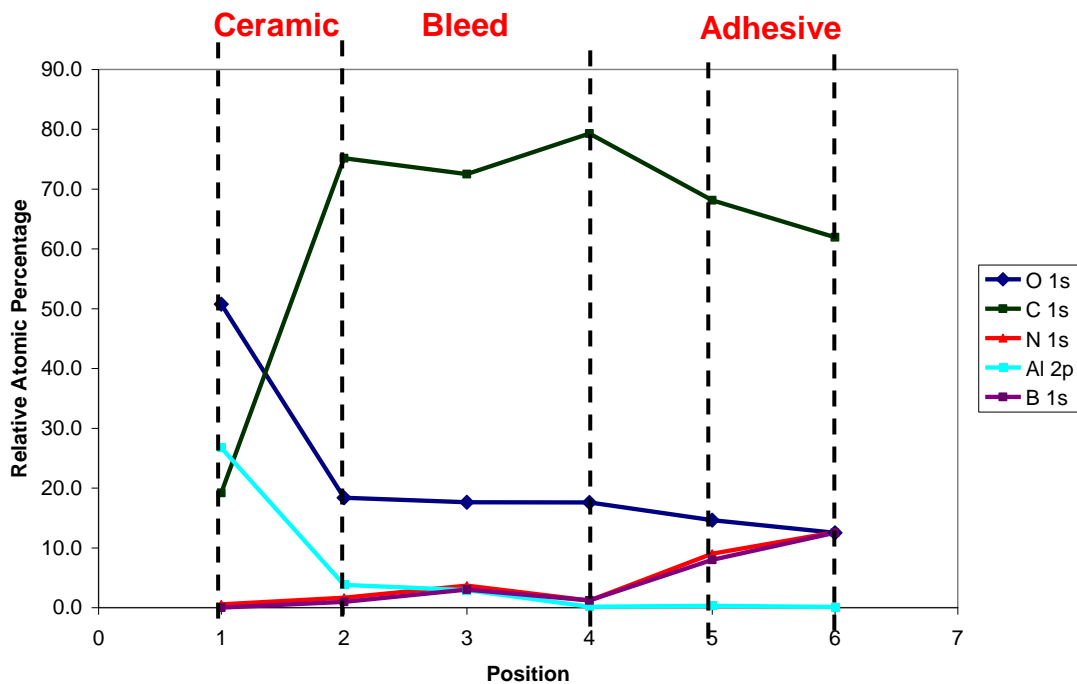
Figure 5.1-32 Relative atomic percentage plot for oxygen, carbon, nitrogen, aluminium and boron from aluminium oxide sled (position 1) epoxy bleed (positions 2, 3 and 4) and bulk 930-4 adhesive (positions 5 and 6)

Much the same trends were seen with the boron nitride filled adhesive as were seen with the silver filled adhesive. It can be seen from Figure 5.1-32 that the behaviour of the aluminium, carbon and oxygen is much the same, as is the markedly higher fraction of nitrogen when the bulk adhesive is reached.

126

A close correlation between the nitrogen signal and the boron signal can be seen, not least because they are bonded together as boron nitride. As expected the nitrogen signal is also slightly higher than the boron signal due to the signal from the curing agent. The high resolution scan of the nitrogen on the bulk boron nitride filled adhesive, Figure 5.1-33, reveals three distinct peaks which represent the same bond types as with the silver filled epoxy. However, in this formulation the N1s/BN peak contributes significantly more to the signal than in the previous case, Figure 5.1-31. The binding energies for the BN and N1s peaks are in the same place, making them indistinguishable, this is also apparent with the C-N and C=N bond.
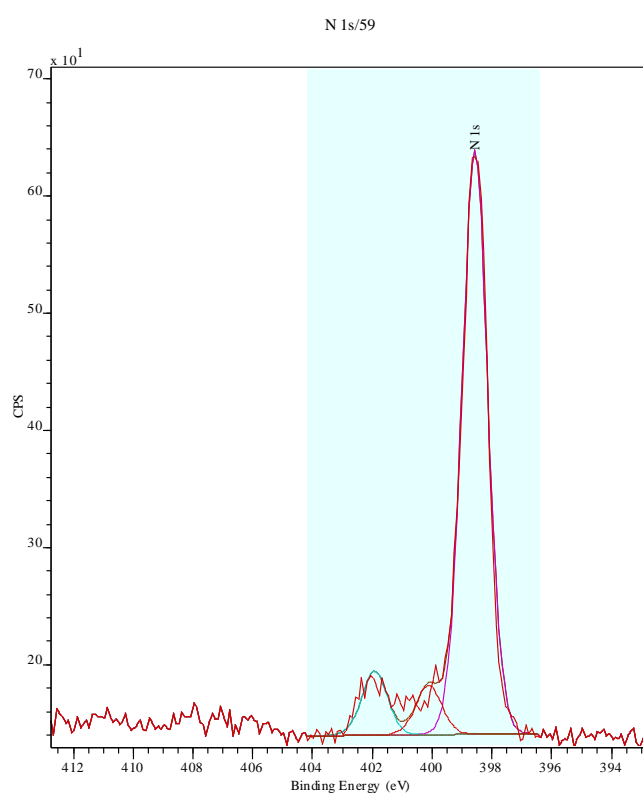
Figure 5.1-33 High resolution spectra of the nitrogen binding energy area showing 3 distinct peaks attributable to N1s/BN, C-N/C=N and pyridine.

Figure 5.1-34 shows the variation in the narrow scan boron peak and change in the relative atomic percentage of boron from broad scan across the surface of the adhesive spot. It is clear that one single peak is present representing boron nitride. However, in this analysis, unlike the analysis of the silver filled adhesive, it is apparent that some boron signal is seen in the epoxy bleed area. This would suggest that the action of the bleed has not only taken lighter

fractions of the carrier material, but also some of the filler material. The particle size quoted for the filler boron nitride powder is $\leq$ 20µm, but no lower value is quoted. It is possible that some of the smaller particles, which were not apparent though inspection with SEM, of BN powder have been carried with the bleed material, and it is they which are responsible for the boron signal on the epoxy bleed area, Figure 5.1-34.
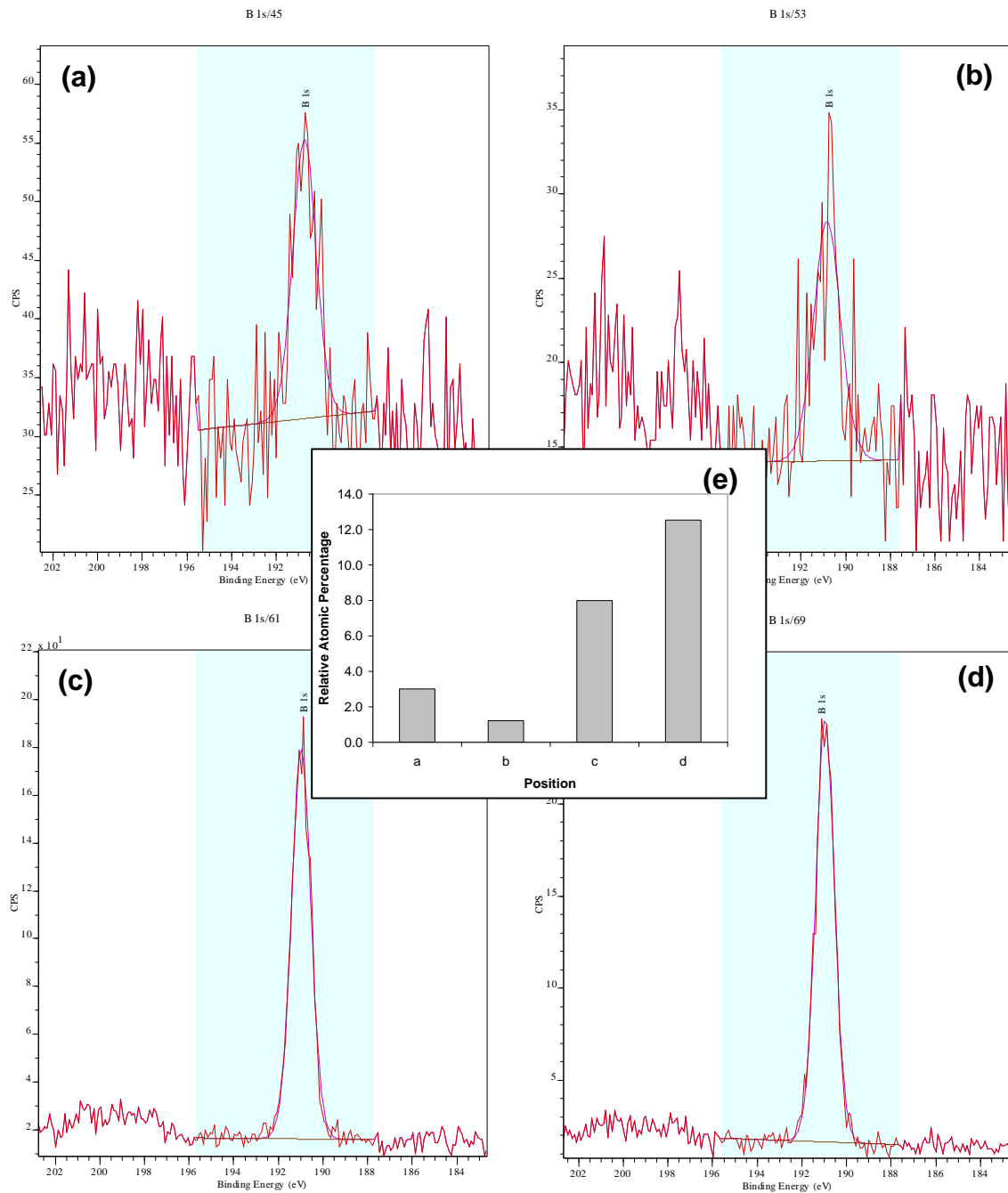
Figure 5.1-34 XPS high resolution spectra of boron for 930-4 adhesive, of epoxy bleed (a) and (b) and bulk adhesive (c) and (d). Plot of atomic percentages (e).
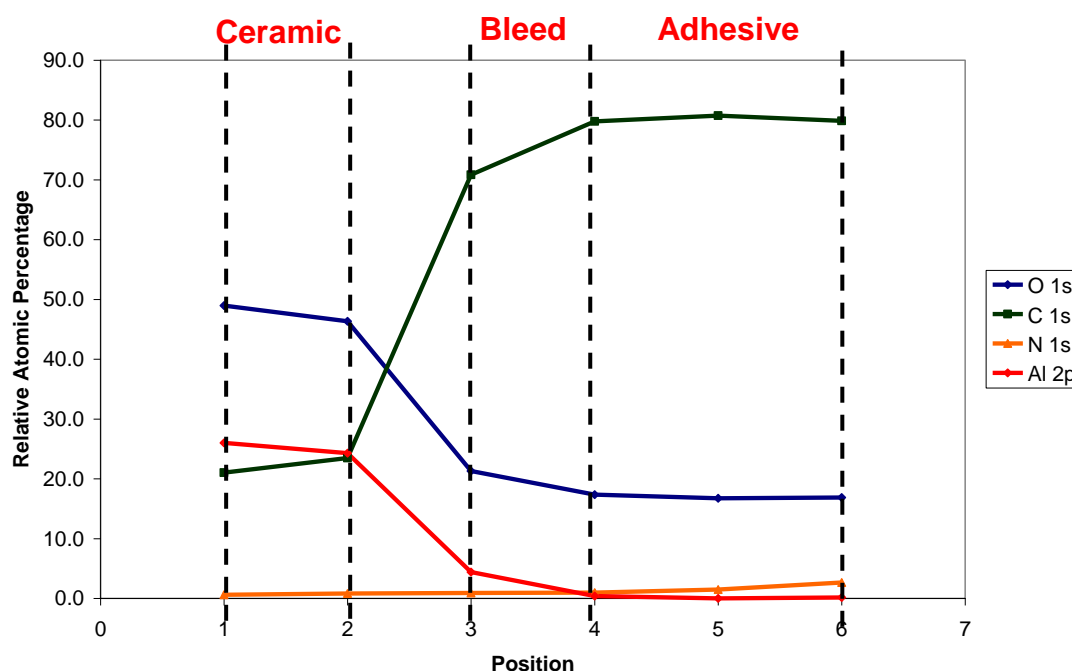
Figure 5.1-35 Relative atomic percentage plot for oxygen, carbon, nitrogen and aluminium from aluminium oxide sled (positions 1 and 2) epoxy bleed (position 3 and 4) and bulk home made DGEBF adhesive (positions 5 and 6)

The XPS analysis of the home made adhesive was easier to interpret than the commercial adhesives due to all of the ingredients, and their fractions, being known. The analysis also let the behaviour of a filler-free adhesive to be compared to those with the fillers. Figure 5.1-35 shows the results of the series of wide scans over the ceramic, bleed area and bulk adhesive surfaces, the relative atomic percentages are given. As with the boron nitride and silver filled adhesives the aluminium and oxygen signals show a high decrease as the analysis moves almost fully onto the epoxy bleed area, due to the surface sensitivity of the XPS method. This adhesive showed a much lower tendency to bleed than the commercial ones, possibly due to its higher molecular weight and greater viscosity, therefore it was difficult to induce bleed sufficient for a full area for analysis. In Figure 5.1-35 it can be seen that the first area quoted as being epoxy bleed is probably not entirely within the bleed area, but some bare ceramic is still present.

Tracing the carbon and oxygen peaks reveals that the majority of oxygen is bonded in an epoxide group at 533.13eV in the bulk adhesive, an increase in the $O1s/Al_2O_3$ peak is seen when the bleed area is reached, and then once the bare ceramic is reached the $O1s/Al_2O_3$ peak fraction increases to 84%

and the epoxide group is no longer present, but a C-O peak is. This is consistent with other data from the nature of the contaminants on the bare ceramic.

The nitrogen bonds present were known from the curing agent and probable reaction between the curing agent and the polymer. Only the predicted peaks were found in the bulk adhesive, showing peaks on the high resolution scan at 398.4eV (N1s), 400-400.17eV (N-C/N=C) and 401.5eV (pyridine). As with the commercial adhesives the nitrogen signal increased up to 3 times the bleed area amount when the bulk material was analysed. However, this was to a much lower degree than with the commercial adhesives (due to the boron nitride presence in the 930-4, and an unknown reason in the silver filled adhesive). Nitrogen was seen to contribute only 3% to the total composition in the bulk adhesive, and 1% in the epoxy bleed. Interestingly, as the analysis moved further into the adhesive the amount of nitrogen increased, suggesting that regardless of bleed occurring, the spreading of the epoxy during the curing process can be linked to the cross linking reactions between the polymer and the curing agent i.e. polymer chains which have crosslinked to a lesser degree have a higher tendency to spread over the surface. The presence of nitrogen in the home made adhesive system is comparable to the boron nitride filled epoxy, which includes the same curing agent and epoxy in its formulation, once the nitrogen signal due to the boron nitride is subtracted from the nitrogen signal the total nitrogen presence tends to be ~1% and less when the epoxy bleed is analysed. The silver filled epoxy contains up to 7.6% nitrogen, this suggests that either a much higher amount of curing agent is used in its formulation (which is probable due to the mix ratio of 1:1 when one of the constituents does not contain epoxy polymer), or additional additives in the formulation contain nitrogen. This is a reasonable assumption to make when considering the MSDS of the material, which quotes no epoxy material in the second component, even though it is liquid and the two components are combined in equal parts. The higher presence of curing agent in the silver filled epoxy could also affect the bleed distance, which was greater for the boron nitride filled adhesive than the silver filled adhesive.

One disadvantage of the XPS method is the inability to determine the length of polymer chains, it is probable that the lighter fractions/shorter chain polymers in the adhesive have a higher tendency to bleed due to their lower tendency to crosslink with other polymer chains and be included in the bulk adhesive macromolecule.

5.1.5 Conclusions

The level of carbon based contamination was found to be a much stronger influence on wetting of the ceramics than surface texture with as-received samples. It seems that to witness the direct effects of roughness on wetting, the contamination will have to be removed first.

The effects of processing of the ceramics tended to be damage to the surface structure by a variety of mechanisms, this will be considered in later work should the cohesion of the ceramic material become important.

Portable hand-held surface roughness measuring machines are not, in this case, particularly suited to giving an accurate representation of a ceramic surface, due to the feature size being such that it is not penetrable by the probe. For a smooth surface this is especially apparent as the surface has been machined to give the smallest feature size possible. A number of other factors can introduce errors into the measurements of portable surface texture equipment, namely vibrations. If the measurements are made in a production line then the samples should be removed to an area isolated from the vibrations before measurements are made. The effect of vibrations on the accuracy of roughness measurements is indicated by the fact the AFM and Zygo are mounted on vibration damping equipment, and even wit the use of this loud noise could have effects on the measurements sufficient to be visual on the method output.

Light based methods of surface measurement are also not suitable for these ceramic samples, for the crystal angles and steep angles of the topography create missing data points due to the incident angle being such that the light is not returned to the sensor. Steep fissures also appear to be present using this method, but their nature and absence with other analysis methods

suggest this is a phenomenon of the method and not an actual surface feature.

The composition of the epoxy bleed is similar to that of the bulk adhesive, showing only an increase in the presence of curing agents in the bulk material, this suggests that the molecules which were not quickly incorporated into the adhesive thermoset polymer system, had a greater tendency to spread across the surface. To solve this issue an epoxy with extremely high molecular weight could be used in formulations, the home made adhesive implemented one of high viscosity and molecular weight and showed markedly less epoxy bleed, however, this would create an epoxy of extreme viscosity when fillers are added, which could be impossible to dispense. For the silver filled epoxy the filler was not seen to migrate with the bleed material, however this was not so with the boron nitride filled epoxy where analysis showed trace amounts of boron nitride present in the bleed material. This was probably due to a population of smaller boron particles mixed in which are more susceptible to being carried by the bleed flow. It is also possible that silver flakes have a larger surface area and are less susceptible to bleed flow due to higher drag, or a reaction of the adhesive constituents to the silver surface incorporating it into the adhesive network.

5.1.6 References

[1] Hsiung, J.C. Pearson, R.A. Lloyd, T.B. A surface energy approach for analyzing die attach adhesive resin bleed Journal of adhesion science and technology 2003 Vol. 17 Issue no. 1 pp 1-14

[2] Burmeister, M. Elimination of epoxy resin bleed through thin film plasma deposition Proceedings of SPIE--the international society for optical engineering 2003 Vol. 5288 pp 780-785

[3] Brewis, D.M. Surface analysis and pretreatment of plastics and metals -- London : Applied Science, 1982

[4] Huntsberger, J.R. Interfacial energies, contact angles, and adhesion. adhesives age 0001-821X 1978 Vol 21 issue 12

[5] Pocius, A.V. Schultz, W.J. Thompson, W.L. Adam, R.A. Elastomers Formed In-Situ in Epoxy Resins: Chemistry and Toughening, The Journal of Adhesion, 1545-5823, Volume 41, Issue 1, 1993, Pages 189 – 202

[6] Zhou, T. Wang, X. Mingyuan, G.U. Liu, X. Study of the thermal conduction mechanism of nano-SiC/DGEBA/EMI-2,4 composites, Polymer, Volume 49, Issue 21, 6 October 2008, Pages 4666-4672, ISSN 0032-3861, DOI: 10.1016/j.polymer.2008.08.023.

[7] Starov, V. M. Garcia, M. Wetting and spreading dynamics /   Boca Raton, Fla. ;   London : CRC/Taylor & Francis,   2007.

[8] Berim, G.O. and Ruckenstein, E. Microscopic Interpretation of the Dependence of the Contact Angle on Roughness *Langmuir*, 21, 17, 7743 - 7751, 2005, 10.1021/la050676d

[9] Dettre, R.H., Johnson, R.E., Advances in chemistry series. No.43, 136 1963

[10] Lee, L.H. 1924- Fundamentals of adhesion /   New York ;   London :   Plenum Press, 1991

[11] Wenzel, R.N. Surface Roughness and Contact Angle J. Phys. Chem., 53, 9, 1466 - 1467, 1949, 10.1021/j150474a015

[12] Cimalla, I. Foerster, C.H. Cimalla, V. Lebedev, V. Cengher, D. Ambacher, O. Wet chemical etching of AlN in KOH solution. Physica status solidi. Volume 3 NO: 6 PG: 1767-1770 2006

[13] Bickermann, M. Schmidt, M.S. Epelbaum, B.M. Heimann, P. Nagata, S. Winnacker, A. Wet KOH etching of freestanding AlN single crystals, Journal of Crystal Growth, Volume 300, Issue 2, 15 March 2007, Pages 299-307, ISSN 0022-0248.

[14] Pavlicek, P. Hybl, O. White-light interferometry on rough surfaces—measurement uncertainty caused by surface roughness. Applied Optics 2008;47(16): 2941–2949.

[15] Carmona, F. Conducting filled polymers, Physica A: Statistical Mechanics and its Applications, Volume 157, Issue 1, 1 May 1989, Pages 461-469

[16] Neff, B. Huneke, J. Nguyen, M. Liu, P. Herrington, T. Gupta, S.K. No-bleed die attach adhesives. Advanced Packaging Materials: Processes, Properties and Interfaces, 2005. Proceedings. International Symposium on , vol., no., pp. 79-81, 16-18 March 2005

[17] Petrie, E.M.   Epoxy adhesive formulations /   New York ;   London :   McGraw-Hill,   2006.

5.2 Surface Parameter Effects on Epoxy Bleed and Bonding

5.2.1 Introduction

In this section of work the relationship between surface properties, epoxy bleed and bonding was studied. In addition to bleed control it is important for the optoelectronic assembly process that the bonds formed between the substrates and optoelectronic components have sufficient shear strength and resistance to thermal fatigue.

It has been seen that the effect of surface roughness is masked by the effects of the contamination on the as received samples. It is, therefore, important to attempt to separate the effects of the surface roughness and chemistry. To do this a method had to be found which would homogenise surface chemistry, but leave the surface profile unchanged. Aluminium oxide and aluminium nitride are both chemically stable. The predominantly adventitious carbon contamination; see *Section 5.1.4.1 Ceramic Sample Surface Chemical Characterisation*, is easily oxidised into carbon dioxide and water. Thus oxidative cleaning methods are suitable. A number of highly oxidative cleaning methods were considered. Plasma cleaning was chosen due to it being a dry cleaning method which needs no further processing. It is also already used in the assembly line of optoelectronics manufacturers. A method was also needed for the comparison of the epoxy bleed on different surfaces. There is no standard way of measuring epoxy bleed so a bespoke method was devised.

Bonding was studied by tensile testing of lap joints and analysis of the failure location of the adhesives. A particular concern was to investigate whether the reduction of the surface energy due to the presence of carbon contamination causes the formation of a composite gas/adherend surface during wetting by the adhesive. This would tend to reduce the degree of mechanical interlocking adhesion due to the introduction of liquid/gas interfaces which would otherwise be solid/liquid adhesive bond interfaces. If the adventitious carbon caused this effect then it would have the potential to produce a bond of unacceptably low breaking shear stress.

The behaviour of the epoxies was also studied on copper surfaces. Copper was used as a cheap substitute for gold, which is a common metallisation material. Epoxy bleed is just as much an issue on metallisations as it is on ceramics.

5.2.2 Background Information

Past researchers investigating the epoxy bleed phenomenon have come to a number of different, often contradictory, conclusions as to the primary causes of resin bleed. The discrepancies arise from the effect of surface properties such as roughness and composition. By contrast there is general agreement regarding which properties of the adhesives favour resin bleed, although it is sometimes concluded that the properties of the resin have no effect at all.

A study by Ireland[1] into commercial epoxies, including the H20E (silver filled epoxy) used in this study, concluded that the cleanliness of adherend surfaces was the primary cause of resin bleed. Ireland offers the first solution to prevent bleed present in the literature, one which has been the subject of other studies[2,3]. The presented solution involves the vacuum baking of parts to induce deposition of organic contaminants, reducing the surface free energy and hence wetting by adhesives placed on inherently highly wettable surfaces. However, one of these studies has suggested that this process can damage gold metallisations and detrimentally affect subsequent wire bonding processes[2].

Ireland identified that different adhesive formulations exhibit different bleed behaviour, but does not investigate the reasons for this. Ireland's work was also limited in scope by not including detailed surface analysis to identify the properties which affect bleed, although the conclusion is drawn that the surface parameters are the driving force of the phenomenon. In 1994 a more detailed experimental study was performed into the phenomenon which focussed upon both the properties of the adhesive and the surface parameters[2]. This investigation concluded that it is more effective to modify the adhesive formulation than the adherend surface. This was done by formulating the adhesive from molecules with higher attraction to each other, making the adhesive more cohesive. This investigation was also the first to

identify the stages in the adhesive application process in which the bleed occurs. It reported up to 250μm of bleed before curing commenced, although it does not link this to an increase in surface energy with increasing temperature, which is possible[4].

In other works which have offered solutions to the epoxy bleed phenomenon through surface modifications, the use of plasma deposition for the application of a thin hydrophobic film[5] has been proposed. However, these methods require masking of sensitive areas, and relatively expensive plasma deposition machines. It is thus not a general process which can be applied to any substrate design without previous development of a mask. The work also offers no detailed analyses of the solutions it presents, and the mechanisms by which the solutions work are not discussed.

One experimental investigation which did cover surface property effects on epoxy bleed was performed in 2002 by Hsiung[6]. Whilst this work offers the most detailed investigation into the surface property effects found in the literature, the authors fail to definitively separate out the effects of surface energy and roughness parameters on the bleed and study only the cumulative effect. While the reasons roughness can affect epoxy bleed are discussed, it is disregarded as a contributor to epoxy bleed on the basis of calculations of the correlation coefficient. It may be objected that the authors consider only R_a as a roughness measure without advancing a justification, a point that the authors themselves acknowledge. In fact R_a is just one of hundreds available[7].

The literature thus shows scope for a detailed investigation into the factors affecting epoxy bleed. It is also apparent from the literature that a suitable epoxy bleed control method has not yet been developed.

5.2.3 Methodology

This section of work set out to identify the contributing factors to the apparently random occurrence of high degrees of epoxy bleed seen on the optoelectronics assembly line. The surface properties identified as potential contributors were surface roughness, surface chemical composition and surface energy. The literature did not offer a study of these parameters

singularly and so the work in this chapter had the aim of separating the parameters for individual study.

It was seen from XPS data, *Section 5.1.4.1 Ceramic Sample Surface Chemical Characterisation*, that adventitious carbon from an unknown source was present on all commercially prepared samples. To ensure homogeneity of samples this had to be removed, in order to allow the effect of contamination to be separated from the other surface properties, i.e. surface texture. Oxygen plasma cleaning was chosen for this purpose as it is dry, quick and used already in the optoelectronics assembly line.

The literature suggests an extremely slow etch rate of aluminium oxide and aluminium nitride with an oxygen plasma[8]. In fact Al_2O_3 and AlN are both used as plasma etch resists when etching different materials[9]. However, a slow etch rate still has the potential to etch weak points on the surface, such as the grain boundaries identified as being weaker in *Section 5.1.4.2 AFM Surface Texture Characterisation*. A short programme of preliminary experiments was therefore carried out to verify that oxygen plasma cleaning did not change the ceramic substrate surface texture while successfully removing the contaminants.

The breaking shear stress of the adhesive bonds between uncleaned and cleaned commercial ceramic samples of the same finish and batch was measured. This was done to ascertain whether the high contamination presence on some samples (and resultant low surface energy) was sufficient to induce adhesive failure. These measurements were also made for reference purposes so the effect of surface modifications in subsequent investigations could be seen.

Finally the occurrence of epoxy bleed was studied on copper and ceramic surfaces. The distance the bleed material spread across the surface was the experimental variable of interest. The maximum distance was chosen as the characteristic quantity due to this being the design limitation on feature spacing to limit the frequency of contamination. The distance was taken to be the maximum distance the material spread normal to a tangent to the adhesive droplet. The epoxy bleed distance was compared to the surface

roughness characterised by the Wenzel ratio and to the components of surface energy. Wenzel ratio was chosen due to its good correlation to epoxy bleed distance measurements, it was not, however, the only parameter considered.

5.2.4 Results

5.2.4.1 Preliminary Effect of Plasma Treatment Study

Plasma treatments were performed for 1 minute, 5 minutes and 10 minutes and the samples were measured with the AFM and contact angle goniometer. The methods and machine set up can be found in *Section 4 Experimental Procedures.* To assess if the ceramics had been etched, specific changes were looked for on the surface – increases in roughness, attack of high surface area to volume ratio features, deepening of weak areas found with the initial AFM study.

Figure 5.2-1 - Figure 5.2-4 below show AFM surface maps for a progression of increasing time of plasma treatment from no treatment, Figure 5.2-1, to a ten minute treatment, Figure 5.2-4, on a polished sample. It can be seen from the figures that there is no indication that plasma etching has attacked the weak areas between the crystals. Darker coloured lines representing deeper areas would be seen between the grains should etching have removed material. The deep areas created by the grinding and polishing, shown as small dark areas, have also not increased in size. This suggests that there has been no further weakening of the surface structure.

Table 5.2-1 shows the AFM R_a values of the plasma etched samples. Included in the table are the values of the surfaces with no treatment for reference. It can be seen that there is no increase in roughness for any of the samples, with all of the figures falling within the range of values measured in the original AFM measurements of the surfaces.
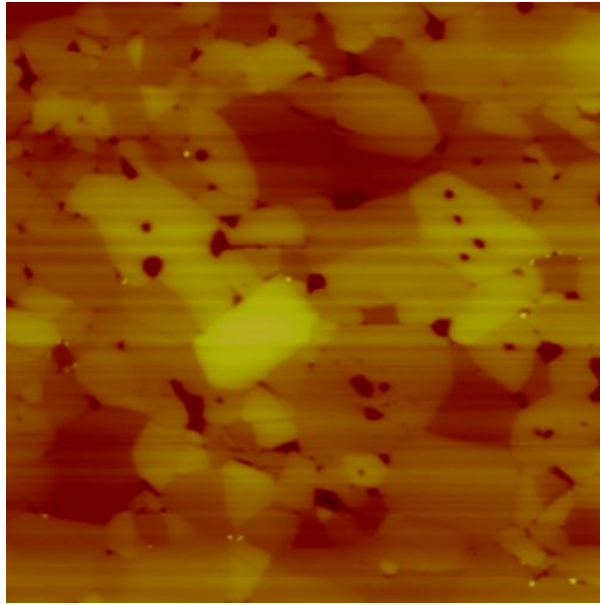
Figure 5.2-1 2d 3d morphology representation AFM height plot of sample 9, analysis area 10µm square.
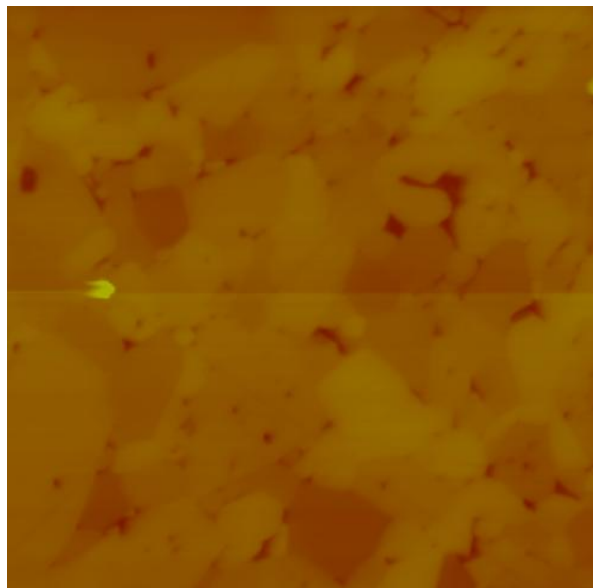
Figure 5.2-2 2d 3d morphology representation AFM height plot of sample 9 following 1 minute oxygen plasma treatment, analysis area 10µm square.
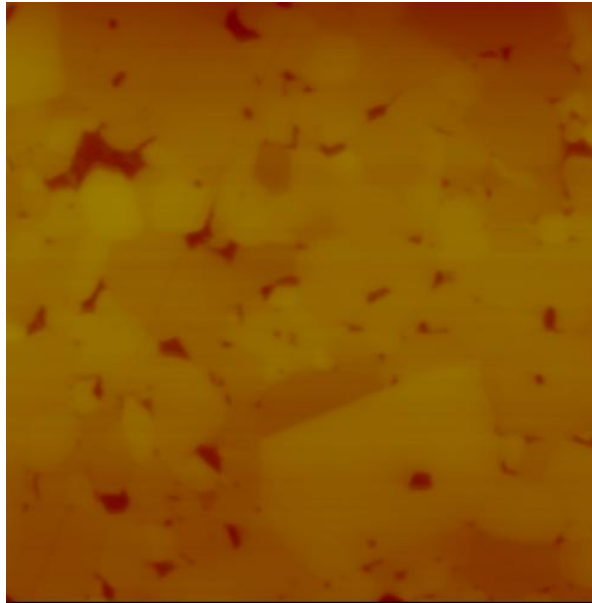
Figure 5.2-3 2d 3d morphology representation AFM height plot of sample 9 following 5 minute oxygen plasma treatment, analysis area 10µm square.
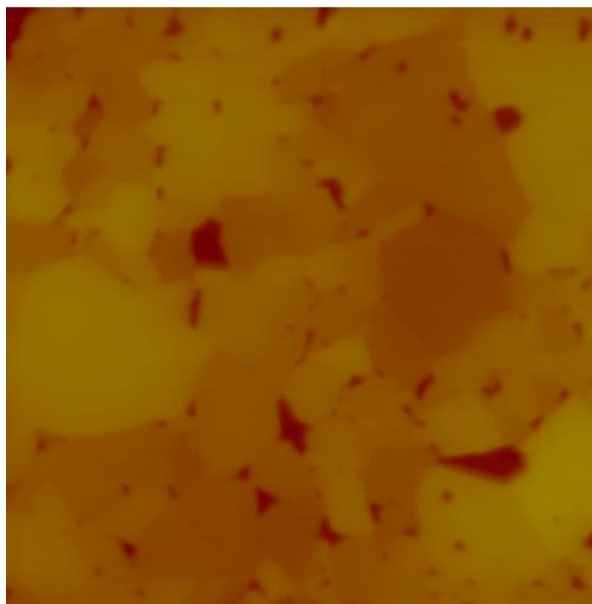
Figure 5.2-4 2D 3D morphology representation AFM height plot of sample 9 following 10 minute oxygen plasma treatment, analysis area 10µm square.

| Treatment | None | 1 min | 5 mins | 10 mins |
Sample	Ra	Ra	Ra	Ra
1	0.1673	0.13154	0.174	0.1406
3	0.0107	0.0116	0.0117	0.0106
8	0.0942	0.0819	0.0875	0.0763
9	0.008	0.0068	0.007	0.0075
10	0.4165	0.40638	0.4365	0.4112

Table 5.2-1 Mean AFM R_a values of plasma etched samples where the treatment times are oxygen plasma exposure times and the R_a value is in μm.
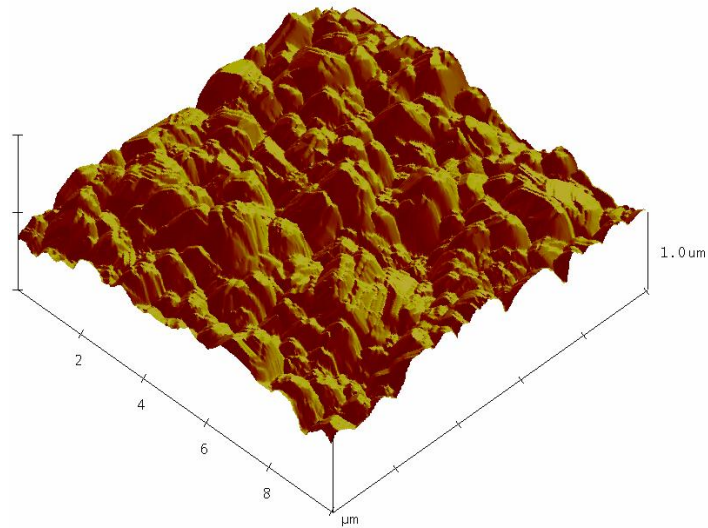
Figure 5.2-5 3D AFM representation of sample 8 surface, analysis area 10μm square.
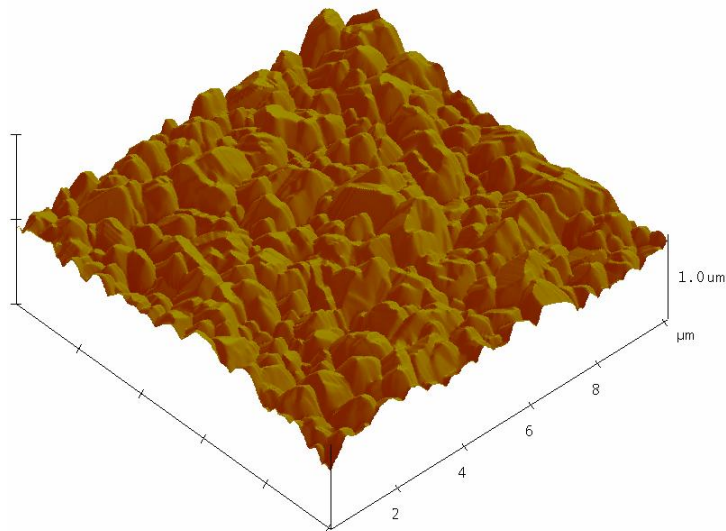
Figure 5.2-6 3D AFM representation of sample 8 surface following 10 minute plasma treatment, analysis area 10μm square.

Figure 5.2-5 above when compared to Figure 5.2-6 shows that on a rough surface which has high surface area to volume ratio features, plasma etching again has no perceivable effect on the surface topology. Table 5.2-1 supports

this conclusion with R_a values which fall in the region of the results which were measured originally.

The above results show that plasma etching does not affect the ceramic surface in a detrimental way. However, this is not a useful result unless the oxygen plasma also oxidised and removed the organic contamination. To verify this the two liquid contact angle method was used to estimate a new figure for effective surface energy.

Table 5.2-2 shows surface free energy and contact angle data for plasma cleaned ceramics. The figures are high due to a high polar fraction of surface free energy, however, higher figures can be found in the literature using the same two liquid contact angle method on ceramics[10].

Sample	Treatment	Water CA	Diiodomethane CA	SE
1	1 min	13.6	37.8	70.81
3	1 min	12.0	48.0	71.95
7	1 min	10.0	41.0	71.88
8	1 min	21.7	43.6	67.81
9	1 min	10.6	42.2	71.79
10	1 min	10.6	48.7	72.44
1	5 min	14.5	40.0	70.59
3	5 min	6.3	42.4	72.67
7	5 min	8.8	39.9	72.07
8	5 min	6.9	41.1	72.49
9	5 min	9.9	41.4	71.92
10	5 min	6.1	42.9	72.74
1	10 min	3.0	45.9	73.36
3	10 min	11.4	41.7	71.57
7	10 min	8.9	41.0	72.12
8	10 min	5.6	40.3	72.63
9	10 min	13.5	51.1	71.91
10	10 min	13.0	39.0	71.01

Table 5.2-2 Contact angle (CA) measurements and effective surface energy (SE) estimations of the plasma cleaned samples where contact angle is in degrees and surface energy in mJ/m^2.
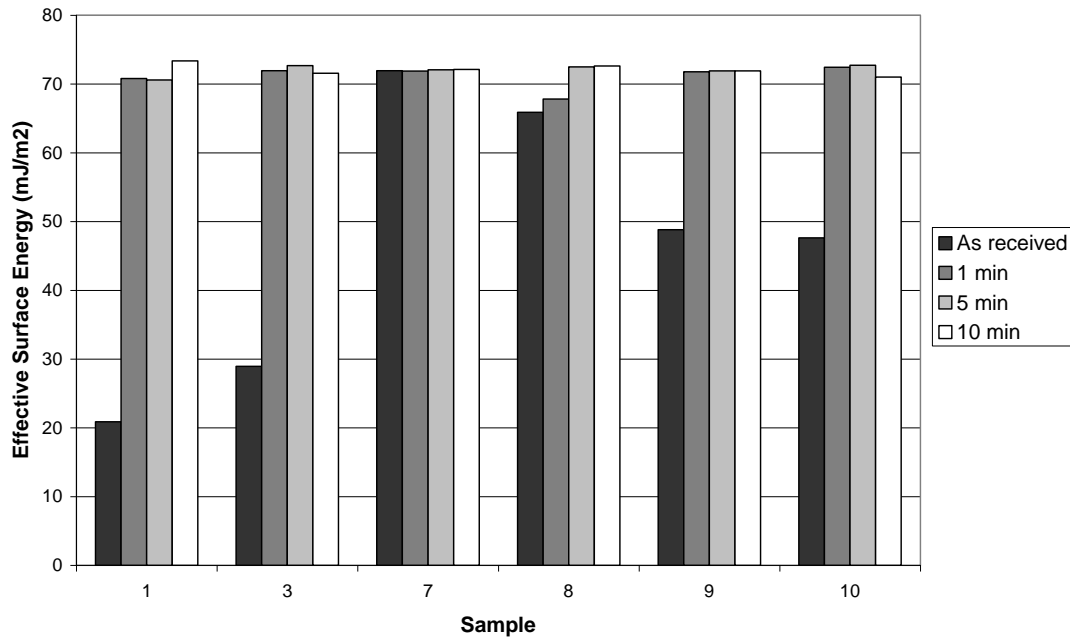
Figure 5.2-7 Graph to show the effect of the plasma cleaning on the effective surface energy.

Table 5.2-2 and Figure 5.2-7 show the effects of the oxygen plasma cleaning upon the effective surface energy of the ceramic surfaces. It is clear that the surfaces have been homogenised to give very similar surface energy values. The surface energy values are still not true and can only be considered effective surface energy values as they are much lower than the values for pure ceramic. Despite the much increased surface energies it is also likely that some small amounts of contamination are still present. The high energy nature of the surfaces would mean that the instant they are removed from the plasma cleaner contamination will begin to build up. As it is not practical to store the ceramics in hermetically sealed storage apparatus, tin foil was used as a storage media after testing since it is commonly held in the surface analysis field to be a effective for maintaining cleanliness.

The treatment time seems to have little effect on the surface energy. This supports the conclusion that contamination is quick to deposit on the surface following treatment. The speed of this deposition could be a useful parameter to allow derivation of a settling time, a time taken for the surface energy to reduce to a point such that bleed does not occur on the surface. This will be

explored in later chapters of this work, *Section 5.3 Identification and Removal of Contamination*.

5.2.4.2 Bond Strength Analysis

Cohesive failure is the failure of a bond through the adhesive and is considered the failure mode which occurs in an ideal bond, for it constitutes evidence that the adhesive has adhered to the adherend and that this is not the weakest interface in the bond[11]. The indicator of cohesive failure in this case is that there are equal amounts of adhesive remaining on the two adherend surfaces following shear failure, as can be seen in . Figure 5.2-8 for a rough sample. Figure 5.2-9 shows a similar cohesive failure occurred on a polished surface.
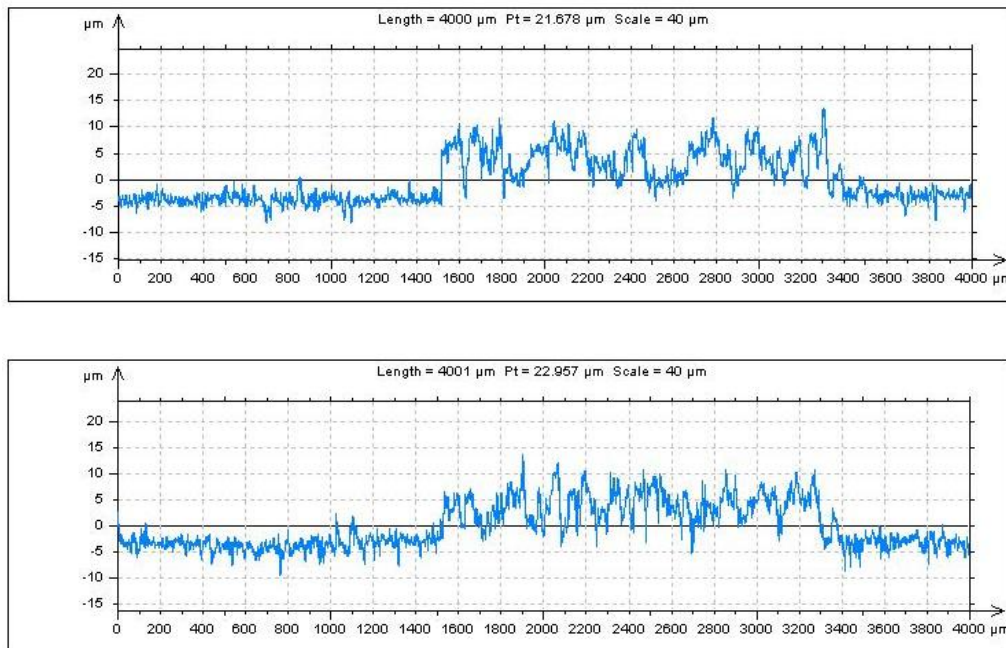
Figure 5.2-8 Talysurf profile of a failed adhesive spot on an Al_2O_3 surface, sample 10 AFM R_a 0.4165μm.
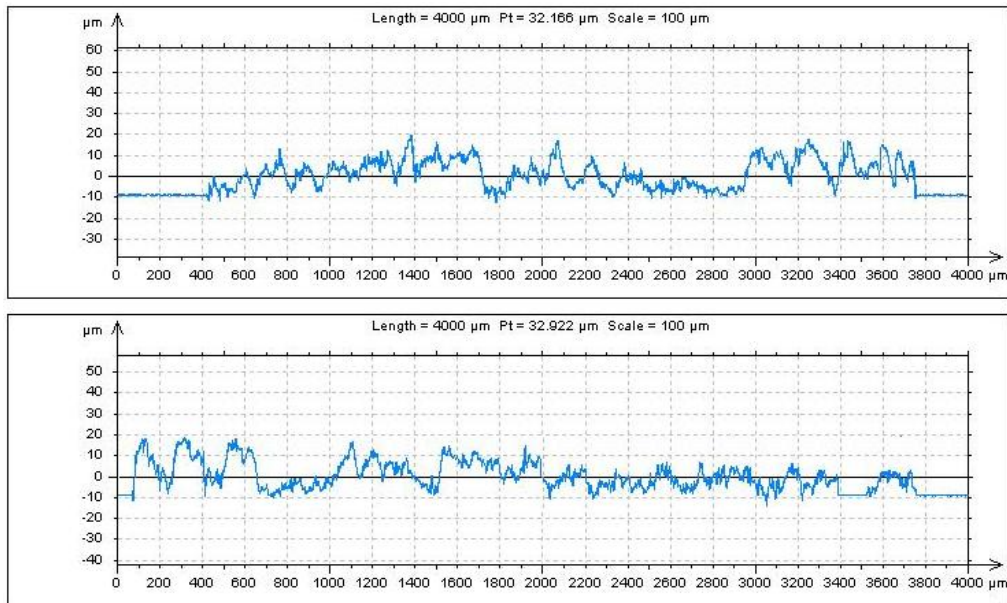
Figure 5.2-9 Talysurf profile of a failed boron nitride adhesive spot on an Al_2O_3 surface, sample 9 AFM R_a 0.00084µm.

Adhesive joints were formed from all the sample types in Table 5.1-1 and following shear testing it was seen that all bonds underwent cohesive failure in the adhesive. Therefore no inferences can be drawn as to the effects of the surface energies and textures on bond strength.

Further evidence for cohesive failure comes from the proportional relationship observed between the measured shear strength and measured bond area. In Figure 5.2-10 it can be seen that the constant of proportionality is dependent on the choice of adhesive, and independent of surface type or treatment.
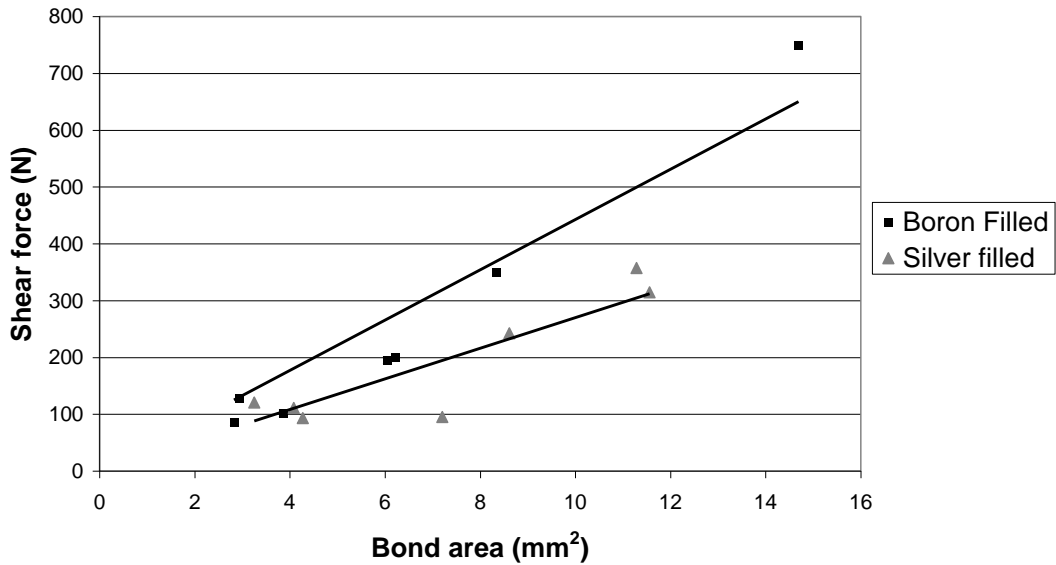
Figure 5.2-10 Comparison of bond area to shear force. lines are least square best fits with intercept constrained to 0

Figure 5.2-11 shows a typical load vs. extension curve seen in the tensile tests. The near constant slope and instantaneous failure suggests the joint underwent elastic deformation followed by brittle fracture. SEM images,

Figure 5.2-12, of the failed adhesive surfaces support this. They show no signs of plastic deformation and the topography of the adhesive consists of sharp jagged profiles typical of brittle failure. The jagged nature of the surface topography in the SEM images is consistent with the Talysurf profiles in Figure 5.2-8 and Figure 5.2-9 . The SEM images of the failed bonds show failure occurred entirely though the adhesive.
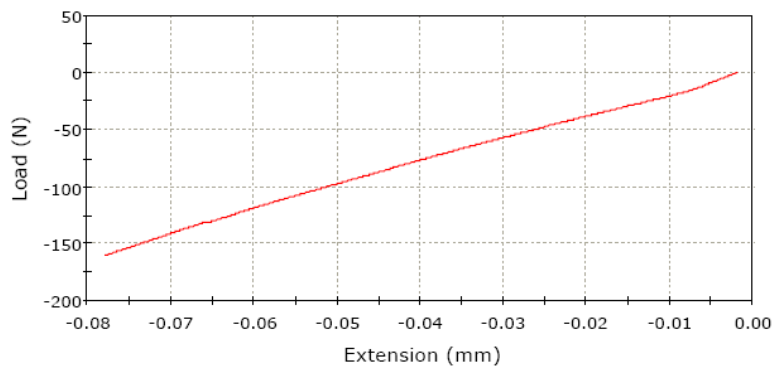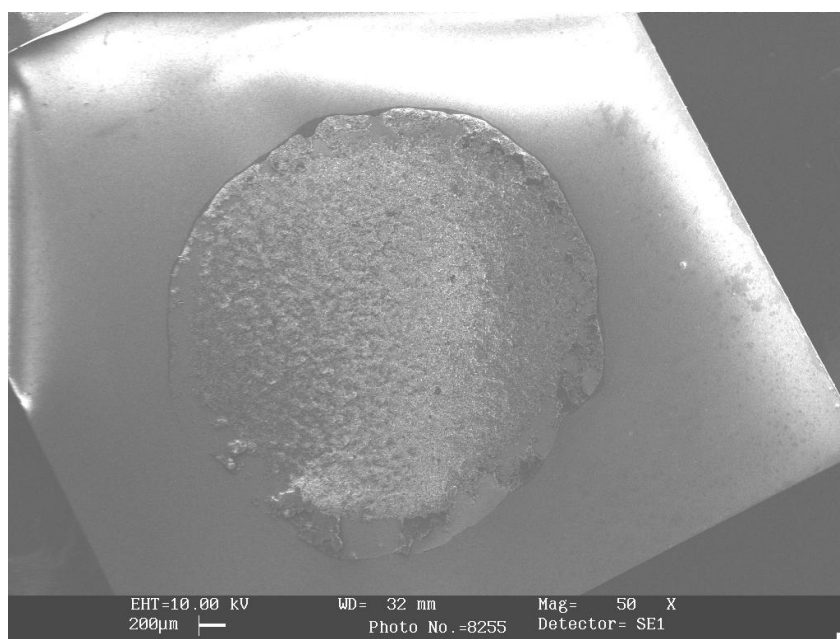
Figure 5.2-12 SEM image of failed boron nitride filled adhesive spot

The bond strengths were not detrimentally affected by thermal cycling, *Section 4.12 Thermal Cycling*. Figure 5.2-13 shows the same correlation between shear force and bond area as seen with the samples which were not cycled, along with comparable shear force values. The failure modes are also comparable to those of the uncycled samples. Figure 5.2-13 also shows the silver filled adhesive has become stronger after thermal cycling. A possible reason for this is that the adhesive continued to cure at the elevated temperatures in the cycles. The adhesive data sheet gives a cure time of 90 minutes at 80°C for the silver filled epoxy. The upper temperature for the thermal cycling was 80°C which could allow further curing to take place. The curing time at this temperature for the boron nitride filled adhesive was 6 hours. This lower curing rate could explain why the silver filled epoxies shear stress increased more than the boron nitride filled epoxy.
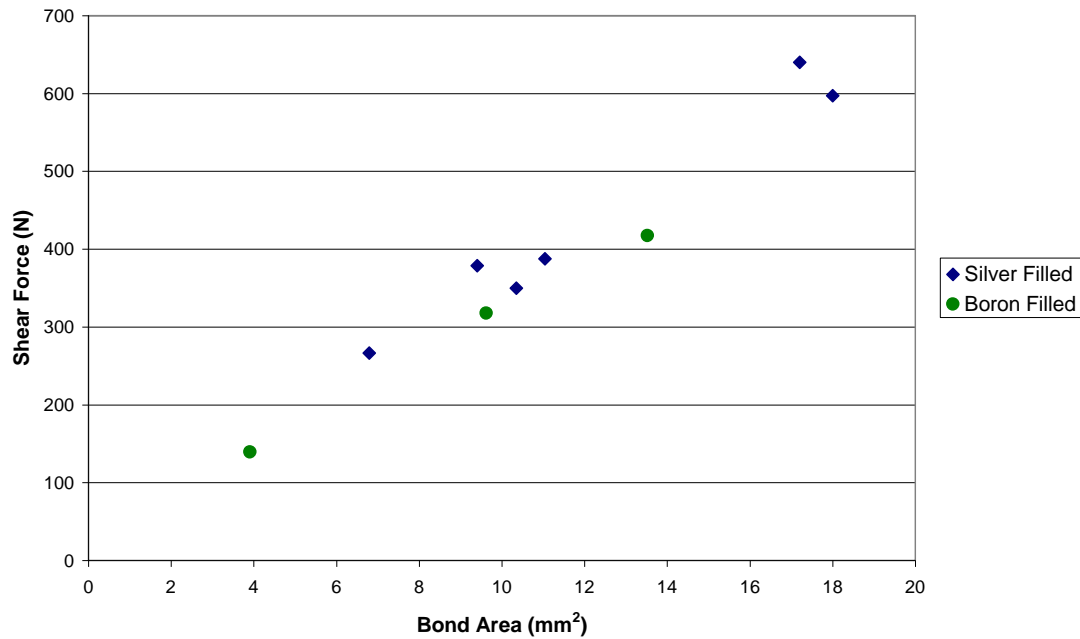
Figure 5.2-13 Comparison of bond area to shear force for thermally cycled samples.

Higher magnification SEM images of the failed silver filled epoxy bonds showed the failure occurred along the boundaries between the epoxy adhesive polymer and the silver flakes. The images suggested that the weak interface is that between the components of the adhesives, and as the other evidence supports, not between the adhesive and the ceramic surfaces. This can be clearly seen in Figure 5.2-14.
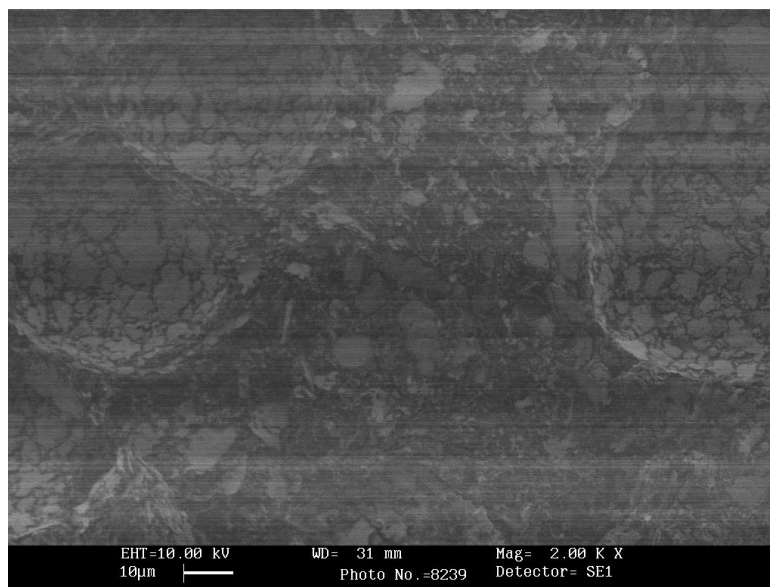
Figure 5.2-14 SEM image of the failure surface in the silver flake filled adhesive showing exposed silver flakes indicating failure at the silver/epoxy boundary.

148

5.2.4.3 Epoxy Bleed

5.2.4.3.1 Ceramics

The resin bleed phenomenon appears not to be exclusively determined to the contaminants found to be present. Figure 5.2-15 shows examples of minimal and pronounced bleed respectively on surfaces which were found to have an equal degree (21%) of carbon contamination. The pronounced bleed occurs on the lapped surface (R_a 0.75µm by AFM), rather than the polished surface (R_a 0.01µm) . It was therefore hypothesised that the bleed materials wetting performance might be sensitive to both topography and composition. Of the samples listed in Table 3.2-1 and Table 5.1-3, significant epoxy bleed visible with no magnification was witnessed on 3 samples all of which had comparatively low carbon contamination and comparatively high surface roughness, samples 5, 6 and 7.
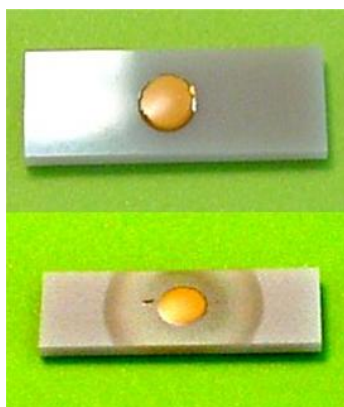
Figure 5.2-15 Top: minimal epoxy bleed on an AlN polished surface with 20.1% carbon contamination, sample 3. Bottom: pronounced epoxy bleed on an AlN lapped surface with 21.1% carbon contamination, sample 7. Sled lengths are 16mm. Adhesives are boron nitride filled in both cases.

The epoxy bleed is highly visible in SEM secondary electron (SE) images. Figure 5.2-16(a) and Figure 5.2-16(b) show a dark band surrounding the bulk adhesive with high contrast to the surrounding area. The bleed can be clearly identified by the lack of filler content. At lower magnification the bleed can be identified from contrast (it appears darker than the bulk adhesive or ceramic surface) as can be seen in Figure 5.2-16(c) and Figure 5.2-16(d). Since excessive spreading of the bleed material leads to invisibility in visible light due to the decreased thickness, SEM examination was chosen as the standard method to assess the extent of bleed in the work described below.

The topic of contrast in SE images is a complex one. However, it seems likely the contrast between the bleed and bulk is due to the higher atomic number of the filler in the bulk increasing the secondary electron yield from that region. See for example Sakai et al[12].
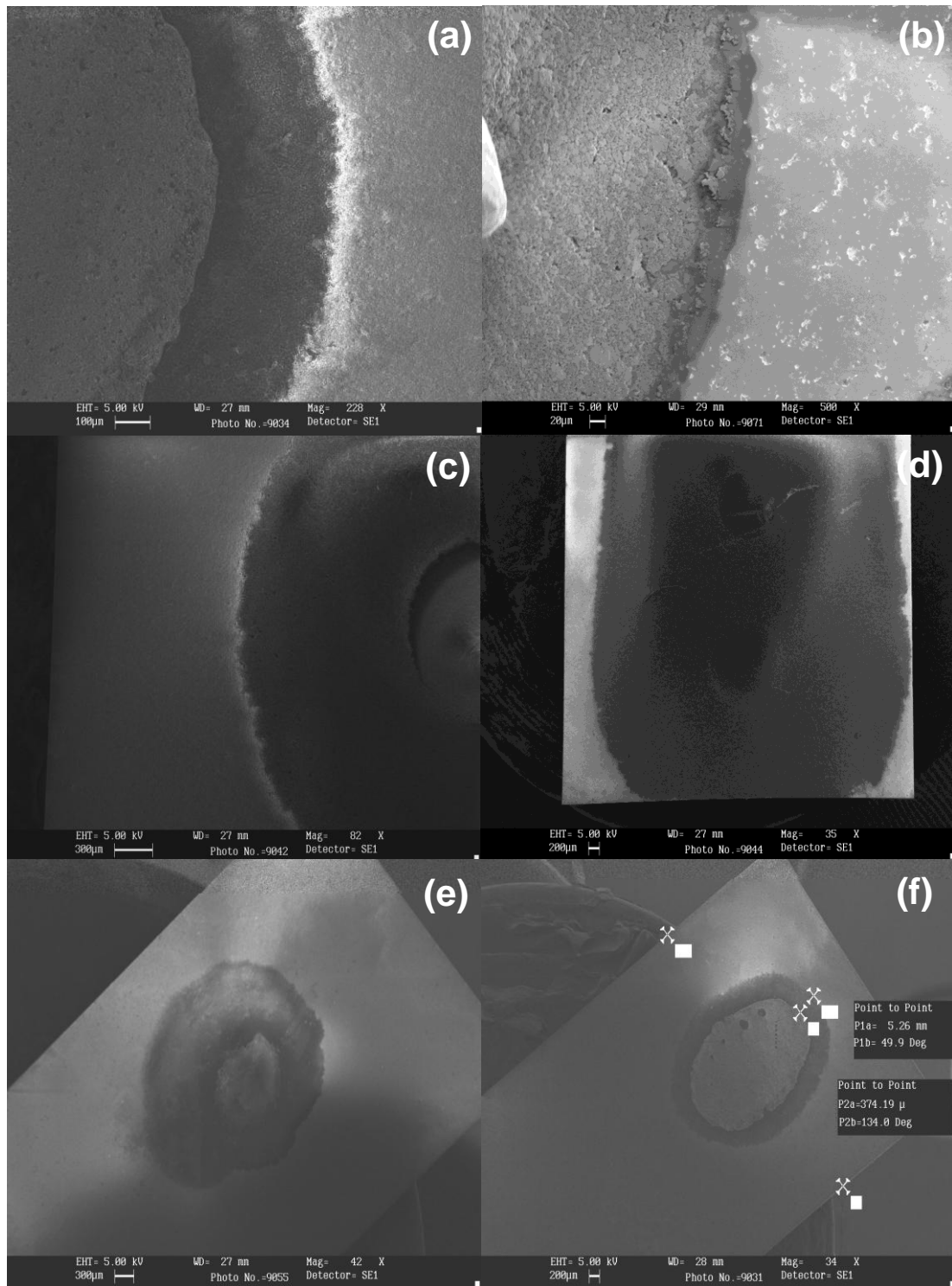
Figure 5.2-16 (a) SEM image of moderate epoxy bleed on an as-fired AlN surface with 21.6% carbon contamination, sample 5. (b) SEM image of limited epoxy bleed on a polished AlN surface with 21.2% carbon, sample 3. (c) SEM Image of maximum bleed seen with the silver

filled adhesive on AlN surface with 21.1% carbon, sample 7. (d) SEM image of maximum witnessed bleed of the boron filled adhesive on AlN, sample 7. (e) Epoxy bleed of a sessile drop on sample 5 surface. (f) SEM image of a failed lap joint with epoxy bleed, showing the epoxy bleed measurement method, sample 5.

Figure 5.2-16(c) and (d) show SEM images of the maximum extent of bleed witnessed for each adhesive. The maximum extent of epoxy bleed was measured as 2.25mm on sample 7, lapped AlN, with the boron nitride filled adhesive, Figure 5.2-16(d). Figure 5.2-16(b), by contrast, shows a minimal bleed distance of ~30µm from the edge of the adhesive spot on a polished AlN sled. Instances of bleed not occurring were also recorded on sample 9, polished alumina, with the boron nitride filled adhesive.

Bleed also occurred when the ceramics were bonded into lap joints, although this was only evident upon analysis after failure. Figure 5.2-16(e) and Figure 5.2-16(f) compare the bleed distance for a failed lap joint and sessile drop on identical material surfaces. It is clear that the bleed distance is double when there is only one surface involved. This was witnessed for a number of samples and suggests there is a finite amount of bleed material thermodynamically available which is shared between the two surfaces in the lap joint.

Insight into the effectiveness of the plasma clean can be gained by analysing the contributions of the polar and dispersive components of the apparent surface energies. The dispersive component remained unchanged following the plasma treatment for all samples, whilst the polar component increased to ~50mN/m for all samples. This suggests that the sample surfaces underwent a chemical change which reduced the hydrophobicity of the surfaces, i.e. the reduction of carbon based contamination. In this picture the unchanged dispersive component represents the effects of the inherent surface properties of the materials, since the polar component is considered to arise from permanent dipole Van der Waals forces, such as those between a polar liquid and carbon based hydrocarbon molecule.

The polar component of the apparent surface energy (mJ/m^2) was approximately equal for all surfaces (standard deviation 1.03) following plasma treatment, however, the surfaces showed vastly different bleed

distances. Bleed was visible to the naked eye with all of the sessile drops except with the silver filled adhesive on samples 9, shown in Figure 5.2-16, and sample 3, both of which have a polished surface. Figure 5.2-17 shows bleed distance plotted versus the AFM measured R_a value for both substrate and adhesive materials and a roughly linear correlation can be seen. The Al_2O_3 data points show more scatter about the linear trend line. It can also be seen that the boron nitride filled adhesive consistently bleeds further at each roughness value for both ceramic types than the silver filled adhesive. This shows that the bleed distance is partly affected by the adhesive formulation, probably because different adhesive additives or the filler properties either inhibit or encourage epoxy bleed. Further investigation of the effects of adhesive composition was beyond the scope of this work, partly because the commercial nature of the adhesives used in this work means the ingredients were not identified.   However, at least for the three adhesives used, the influence of the ceramic surface on the bleed distance, was found to be far stronger than that of adhesive type.
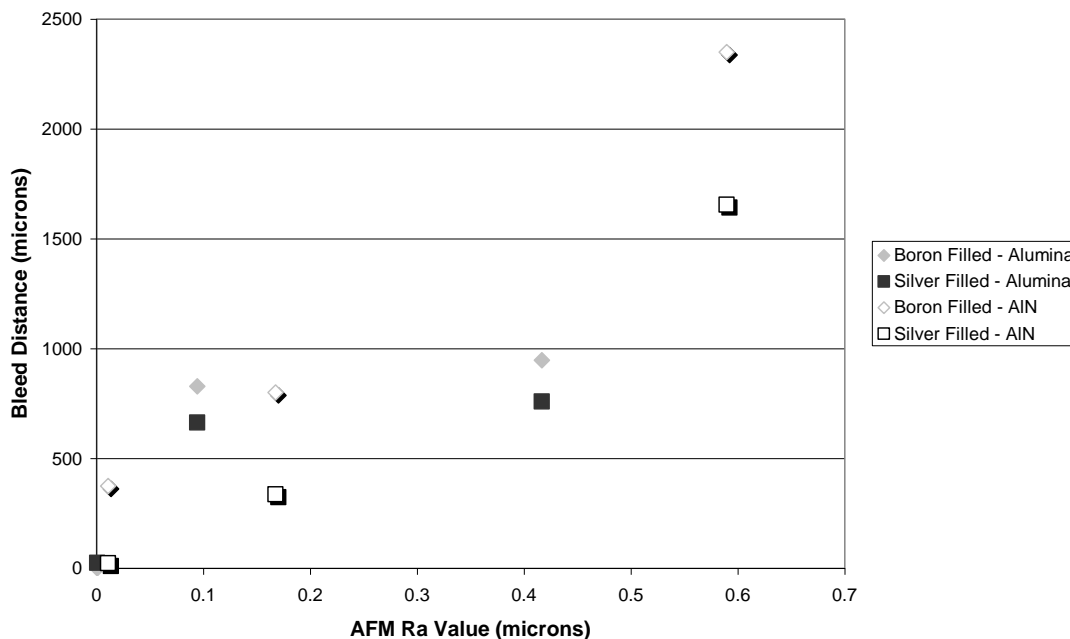
Figure 5.2-17 Graph showing the relationship between epoxy bleed distance and AFM R_a value for cleaned AlN and Alumina with the boron filled and silver filled adhesives.

It can be seen in Figure 5.2-18 and by comparison with Figure 5.2-17, that although the dispersive component of the apparent surface energy is strongly

linearly correlated to the roughness, irrespective of surface material, the mean variation in the dispersive component of surface energy (2%) is much smaller than the observed mean variation in bleed distance (68%). It therefore seems likely that the bleed distances are indeed being determined solely by the ceramic surface texture after plasma cleaning, for each epoxy type.
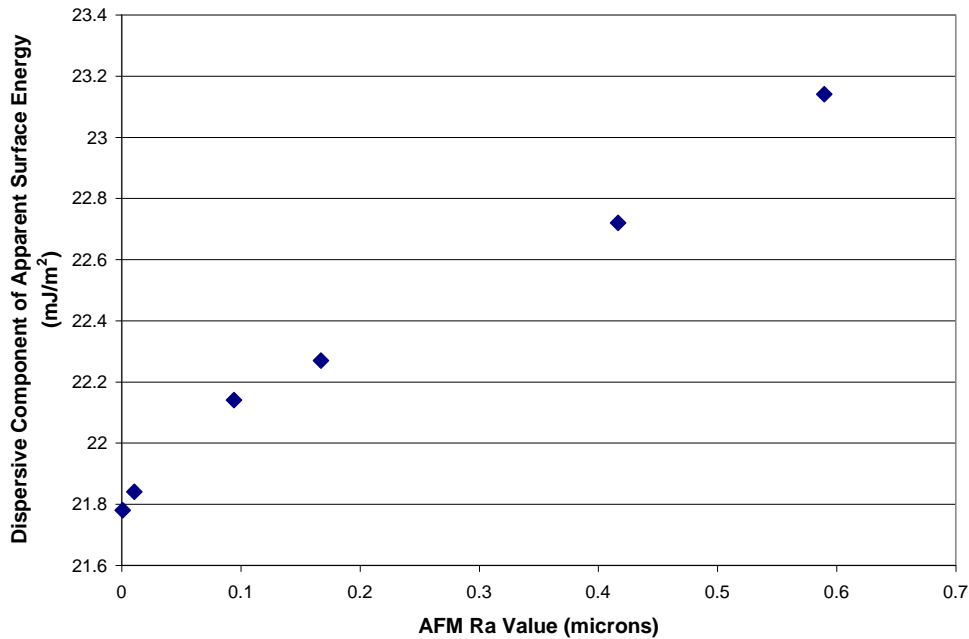
Figure 5.2-18 A graph to show the relationship between AFM R_a value and the dispersive component of apparent surface energy for 1 minute plasma cleaned AlN and Al_2O_3 samples.

5.2.4.3.2   Copper

Copper coupons were prepared using the methods in *Section 4.2 Copper Surface Preparations.* Mechanical surface preparations were performed with varying grades of sand paper to achieve different surface roughnesses. All copper samples were cleaned using a dilute HCl etch before adhesives were applied. Plasma cleaning was seen as unnecessary due to the effectiveness of a HCl etch at producing an oxide free copper surface.

Table 5.2-3 shows the maximum bleed distances measured on copper surfaces of the given AFM R_a values. It can be seen that a similar correlation is seen with copper as with ceramics. This suggests that the relationship between roughness and epoxy bleed distance is consistent over different materials.

153

Finish	Ra	Bleed (µm)
P240	0.3322	>1000
P600	0.0554	760
P1200	0.0267	65
6 Micron	0.0191	65
1 Micron	0.0061	20

Table 5.2-3 Boron nitride epoxy bleed distances compared to AFM R_a values are in microns and were measured using an AFM. 'Finish' is the final grade of sand paper or polishing cloth used.

.
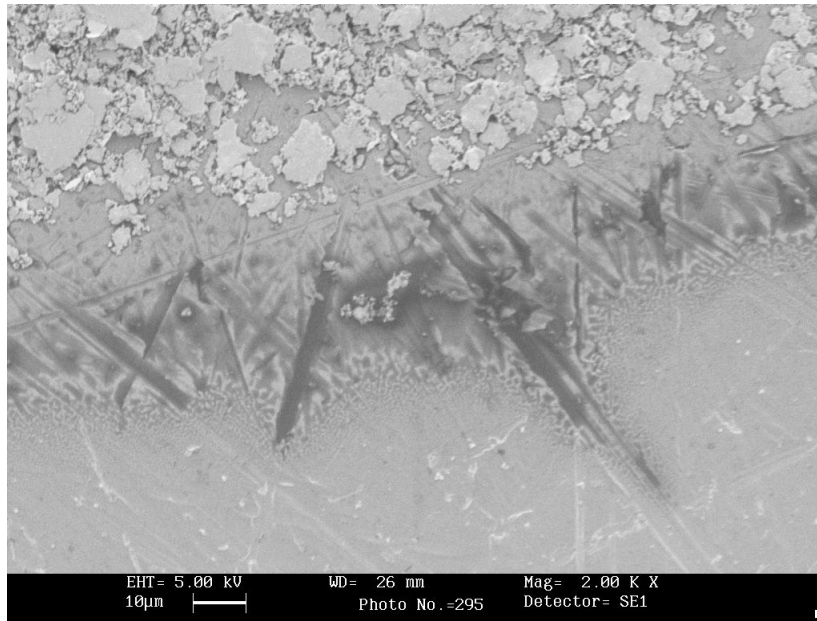
Figure 5.2-19 Epoxy bleed of the silver flake filled epoxy on a P1200 finish copper coupon, 2000X.
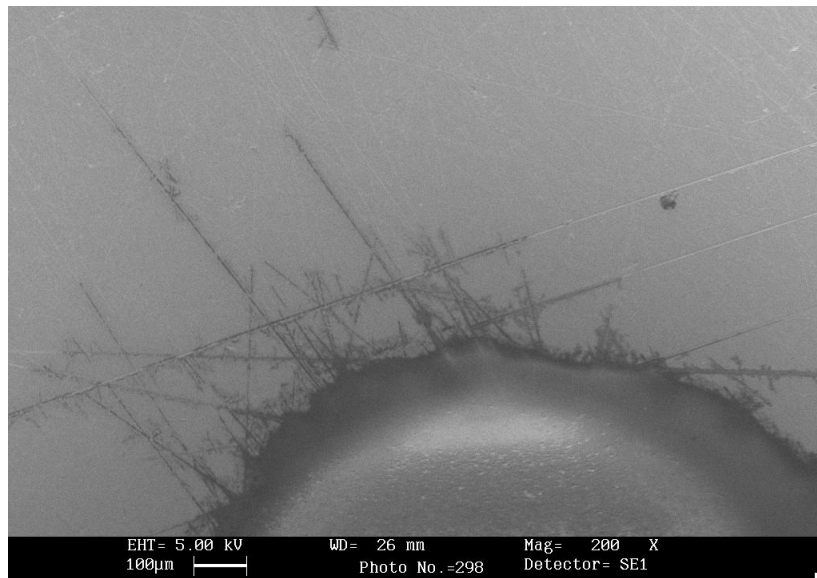
Figure 5.2-20 Epoxy bleed of the boron nitride filled epoxy adhesive on a P600 finish copper coupon surface, 200X.

Figure 5.2-19 and Figure 5.2-20 show the epoxy bleed material spreading along surface grooves away from the edge of the adhesive. It is clear from these images that capillary action is the main mechanism causing the spread. The material removal mechanism of the copper surface preparation is the cause of the directional groove pattern which results in a preferential direction of bleed.

5.2.5 Conclusions

For the adhesive/adherend systems investigated all joints failed cohesively. The mechanical surface preparation and surface chemistry had no influence on measured bond strength. This means that there is scope for engineering the surfaces in the study to reduce bleed without affecting bond strength or thermal fatigue resistance.

Apparent surface energy alone is not sufficient information to determine the degree of epoxy bleed on a surface. This chapter has highlighted that surfaces of very low roughness and high surface energy can still resist epoxy bleed, and that surfaces of equal apparent surface energy but different roughnesses show different bleed behaviour. If the components of apparent surface energy are considered separately a clear linear correlation can be seen between the dispersive component and the bleed distance. The bleed distance is also linearly correlated with the AFM R_a value, indicating that the surface texture is directly linked to the dispersive component of surface energy. It can therefore be concluded that surface texture does have a direct effect upon the bleed distance, once contamination is removed. This gives rise to the possibility of varying surface texture as a means of epoxy bleed control. Copper surfaces have also shown a similar link between roughness and epoxy bleed distance, with the mechanism of spreading likely to be capillary action on all ground finish materials. The bleed material showed a tendency to follow grooves on a copper surface, a result which could be exploitable.

Plasma cleaning is a highly effective method of removing organic contamination from the ceramic surfaces. It has shown to have no effect on

the surface topology of the ceramics whilst effectively removing the organic contamination.

5.2.6 References

[1] Ireland, J. Epoxy bleedout in ceramic chip packages, International Journal of Hybrid Microelectronics, Vol 5, No 1, 1982

[2] Marks, M.R. Thompson, J.A. Gopalakrishnan, R. An experimental study of die attach polymer bleedout in ceramic packages, Thin Solid Films, Volume 252, Issue 1, 15 November 1994, Pages 54-60, ISSN 0040-6090, DOI: 10.1016/0040-6090(94)90825-7.

[3] Tan N.X. Lim K.H.H. Bourdillon A.J. Analysis of coatings which inhibit epoxy bleeding in electronic packaging, Journal of Materials Science: Materials in Electronics, Volume 8, Number 2, 1997 , pp. 73-77(5)

[4] Neumann, A.W. Haage, G. Renzow, D. The temperature dependence of contact angles polytetrafluoroethylene/N-alkanes, Journal of Colloid and Interface Science, Volume 35, Issue 3, March 1971, Pages 379-385, ISSN 0021-9797, DOI: 10.1016/0021-9797(71)90136-6.

[5] Burmeister, M. Elimination of epoxy resin bleed through thin film plasma deposition Proceedings of SPIE--the international society for optical engineering 2003Vol. 5288pp 780-785

[6] Hsiung, J.C. Pearson, R.A. Lloyd, T.B. A surface energy approach for analyzing die attach adhesive resin bleed Journal of adhesion science and technology 2003Vol. 17Issue no. 1pp 1-14

[7] Whitehouse, D. J. Handbook of surface metrology /   Bristol :   Institute of Physics Publishing,   1994

[8] Williams, K.R. Gupta, Kishan, G. and Wasilik, Matthew, W Etch rates for micromachining processing - Part 2.. 6, California : IEEE, 2003, Jounal of microelectromechanical systems, Vol. 12, pp. 761-777.

[9] Kolari, K. High etch selectivity for plasma etching SiO_2 with AlN and Al_2O_3 masks. 85, Finland : Science Direct, 2008, Vol. Microelectronic Engineering, pp. 985-987.

[10] Smay, G.L. Surface energy determinations of tin oxide coated soda lime silica glass. Journal of the American Ceramic Society Volume 71, Issue 4, Pages 217-219 1988

[11] Pocius, A.V.   Adhesion and adhesives technology :   an introduction /   Cinncinati, Ohio : Hanser Gardner,   2002.

[12] Sakai, Y. Yamada, T. Suzuki, T. Ichinokawa, T. Contrast mechanisms of secondary electron images in scanning electron and ion microscopy, Applied Surface ScienceVolumes 144-145, , April 1999, Pages 96-100.

5.3 Identification and Removal of Contamination

5.3.1 Introduction

It has been seen in the work described in previous chapters that the carbon based contamination of ceramic surfaces reduces surface free energy and inhibits epoxy bleed, see *Section 5.1.4.1 Ceramic Sample Surface Chemical Characterisation*. The origin of this contamination can be from a number of sources including atmosphere, handling, surface treatments and outgassing from storage media. Whilst allowing contamination to remain on the surface can be an effective means of inhibiting the epoxy bleed, it is likely not to be a reliable solution for a manufacturing process due to lack of controllability.

A study of environmentally derived contamination was carried out, to evaluate the likely magnitudes of its effects on adhesive flow. The first aim of this section of the work was to identify and quantify sources of contamination in the factory environment. Storage methods used in industry were recreated for the purpose of this study with storage of samples in tin foil used for comparison. Samples were stored in commercial polymer waffle packs in a variety of atmospheres which they might experience in industry, on an industrial site, for one month.

A second aim was to qualify the effectiveness of industrial cleaning methods that could be used by an optoelectronics assembler to remove contamination and homogenise surfaces part-to-part after receipt. Of particular interest was whether there are present substances which are not readily removed by established cleaning methods used in the industry. Substances which may originate from the waffle packs themselves by outgassing and chemical species whose presence do not produce the advantageous effect of lowering the surface energy of the ceramics were also of interest.

For this work different samples to those in *Section 5.1 and 5.2* were used. Aluminium oxide and aluminium nitride were supplied in a single batch as 75mm x 75mm tiles with the surface preparation of as fired only. Since the

effects of roughness had been previously quantified, it was not felt necessary to include this as an experimental variable in this stage of the work.

XPS measurements were made following cleaning and storage to identify the composition of the storage related contamination and its source. Both the degree of carbon contamination, and the functional group constituents of any adsorbed species are known to affect surface energy and epoxy bleed. Therefore narrow band XPS spectra for carbon were analysed for all samples for chemical identification. The adhesive bleed performance on the samples was measured to enable the assessment of the practical effects of the carbon presence.

Of the many methods which could be employed to remove the surface contamination, solvent, plasma cleaning and firing were chosen to be studied for their effectiveness at removing organics and due to their availability to industry. XPS was again performed on samples following cleaning.

Finally the origin of the contaminants from the different parts of the storage media and rate of adsorption was identified by storing samples for 28 days and measuring their contact angles with water and diiodomethane after 1 day, 2 days, 7 days, 14 days and 28 days. The samples were stored under a variety of conditions with the design of experiment focussed around the industry standard waffle pack with polyethylene and lint free paper inserts. The effectiveness of tin foil at preventing contamination build-up was also studied. The time taken for epoxy bleed resistance to develop due to sufficient surface loading of adventitious carbon was measured.

5.3.2 Background Information

The adsorption of contamination onto high energy aluminium oxide and aluminium nitride surfaces can be detrimental to the quality and reliability of optoelectronic assemblies. Assemblies are frequently hermetically sealed, before being baked for 12 hours at 150°C, to remove all traces of water and other contaminants which could affect the in service performance. Throughout the production line a number of other cleaning processes are also implemented to ensure cleanliness prior to delivery to the customer. However,

in some instances contamination can lead to beneficial results arising from the surface property changes resulting from the adsorption. An example of the advantageous effects of the contamination is its effects on the epoxy bleed phenomenon. The presence of carbon based contamination can lead to a lowering of surface free energy, which is one driving force of epoxy bleed[1]. The origin of this contamination can be from a number of sources, namely: atmosphere, handling, surface treatments and outgassing from storage media[2]. Contamination arising from handling and surface treatments can be straightforwardly controlled or avoided, but that which originates from storage media or the atmosphere is more difficult to manage. Depending on this contamination for the control of epoxy bleed is likely not to be a viable solution because of the potentially random nature of the contamination composition and quantity. In this chapter the variation is quantified through study of adsorption of contamination from the atmosphere and from storage media, and measurement of its performance in the inhibition of epoxy bleed.

The removal of storage contamination may also be important for quality of optoelectronic assemblies. The work described in *Section 5.2.4.2 Bond Strength Analysis* did not show a weakening of the adhesive/adherend bond due to contamination, but there could still be implications for other assembly processes such as the application and adhesion of conductive metal tracks. The presence of contamination on the surfaces could also affect any steps taken to control the epoxy bleed. The work reported in *Section 5.2 Surface Parameter Effects on Epoxy Bleed* showed that the carbon loading due to adsorption was sufficient to control bleed in some cases, where adsorption gave sufficient coverage to reduce the effective surface energy to $<30mJ/m^2$. However the variability over sample sets, due to the ceramics being commercially sourced with no chemical specifications defined by the supplier or customer, meant adsorption was inconsistent.

Adsorption is the adhesion of molecules of gas, liquid, or dissolved solids to a surface. In the case studied in this instance adsorption is taken to be the adhesion of adventitious carbon (carbon based organics such as alkanes, alkenes, ketones, alcohols etc originating from the atmosphere or expelled by polymeric materials used to store substrates) onto ceramic surfaces which

would otherwise consist of aluminium and oxygen (2:3 ratio in Al_2O_3) with trace bulk contaminants or aluminium and nitrogen (1:1 ratio in AlN) with trace bulk contaminants. The presence of hydroxyl groups on the surfaces is also likely, as aluminium oxide forms a hydroxyl layer upon exposure to moisture. The process of adsorption creates a film of the adsorbate (adventitious carbon) on the surface of the adsorbent (ceramic), initially by van der Waals interactions. The presence of this layer can affect the adhesion properties of the surface, as the layers of atoms involved in the adhesion processes can be completely replaced by adsorbate material, changing the properties of the surface which could be inherently of high energy, to being low energy and non wettable.

5.3.3 Methodology

The purpose of the investigation outlined in this chapter was to identify the source of organic, surface energy reducing, contaminants which were found to be present on the commercial samples analysed. This work also had the aim of assessing the possibility of exploiting the adsorbed thin films for epoxy bleed control in the assembly line. To cover the likelihood that such exploitation should not be possible, cleaning methods were investigated to ensure that the process of adsorption could be reversed to a sufficient degree to ensure consistency of surface chemical character for production, whilst leaving the ceramic material unchanged.

For this investigation the effects the build up of contamination had on the distance the epoxy bleed spread was of interest. The reason for this was that experience in industry is of the seemingly random occurrence of bleed on ceramic tiles which are apparently identical. It was theorised that the reason for the random occurrence was variation in the lengths of the time the ceramics had spent in environments in which contamination could accumulate. The cleaner and newer parts are, the more likely the bleed will spread uncontrollably and interfere with the product. This investigation had the aim of finding out if a storage time of one month would be sufficient to stop the bleed occurring. Samples were therefore stored in conditions replicating those that might be experienced during production. Identical samples were sourced from a single supplier, prepared, and stored in waffle packs, the

standard storage method for samples in industry. To replicate different typical storage atmospheres the samples were shipped to an industrial site and stored for varying amounts of time before being recovered and analysed.

The conditions the waffle packs are likely to encounter once shipped are variable. Since temperature, humidity and atmospheric composition of the storage area could all have an effect on the composition and amount of contamination build up on the ceramic surfaces, the samples were stored at the industrial site and in a laboratory under a number of different storage conditions to assess the effects of these variables.

5.3.4 Experimental Details

Aluminium oxide and aluminium nitride tiles of 1mm thickness were diced into 5mm x 14mm samples using a CO_2 laser. The laser processing of ceramics is investigated in more depth in other sections of this work. The diced samples were then put into deionised water and treated with ultrasonics for five minutes to remove any residue from the laser cutting process. Following the sonic treatment the samples were rinsed in IPA to begin organics removal and to aid drying. Samples were then dried in a flow of air at 60°C for ten minutes. When the samples were dry they underwent one minute of treatment in a 300 W oxygen RF (13.56 MHz) plasma at a flow rate of 100sccm. Oxygen plasma was used for its effectiveness at organic molecule oxidation[3,4], since organic molecules had been seen to form the majority of surface contamination in previous work[1]. Following plasma treatment the samples were transferred to the storage media. To reduce particulate contamination in the short time between plasma cleaning and sealing of the storage media the process was undertaken in a class ten thousand (ISO 7) clean room.

The storage conditions studied included: storage in a clean room in Shenzhen, China with uncontrolled temperature, storage in a nitrogen cabinet in Shenzhen, China with uncontrolled temperature, storage at 100% humidity at 25°C controlled to ±1°C in an environmental chamber at Loughborough University and storage in tin foil in a class ten thousand (ISO 7) clean room at Loughborough University. All samples were stored for thirty days before being

analysed with XPS, contact angle measurements and bleed distance measurements. During shipping all polymer waffle packs were sealed in polythene bags to protect them from any uncontrollable conditions in transit. The waffle packs used in the study were polycarbonate with added carbon powder and were manufactured by Entegris.

The cleaning methods implemented were: oxygen plasma cleaning, firing and a combination of solvent cleaning and oxygen plasma cleaning. The plasma cleaning method used had the same parameters, 300 W oxygen RF (13.56 MHz) plasma at a flow rate of 100sccm, as the initial cleaning of the surfaces before storage. Plasma cleaning was done for one minute and five minutes. Two times were used to assess the time variable, since although the results of the previous work reported in *Section 5.1 Characterisation of Surfaces and Adhesives* involving plasma cleaning suggested that a treatment longer than 1 minute had a negligible further effect on the effective surface energy, a chemical change in the surface is still possible. Plasma cleaning was used on its own as well as coupled with a solvent clean. The plasma treatment was done for one minute following an IPA wash and air dry where the solvent was involved. The solvent was used for two reasons; firstly IPA is highly effective at dissolving organics and could complement the plasma cleaning method, and secondly using IPA allows for a much shorter drying time and so less exposure to air in the drying process. The firing was performed using a sample dryer with an air flow at 400°C, which is said to be the minimum temperature for successful removal of organics. Samples were exposed to the air flow for 5 minutes. Following cleaning, samples were not returned to waffle packs but were sealed into tin foil pouches until further analysis took place within 24 hours.

Samples were analysed using XPS, contact angle measurements and bleed distance measurements. XPS wide scans of three regions on the surface of each stored sample were recorded. A narrow band scan around the carbon binding energy area was also made for each sample. All XPS analyses were performed with the Kratos AXIS ULTRA by the methods described in *Section 4.3 X-ray Photoelectron Spectroscopy*. Contact angle measurements and apparent surface energy estimations were made on the stored samples as

well as on cleaned samples. The surfaces were tested with diiodomethane and water and an estimation of the surface energy was made using the Owens Wendt method.

Bleed distance was measured using scanning electron microscopy according to the method described in *Section 4.13 Epoxy Bleed Measurements*.

5.3.5 Results and Discussion

5.3.5.1 Storage Results

The degree of adsorption of organic contamination onto the ceramic surfaces post storage was consistent with that observed on the commercial samples studied previously, *Section 5.1.4.1 Ceramic Sample Surface Chemical Characterisation*. It can be concluded that its presence is not due to bad practice or equipment related contamination, but that the contamination has another source.

Storage Conditions/Material	No.	O	Al	Si	C	N	F	Na	K	Ca
Foil AlN	1	53.7	19.5	4.5	12.6	4.4	4.4	0.3	0.6	0.2
Nitrogen AlN	2	45.6	18.0	2.9	26.0	3.1	1.7	1.4	1.1	0.2
100% humidity 25°C AlN	3	44.7	15.5	3.5	29.2	3.3	1.1	0.8	1.7	0.3
Clean Room AlN	4	44.8	18.6	2.6	27.9	4.1	1.5	0.5	0.4	0.2
Foil Al_2O_3	5	46.4	19.1	4.1	19.2	0.4	8.0	1.8	1.5	0.2
Nitrogen Al_2O_3	6	44.2	17.6	5.3	29.7	0.6	1.2	0.6	0.8	0.2
100% humidity 25°C Al_2O_3	7	40.0	12.5	9.4	36.4	0.5	1.2	0.6	0.1	0.1
Clean Room Al_2O_3	8	45.4	17.8	4.6	29.4	0.5	1.1	0.8	0.6	0.2

Table 5.3-1 Relative atomic composition percentage of stored ceramics, mean values of three measurements made with XPS. Foil means stored in foil. All other samples stored in waffle packs

Table 5.3-1 above gives the relative atomic percentages of all of the elements detected on the stored sample surfaces. The detection of any element with a presence higher than 0.1 relative atomic percentage was recorded. As before it can be concluded that the presence of group 1 and 2 metals can be associated with the purity of the as received ceramics, see *Section 5.1.4.1 Ceramic Sample Surface Chemical Characterisation.* The presence of silicon on the surfaces once again cannot be attributed to any specific source. Mould

163

release agents from the injected moulded waffle packs could explain its presence on the samples stored in waffle packs, but not those stored in the tin foil. The presence of the aluminium, oxygen and nitrogen can all be attributed to the ceramic materials, AlN clearly shows a higher percentage of nitrogen on the surfaces than the alumina, which was to be expected. Both of the ceramics show a high degree of oxygen on the surfaces. This supports the hypothesis of a presence of an aluminium oxide layer on the aluminium nitride surfaces. This also explains the lower than expected nitrogen value for the AlN, which should be in a 1:1 ratio to the aluminium signal, should no other aluminium compound be present. The oxygen is present at a higher concentration than the 2:3 aluminium to oxygen ratio that would be expected for Al_2O_3 It can therefore be concluded that the oxygen signal can be partially attributed to the organic contamination.

A statistical measure, the correlation coefficient r was calculated using Equation 5.3-1 below for pairs of elements in Table 5.3-2:

$$r(X,Y) = \frac{\sum (x - \bar{x})(y - \bar{y})}{\sqrt{\sum (x - \bar{x})^2 \sum (y - \bar{y})^2}}$$

Equation 5.3-1

The element combinations which gave an absolute value higher than 0.7, which denotes some element of correlation, are shown in Table 5.3-2 below. The data analysis technique proved to be moderately useful for highlighting potential correlations between elements but offers no interpretation as to why the correlation identified exist.

AlN			Al_2O_3		
Element 1	Element 2	r	Element 1	Element 2	r
F	O	1.00	Al	O	0.99
F	C	-1.00	Si	O	0.99
C	O	-1.00	Si	Al	0.99
Si	O	0.89	F	C	0.88
Si	C	-0.85	C	O	-0.87
Al	C	-0.71	Al	C	-0.86
C	N	-0.70	Si	C	0.83
			N	F	-0.83

Table 5.3-2 Relative atomic composition percentage correlations for AlN and Al$_2$O$_3$ on stored samples.

The correlation between the substances of low relative percentage are not considered in this table. This is because the quantification resolution of the method is ~1% so correlations between substances of relative presence <1% cannot be considered significant. The important conclusions which can be drawn from the correlation data are the negative correlations between carbon and oxygen. This suggests that the contaminants may be inhibiting the signal from the oxide, perhaps due to the increased depth of the ceramic surface. The data also suggests that the silicon is not associated with the carbon, since the AlN shows a negative correlation and aluminium oxide positive.
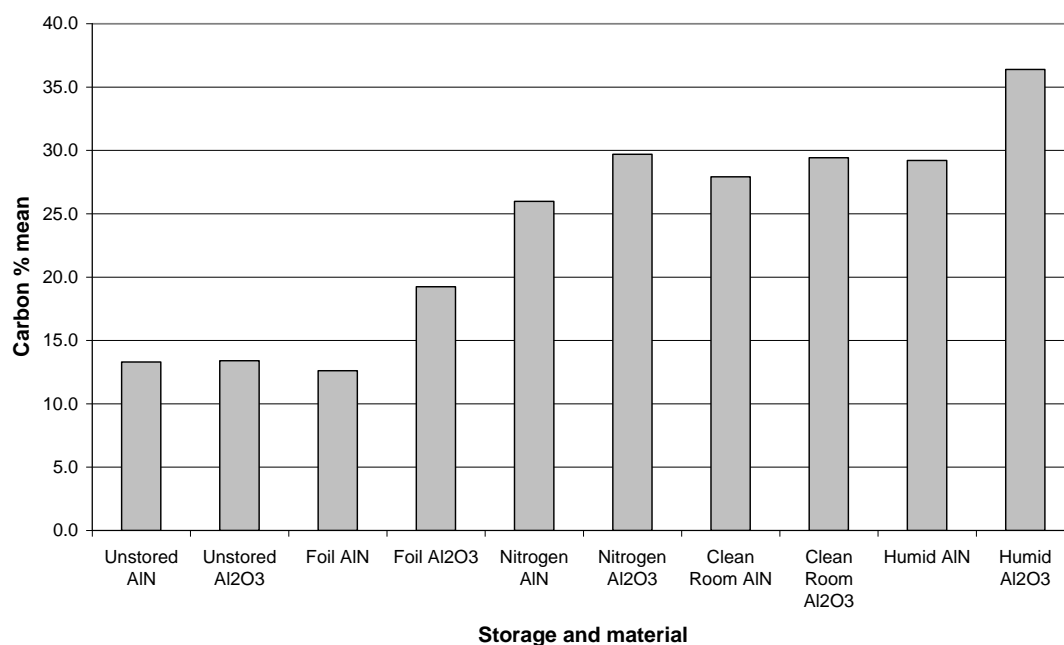
Figure 5.3-1 Relative carbon atomic percentage for all stored samples showing the effect of storage on the build up of contamination following the initial clean.

Figure 5.3-1 shows the variation of carbon adsorption with respect to storage method. The unstored parts are ones which had been subjected to plasma cleaning only and analysed within 24h. Interestingly the tin foil wrapped samples show little or no contamination build up compared to the other storage methods. Tin foil is widely regarded to be effective at protecting samples from airborne contaminants[5]. This could be for a number of reasons including its manufacturing method including a corona discharge cleaning

165

stage, it being tightly rolled excluding air between the layers, and tin foil having a greater affinity for contamination build up than the ceramics stored in it.

It could also be surmised from Figure 5.3-1 that a source for the contamination is the waffle packs used for storage and as this source was not present in the tin foil the ceramics did not absorb the same degree of contamination. The waffle pack stored samples are mostly within the range of 25-30% relative carbon coverage. The high mean value for the aluminium oxide stored under high humidity of 37% is due to a single high result of 49% from the three measurements, the other two being within the 25%-30% range. This suggests that the distribution of contamination on the surfaces is not completely uniform.
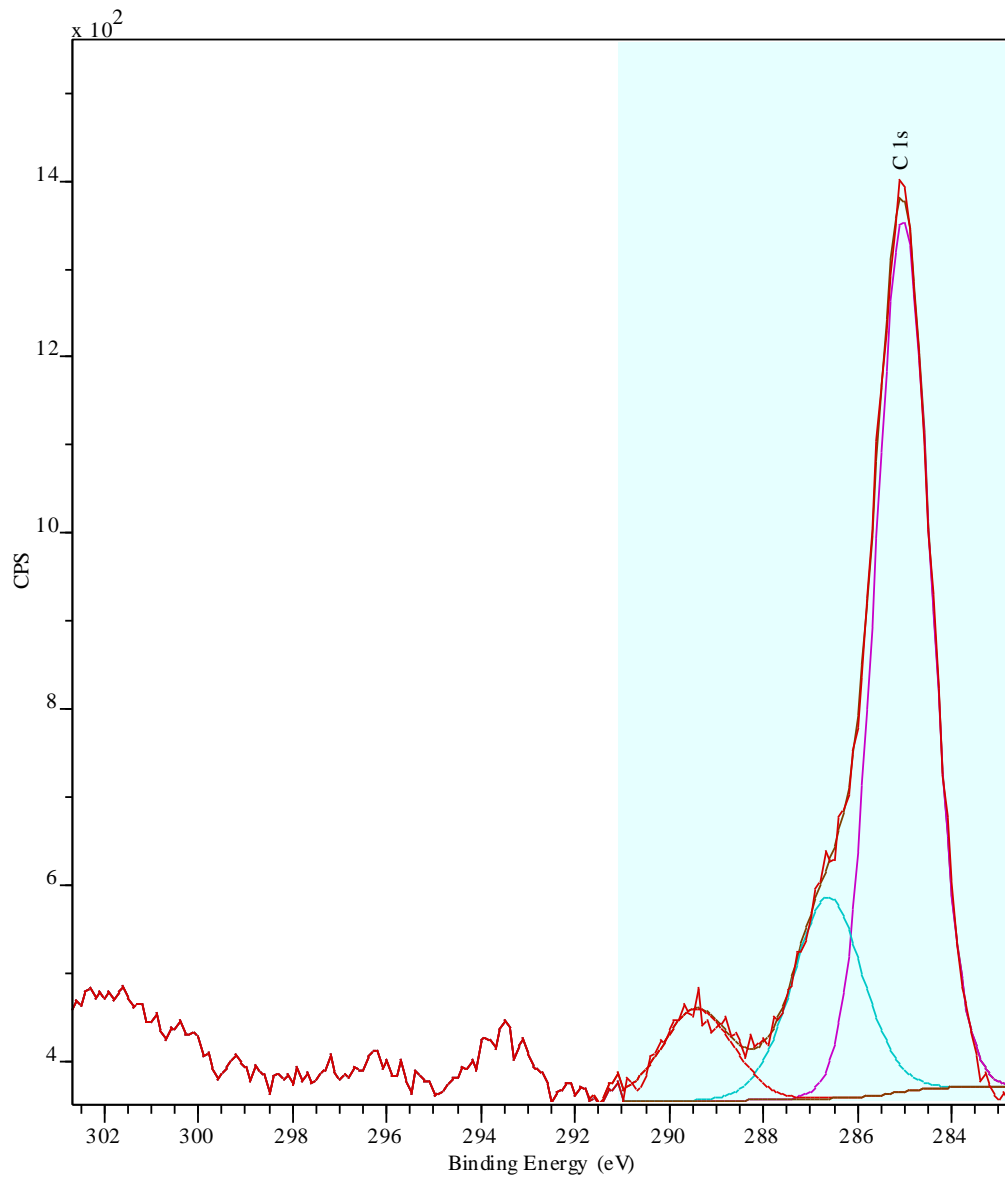
Figure 5.3-2 Narrow scan spectra of carbon peaks for sample 1, corrected to 285eV. Where the purple peak is the C1s peak, the green peak the C-O peak and the red peak the COOR peak.

Figure 5.3-2 shows the peaks fitted to the XPS narrow scan spectrum from sample 1 (Foil stored AlN) whilst Figure 5.3-3 below shows the peaks fitted to the spectrum from sample 8 (Al_2O_3 stored in a clean room).
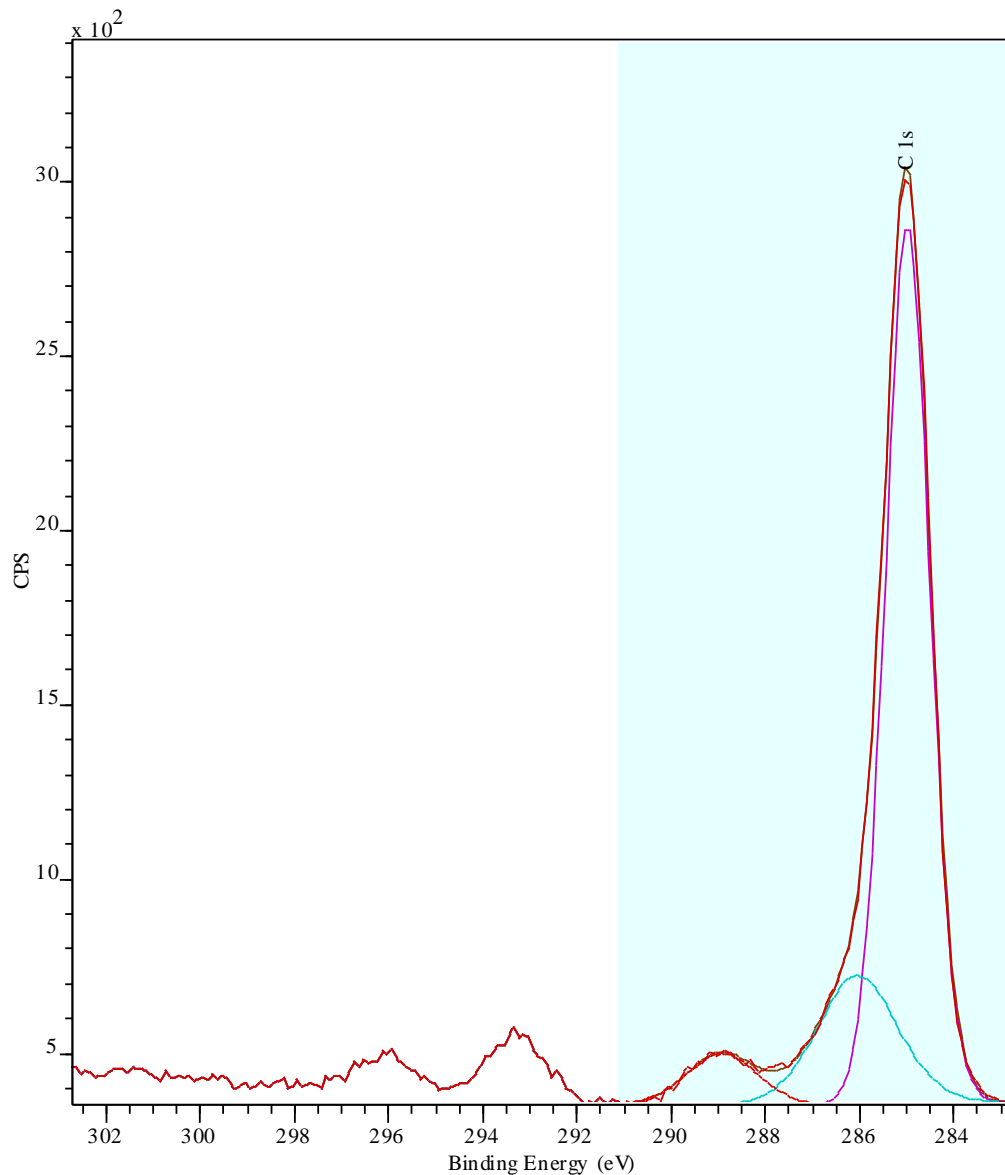
Figure 5.3-3 Narrow scan spectra of carbon peaks for sample 8, corrected to 285.00eV.

It can be seen that although the amount of carbon measured to be on the surface and listed in Table 5.3-1 is very different, the narrow band spectra which provide the best method of identifying the bond types present are very similar suggesting similar functional groups. It can also be seen from the figures that the counts per second (CPS) value is over double the value for sample 8 when compared to sample 1. This is due to the higher percentage presence of carbon on sample 8 (29.4 at %) than sample 1 (12.6 at%). However, it should also be noted that the ratios of the peak magnitudes are almost identical, suggesting that the chemical nature of the contamination is

very similar. The fitted bond type peak ratios are shown in Table 5.3-3 below. The peaks were placed for fitting at the positions listed in *Section 4.3 X-ray Photoelectron Spectroscopy.*

Sample	No.	C1s	C-O	O-C=O
Foil AlN	1	70.15	20.46	9.39
Nitrogen AlN	2	78.64	15.94	5.42
Humid AlN	3	82.19	11.90	5.91
Clean Room AlN	4	76.00	20.09	3.91
Foil Al2O3	5	78.28	15.51	6.21
Nitrogen Al2O3	6	70.47	24.45	5.08
Humid Al2O3	7	75.17	24.83	0.00
Clean Room Al2O3	8	73.52	19.48	7.00

Table 5.3-3 Relative bond type percentages from XPS spectra of all stored samples.

It can be seen from Table 5.3-3 that 70-80% of the carbon bonds are C-C and C-H bonds, 10-25% are C-O bonds and the remainder are carboxylic acid COOR bonds. The data suggests that the composition of the organic contamination was principally carbon, oxygen and hydrogen with no presence of other elements. The nature of the contamination suggests that it either came from the atmosphere and not the polycarbonate waffle packs, or that the compositions of atmospheric adventitious carbon is similar to that which might be outgassed from polymers. Reasons for this are the similarity of the distribution of bond types of the foil stored samples and the waffle pack stored samples, as noted in the comparison of samples 1 and 8 above. Further evidence to suggest that the polycarbonate has not outgassed monomers or oligomers onto the surface is the lack of evidence of a carbonate group, i.e. a C=O peak at 287.8eV is not seen in any of the XPS spectra, which would be expected from polycarbonate. There is still the possibility of the source of the contamination being other constituents of the waffle packs, such as outgassed polymer additives and leached carbon filler. A study aimed at identifying the source of the storage contamination is described in *Section 5.3.5.3 Contamination Rate and Source.* An important finding from this work is that the waffle packs do not offer contamination protection.

The results of contact angle measurements on the storage samples are summarised in Table 5.3-4 below.

Sample	Carbon %	Water CA	Diiodomethane CA	SE	
Foil AlN	12.6	55.3	54.6	45.34
Foil Al2O3	19.2	53.8	48.2	50.65
Nitrogen AlN	26.0	104.7	65.6	25.9
Nitrogen Al2O3	29.7	100.3	62.7	27.05
Clean Room AlN	27.9	102.3	72.1	21.44
Humid AlN	29.2	104.2	69.9	22.99

Table 5.3-4 Contact angle and surface energy data of stored samples. CA = contact angle (degrees), SE = surface energy (mJ/m^2).

The table shows a correlation between effective surface energy and carbon percentage, similarly to that reported in *Section 5.1.4.1 Ceramic Sample Surface Chemical Characterisation*. Correlation was not seen between the effective surface energy and the bond types found in the carbon high resolution narrow band scan. However, correlation was seen between the relative atomic percentage of oxygen and carbon and the effective surface energies (r = 0.99 and -1.00 respectively). The negative correlation between the surface energies and the relative atomic percentage of carbon was consistent with data acquired from commercial samples.
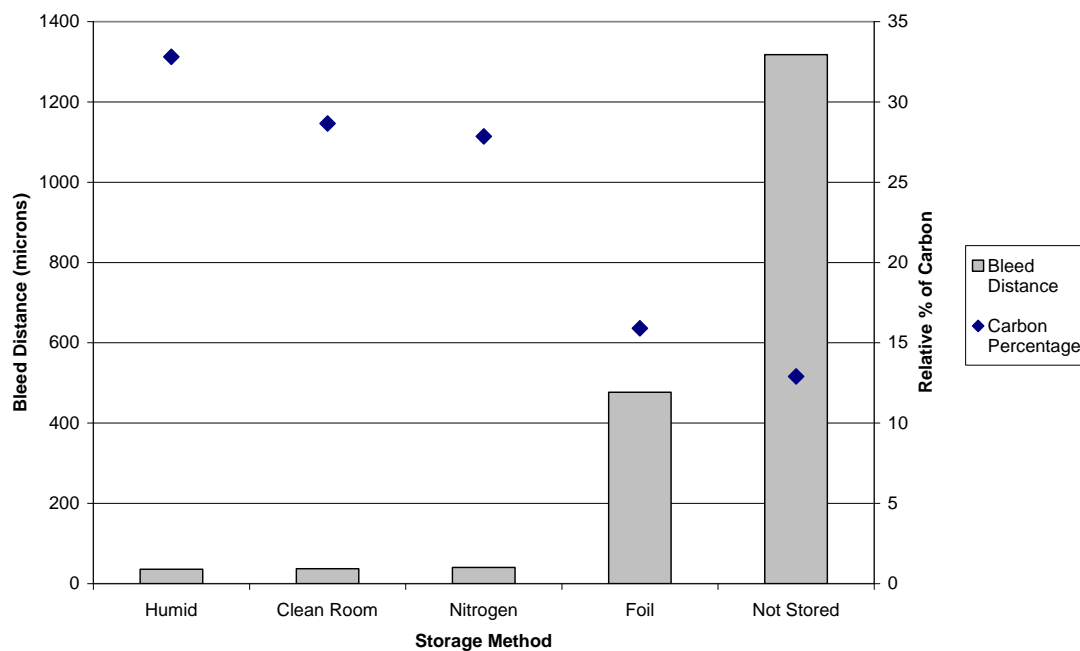
Figure 5.3-4 Epoxy bleed distance of the 930-4 epoxy compared to relative atomic carbon percentage on stored AlN surfaces.

Figure 5.3-4 above shows the results of the maximum epoxy bleed distance measurements on the aluminium nitride stored samples. A correlation between the amount of organic contamination present and the bleed distance can be seen. The correlation is similar for aluminium oxide (results not shown). As the bleed distance for all the waffle pack stored samples is negligible at <50µm, it seems that the storage of samples in waffle packs for one month is sufficient to stop the bleed occurring. However, ceramic sleds experience cleaning steps during manufacture which may remove the bleed resistance. This is considered in the following section.

5.3.5.2 Cleaning Results

A number of samples stored under all conditions were cleaned using a variety of methods described given in the experimental procedure section of this chapter. Table 5.3-5 and Figure 5.3-5 show the relative atomic composition percentages obtained from XPS spectra from the cleaned samples.

Cleaning method/material	No.	O	Al	Si	C	N	F	Na	K	Ca
1 Min Oxygen Plasma AlN	9	52.1	16.7	5.8	15.2	5.2	4.6	0.2	0.0	0.3
5 Min Oxygen Plasma AlN	10	54.7	18.0	5.8	13.3	4.4	3.6	0.2	0.0	0.2
IPA + Oxygen Plasma AlN	11	54.8	18.7	5.9	12.2	4.5	3.6	0.2	0.0	0.0
Fired AlN	12	53.9	19.6	4.1	15.4	5.4	0.0	0.7	0.7	0.3
1 Min Oxygen Plasma Al_2O_3	13	56.6	19.7	5.4	12.7	1.0	4.6	0.1	0.0	0.2
5 Min Oxygen Plasma Al_2O_3	14	56.8	20.3	5.6	12.0	0.5	3.7	0.5	0.6	0.4
IPA + 1 Min Oxygen Plasma Al_2O_3	15	56.4	19.8	6.0	12.9	0.9	3.2	0.4	0.2	0.2
Fired Al_2O_3	16	54.6	22.1	3.5	16.3	0.3	0.5	1.2	1.3	0.2
1 Min Oxygen Plasma Al_2O_3	17	55.6	19.7	5.5	13.4	0.9	4.8	0.0	0.1	0.1
5 Min Oxygen Plasma Al_2O_3	18	57.6	20.4	5.9	12.5	0.7	2.9	0.0	0.0	0.0
IPA + 1 Min Oxygen Plasma Al_2O_3	19	57.5	20.4	6.0	12.1	0.8	3.3	0.0	0.0	0.0
Firing Al_2O_3	20	57.1	21.2	5.1	14.9	0.3	0.5	0.4	0.5	0.2

Table 5.3-5 Relative atomic composition percentage of cleaned ceramic surfaces, mean values of three measurements made with XPS. Samples 17-20 had not undergone storage.
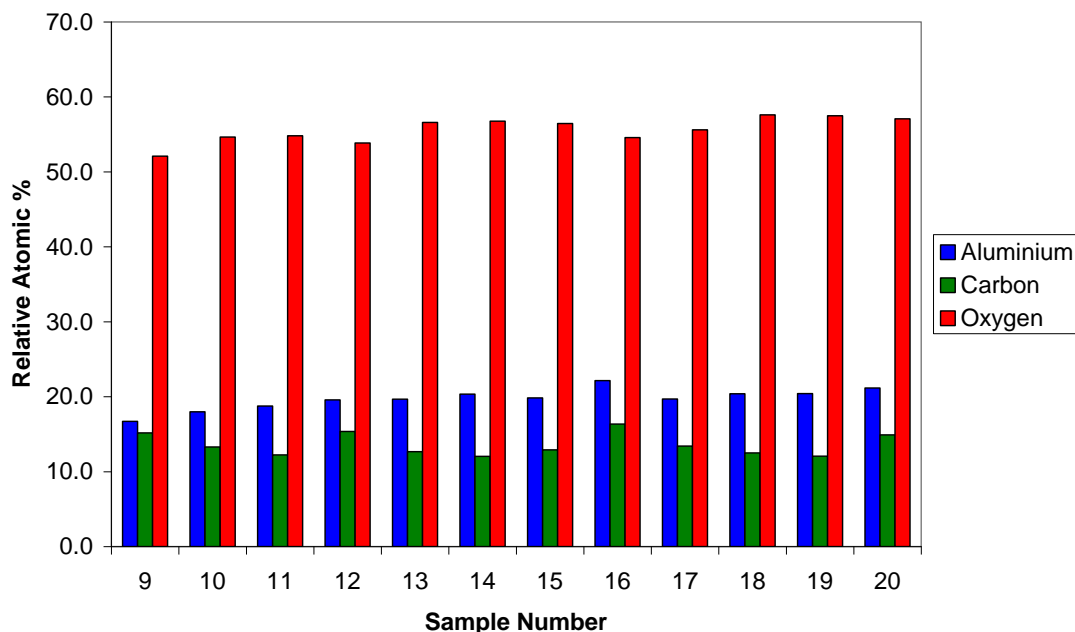
Figure 5.3-5 Relative atomic percentages of aluminium, carbon and oxygen on all cleaned AlN and Al$_2$O$_3$ surfaces.

It can be seen by comparing Table 5.3-5 and Figure 5.3-5 to Table 5.3-1 that the carbon percentage has been significantly reduced by all of the forms of cleaning. However, some carbon still remains suggesting that either the contamination is readsorbing before XPS measurement or that it was not completely removed. Table 5.3-5 also shows the increased effectiveness of the plasma cleaning when the process time is increased from one minute to five minutes. This suggests that all of the carbon was not removed under cleaning and hence that the processes are not 100% effective. However, for a five-fold increase in process time only 1-2 at % extra carbon is removed, which is a negligible difference from the point of view of wetting and epoxy bleed. It should be noted that all cleaned samples showed an effective surface energy in excess of 70mJ/m^2 and an epoxy bleed distance consistent with this surface energy and the sample roughnesses. Samples 17-20 had not undergone any storage. Instead these were prepared freshly for the XPS study. It can be seen that there is very little difference between the composition of the stored and unstored cleaned samples, suggesting that the extra contamination which arose from the storage conditions was completely removed by cleaning.

172

Oxygen plasma cleaning also seems to be effective at removing fluorine contamination. It can be seen in Table 5.3-5 that the fluorine detected is further reduced by around 1 at % by the extended processing time.

As the silicon signal is unchanged after cleaning, it would appear that the silicon is not linked to any other of the elements detected and could be a bulk constituent.

All samples show an increased signal from the aluminium following cleaning, by on average 10%, corresponding to an average increased signal of 2.5 at%.

The reduction in the quantity of carbon is accompanied by an increased detection of oxygen. An associated change in bond type distribution is seen in the narrow band carbon spectra shown in Figure 5.3-6 and Figure 5.3-7. As shown in Table 5.3-6 the quantities of carbon-oxygen bonds have increased dramatically.

As with the as received aluminium oxide, there was a consistent presence of silicon in the XPS data which could not be explained. It was not found to have any influence on the wetting behaviour of the ceramics and so its presence was not pursued any further.
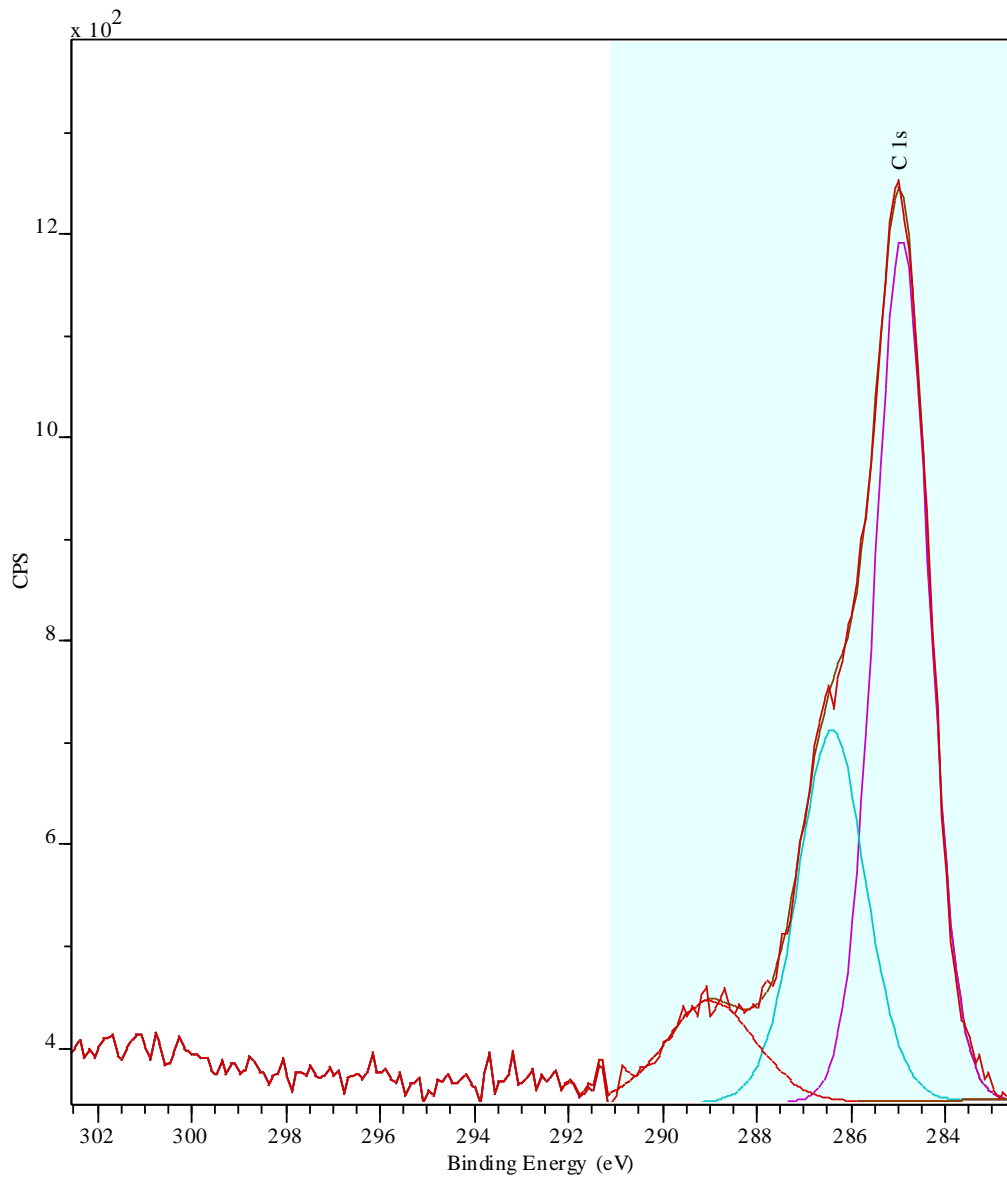
Figure 5.3-6 Narrow scan spectra of carbon peaks for sample 18 (unstored 5 min oxygen plasma cleaned $Al_2O_{3)}$, corrected to 285.00eV.
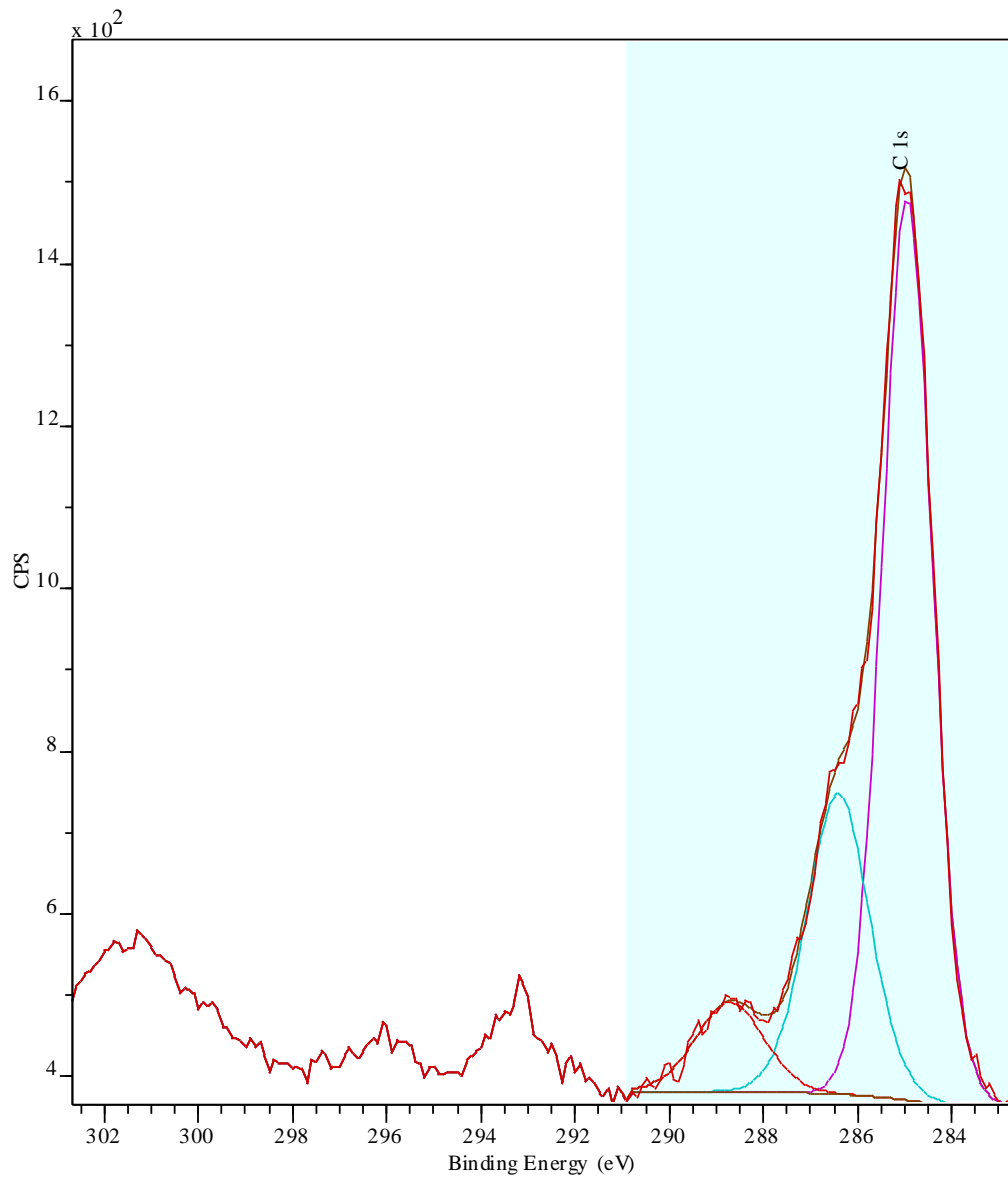
Figure 5.3-7 Narrow scan spectra of carbon peaks for sample 12 (fired AlN which had been stored in a waffle pack in a clean room), corrected to 285.00eV. Peaks outside the area highlighted in blue can be attributed to trace potassium.

Sample	No.	C1s	C-O	O-C=O
1 Min Oxygen Plasma AlN	9	70.1	23.1	6.8
5 Min Oxygen Plasma AlN	10	61.7	28.9	9.4
IPA + Oxygen Plasma AlN	11	63.7	29.8	6.6
Firing AlN	12	64.5	26.8	8.7
1 Min Oxygen Plasma Al_2O_3	13	59.2	31.8	9.1
5 Min Oxygen Plasma Al_2O_3	14	58.9	36.5	4.6
IPA + 1 Min Oxygen Plasma Al_2O_3	15	69.0	23.9	7.1
Fired Al_2O_3	16	64.4	25.1	10.5
1 Min Oxygen Plasma Al_2O_3	17	62.7	32.4	5.0
5 Min Oxygen Plasma Al_2O_3	18	57.8	30.9	11.4
IPA + 1 Min Oxygen Plasma Al_2O_3	19	51.9	39.9	8.2
Firing Al_2O_3	20	59.5	30.0	10.5

Table 5.3-6 Relative bond type percentages from XPS spectra fitting for cleaned samples.

In fact the relative percentage of C-O bonds has increased from 10-25% in Table 5.3-3 to 23-40%. This result indicates that the plasma has probably oxidised the organic contamination. A further conclusion is that the contamination which is present after cleaning is not entirely due to readsorption. More evidence for this is that the contaminant composition following cleaning is not similar to the tin foil stored samples, but is more heavily oxidised. This suggests that the composition of the contamination on a ceramic surface stored in tin foil changes over time, but does not increase by a large amount. The cleaned samples were stored in tin foil before analysis.

The relative percentages of carbon bond types were multiplied by the total carbon signal to get figures for atomic surface percentages for three AlN samples. These were the nitrogen stored AlN, and the 1 minute and 5 minute plasma cleaned AlN, samples 2, 9 and 10 respectively (all of which were nitrogen stored to allow comparison). The total carbon atomic percentages were 26, 15.2 and 13.3 respectively which showed a decrease in carbon on the surface due to cleaning. There was shown to be an accompanying slight decrease in the total presence of each of the C-O and COOR groups, which was significantly less than the reduction of the C-C/C-H percentage. This could be due to oxidation of the carbon contaminants (although one would expect an increase in their prevalence), or it could be due to the increased resistance of the COOR groups to removal due to chemisorption[6], or a

resistance to further oxidation. This relationship is seen continually when similarly stored samples are compared following different cleaning methods, samples 8, 13 and 16 show the same pattern, as do samples 7, 14 and 15. The hypothesis of remnant carbon which is more difficult to remove due to the combined effects of chemisorption and high oxygen content, as opposed to the physical adsorption of saturated hydrocarbons, could explain the incomplete removal of carbon contamination by plasma cleaning. However, due to the affinity of the ceramics for adventitious carbon, readsorption is almost certainly responsible for some of the detected presence following cleaning.

The effective surface energy measurements of the cleaned ceramics show a linear correlation to surface carbon content as seen in *Section 5.1.4.1 Ceramic Sample Surface Chemical Characterisation* and Table 5.3-4. Extrapolating a least squares linear fit to the data in Figure 5.3-8 yields a zero carbon surface energy for the ceramics of approximately 50mJ/m^2. Figure 5.3-8 also suggests that the surface energy does not vary linearly with carbon concentration at low carbon concentration. In fact the surface energy of pure aluminium nitride is not 50mJ/m^2 as the extrapolated best fit line suggests, but estimates in the literature for both AlN and alumina lie in the range of 1J/m^2 which is significantly higher[7,8]. This would fit with theories of the effect of heterogeneity on the contact angle of a system[9], the Cassie Baxter wetting regime, a speculation explored in greater detail in *Section 5.4 Application of Wenzel and Cassie Theory to Experimental Data*.

The surface energy estimations for the plasma cleaned samples suggest that the oxidation of the organic contamination/higher relative prevalence of oxygen containing species, reduces its hydrophobicity. This can be seen in Figure 5.3-8 where the effective surface energy of the point representing the averaged cleaned sample data lies far above that for the trendline for the contaminated samples (71 mJ/m^2 as against 40 mJ/m^2 extrapolated value). This oxidation effect is consistent with data collected upon the surface energy effects of plasma treatment on polymer surfaces[10].
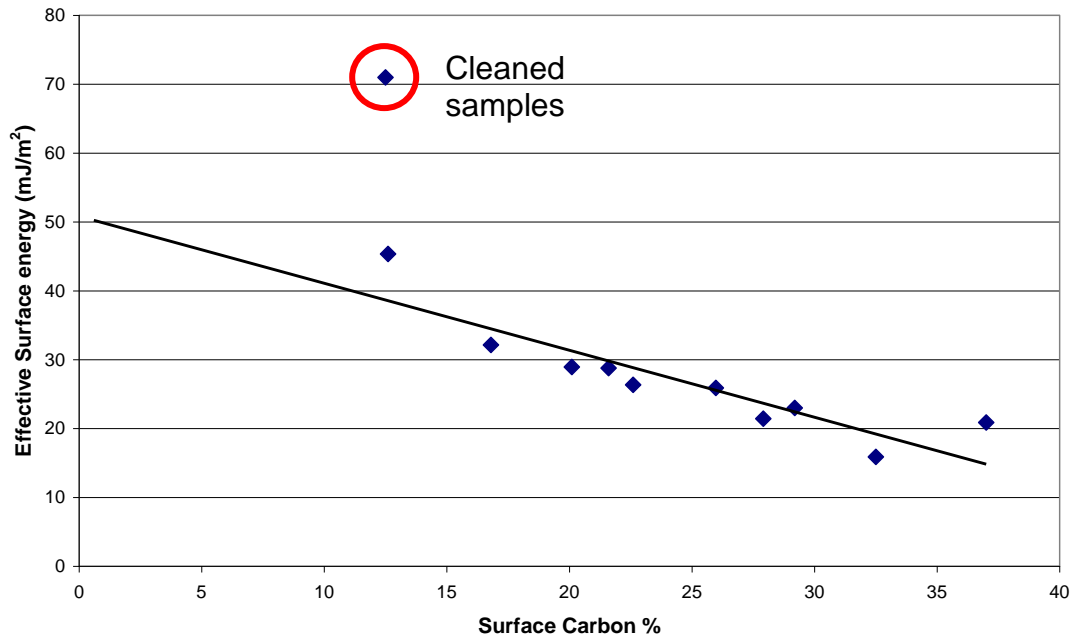
Figure 5.3-8 Carbon % compared to effective surface energy for all contaminated samples and the mean value of cleaned samples. The line is a linear fit to the contaminated sample data.

Table 5.3-7 compares values of correlation coefficient for pairs of elements before the samples were cleaned and following cleaning. It can be seen that the correlation coefficient was unchanged only for Si-O in Al_2O_3. There is still a high absolute value of r for carbon and oxygen post-clean, although it is reduced probably due to the extra ceramic surface exposed and the oxygen associated with this. Correlation was not found between effective surface energy and the presence of any of the non-bulk elements, excluding carbon. There was also no correlation found between the percentage distribution of the carbon bond types, which showed variation, and the effective surface energy, which was consistently >70mJ/m^2. This shows the effectiveness of the cleaning methods to equalise the surfaces in terms of effective surface energy.

AlN			
Element 1	Element 2	r Pre Clean	r Post Clean
F	O	1.00	-0.23
F	C	-1.00	-0.41
C	O	-1.00	-0.77
Si	O	0.89	0.03
Si	C	-0.85	-0.62
Al	C	-0.71	-0.10
C	N	-0.70	0.92
Al_2O_3			
Element 1	Element 2	r Pre Clean	r Post Clean
Al	O	0.99	-0.40
Si	O	0.99	0.79
Si	Al	0.99	-0.82
F	C	0.88	-0.78
C	O	-0.87	-0.70
Al	C	-0.86	0.80
Si	C	0.83	-0.90
N	F	-0.83	0.89

Table 5.3-7 Relative atomic composition percentage correlation coefficients (r) for AlN and Al_2O_3 on stored and cleaned samples.

5.3.5.3 Contamination Rate and Source

The contamination rate and source was determined experimentally by storing samples and conducting measurements after 24h, 48h, 1 week, 2 weeks and 4 weeks. The storage conditions investigated were:

1. Open to the atmosphere in a clean room (air)

2. Stored in carbon loaded polycarbonate waffle packs with supplied inserts in a clean room (polythene and lint free paper), (Waf/Ins)

3. Stored in waffle packs with no inserts in a clean room, (Waf)

4. Stored in a waffle pack sealed in tin foil in a clean room, (Waf/Foil)

5. Stored in a waffle pack containing both inserts, wrapped in tin foil, in a clean room, (Waf/Foil/Ins)

6. Stored in a sealed tin foil pouch in a clean room (Foil)

7. Stored in a waffle pack with only the paper insert, wrapped in tin foil, in a clean room (Waf/Foil/Paper).

Storage Condition	Material	Sample Number
Air	AlN	21
Air	Al_2O_3	22
Waf/Ins	Al_2O_3	23
Waf/Ins	AlN	24
Waf	Al_2O_3	25
Waf	AlN	26
Waf/Foil	Al_2O_3	27
Waf/Foil	AlN	28
Waf/Foil/Ins	Al_2O_3	29
Waf/Foil/Ins	AlN	30
Foil	AlN	31
Waf/Foil/Paper	AlN	32
Waf/Foil/Paper	Al_2O_3	33

Table 5.3-8 Storage conditions for samples in rate of contamination study. Waf = waffle pack, ins = lint free paper and polyethylene insert, Foil = tin foil storage, Air = storage in open air, and paper = storage with just lint free paper insert.
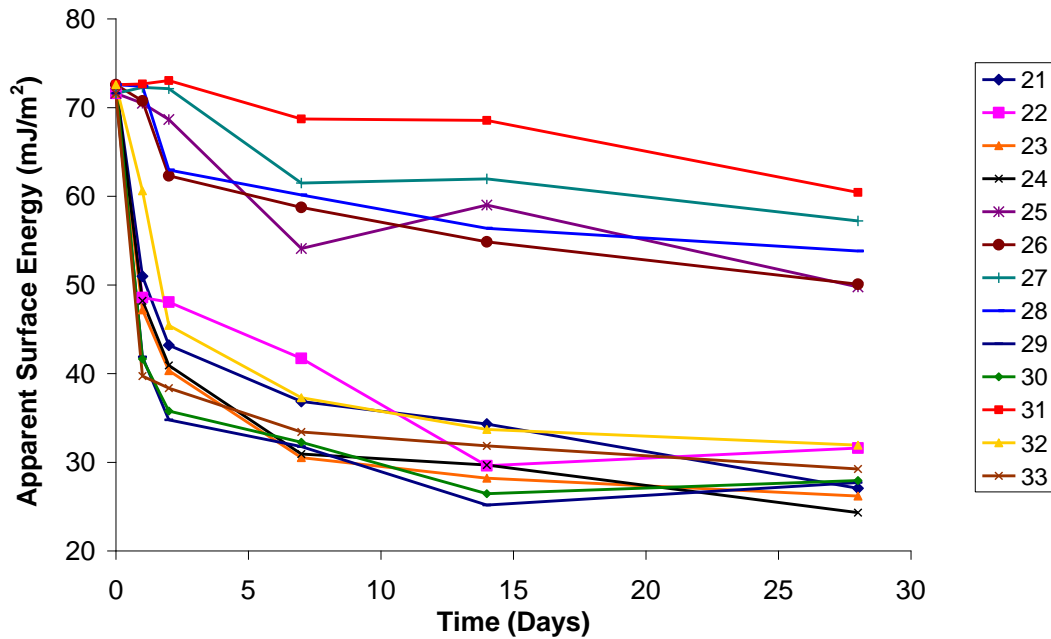
Figure 5.3-9 Graph showing the change in apparent surface energy over compared to time spent stored under various conditions. The samples fall into two clear groups, Samples 25-28 and 31 with relatively high surface energies, and the remaining samples.

Sample	1 day	2 days	7 days	14 days	28 days
21	48.0	60.4	72.8	72.9	98.2
22	51.3	52.9	61.6	87.7	91.5
23	53.1	61.4	85.7	103.0	108.4
24	51.6	62.8	85.9	99.8	99.3
25	16.2	21.1	43.7	36.9	49.4
26	15.0	31.8	37.2	42.6	49.4
27	5.3	11.0	33.4	35.5	39.5
28	7.7	30.9	35.2	40.5	44.3
29	60.0	74.3	91.6	102.5	113.3
30	61.0	71.0	95.3	100.3	93.0
31	4.9	4.5	20.9	21.1	34.9
32	35.5	55.7	68.8	75.7	75.0
33	62.3	65.3	96.7	72.1	80.4

Table 5.3-9 Water contact angles (°) for samples measured at the given time intervals.

It can be seen from Table 5.3-9 and Figure 5.3-9 that for all stored samples the general trend was for the water contact angle to increase with time and hence the apparent surface energy to decrease with time. This is attributed to the adsorption of hydrophobic organic contaminants explored in the previous part of this chapter.

One of the obvious conclusions to draw from the above data is the effectiveness of tin foil as a storage medium which will maintain cleanliness. It can be seen in Figure 5.3-9 that the samples fall into two clear groups, samples 25-28 and 31 with relatively high surface energies, and the remaining samples. The high surface energy group consists of foil wrapped samples without the polymer insert from the waffle packs.

Table 5.3-9 shows that the foil stored sample 31 shows a moderate change in contact angle over the 4 week storage period from 4.9° to 34.9°, which is a fraction of the change exhibited by other samples, such as sample 30 (Waf/Ins/Foil, AlN) which showed a contact angle of 61° after just 24 hours, and samples 23 and 29 (Waf/Ins, Waf/Foil/Ins Al_2O_3) which showed water contact angles of over 100° after a month of storage.

The question of the source of the majority of contaminants appears to be answered by the results for samples 27-30, where 27 and 28 were stored without inserts and exhibit a much smaller change in surface energy than and 29 and 30 which were stored with both polymer and lint free paper inserts. The polymer insert and lint free paper therefore appear to be the source of the majority of contaminants. However, the results for samples 25-28 and sample

31 highlight another potential source for the contaminants. The tin foil stored sample number 31 exhibits a consistently lower contact angle than the samples stored in the plain waffle packs, which in turn exhibit a consistently higher contact angle than those stored in waffle packs and tin foil. This could mean that the tin foil offers enhanced protection from the atmosphere, that the waffle packs outgas slightly (but less than the polymer insert and lint free paper) or that the tin foil itself adsorbs contaminants leaving less to be adsorbed onto the surfaces. The results suggest that all of these possibilities are responsible for the contaminants to a certain degree. The waffle pack probably outgases, because sample 31 (tin foil, AlN) always exhibits a lower contact angle than samples 25-28 (25 – Waf Al_2O_3, 26 - Waf AlN, 27 - Waf/Foil Al_2O_3, 28 - Waf/Foil AlN). The aluminium foil probably offers good protection from adventitious carbon from the atmosphere, because samples 31 (Tin foil AlN) and 27-28 (27 - Waf/Foil Al_2O_3, 28 - Waf/Foil AlN) show lower contact angles than samples 25 and 26 (25 – Waf Al_2O_3, 26 Waf AlN).

Figure 5.3-9 and Table 5.3-8 shows that the industry method of storing the samples in waffle packs with polymer and lint free paper inserts is equivalent to leaving samples open to the atmosphere of a class 10,000 clean room, in terms of organic contamination. The rate of contamination of a sample stored in the industrially adopted method is faster than the adsorption rate of adventitious carbon from the atmosphere. Sample 22 (Air Al_2O_3) shows a consistently lower surface energy than the measurements made with sample 23 (Waf/Ins Al_2O_3), the same was seen with AlN, samples 21 (Air AlN) and 24 (Waf/Ins AlN).

Figure 5.3-9 shows that the adsorption rates of the samples which adsorbed adventitious carbon at a lower rate (25-28 and 31) over the time were relatively constant during the measurement periods. It is likely that that the surface loadings of contamination would eventually reach that seen on the highly contaminated samples. By contrast the contamination loadings on the highly contaminated samples 21-27, 29-30 and 32-33, levelled off after an initial high adsorption rate period, suggesting the equilibrium position of adsorption rate matching desorption rate was reached after 28 days.

To separate the effects of the two different insert types, lint free paper inserts were used alone with waffle packs and tin foil for samples 32 and 33. It was observed that the contamination rate and magnitude were less with only paper than when polyethylene inserts are included, but more than the rate and magnitudes observed with waffle packs only or packing with tin foil. It can therefore be concluded that both the lint free paper inserts and polyethylene inserts are responsible for outgassing and the subsequent adsorption onto the ceramic surfaces.

Interestingly the samples which showed the highest degree of contamination, as inferred from contact angles, were those stored by the industry recommended method, with lint free paper and polyethylene inserts. However, the apparent surface free energies reached by these samples, $26.19 mJ/m^2$ and $24.31 mJ/m^2$ for aluminium oxide and aluminium nitride respectively, lie only slightly inside the surface energy threshold value ($30 mJ/m^2$) below which the degree of epoxy bleed is considered to be acceptable. Thus if storage were to be used as a method of controlling epoxy bleed it is possible that heterogeneity over samples and between batches could still result in epoxy bleed due to natural variation in the sample conditions and tendency to adsorb contaminants (and also varying partial pressure of contaminants and temperature of storage conditions).

5.3.6 Conclusions

The aim of this section of the work was to test the hypothesis that while storing ceramics for an extended period of time will allow build up of sufficient contamination to stop bleed occurring, samples fresh from suppliers will not have built up sufficient contamination to reduce the surface free energy to a degree such that bleed will not occur.

Following the cleaning of samples and storage under different conditions it was found that the composition of the contamination on the surfaces was not linked to their storage method, but that the quantity of contamination was. Storing ceramics in polymer waffle packs does not protect them from build up of carbon contamination regardless of storage atmosphere. The use of tin foil for storage can reduce the degree of contamination significantly, but not

prevent build up entirely. A high degree of bleed was seen in both samples cleaned but not stored, as well as in samples cleaned after storage, showing the effects of storage contamination are easily reversed.

The surface carbon concentration was found to be a good predictor of the degree of bleed. It was also found that a moderate degree of contamination, around 30 at% of carbon, reduces bleed to a insignificant level. However, relying on environmental exposure to produce the required level of carbon on ceramic surfaces is a risky strategy for an OEM because it introduces a poorly controlled parameter into the production process

To deal with this two strategies are suggested. One is to use contact angle measurement as a screening procedure. The other is to put the ceramic surfaces into a known state, by routinely cleaning on receipt followed by a suitable treatment to reduce the surface energy. The use of surface treatments will be addressed in later sections of this work.

The effective surface energy was found to vary non-linearly with degree of carbon contamination. A theoretical explanation of this observation is given in *Section 5.4 Application of Wenzel and Cassie Theory to Experimental Data*.

The cleaning methods used in this investigation successfully achieved the intended result of increasing the effective surface energy. The main sources of the contaminants when ceramics are stored in waffle packs appears to be the inserts, polyethylene sheet and lint free paper sheet, at approximately equal fractions. When stored with inserts the ceramics were observed to adsorb organics at a higher rate than if they were exposed to the atmosphere. It was found that excluding the inserts from the waffle packs offers better protection from organic contaminants during storage, although some build up still occurs.

It seems that the adsorption of contaminants accounts for the observed variability[3] in industrial experience across batches of seemingly identical parts, and the random occurrence of epoxy bleed. It was found that storing samples for an extended period allows sufficient contamination to adsorb to give rise for marginal conditions for epoxy bleed inhibition. Although epoxy

---

[3] Communication from Paul Firth of Oclaro plc

bleed was controlled by storage related contamination in this study, heterogeneity over surfaces could still cause problems in the production line were this contamination to be relied on to prevent bleed. In addition the length of time required to build up such levels is at least 28 days, which is probably not economically viable.

5.3.7 References

[1] Williams, O. Liu, C. Webb, D.P. Firth, P. Epoxy adhesive behaviour on ceramic surfaces in commercial optoelectronic assemblies, International Journal of Adhesion and Adhesives, Volume 30, Issue 4, June 2010, Pages 225-235

[2] Saga, K. Hattori, T. Identification and Removal of Trace Organic Contamination on Silicon Wafers Stored in Plastic Boxes Koichiro Saga and Takeshi Hattori, J. Electrochem. Soc. 143, 3279 (1996), DOI:10.1149/1.1837198

[3] Tezuka, M. Yajima, T. Oxidation of aromatic hydrocarbons with oxygen in a radiofrequency plasma, *Plasma Chem. Plasma Process.* 16 (1996), pp. 329–340

[4] Tezuka, M. Yajima, T. Oxidation of Cycloalkanes in a Radiofrequency Plasma. Bulletin of the Chemical Society of Japan, 1991

[5] Shelton, L.R. Field guide for collecting samples for analysis of volatile organic compounds in stream water of the National Water-Quality Assessment Program: U.S. Geological Survey Open-File Report 97-401, 14 p. 1997

[6] Karaman, M.E. Antelmi, D.A. Pashley, R.M. The production of stable hydrophobic surfaces by the adsorption of hydrocarbon and fluorocarbon carboxylic acids onto alumina substrates. Colloids Surf A 182:285–298 2001

[7] Asai, H. Iwase, N. Suga, T. Influence of ceramic surface treatment on peel-off strength between aluminum nitride and epoxy-modified polyaminobismaleimide adhesive. *Advanced Packaging, IEEE Transactions on* , vol.24, no.1, pp.104-112, Feb 2001

[8] Guzman-Castillo, M.I. Bokhimi, X. Rodriguez-Hernandez, A. Toledo-Antonio, A. Hernandez-Beltran, F. Fripiat, J.J. The surface energy of quasi-amorphous [gamma] alumina calculated from the temperature of the [gamma]-->[alpha] transition, Journal of Non-Crystalline Solids, Volume 329, Issues 1-3, 7th Int. Workshop on Non-Crystalline Solids, 1 November 2003, Pages 53-56, ISSN 0022-3093, DOI: 10.1016/j.jnoncrysol.2003.08.012.

[9] Somorjai, G.A, Principles of surface chemistry, Englewood Cliffs, New Jersey, Prentice-hall, Inc, 1972

[10] Mittal, K. L. 1945- Polymer surface modification : relevance to adhesion / Utrecht : VSP, 1996

5.4 Application of Wenzel and Cassie Theory to Experimental Data

5.4.1 Introduction

In this work, and extensively in the literature, application of the Young equation and related expressions is not directly meaningful due to the assumptions it makes. Surface texture and chemical heterogeneity are not taken into account in the early surface energy works. Such effects were considered by later authors such as in the work by Wenzel on the effect of roughness upon contact angle[1], or the work by Cassie on the effect of roughness and chemical heterogeneity combined[2].

Wenzel and Cassie models were also used to interpret the experimental data and were studied to determine their validity for this work. A modification to the Cassie model to cover the case of a heterogeneous surface consisting of fully wetting and partially wetting micro-regions is also proposed.

In this work the effects of the surface properties of roughness and chemical heterogeneity upon epoxy bleed have been experimentally determined, *Section 5.2 Surface Parameter Effects on Epoxy Bleed*. However the predictions of models for rough and chemically heterogeneous surfaces have not yet been correlated with experimental results. This section of work aims to analyse experimental results from previous chapters using the Wenzel and Cassie theories.

5.4.2 The Cassie Model

The theory widely adopted to predict the effects of chemical heterogeneity on the contact angle of a solid/liquid system was first described by Cassie in 1952[2] in the form of the equation:

$$\cos\theta = f_1 \cos\theta_1 + f_2 \cos\theta_2$$

Equation 5.4-1

Where f_1 is one fraction of interface, and f_2 is another.

Cassie's equation represents the weighted averaging of the surface tensions on the two surface types in the system. It was later proposed by Israelachvil[3]

that the forces be averaged and not the surface tensions, leading to the expression:

$$(1 + \cos\theta)^2 = f_1(1 + \cos\theta_1)^2 + f_2(1 + \cos\theta_2)^2$$

Equation 5.4-2

It is evident from the equations that the models proposed by Cassie and Israelachvil only treat situations in which all surface fractions yield non zero contact angles, i.e. are partially wetting.

To address the problem of treating inhomogeneous compound surfaces consisting of completely wetting and partially wetting components Equation 5.4-3 is proposed. It is derived by substituting interfacial tensions and not contact angles, in the Young equation.

$$\left(1 + \left(\frac{\gamma_{SV} - \gamma_{SL}}{\gamma_{LV}}\right)\right)^2 = f_1\left(1 + \left(\frac{\gamma_{SV1} - \gamma_{SL1}}{\gamma_{LV1}}\right)\right)^2 + f_2\left(1 + \left(\frac{\gamma_{SV2} - \gamma_{SL2}}{\gamma_{LV2}}\right)\right)^2$$

Equation 5.4-3

The resultant contact angle for the composite surface is then given by:

$$(1 + \cos\theta)^2 = f_1\left(1 + \left(\frac{\gamma_{SV1} - \gamma_{SL1}}{\gamma_{LV1}}\right)\right)^2 + f_2\left(1 + \left(\frac{\gamma_{SV2} - \gamma_{SL2}}{\gamma_{LV2}}\right)\right)^2$$

Equation 5.4-4

Applying this equation to experimental data, along with the Owens Wendt model, yields surface energies for bare ceramic in the region of 80mJ/m^2. This value is much lower than expected as pure clean ceramics can have a surface energy[4] ~1J/m^2. However, surface energies derived from Owens Wendt equation have a maximum value which is related to surface tensions of test liquids used, giving the surface energy estimation an upper limit. It may also be that because of the high affinity for adsorbates the ceramics have, that contact angle methods cannot be used to measure the true surface energy of aluminium oxide and aluminium nitride. This is because the speed at which contamination adsorbs makes measuring an uncontaminated sample impossible. Thus test liquid methods are useful for measuring and predicting the properties of the practical surfaces in this study, which will always be

contaminated to some degree, but for measuring the actual properties of clean ceramics it is not useful.

5.4.3 The Wenzel Model

The contact angle data was also analysed using the Wenzel equation, *Section 2.4.3 The Effect of Surface Roughness*, to attempt to account for the effect of roughness upon the contact angle. Applying the Wenzel model to extract the expected contact angle for a flat surface from samples with different roughnesses but the same surface chemistry, should yield equal contact angles. However, it was found that the Wenzel theory produced varied contact angles where it should have made them equal.

Sample	Liquid	CA	A/Ao	CA
1	Water	8.9	1.20778	35.1
1	Diiodomethane	41.0	1.20778	51.3
3	Water	10.6	1.00235	11.3
3	Diiodomethane	42.0	1.00235	42.2
7	Water	13.0	1.63006	53.3
7	Diiodomethane	39.6	1.63006	61.8
8	Water	10.1	1.12520	28.9
8	Diiodomethane	41.4	1.12520	48.2
9	Water	10.6	1.00208	11.2
9	Diiodomethane	42.2	1.00208	42.3
10	Water	10.6	1.31494	41.6
10	Diiodomethane	48.7	1.31494	59.9

Table 5.4-1 Original measured contact angle (CA left column)and the expected flat surface contact angle extracted using the Wenzel equation (right column CA). Where the sample number is as in *Section 5.1 Characterisation of Surfaces and Adhesives*, CA is contact angle in °, and A/Ao is the Wenzel roughness factor.

However, it was seen in this work that there is a strong correlation between the Wenzel roughness factor measurement and the distance of epoxy bleed, *Section 5.2.4.3.1 Ceramics*. So although the Wenzel theory does not explain the variation in contact angle seen in this work, his method of defining roughness appears to be useful.

5.4.4 Conclusions

A method suitable for analysing chemically heterogeneous surfaces of at least one inherently wettable constituent has been shown. Using this method it has been shown that 15% saturated hydrocarbon coverage is not sufficient to induce the total surface energy reduction of the ceramics which has been seen in experimental work, and that some other adsorbate is probably involved.

The Wenzel model is not a suitable model for predicting the effect of roughness on the contact angles of liquids on ceramics.

5.4.5 References

[1] Wenzel R.N. Surface roughness and contact angle. Journal of Physical Chemistry 1949;53(9):1466–7

[2] Cassie, A. B. D. *Discuss. Faraday SOC.* 1952, *75,* 5041

[3] Israelachvili, J.N. Gee, M.L. Contact angles on chemically heterogeneous surfaces, , Langmuir 1989 5 (1), 288-289

[4] Guzman-Castillo, M.L. Bokhimi, X. Rodriguez-Hernandez, A. Toledo-Antonio, A. Hernandez-Beltran, F. Fripiat, J.J. The surface energy of quasi-amorphous [gamma] alumina calculated from the temperature of the [gamma]-->[alpha] transition, Journal of Non-Crystalline Solids, Volume 329, Issues 1-3, 7th Int. Workshop on Non-Crystalline Solids, 1 November 2003, Pages 53-56, ISSN 0022-3093, DOI: 10.1016/j.jnoncrysol.2003.08.012.

5.5 Self Assembled Monolayers

5.5.1 Introduction

The work described in previous chapters, *5.2 and 5.3*, and work by others has identified the effectiveness of surface energy manipulation for the control of epoxy bleed. It has been shown in the background chapter that existing literature dealing with thin film technologies for surface energy manipulation usually includes treatment in a vacuum oven[1], or requires plasma deposition apparatus, the literature describing which originates from the manufacturer[2]. The use of self assembled monolayers (SAMs) to treat optoelectronic substrates, however, has not been described. Possible reasons for this are that SAMs are known to act as anti-adhesion layers[3], and the potential complexity of including an aqueous/wet treatment in the assembly process. Work has been described in which the use of SAMs is proposed for the treatment of surfaces in electronics applications, such as the use of alkanethiols for the oxidation protection of copper to allow fluxless soldering[4,5].

The use of surface energy modification methods always carries the risk of the reduction of adhesion levels to an unacceptably low level. Because of this, careful consideration must be given to the SAM chemistry chosen. Ideally the SAM will not survive the thermal curing process and will break down under elevated temperature so as to not affect adhesion to a great degree. If a thermal breakdown mechanism is not possible then the alternative is optimisation by balancing adhesion strength with bleed control.

In this section alkanethiol, fatty acid and trichlorosilane SAMs are considered for the coating of ceramic substrates and interconnection metallisations. Their presence was confirmed and their effects upon the properties of the ceramic substrates was characterised with the use of contact angle and adhesive behaviour measurements. The SAMs are studied with special attention to their potential ability to minimise epoxy bleed. The effect of the coatings on adhesion was determined by lap shear tensile testing. The practical limitations of the SAMs for use in optoelectronic assembly was also of interest.

Consequently their response to the cure temperatures of the adhesives and stability over time was assessed and is described in this chapter.

To determine any effect on the properties of electrically conducting bonds, the conductivity of silver flake filled epoxy adhesive joints on organic monolayer treated surfaces was also studied. Finally a method for SAM coating heterogeneous surfaces consisting of ceramic and metallisations was developed and tested. The method is the subject of a patent application[6].

5.5.2 Background

A general introduction to the formation and structure of self assembled monolayers can be found in the literature review in *Section 2 Literature Review*. In this section specific details of SAM molecules which would be expected to bond to the material surfaces considered in this work. The surfaces on which it would be required to form SAM layers for optoelectronics are Al_2O_3, AlN, copper, and gold, and suitable candidates were identified from the literature.

Monolayers which form stably on aluminium oxide are silanes[7,8,9,10] carboxylic acids[8,11,12,13,14] and phosphonic acids[14,15] and those which form on copper and gold are alkanethiols[13,16] and variants which form the same bond type. In terms of wettability the literature quotes varying figures for the surface energies and contact angles of SAM modified surfaces. In general the surface energy is highly dependent on the terminating end groups of the SAM molecule and the chain length. However, providing the chain length is higher than 8 carbons and the terminating end groups is a methyl or containing fluorine or chlorine, then the contact angles of water reported are always >90°.

Both XPS data of AlN from this study, and reports in the literature suggest that AlN forms a thin layer of aluminium oxide on its surface[17]. It is therefore probable that monolayers suited to bonding to aluminium oxide may also be used for the treatment of aluminium nitride. This is especially the case for optoelectronics manufacturing since steps are not taken to remove oxide layers from aluminium nitride materials.

5.5.2.1 Fatty Acid Monolayers on Ceramic Surfaces

The bonding mechanism between a carboxylic acid and aluminium oxide, shown in Figure 5.5-1, requires the aluminium oxide to first be hydroxylated. This happens spontaneously due to the surface energy of the material for both aluminium oxide and aluminium nitride, and the presence of water vapour in the atmosphere. Fatty acid monolayers can also be applied from an aqueous solution[12], which encourages the hydroxylation of the surface in-situ.
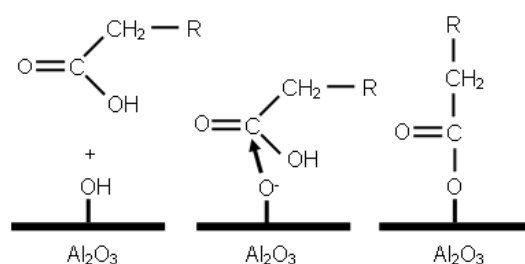
Figure 5.5-1 Reaction between aluminium oxide surface and carboxylic acid, where R is a carbon chain which can be saturated with hydrogen, fluorine or chlorine.

A fatty acid molecule bonded to an aluminium oxide surface is reported to have a tilt angle close to zero[13], allowing it to form close packed, potentially more ordered monolayers on aluminium oxide than on other surfaces[18]. Highly ordered, stable monolayers of fatty acids reportedly form on aluminium oxide at low concentrations (0.01mM) and at high speed[16]. This makes them attractive for use in an optoelectronics assembly line since the treatment time would be small, and the apparatus required relatively simple.

In addition to the ease of application the predicted stability of the monolayers is also good, with the free energy of adsorption calculated to be -38.5kJ/mol for stearic acid ($CH_3(CH_2)_{16}COOH$) on aluminium oxide[19]. In terms of the practical change in surface conditions caused by the adsorption of fatty acid monolayers, as measured by contact angles, the results vary widely[12,16] and are highly sensitive to application methods and initial surface conditions.

5.5.2.2 Organosulphur Monolayers on FCC Metallic Surfaces

Organosulphur monolayers applied to gold surfaces are perhaps the most widely studied self assembled monolayers. The organosulphur molecules which form stable SAMs on gold surfaces can take the form of alkanethiols,

dialkyl disulphides, dialkyl sulphides, alkyl xanthates and dialkylthicarbamates[13], amongst others. Alkanethiols are the most widely studied monolayer upon gold, and are known to bond to other coinage metals[20], amongst other substances not of interest to this study[13]. The bonding mechanism between an alkanethiol and gold surface is usually described by the reaction:

$$R - S - H + Au_n^0 \rightarrow R - S^- - Au^+ \bullet Au_n^0 + \frac{1}{2}H_2$$
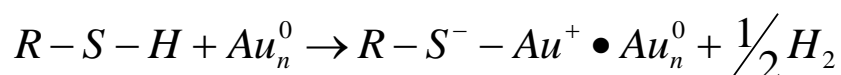
This is an oxidative/reductive reaction consisting of the oxidation of the S-H group producing a bond to the gold surface and the reductive elimination of hydrogen which produces hydrogen molecules. The reaction requires a clean, oxide free surface which is easy to obtain with gold and hence perhaps the reason gold has been studied in such depth. A similar reaction occurs when alkanethiols are exposed to silver[21] and copper[22], producing chemisorbed monolayers with similar structures but different tilt angles[20]. The wetting properties of the resultant coatings are very similar, with both polar and dispersive components of surface energy being similar for monolayers on the three different metal surfaces[20]. However increased attention to detail is required for the application of alkanethiols to silver and copper due to the presence of a native oxide layer. This is especially problematic in the case of copper. Once the oxide is removed SAMs are even used as a method of impeding its reformation[4,5]. Quoted values[20] for polar and dispersive liquid contact angles suggest that application of alkanethiols will reduce the apparent surface energy of a surface sufficiently to stop epoxy bleed, and that the difference in surface energy between octadecanethiol coated copper, silver and gold surfaces is <1mJ/m^2 (values calculated using the Owens Wendt method, being 19.59, 18.67 and 19.26mJ/m^2 for copper, silver and gold respectively).

5.5.2.3 Silane Monolayers on Ceramic Surfaces

In this work the silanes used consisted of organic long chain molecules with a terminating group containing a silicon atom which is saturated with hydrogen (a methylsilane), chlorine (a chlorosilane) or another molecule. The main

group of silanes used were trichlorosilanes of the form $CH_3(CH_2)_nSiCl_3$. Trichlorosilanes are known to bond to hydroxylated aluminium oxide, silicon dioxide and copper (II) oxide with a strong, covalent Si-O bond[23]. Monolayers bond strongly to hydroxylated ceramic surfaces with enthalpies higher than those of alkanethiols and fatty acids[16]. Reported contact angle values[24] for octadecyltrichlorosilane give a figure of $19.57mJ/m^2$ for apparent surface energy, which is sufficient for epoxy bleed control. However, the stability reported in the same work suggests that surface bonded octadecyltrichlorosilane has extraordinary resistance to thermal processing, which could lead to adhesion issues. It is possible that octadecyltrichlorosilane would be useful in optoelectronic assembly only for patterning processes where SAMs are used as a wetting barrier, and not as a homogeneous surface coating.

5.5.3 Methodology

Epoxy bleed has been referred to numerous times as a phenomenon relating to the interaction between surface energy and surface tension, both in this work, and in the literature. Thus the key parameter to evaluate when working with SAMs for bleed control is the apparent surface energy, that being the measurable surface energy determined by contact angle methods which do not destroy the applied monolayers. This measurement method is particularly appropriate as both it, the phenomenon to be controlled (bleed), and adhesion involve wetting processes controlled by the top few angstroms of a surface. For these reasons contact angle analysis is used extensively throughout this work.

The identification of a large presence of organic contaminants on the as-received surfaces suggested a cleaning process would first be needed to remove contaminants which may interfere with chemisorption of SAM molecules. Plasma cleaning was therefore used to remove the majority of organic contaminants from the ceramics and a dilute HCl etch was used to remove the native oxide layer from copper samples.

The first step in this section was the application and verification of formation of monolayers to the ceramic surfaces. Verification was judged by the change in

surface energy before and after application, measured by the two liquid contact angle method. The effect of chain length on the change in surface free energy was also identified by contact angle measurements.

As with the previous chapters, adhesive joint strength testing, failure mode analysis and epoxy bleed measurements were performed where necessary to determine the effects of the monolayers upon the properties of bonding bleed.

Gold is the top layer metallisation material of choice in Oclaro's optoelectronic assembly interconnections. Copper is used as a proxy material in this work, the justification for this can be found in *Section 3 Methodology*.

For the coatings to be a successful solution to the epoxy bleed phenomenon they had to show effectiveness in consistently resisting bleed surfaces encountered in optoelectronic manufacture, i.e. aluminium oxide and aluminium nitride, and sample surface roughnesses over the range R_a value 0.00084-0.58951µm). Therefore samples over this range of roughness were coated and analysed.

The 90° wetting envelope of a surface (see *Section 2.4.9 Calculating and Interpreting the Wetting Envelope*) was used to interpret the surface energy results. The wetting envelope can be used to predict the formation of a composite bond. Adhesion studies frequently cite as a the general rule that poor adhesion results from an adhesive contact angle of >90°, the wetting envelope line represents the range of liquid parameters which will form a 90° contact angle, where below this line the contact angle will be <90° and above it >90°.

In this study SAM coated samples were generally used within two hours of coating. In an optoelectronics assembly line, such efficiency is not always possible and ceramic substrates may be stored for up to a month prior to use[4]. The implications of this potential storage time for the effectiveness of the coatings were therefore assessed by contact angle and epoxy bleed measurements.

---

[4] Communication from Paul Firth of Oclaro plc (optoelectronics manufacturer)

Optoelectronic substrates surfaces do not consist of a single material, but instead carry metallisation patterns for interconnections. Epoxy bleed is a problem on both the ceramic and metallisation surfaces. Consequently a multi-stage coating method to produce a uniform surface energy on ceramics with gold or copper metallisations was developed and tested. The method is was the subject of a patent application, *Section 9.2 Appendix 2 – Patent Application*.

The Epo-Tek H20E conductive epoxy loaded with silver used in this work is used in optoelectronic assemblies to form an electrically conductive bond between components and metallisations, where solder is not a suitable alternative. It was surmised that using a surface modification technique, which introduces an intermediate organic electrically insulative layer in the bond, could cause issues with conductivity. To test for this an experiment was devised to measure the resistance on bonds formed between modified and unmodified copper coupons. A four point probe test was used to measure this to mΩ resolution. Also of interest in this experiment was the effect of roughness upon the electrical conductivity. It has been shown previously that the silver flakes in the adhesives are larger than the peak-to-peak distance of the roughness profiles of the samples used in this study. It was theorised that the flakes would not penetrate effectively into the roughness profile, reducing the contact between silver and copper and increasing the interfacial resistance. Therefore some samples were prepared with a granular surface finish simulating that of an as-fired ceramic, as well as a polished finish.

Finally octadecyltrichlorosilane monolayers are tested for their effectiveness as wetting barriers. These monolayers were applied to ceramics before being selectively removed with an oxygen plasma.

5.5.4 Materials and Methods

SAM compounds were sourced from Sigma Aldrich and Alfa Aesar and were purchased in the highest purity available, Table 5.5-1. Different chain lengths of each chemical family were purchased to allow study of the effect of chain length.

Compound	Structure	CAS number	Source	Purity
Perfluoropropionic acid	CF_3CF_2COOH	422-64-0	Sigma Aldrich	97%
Perfluorooctanoic acid	$CF_3(CF_2)_6COOH$	335-67-1	Sigma Aldrich	96%
Perfluorododecanoic acid	$CF_3(CF_2)_{10}COOH$	307-55-1	Sigma Aldrich	95%
Perfluorooctadecanoic acid	$CF_3(CF_2)_{16}COOH$	16517-11-6	Alfa Aesar	97%
Hexyltrichlorosilane	$CH_3(CH_2)_5SiCl_3$	213-178-1	Sigma Aldrich	97%
Octadecyltrichlorosilane	$CH_3(CH_2)_{17}SiCl_3$	112-04-9	Sigma Aldrich	90%
Pentanethiol	$CH_3(CH_2)_3CH_2SH$	110-66-7	Sigma Aldrich	98%
Octadecanethiol	$CH_3(CH_2)_{16}CH_2SH$	2885-00-9	Sigma Aldrich	98%

Table 5.5-1 Compounds used for SAMs, their structures and source.

The range of hypotheses tested in this section of the work required a number of different ceramic substrate types of varying surface properties. In the description of the experimental work in this chapter, substrates labelled 'commercial samples' are those which were prepared and diced by LEW Techniques (see *Section 5.1 Characterisation of Surfaces and Adhesives*). These substrates were used primarily when studying the effects of roughness. The lab prepared substrates (see *Section 5.3 Identification and Removal of Contamination*) were also used in this work and were labelled 'lab prepared'

5.5.5 Results and Discussion

The application of SAMs from solutions and the preparations of surfaces was performed according to the methods in *Section 4 Experimental Procedures*.

5.5.5.1 Characterisation of SAM Coated Ceramics

5.5.5.1.1   *Study of Chain Length*

Sample	Batch	SAM	Material	Water CA	Diiodomethane CA	SE
1	1	3	Al_2O_3	9.2	74.2	81.33
2	1	8	Al_2O_3	79.7	86.8	25.35
3	1	12	Al_2O_3	91.0	94.0	17.55
4	1	3	AlN	52.4	102.4	61.94
5	1	8	AlN	75.6	95.1	30.09
6	1	12	AlN	106.9	101.8	9.76
7	2	12	Al_2O_3	118.0	107.4	6.46
8	2	3	AlN	35.2	70.7	63.73
9	2	8	AlN	98.9	105.3	13.08
10	2	12	AlN	105.7	103.3	9.98
11	3	3	AlN	48.4	66.4	50.93
12	3	3	Al_2O_3	35.8	61.4	60.78
13	3	8	AlN	83.6	87.2	22.51
14	3	8	Al_2O_3	96.4	99.3	14.35
15	3	12	AlN	114.5	108.9	6.79
16	3	12	Al_2O_3	103.1	111.5	11.08
17	4	18	Al_2O_3	112.4	107.8	7.42
18	4	18	Al_2O_3	121.4	113.1	5.00
19	4	18	AlN	122.1	110.8	5.35
20	4	18	AlN	122.2	111.4	5.22

Table 5.5-2 Initial contact angle measurements of carboxylic acid coated aluminium oxide and aluminium nitride, where CA is contact angle in degrees and SE is surface energy in mJ/m^2. SAM refers to the carbon chain length where 3 is perfluoropropionic acid, 8 is perfluorooctanoic acid, 12 is perfluorododecanoic acid and 18 is perfluorooctadecanoic acid. The batches were prepared on separate days.

Table 5.5-2 shows the results of contact angle measurements on fluorinated carboxylic acid coatings on aluminium nitride and aluminium oxide. Each batch was prepared separately on different days to test for preparation sensitivity. All samples were tested following coating within 2 hours of coating completion.

It can be seen from Table 5.5-2 that perfluoropropionic acid (chain length 3) does not yield consistent performance on either of the ceramic surfaces. The SAMs do appear to be more oleophobic than hydrophobic, suggesting modifications affected the dispersive component of surface energy whilst leaving the polar component relatively unchanged (e.g. for sample 1 the values are 6.55 and 75.08mJ/m^2 for the dispersive and polar components of surface energy respectively). The reasons for this are not apparent. However, the lack of hydrophobicity means the coating would not be fully effective for prevention of epoxy bleed unless the bleed material is highly non-polar.

Coatings of perfluorooctanoic acid (chain length 8), samples 2, 5, 9, 13 and 14 show a range of values for apparent surface free energy from 13.08mJ/m^2 to 30.09mJ/m^2 which are independent of the bulk substrate material. This result shows that the fatty acid molecules do indeed chemisorb onto hydroxylated aluminium nitride probably due to the native aluminium oxide layer. The range of values measured for perfluorooctanoic acid means that consistency in controlling epoxy bleed could be an issue as one of the measurements lies outside the safe surface energy of 30mJ/m^2. However, the two highest values of surface energy for this SAM were exhibited by samples 2 and 5, both of which are from batch one. One explanation of the variation observed is that there was a particular problem with this batch caused by lack of experience with the application method or human error contributing to a lesser quality coating. This suggestion is made more likely by the fact that the surface energy obtained for sample 3 of batch 1 was the highest seen for perfluorododecanoic acid, at 17.55mJ/m^2.

The contact angles measured were yet higher (>100° for water, excluding batch 1), and the values more consistent batch to batch, for perfluorododecanoic acid (12 carbon chain). Surface heterogeneity therefore seems to affect the longer chain molecules less, possibly because they are able to extend across surface sites where there is no SAM attachment. Defects are extremely difficult to avoid in any SAM, however longer chain molecules seem to be more effective coatings when defects are present, this view is also supported by the literature[25].

Such defects may be related to the contamination previously seen by XPS on cleaned samples consisting of quantities of contamination in the form of group 1 and 2 metals and organic contaminants, see *Section 5.3 Identification and Removal of Contamination*. Whilst it is likely that the SAM bonding displaces some weakly physisorbed organic contaminants, the XPS results reported in *Section 5.3* suggest that plasma cleaning might encourage chemisorption of organics so that some contamination would not be displaced, and the SAM would consequently be expected not to bond or bond weakly. Group 1 and 2 metals would also interrupt the uniformity of the coating because of the associated presence of other metal oxides or other

metal species could create sites which are incompatible with the fatty acid group. Increasing the chain length again, with perfluorooctadecanoic acid (chain length 18), results in increased contact angles, decreased surface energy and a further increase in batch to batch reproducibility of hydrophobicity and oleophobicity. From the point of view of bleed resistance, both perfluorododecanoic acid and perfluorooctadecanoic acid produce modified surfaces of sufficiently low apparent surface energy, with great enough consistency, to be potential candidates for use in manufacture.
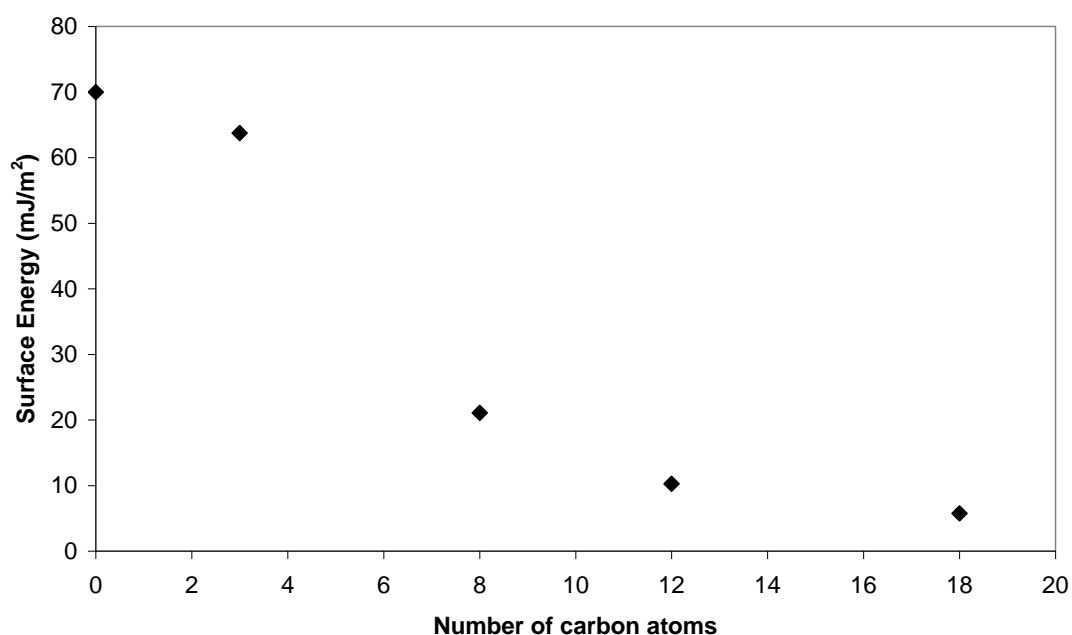
Figure 5.5-2 Graph showing the relationship between fatty acid SAM molecule chain length and average apparent surface energy.

Figure 5.5-2 shows the relationship between the carbon molecular chain length and the average measured apparent surface free energy. It can be seen that longer chain molecules are more effective at reducing the surface energy. Whilst it has been shown in the literature[16] that monolayer chain length below can affect its contact angle only below 8 carbon atom chain. The current study shows a continued decrease of surface energy with increasing carbon chain length >8. However, the study in the literature was for thiols on gold surfaces, and monolayers of other types might show different properties. In the current study using fatty acid monolayers on commercial aluminium oxide and aluminium nitride, the best explanation for the observed results appears to be defects and the ability for longer chain molecules to protect these defects from penetration of the probe liquids.

Figure 5.5-3 shows the region near the carbon response peak of an XPS spectrum for perfluorooctadecanoic acid on aluminium oxide. Two peaks can clearly be seen which correspond to C1s and CF_2[26]. Although a peak for CF_3 would also be expected in the spectrum at ~293eV[27], it may either be hidden by the noise in the signal or the CF_3 fraction present in the sample may have been reduced due to the sensitivity to damage of fluorinated polymeric materials to X-rays[28]. The bond area ratio of the CF_2 to the C1s peak is approximately 48:52 which favours the C1s peak more than expected. This suggests that organic contaminants may still be present in high quantities on the surface, as a signal primarily from CF_2 with trace COOR and CF_3 would be expected from a uniformly coated surface[29].
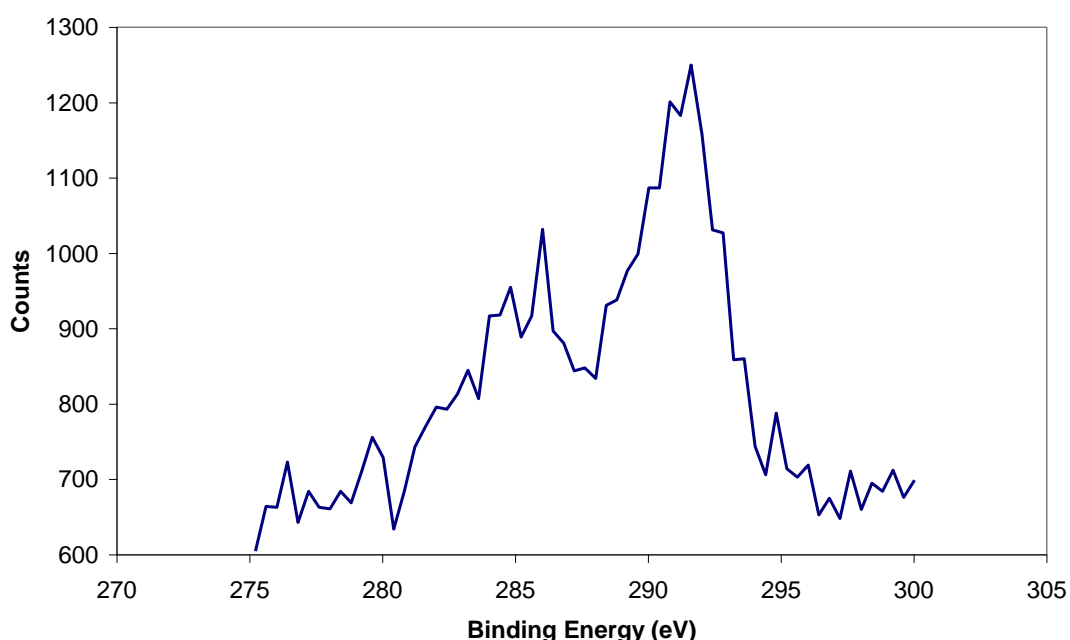
Figure 5.5-3 XPS carbon peak area for aluminium oxide coated with perfluorooctadecanoic acid.

5.5.5.1.2   Study of Roughness
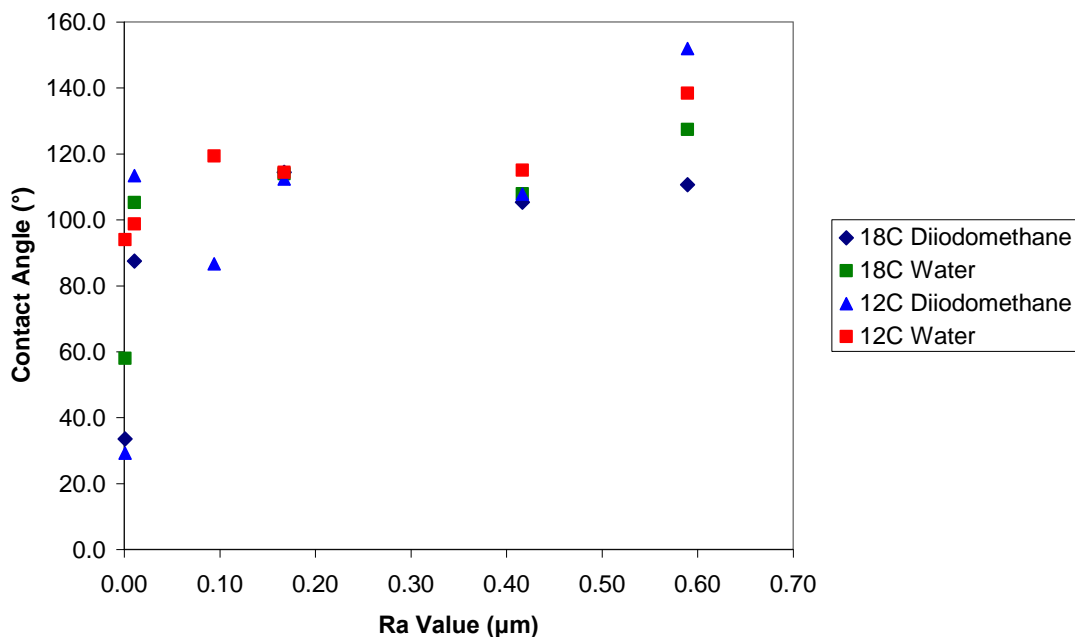
Figure 5.5-4 Contact angle data for perfluorooctadecanoic acid (18 carbon chain) and perfluorododecanoic acid (12 carbon chain) coated commercial samples.

Figure 5.5-4 shows the contact angle data for commercial samples coated with fluorinated fatty acid monolayers. The roughness values are from the AFM measurements reported in *Section 5.1.4.3 Surface Texture Parameter Measurement*.

It can be seen from the figure that there is a general trend for roughness to increase contact angles of both liquids, and as a result of this the calculations of surface energy are also lower. Sample 9, (polished Al_2O_3), exhibited consistently lower contact angles. It was thought this may be a side effect of polishing induced surface damage. However, as sample 3 (polished AlN) did not show the same effect, and the exact processing of sample 9 was not known, and given that only this sample produced this effect, it was considered unnecessary to explore this any further.
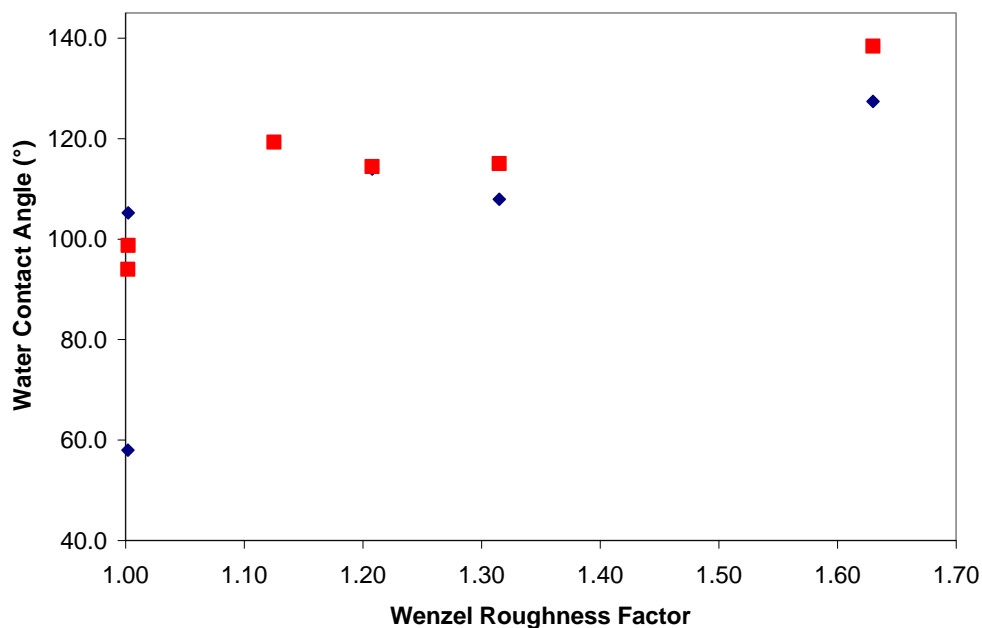
Figure 5.5-5 Plot of water contact angles against AFM Wenzel Roughness Factor value for perfluorooctadecanoic acid (18C chain) and perfluorododecanoic acid (12C chain) coated commercial aluminium oxide and aluminium nitride samples.

Figure 5.5-5 shows the general trend for the water contact angle to increase is also there when the Wenzel roughness factor is used as a measure of roughness. This correlation was also seen for diiodomethane contact angles with both roughness parameters.
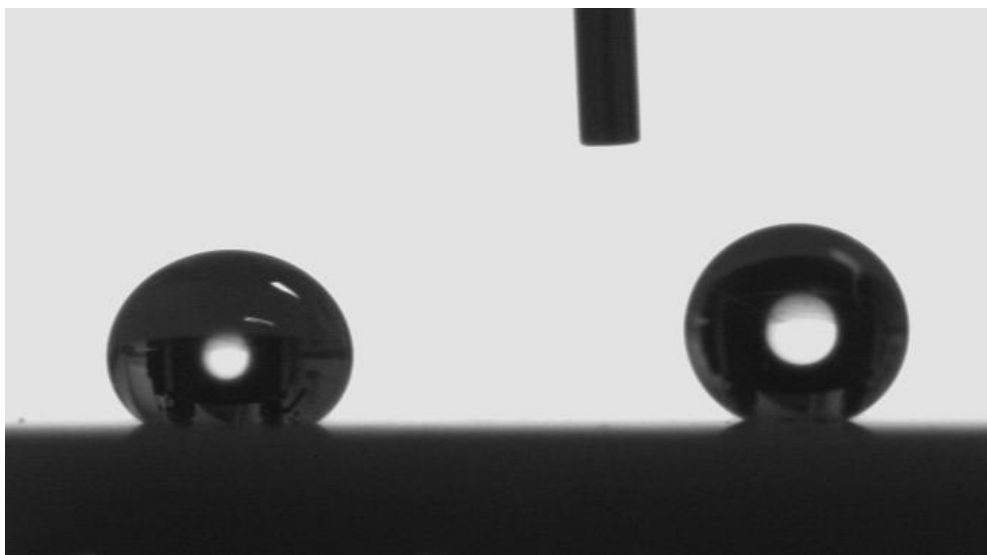
Figure 5.5-6 Water (right) and diiodomethane (left) droplets on a perfluorododecanoic acid treated AlN surface with high roughness R_a 0.589μm. Contact angles for both liquids >140°, sample surface energy 0.9mJ/m^2.

Figure 5.5-6 above demonstrates the hydrophobicity and oleophobicity of a perfluorododecanoic acid modified surface. The contact angles shown are

both in excess of 140°, and the effective surface energy calculated from the contact angles was 0.9mJ/m^2. The high contact angles are due to the combined effect of the SAM coating and of the high roughness of the sample.

Results such as this caused concern for the magnitude of the adhesion strengths which might be expected to be obtained for joints formed on fatty acid SAM treated surfaces. since it is generally accepted that good wetting is imperative for good adhesion[30].

5.5.5.1.3   *Adhesive Joint Strength Testing*
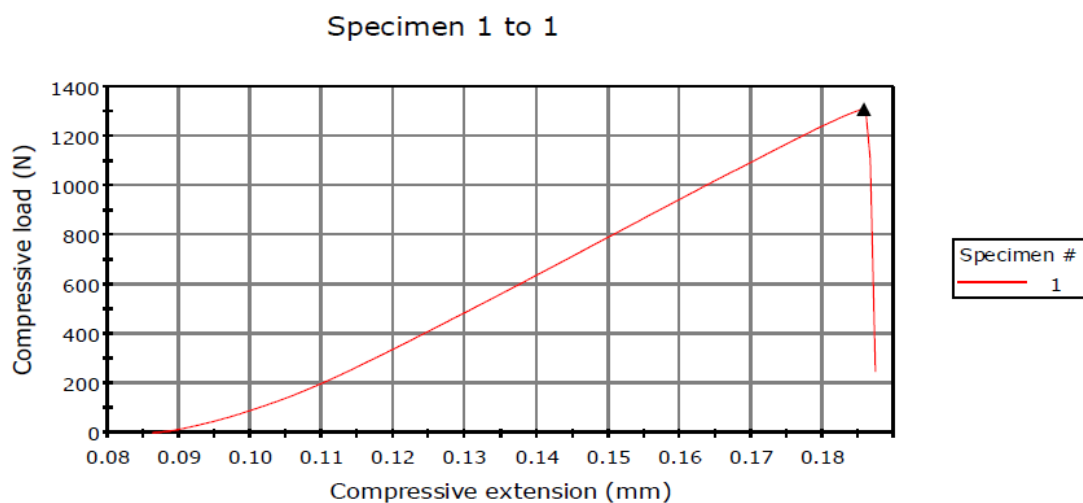
Figure 5.5-7 Tensile testing curve for perfluorododecanoic acid coated sample 1. Single lap shear joint bonded with home made adhesive.
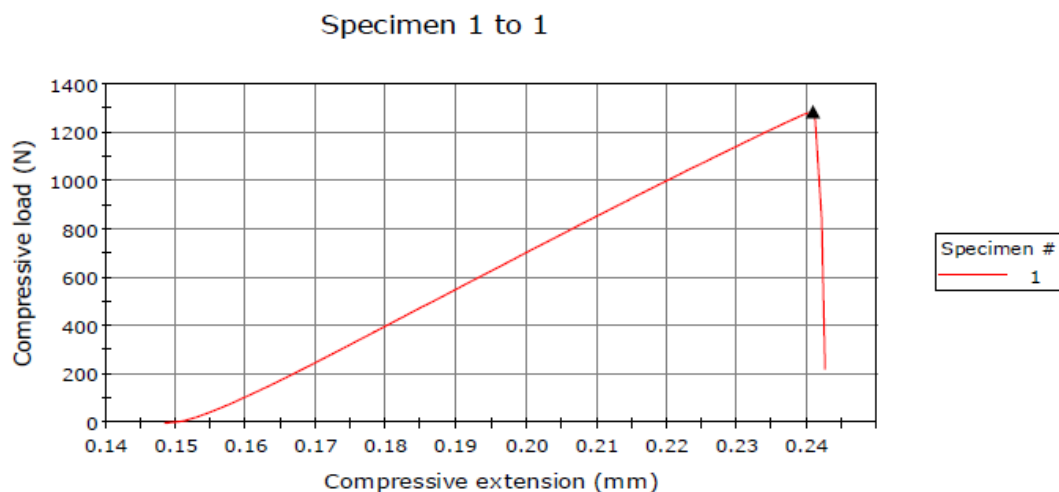
Figure 5.5-8 Tensile testing curve for perfluorooctadecanoic acid coated sample 3. Single lap shear joint bonded with the home made adhesive.

Single lap shear joints were prepared and tested until failure according to the methods given in *Section 4.11 Tensile Testing.* Joints were prepared with

both commercial adhesives and the home made adhesive, with commercial ceramic samples and with the lab prepared samples. The home made adhesive was used to avoid the filler material inducing cohesive failure in lap joints, as observed in *Section 5.2.4.2 Bond Strength Analysis*. Surprisingly in view of the low surface energies, cohesive failure was observed for all the samples tested. In addition the chain length of self assembled monolayer used had no effect on adhesion strength, and neither did roughness. This was not expected as it appears to contradict adhesion theory[31]. Figure 5.5-7 and Figure 5.5-8 show some representative results from the tensile testing investigation. It is clear that extremely strong bonds are formed between samples which have an effective surface energy lower than 13.9mJ/m^2. Bond areas were in the region of 16mm^2 and load-at-failure >1200N, giving breaking shear stresses >75N/mm^2. This is more than the observed 60N/mm^2 of the as-received samples and the unfilled adhesive seen previously. Thus it appears use of the fatty acid SAMs allows surface energy to be reduced with no detrimental affect on adhesion. The reasons for this are explored in *Section 5.5.5.5 Adhesive Wetting on SAM Coated Ceramics below*.

5.5.5.1.4 Epoxy Bleed Control

Epoxy bleed was measured on fatty acid (carbon chain lengths 3, 8, 12 and 18) coated surfaces using the adhesives H20E, 930-4 and the home made adhesive, using the method described in 4.13 Epoxy Bleed Measurements. In contrast to the previous results, *Section 5.2.4.3 Epoxy Bleed*, the 930-4 boron nitride filled adhesive was not seen to bleed a greater distance than the other adhesives. The adhesive bleed distance was found to be determined by the substrate modification and not the adhesive. Figure 5.5-9 below shows the results of the epoxy bleed measurements on different fluorinated fatty acid SAM coated Al$_2$O$_3$ lab prepared samples, with boron nitride filled 930-4 adhesive.
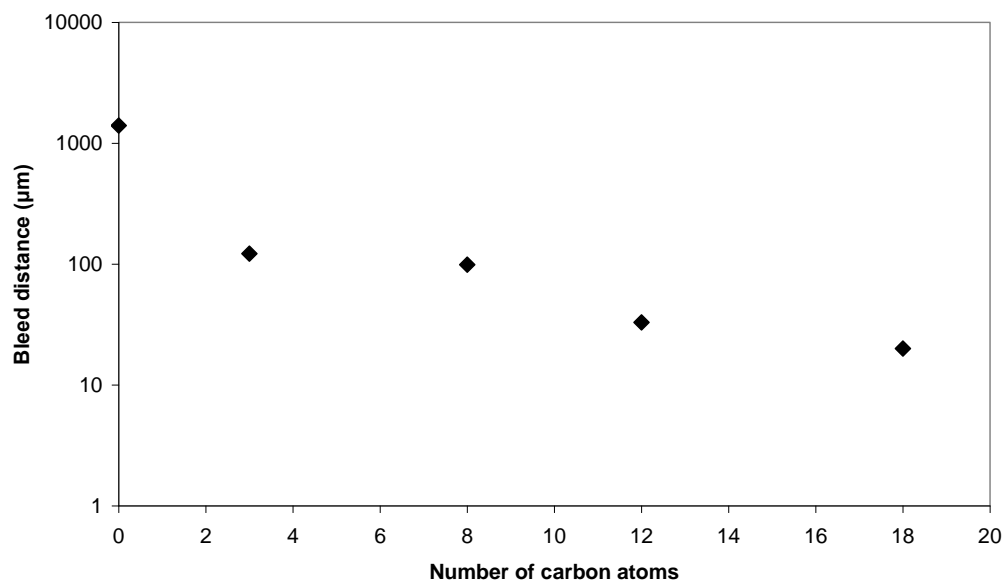
Figure 5.5-9 Graph showing the relationship between the chain length of a fluorinated fatty acid SAM and the maximum bleed distance (930-4 epoxy) witnessed following coating, application of adhesive and curing.

The coatings are highly effective at reducing bleed with a maximum reduction from 1400 microns to 25 microns, which was seen with the longest chain SAM. It is clear from Figure 5.5-9 that a longer chain molecule used for the SAM will reduce bleed more effectively than a SAM prepared from a shorter chain. This is probably due to the defect related mechanism discussed in *Section 5.5.5.1.1 Study of Chain Length*.
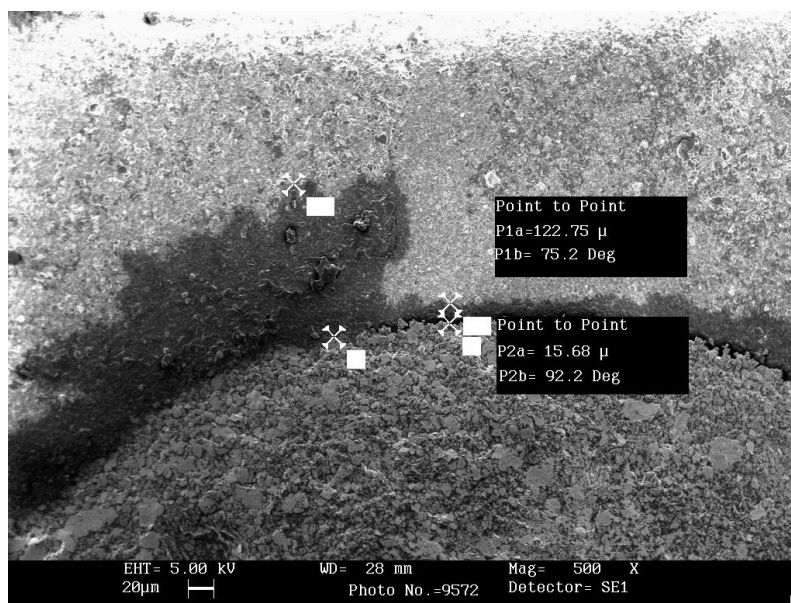
Figure 5.5-10 SEM image of epoxy bleed from silver filled epoxy (H20E) on a perfluoropropionic acid coated aluminium nitride surface.

Figure 5.5-10 shows an SEM image of epoxy bleed from H20E (silver filled) adhesive on a CF$_3$CF$_2$COOH (perfluoropropionic acid) modified aluminium nitride surface. It is clear that while the very short chain coating has not completely stopped bleed, it has reduced it markedly from the distance spread on an unmodified surface. Table 5.5-3 shows that the perfluoropropionic acid coating reduced mainly the dispersive component of surface energy. Thus the reduction in the epoxy bleed distance as a result of the perfluoropropionic acid modification would suggest that the bleed material is largely non-polar.
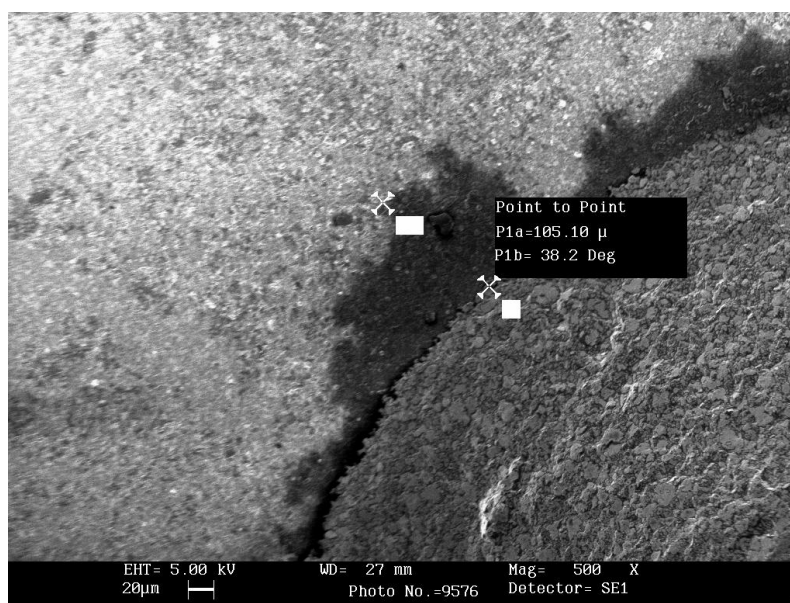
Figure 5.5-11 SEM image of epoxy bleed from silver filled epoxy (H20E) on a perfluorooctanoic acid coated aluminium nitride surface.

Figure 5.5-11 shows the maximum epoxy bleed distance from silver filled (H20E) adhesive is slightly less with the longer perfluorooctanoic acid (8 carbon atoms) (105μm) than with perfluoropropionic acid (3 carbon atoms) (122μm). This is consistent with the surface energy measurements obtained with the two modifications. Figure 5.5-12 shows the correlation between the dispersive component of apparent surface energy and the distance epoxy bleed has spread. There is also a correlation seen between bleed distance and the polar component of surface energy for the SAM coated surfaces. However, unlike for the dispersive component, the bleed distance does not tend towards that for an untreated surface with reducing chain length (increasing SE). It is unclear why this should be the case. This relationship

208

between bleed and the dispersive component of surface energy has been seen on unmodified ceramic surfaces in *Section 5.2.4.3 Epoxy Bleed*.

SAM	Polar SE	Dispersive SE
3	54.8	9.0
8	14.9	6.1
12	5.3	5.0
18	1.5	4.3

Table 5.5-3 Mean dispersive and polar components contributions to total surface energy of SAM modified ceramics where SAM number refers to carbon chain length of fatty acid. Polar SE is the polar component of surface energy (mJ/m^2) and dispersive SE is the dispersive component of surface energy (mJ/m^2).
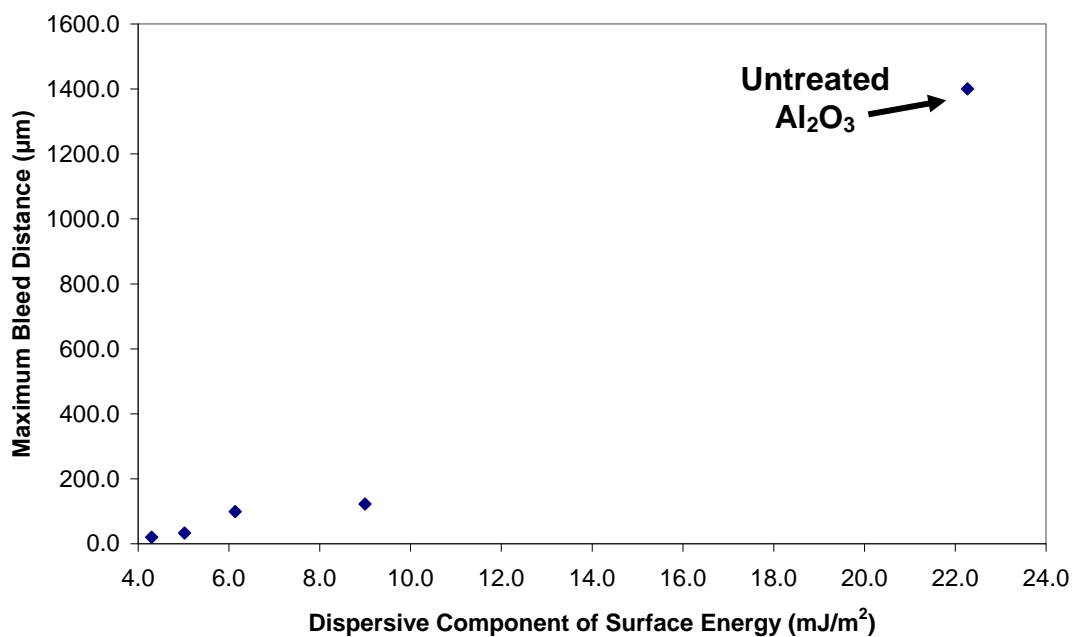
Figure 5.5-12 Plot of dispersive component of apparent surface energy against maximum epoxy bleed distance for fatty acid SAM modified surfaces, and an untreated surface.
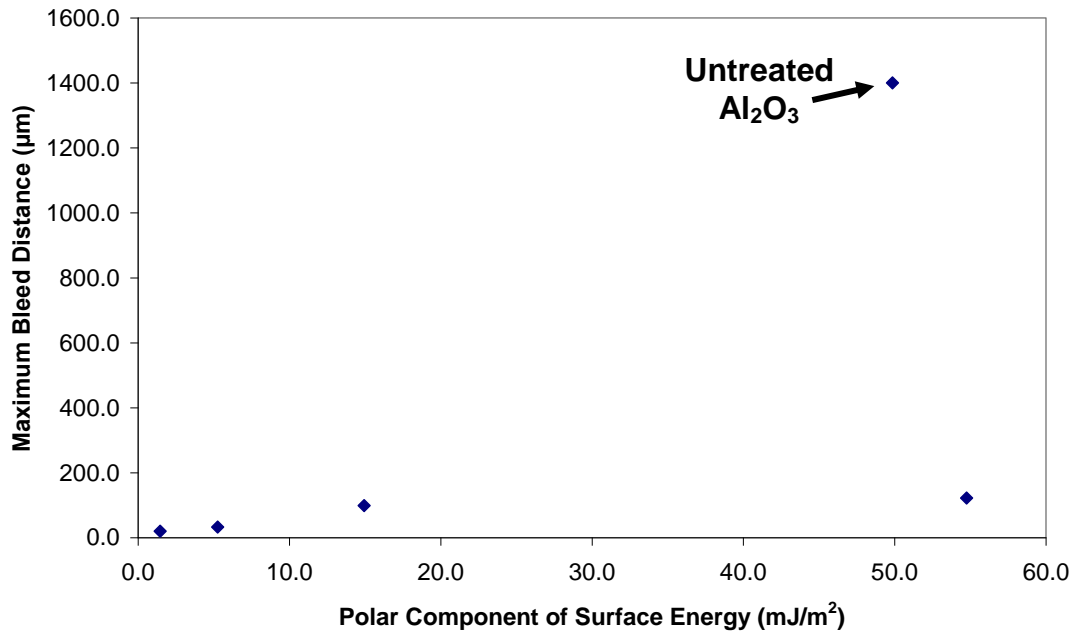
Figure 5.5-13 Plot of polar component of apparent surface energy against maximum epoxy bleed distance for fatty acid SAM modified surfaces, and untreated surface.
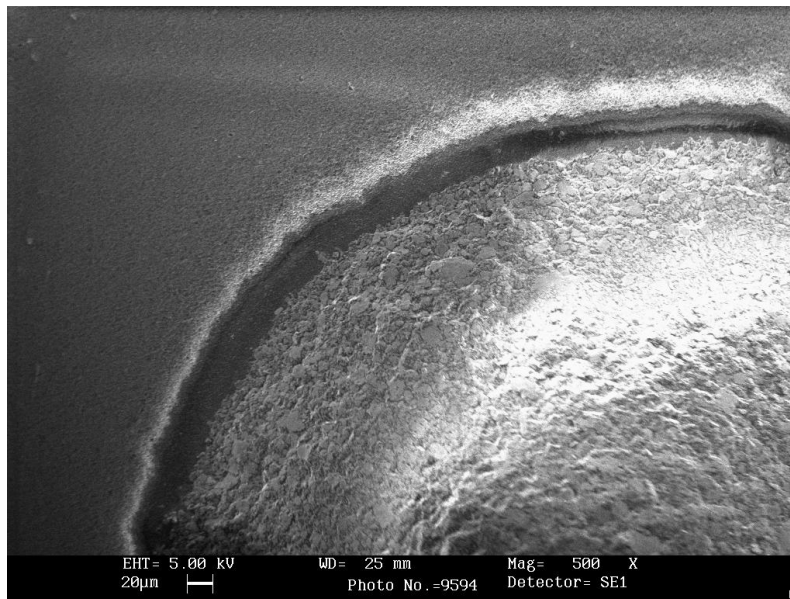
Figure 5.5-14 SEM image of epoxy bleed from silver filled epoxy (H20E) on a perfluorododecanoic acid coated aluminium nitride surface.
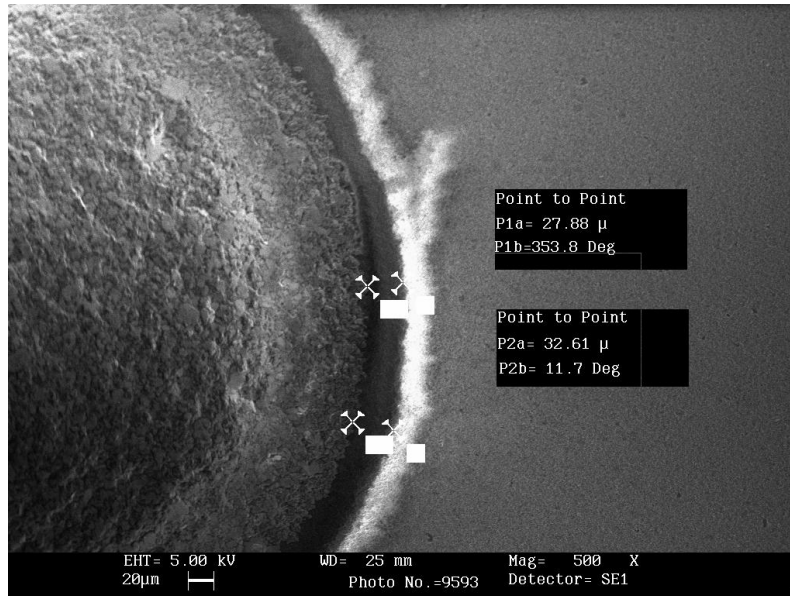
Figure 5.5-15 SEM image of epoxy bleed from silver filled epoxy (H20E) on a perfluorododecanoic acid coated aluminium oxide surface.

Figure 5.5-14 and Figure 5.5-15 show the more consistent performance of the higher chain length SAM (perfluorododecanoic acid, 12 carbon atoms) at inhibiting epoxy bleed, when compared with Figure 5.5-10 and Figure 5.5-11 for the short chain SAM coatings. For the short chain coatings although the majority of the circumference of the adhesive spot shows limited bleed of ~30µm, there were discrete areas where bleed occurred to an unacceptable amount of >100µm. The longer chain SAMs, whilst not stopping bleed completely, demonstrate higher consistency at repelling the bleed (~30µm halo for perfluorododecanoic acid, ~20µm halo for perfluorooctadecanoic acid) with no discrete areas of more extensive bleed. The more constant bleed distance around the circumference suggests enhanced homogeneity of the coating over the shorter chain molecules. This result supports the previous conclusion that the lower surface energy achieved with longer chain length is due to enhanced homogeneity in the structure of the SAM, and not a direct effect of the chain length itself.

It can be also be seen that the substrate bulk material does not have an effect on the bleed distance, with similar results produced for both AlN and Al_2O_3.

The discussion above has treated the occurrence of epoxy bleed as an expected result. In fact it is unexpected that a liquid with a surface tension above 10mN/m should spread over surfaces with such low apparent surface

energies, <1mJ/m^2 for sample 7 treated with perfluorododecanoic acid and consistently < 6mJ/m^2 for samples treated with perfluorooctadecanoic acid.

5.5.5.2 Stability of SAMs Over Time

Figure 5.5-16 shows the water contact angle measurements for aluminium oxide and aluminium nitride coated with three different fatty acid monolayers at differing lengths of time after preparation.

It is clear from the data that the monolayers formed by perfluoropropionic acid (chain length 3) are not stable and homogenous. There is extremely large variation between sample sets with no general trend. Therefore this SAM should be ruled out as a potential solution to epoxy bleed because it fails to provide any of the properties required. The perfluorooctanoic acid and perfluorododecanoic acid show a general trend for increasing contact angle over the first 48 hours which then stabilises, and remains stable to the end of the experiment at 28 days.
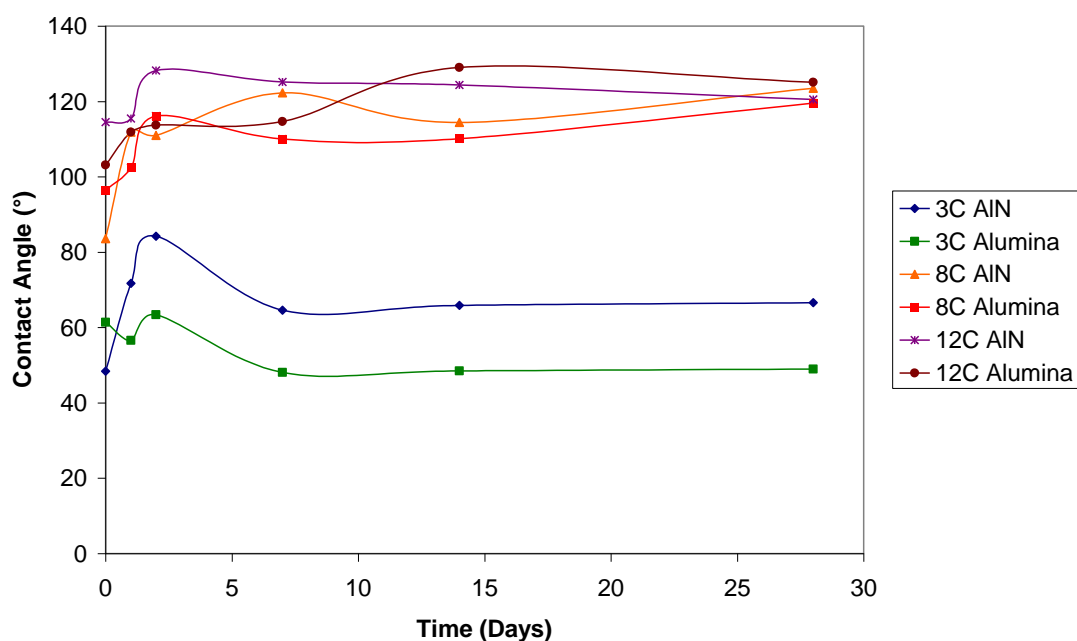
Figure 5.5-16 Plot of the change in water contact angles for perfluoropropionic acid (3C), perfluorooctanoic acid (8C) and perfluorododecanoic acid (12C) coated aluminium nitride and aluminium oxide over 28 days.

It is possible that the increase in contact angle is due to contaminants adsorbing. However, this would only account for a small increase since the absorption rates are small (as measured with tin foil wrapped samples in *Section 5.3 Identification and Removal of Contamination*). It seems that

increased ordering of the SAMs in the time after application is more likely to be the cause. The increased water and diiodomethane contact angles would be due to their increased exposure to CF_3 groups as the chains become more ordered and the CF_2 backbone is less exposed.

The results suggest that in industrial use the SAMs should consistently repel bleed up to and exceeding 28 days after application of the monolayer. Tests with the commercial and home made adhesives confirmed that the coatings were equally as effective at inhibiting bleed after 28 days as they have been shown to be immediately after application.

5.5.5.3 Thiol Coating of Copper

Gold is a frequently used top layer metallisation material for interconnects in optoelectronic assemblies. As explained previously, copper is used in this work as a cheap substitute for gold.

Octadecanethiol was chosen as a copper coating agent as extensive work has been done with this particular SAM, and it was known to be stable and durable. Copper samples were first polished, mounted and etched. Octadecanethiol SAMs were then applied using the methods outlined in *Section 4 Experimental Procedures*. Pentanethiol was also tested in the same experiments so the effect of chain length could be probed.

The octadecanethiol coated samples yielded mean contact angles of 126.6° and 96.3° for water and diiodomethane. These values equate to an apparent surface energy of 11.04mJ/m^2 which was lower than reported in the literature[20], and were regarded as indicating an acceptable quality of coating. The mean pentanethiol contact angles were 105.9° and 65.4° which were equivalent to an apparent surface energy of 26.36mJ/m^2.

Epoxy bleed measurements were also made for copper using the same method as with the fatty acid monolayers. It was found that epoxy bleed was controlled to within 25µm of the edge of the droplet with an octadecanethiol self assembled monolayer, and 40µm of the edge of the droplet with pentanethiol. The effect of roughness seen with untreated copper, *Section 5.2.4.3.2 Copper*, was not seen with monolayer treated copper, i.e. the bleed material did not spread along the scratches.

Lap shear joints were prepared between copper coupons as described in *Section 4.2 Copper Surface Preparations*. Unlike the fatty acid monolayers, a change in shear strength was seen between treated and untreated surfaces. In addition there was an effect of chain length.
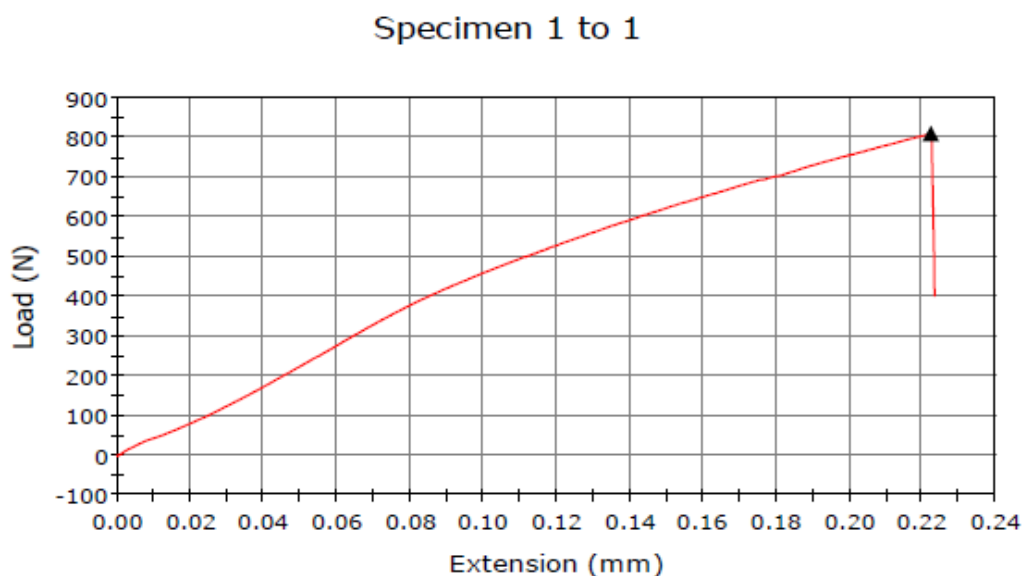
Figure 5.5-17 Load vs. extension plot for pentanethiol coated copper single lap joint prepared with home made adhesive, showing a breaking shear force of 808.82N.
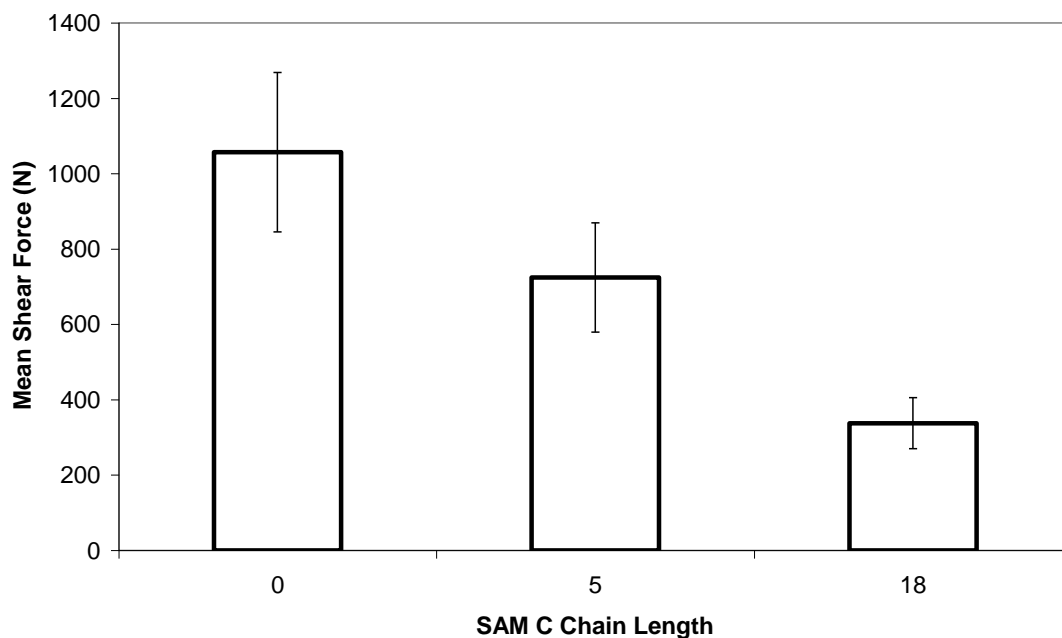
Figure 5.5-18 Chart to show the effect of SAM chain length upon mean breaking shear force of copper lap joint samples prepared with home made adhesive. Chain length 5 denotes pentanethiol and 18 octadecanethiol treatment.

214

Figure 5.5-17 shows a typical force versus extension plot for a bond prepared with the home-made adhesive between two copper coupons both coated with pentanethiol. It can be seen in Figure 5.5-18 that the breaking shear force is on average (at least 5 joints prepared for each condition) 30% weaker than a bond produced from untreated copper pieces with the same adhesive. Unlike with the fatty acid monolayers, this result is consistent with the measured surface energy changes. Figure 5.5-19 shows the 90° wetting envelope for a copper surface modified with pentanethiol. It can be seen that there is only a small range of tensions over which the contact angle of the adhesive on the surface would be expected to be <90°. Only if the surface tension components of the adhesive fall within this region would it be expected that the SAM would cause no reduction in shear force. In fact it is probable that the actual adhesive properties lie slightly outside of the wetting envelope for this coating, consistent with the measured adhesion strength being 30% lower. This conclusion suggests that the adhesive has predominantly dispersive components of surface tension, for if this were not the case no reduction in breaking shear stress should be seen as the point on Figure 5.5-19 corresponding to the adhesive properties would then lay far outside of the 90° wetting envelope. However, this assumption is supported by evidence from the epoxy bleed measurements.

Figure 5.5-20 shows the wetting envelope for octadecanethiol coated copper. It can be seen that not only is there no intersection between the adhesive properties line and the wetting envelope, but also that the lines do not even pass close to each other. This is consistent with the reduced adhesion strength over the pentanethiol in Figure 5.5-18.
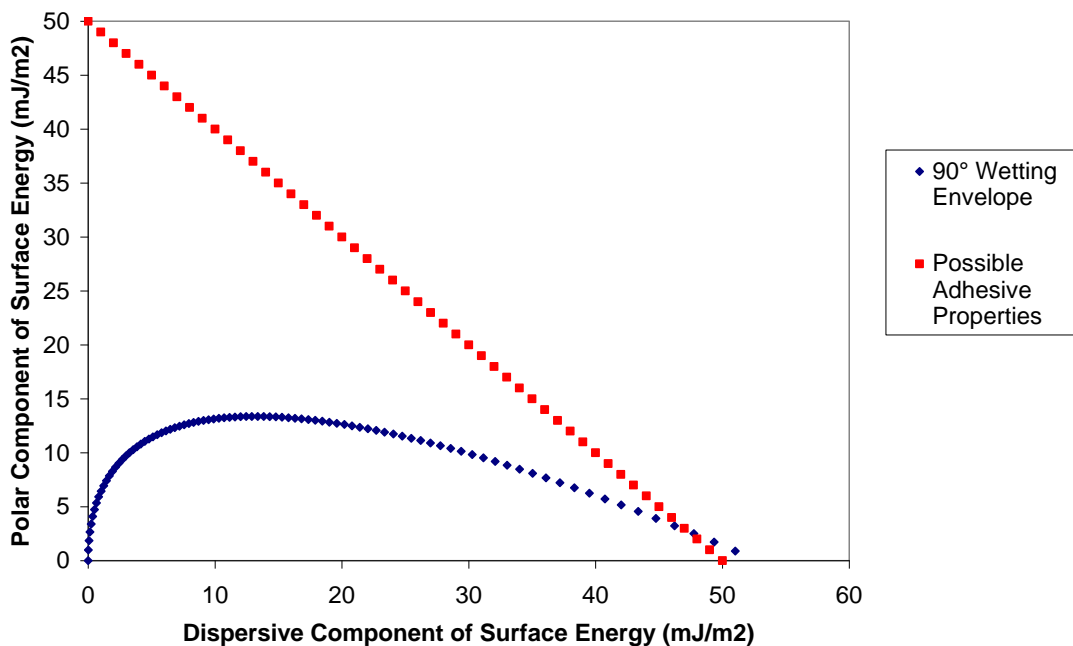
Figure 5.5-19 90° wetting envelope for a copper sample modified with pentanethiol with a plot for the possible adhesive properties of the home made adhesive (of total surface tension 50.09mN/m)
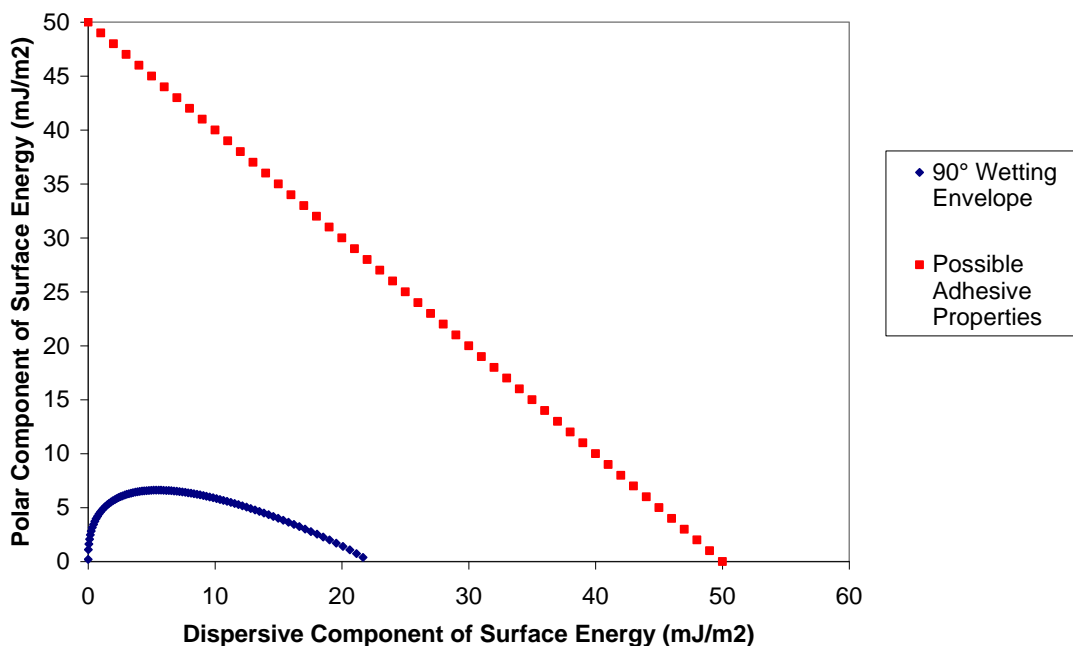
Figure 5.5-20 90° wetting envelope for a copper sample modified with octadecanethiol with a plot for the possible adhesive properties of the home made adhesive (of total surface tension 50.09mN/m)

Finally the stability of the surface energy of the coatings over time was determined. Figure 5.5-21 shows that unlike the fatty acid monolayers, octadecanethiol has a slight trend for the increase of surface energy over time. This is likely due to the penetration of oxygen through the monolayer[4]

and oxidation of the underlying copper, weakening the crystallinity of the coating and the homogeneity seen by the test liquids.
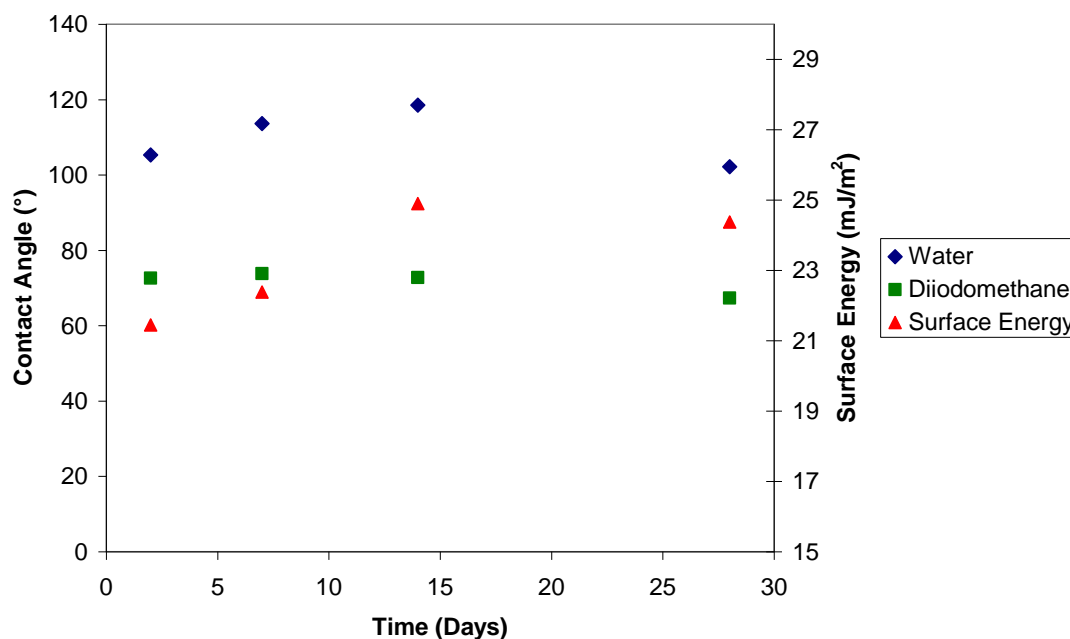
Figure 5.5-21 Results of storage contact angle experiment on thiol treated copper.

5.5.5.4 OTS Coating of Ceramics

A similar series of experiments was undertaken with octadecyltrichlorosilane (chain length 18) and hexyltrichlorosilane (chain length 6) as with the thiols. The data for the contact angle and surface energy properties of the surfaces is given in Table 5.5-4. Interestingly lower dispersive components of surface energy are seen for hexyltrichlorosilane than octadecyltrichlorosilane, this trend was not seen with other SAM types. The lower dispersive component of surface energy translates into a lower calculated surface energy. However the hexyltrichlorosilane does show a lower hydrophobicity than the octadecyltrichlorosilane.

SAM	Material	Water CA	Diiodomethane CA	Pol	Disp	SE
18	AlN	110.7	84.3	0.31	14.88	15.19
18	Al_2O_3	115.7	84.2	0.00	15.91	15.91
6	AlN	98.1	89.7	5.03	9.77	14.79
6	Al_2O_3	100.6	88.1	3.51	10.98	14.48

Table 5.5-4 Contact angle and surface energy data for silane modified aluminium oxide and aluminium nitride where CA is contact angle in °, Pol is polar component of surface energy in mJ/m^2, Disp is dispersive component of surface energy in mJ/m^2 and SE is total surface

energy in mJ/m^2, those labelled 18 are octadecyltrichlorosilane (18 C chain) treated samples and those labelled 6 are hexyltrichlorosilane (6 C chain) treated samples.

For the first time in this work epoxy bleed was seen to be completely eradicated by the treatments. No visible bleed was present with the home made adhesive or either of the two commercial adhesives. The reason for this is investigated in *Section 5.5.5.5 Adhesive Wetting on SAM Coated Ceramics*.

Coating	Home Made	BN	Sil
6	327.96	350.47	80.97
18	120.345	59.68	6.89

Table 5.5-5 Mean breaking shear force (in N) data for octadecyltrichlorosilane (18 C chain) and hexyltrichlorosilane (6 C chain) with home made adhesive boron nitride filled adhesive (BN) and silver filled adhesive (Sil).

Table 5.5-5 shows the breaking shear force data for single lap shear joints prepared between the different adhesives and the ceramic adherends. For the home made adhesive both of the coatings show a large decrease from the untreated surface breaking shear force of 714N. However, unlike with the thiols, no correlation is seen between surface energy and breaking shear force. But there is a correlation with chain length.
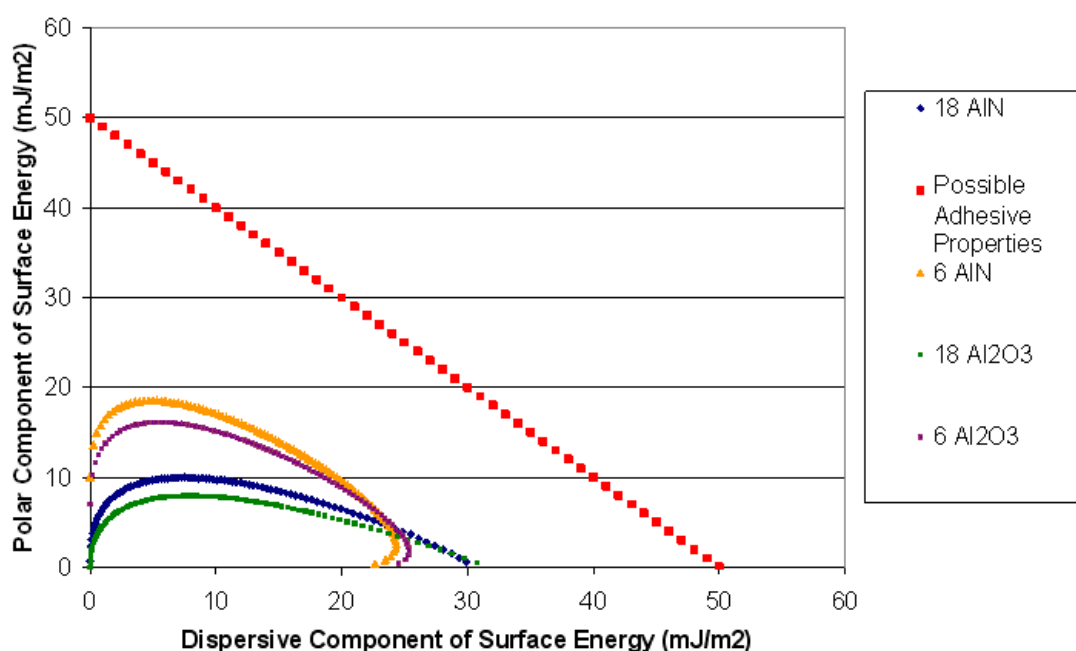
Figure 5.5-22 Plot of 90° contact angles for octadecyltrichlorosilane modified surfaces (labelled 18) and hexyltrichlorosilane modified surfaces (labelled 6). Linear line represents possible adhesive properties for the home made adhesive with a surface tension of 50.09mN/m.

Figure 5.5-22 shows the 90° wetting envelopes for the two different silane coatings on the two different materials. It is clear that all samples would be expected to give a contact angle >90° consistent with the observed reduction

in shear force over an untreated surface. However, despite the similar surface energies calculated for the two coatings the joints prepared with octadecyltrichlorosilane and hexyltrichlorosilane fail at different shear forces. The reason for this is explored in *Section 5.5.5.5 Adhesive Wetting on SAM Coated Ceramics*.

The stability of the silane monolayers was studied as with the fatty acid SAMs and thiol SAMs. Table 5.5-6 and Table 5.5-7 show that there was some variability over time, but no general trends of increasing or decreasing contact angles or surface energy are seen. The coatings were stable up to 28 days, and bleed measurement performed at 28 days continued to yield a zero bleed distance.

Time (days)	Water CA	Diiodomethane CA	SE
2	128.9	89.4	15.91
7	138.7	72.0	36.15
14	141.6	95.6	15.75
28	130.4	95.9	12.11

Table 5.5-6 Results of storage contact angle experiment on octadecyltrichlorosilane treated AlN where CA is contact angle in ° and SE is apparent surface energy in mJ/m^2.

Time (days)	Water CA	Diiodomethane CA	SE
2	132.2	89.5	16.93
7	129.1	85.0	19.28
14	130.5	93.1	13.93
28	133.3	93.8	14.26

Table 5.5-7 Results of storage contact angle experiment on octadecyltrichlorosilane treated Al$_2$O$_3$ where CA is contact angle in ° and SE is apparent surface energy in mJ/m^2.

5.5.5.5 Adhesive Wetting on SAM Coated Ceramics

In the work reported in this section the reasons for the discrepancies observed between surface wetting measurements and adhesive behaviour for the fatty acid SAMs were explored. In particular the dynamic wetting behaviour of the adhesives was studied to see if the adhesive contact angles could be correlated with shear force data, even though contact angle measurements with water and diiodomethane could not.

One of the simplest explanations for the behaviour of the adhesive was that under cure conditions at 150°C the fatty acid coatings undergo a breakdown which allows the adhesive to adhere to the underlying ceramic. To test this hypothesis ceramics were coated with fatty acid monolayers and then

underwent a typical temperature treatment for adhesive cure, 150°C for 30 minutes.

SAM	Material	Water CA	Diiodomethane CA	SE
3	Al_2O_3	78.9	64	29.31
3	AlN	55.9	69.4	44.59
Mean 3	Both	36.2	75.02	63.7
8	Al_2O_3	99.2	81.5	17.01
8	AlN	105.2	81.4	16.54
Mean 8	Both	86.8	94.7	21.1
12	Al_2O_3	133.6	115.2	4.24
12	AlN	128	112.4	4.79
Mean 12	Both	106.5	104.5	10.3

Table 5.5-8 Surface energy and contact angle data for perfluoropropionic acid (3 C chain), perfluorooctanoic acid (8 C chain) and perfluorododecanoic acid (12 C chain) coated AlN and Al_2O_3 surfaces following an adhesive cure schedule of 150°C for 30 minutes. Where CA is contact angle in ° and SE is apparent surface energy in mJ/m^2. Those labelled 'Mean' are mean values from the original treatments which were not heat treated, included for comparison.

Table 5.5-8 shows that the coatings are stable after exposure to elevated temperatures. The water and diiodomethane contact angles are similar to those measured when no thermal treatment was applied, Table 5.5-2. These measurements suggest that the unexplained bond strength is not due to thermal breakdown of the coating.

Using the contact angle goniometer, *Section 4.4 Contact Angle*, time resolved measurement of the contact angles of the adhesives on the fatty acid modified surfaces was attempted. This was found to be problematic with the silver adhesive due to its thixotropic nature and resistance to forming an equilibrium sessile drop shape.
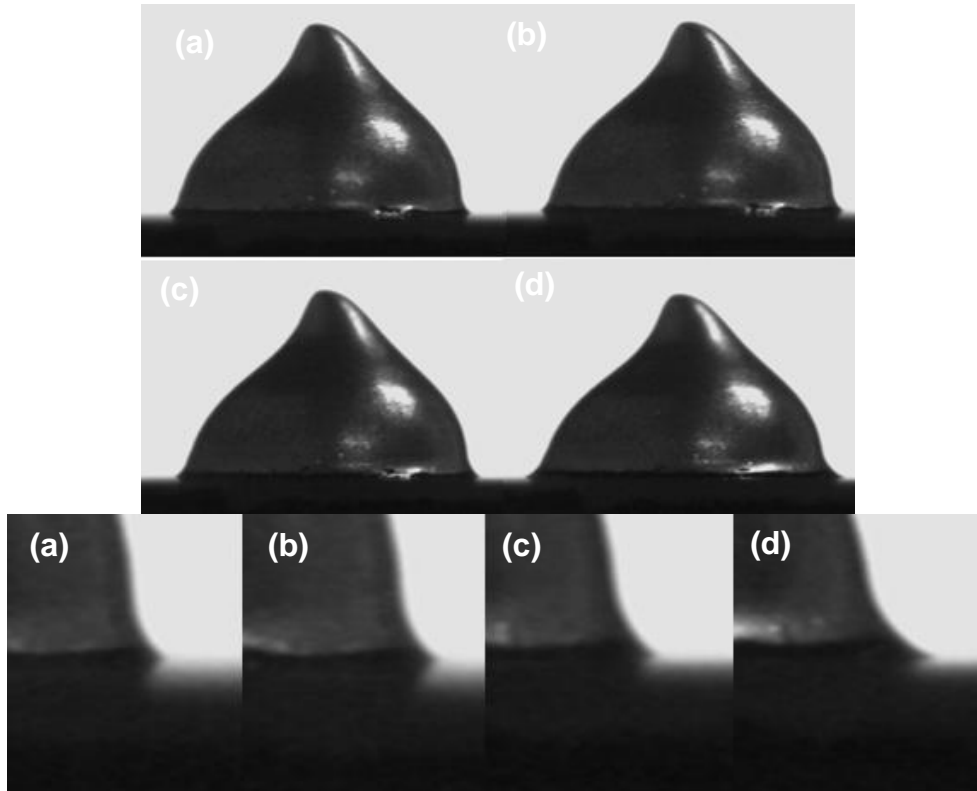
Figure 5.5-23 Wetting of the thixotropic silver filled adhesive on a perfluorooctadecanoic acid treated aluminium oxide surface after (a) 10 minutes (b) 20 minutes (c) 30 minutes (d) 60 minutes.

However, it was noticed, whilst attempting to measure the contact angle, that the adhesive footprint was slowly growing in area on the modified surface, suggesting wetting of the adhesive despite the unfavourable difference in surface energy/tension. Figure 5.5-23 shows the slow migration of the three phase interface of the adhesive across the surface of perfluorooctadecanoic acid coated aluminium oxide over an hour long period.

The experiment was repeated for boron nitride filled adhesive (930-4) which formed an equilibrium sessile droplet shape, allowing the contact angle to be measured. This is due to the boron nitride filled adhesive being shear thinning and not shear thickening as with the silver filled (H20E) adhesive. Figure 5.5-24 shows the migration of the three phase interface of a droplet of the adhesive across perfluorododecanoic acid coated aluminium nitride.
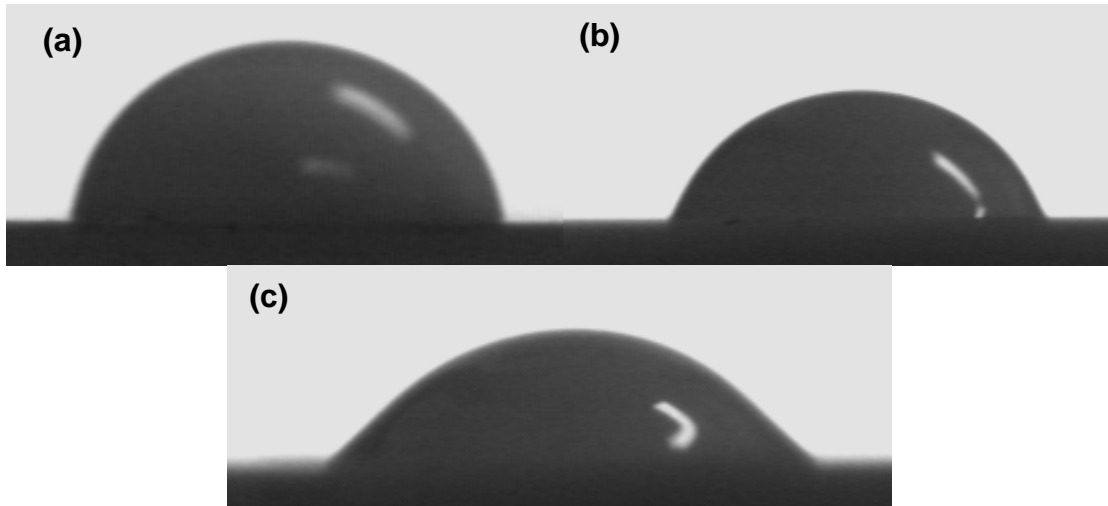
Figure 5.5-24 Wetting of boron nitride loaded epoxy (930-4) on a perfluorododecanoic acid coated aluminium nitride surface after (a) 30 minutes (b) 60 minutes (c) 120 minutes
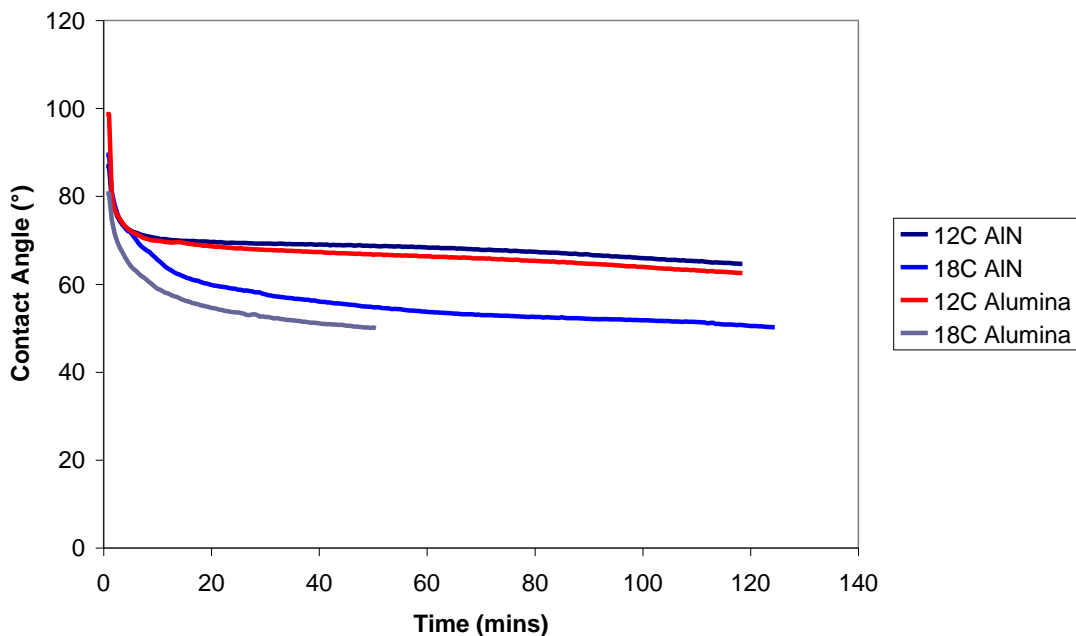
Figure 5.5-25 Plot of the change of contact angles of boron nitride filled adhesive on aluminium nitride and aluminium oxide surfaces coated with perfluorododecanoic acid (12C) and perfluorooctadecanoic acid (18C).

Figure 5.5-25 shows the change in contact angle over time for the boron nitride filled adhesive over aluminium oxide and aluminium nitride surfaces modified with the two long chain fatty acid SAMs, perfluorododecanoic acid and perfluorooctadecanoic acid. It can be seen that both systems reduce in contact angle quickly after application from >90° to ~70° before an almost constant rate of contact angle reduction is reached after 10 minutes. Interestingly the perfluorododecanoic acid produced consistently higher contact angles for both aluminium oxide and aluminium nitride. The reason for

this is not clear. The above graph shows the adhesive does in fact wet the coated surfaces, despite the apparently unfavourable surface energies/tensions. Good wetting is consistent with good adhesion, but the reason why the wetting itself occurs is not clear.
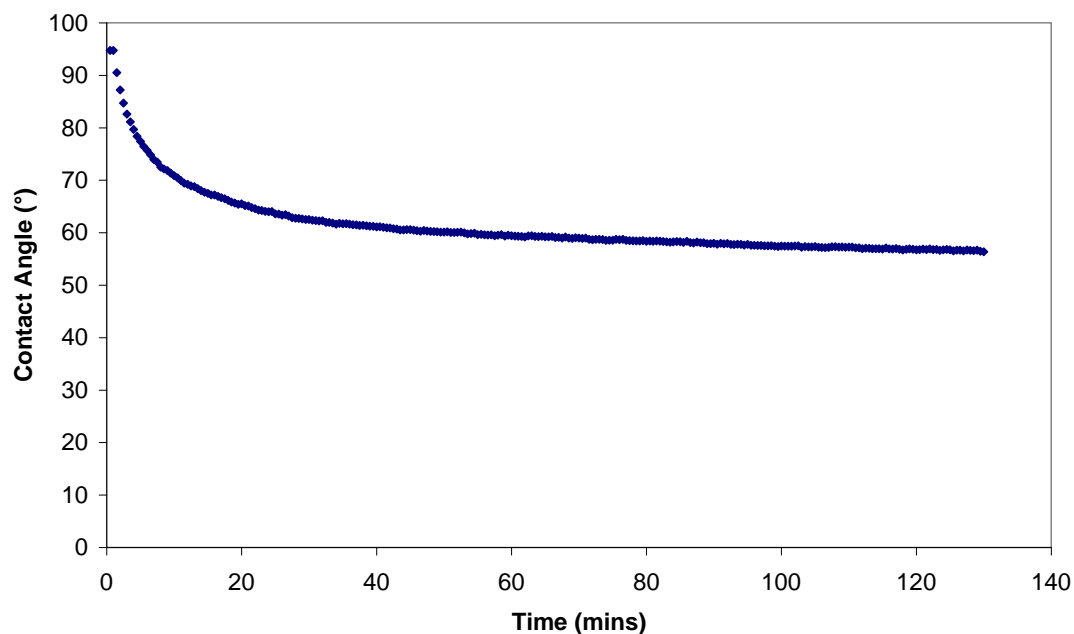
Figure 5.5-26 Plot of the change of contact angle of home made adhesive on aluminium oxide coated with perfluorooctadecanoic acid

The experiment was repeated for the home made adhesive and yielded much the same result, Figure 5.5-26. For comparative purposes the home made adhesive was also applied to clean aluminium oxide and aluminium nitride samples and the change in contact angle was recorded over 3 hours. Figure 5.5-27 shows the results of this experiment. Here the adhesive behaves differently. After an initial wetting phase which is time dependent due to the viscosity of the adhesive, the contact angle stabilises at around 50°.
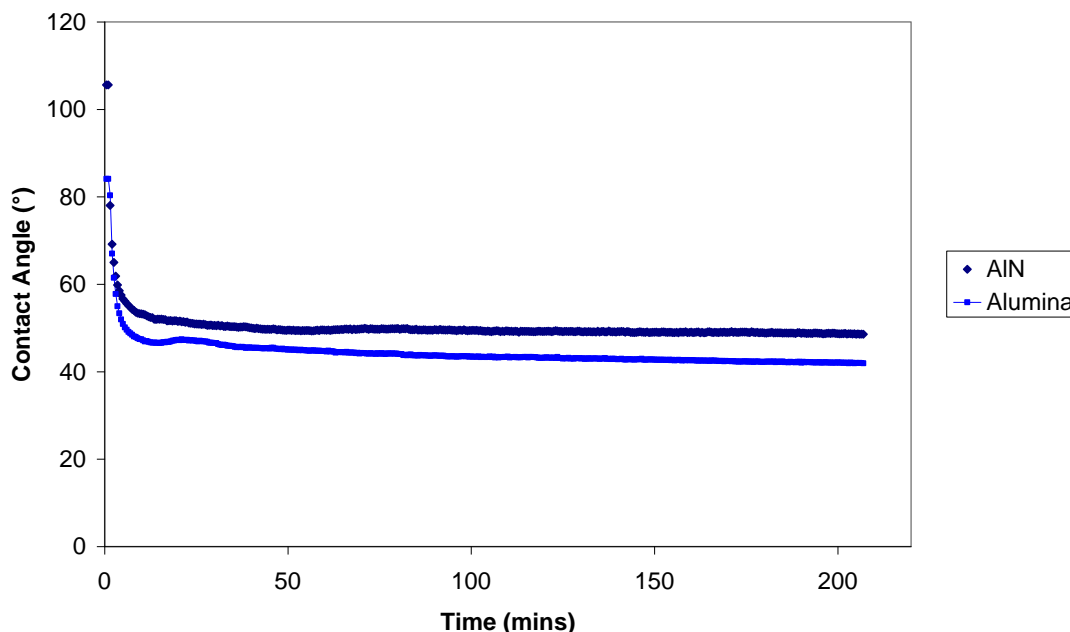
Figure 5.5-27 Plot of the dynamic contact angles of the home made adhesive on untreated aluminium nitride and aluminium oxide surfaces

It was hypothesised that particular constituents of the adhesive could be causing the time dependent wetting behaviour seen with the epoxy adhesives on the fatty acid modified surfaces. To test this an experiment was devised where the behaviour of the different components of the home made adhesive were measured separately. Lab prepared ceramics were coated with fatty acid monolayers and wetting measurements performed with the 3 components of the home made adhesive, 1,2-propanediol (solvent), 2-ethyl-4-methylimidazole (curing agent) and poly[(phenyl glycidyl ether)-co-formaldehyde] (plastic component).
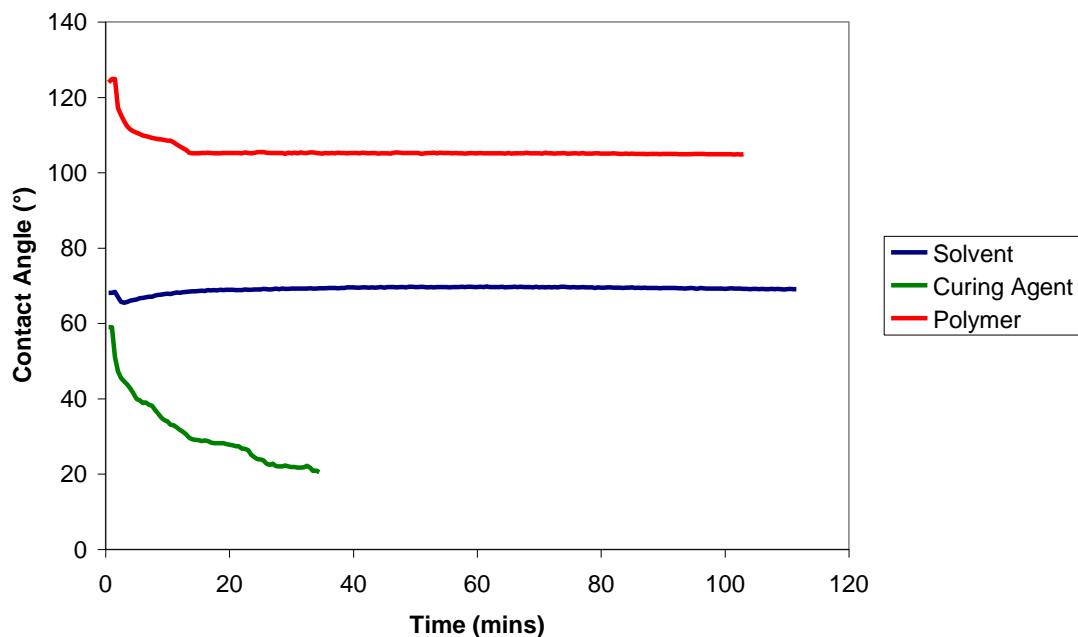
Figure 5.5-28 Contact angles over time for the curing agent and solvent components of the adhesive on perfluorooctadecanoic acid coated aluminium oxide.

Figure 5.5-28 shows a plot of the contact angles of the curing agent dissolved in 1,2-propanediol, the polymer constituent of the adhesive and 1,2-propanediol. It can be seen in Figure 5.5-28 that the curing agent solution did not form a stable contact angle on the surface and that the solvent by itself does not show the same behaviour. It therefore seems probable that the wetting behaviour is due to the reactive curing agent stripping off the fatty acid monolayer and that it has the same effect when mixed in to the adhesive.

Due to the covalent bond between the SAM material and the hydroxylated aluminium oxide surfaces, it was theorised that the behaviour of the curing agent could be a property of the liquid and not a surface phenomenon. Contact angles were plotted in the same way for the boron nitride filled adhesive on a clean Teflon surface. This was done for comparative purposes as a Teflon surface is chemically equivalent to a homogenously coated fluorinated fatty acid surface. Each consists of saturated fluorocarbons. This result was compared with a plot of the behaviour of the adhesive on an octadecanethiol coated copper surface, a perfluorooctadecanoic coated surface and a perfluorododecanoic acid coated surface as shown in Figure 5.5-29.

225
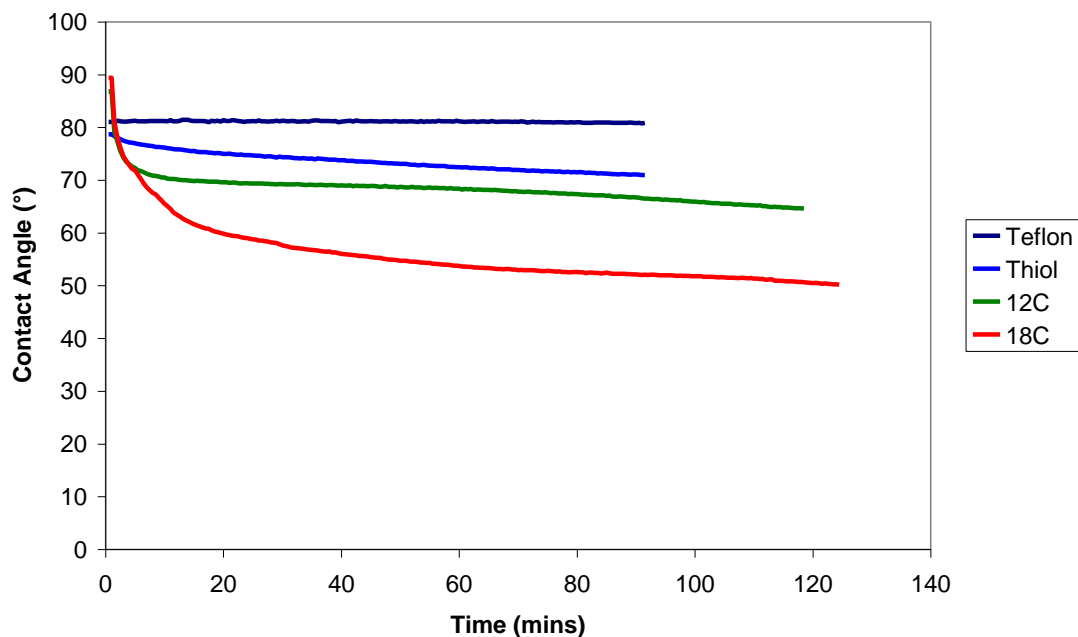
Figure 5.5-29 Dynamic Contact angles of boron nitride filled adhesive on Teflon, octadecanethiol (18C) coated copper surface, perfluorododecanoic (12C) acid coated aluminium nitride surface and perfluorooctadecanoic acid (18 C) coated aluminium nitride.

The boron nitride filled adhesive formed a stable contact angle on the Teflon surface. However, similar behaviours of gradually reducing contact angle were seen with the SAM coated surfaces. Although decrease for the octadecanethiol is initially slower than that for the fatty acid spreading, the rates are approximately equivalent after 20 minutes.
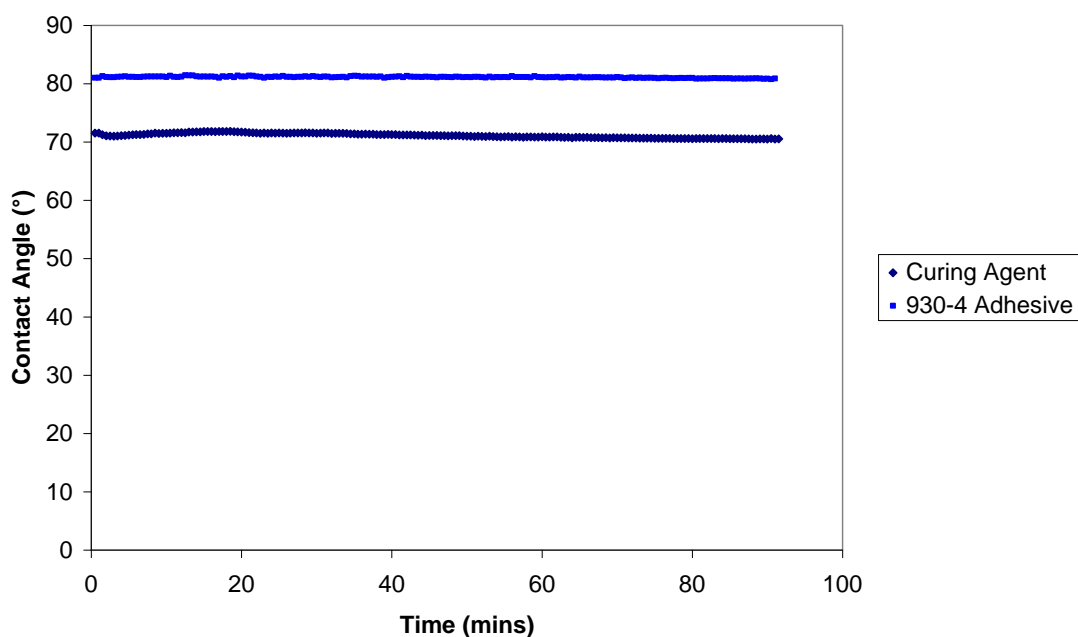
Figure 5.5-30 Plot of change in contact angles of curing agent and boron nitride filled adhesive on a Teflon surface over 90 minutes.

To confirm that the curing agent shows no unexpected wetting behaviour on a Teflon surface the curing agent solution was also applied to Teflon, as shown in Figure 5.5-30, along with the boron nitride data from the previous figure for comparison. A stable contact angle was also formed by the curing agent. The results shown in the two figures suggest that there is indeed an interaction between the curing agent and the fatty acid coated ceramics and that the reduction of the contact angle is not a physical equilibration phenomenon.
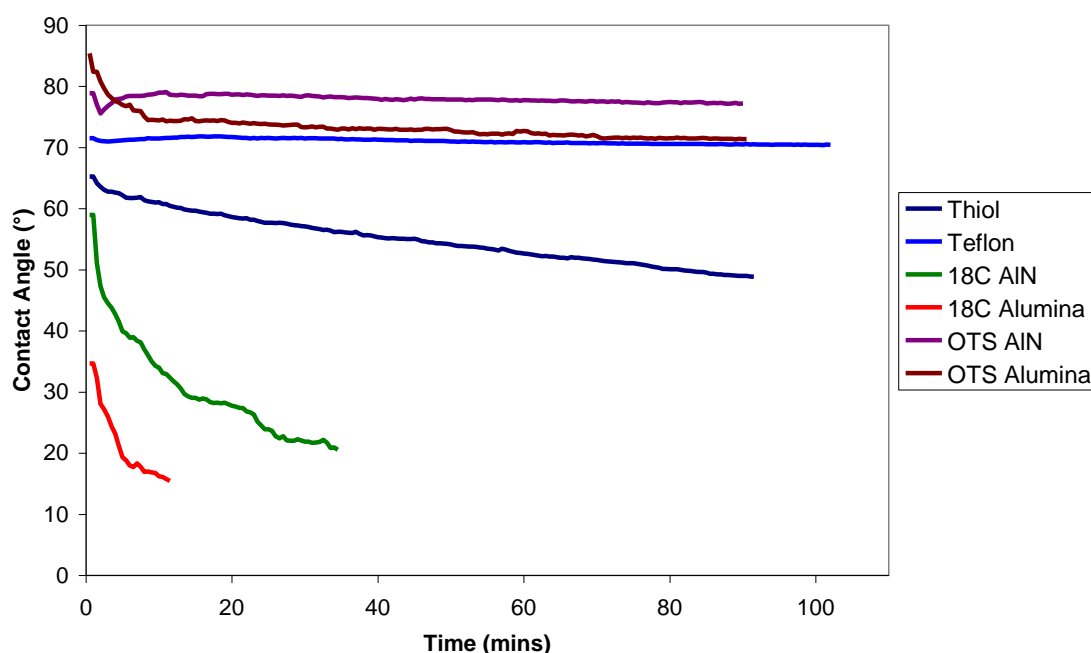
Figure 5.5-31 Plot of the contact angle change of the curing agent on an octadecanethiol coated copper surface, Teflon, perfluorooctadecanoic acid and octadecyltrichlorosilane coated aluminium nitride and aluminium oxide.

Plots of the changing contact angle of the curing agent in solution behaviour on SAM modified surfaces are shown in Figure 5.5-31. It seems from the results that the rate of wetting is proportional to the strength of the covalent bond formed between the SAM molecule and the substrate[16]. Only Teflon is seen to have a stable contact angle for the curing agent over time. The interpretation of Figure 5.5-31 explains the higher than expected shear forces for the bonds seen in *Section 5.5.5.1.3 Adhesive Joint Strength Testing*. The curing agent seems to displace, or remove the low surface energy effects of, the underlying self assembled monolayer. This is consistent with the correlation observed between the wetting rate and the bleed resistance efficacy of the SAM on the wetted surface. The slower wetting rate and hence reduced rate of displacement seen with the octadecyltrichlorosilane is

probably due to its strong Si-O covalent bond and the inter-chain Si-O-Si bonds which are known to form in the presence of sufficient water[16]. The tenacity of this monolayer probably inhibits the contact between adhesive and ceramic, resulting in only weak attraction between monolayer and adhesive and therefore a weak adhesive bond.

Adhesives and the curing agent were left on surfaces for up to 24 hours to see if the contact angle changed consistently over this time. The contact angles continued to decrease, especially for the curing agent as shown in Figure 5.5-32. The adhesives continued to spread, but because they were complete formulations they slowly cured as the experiment progressed, with wetting stopping after approximately 7 hours.
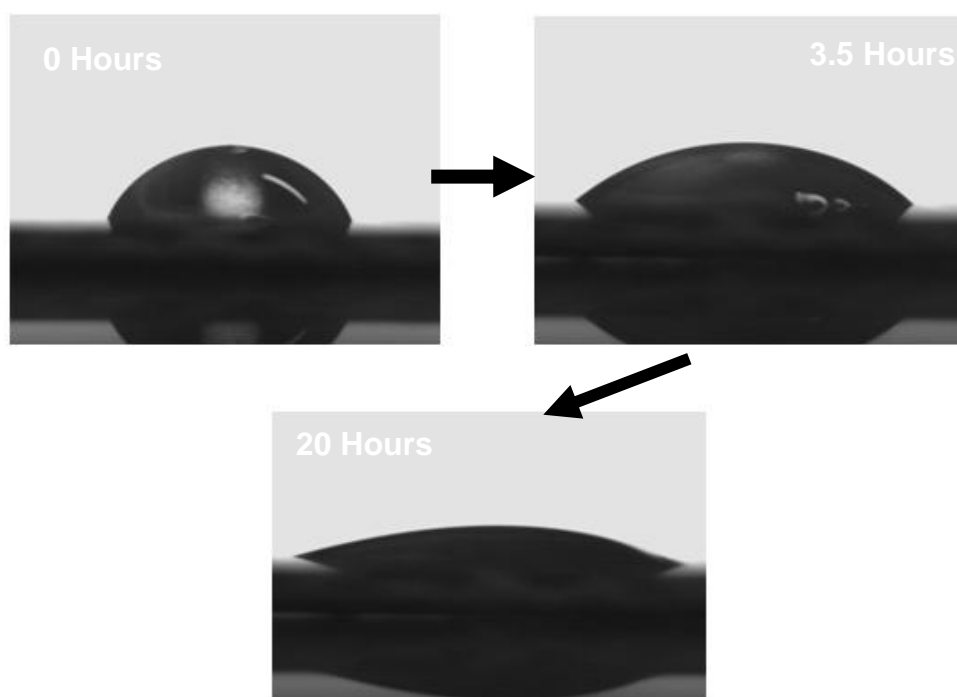
Figure 5.5-32 Change in contact angle of 2-ethyl-4-methylimidazole (dissolved in 1,2-propanediol) over 20 hours on a octadecanethiol treated copper surface.

The effect of roughness upon the wetting of adhesives on the fatty acid coatings was also studied as roughness has been seen to increase bleed distance, *Section 5.2.4.3 Epoxy Bleed*.
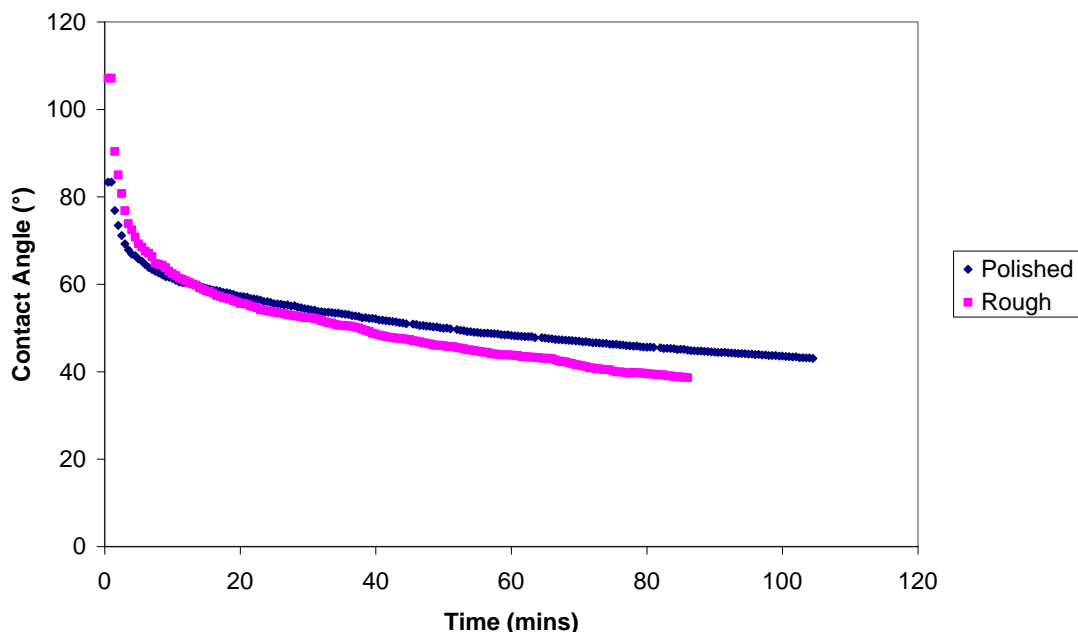
Figure 5.5-33 Plot of boron nitride adhesive contact angles on a rough (sample 7 from the commercially prepared sample set, lapped AlN, R_a 0.59µm) and polished (sample 3 from the commercially prepared sample set, polished AlN, R_a 0.01µm) surface coated with perfluorooctadecanoic acid (18 C chain).

Figure 5.5-33 shows a small difference in wetting behaviour of the boron nitride filled adhesive on perfluorooctadecanoic acid (18 C chain) coated surfaces of different roughness. After 30 minutes the rough surface (AFM R_a 0.58951µm) showed a slightly higher wetting rate than the polished surface (AFM R_a 0.01074µm). The difference is too small for there to be any likely effect on bonding strength.

5.5.5.5.1 *Behaviour of Adhesives on Adventitious Carbon Contaminated Ceramics*

The behaviour of the curing agent was also measured for AlN and Al_2O_3 samples with adventitious carbon contamination, the characterisation of which is reported in *Section 5.3 Identification and Removal of Contamination* (R_a ~0.2µm, as-fired, stored in polymer waffle packs in a clean room for one month). The samples exhibited approximately 30% adventitious carbon signal and an apparent surface energy of 23mJ/m^2. The results of this experiment are shown in Figure 5.5-34. The same gradual wetting behaviour is seen as with the fatty acid coatings. A noticeable difference is in the initial wetting period which is qualitatively different for a fatty acid coating. In the first 10 minutes the contact angle on the fatty acid coating drops quickly, following

which the wetting rate slows, and becomes approximately equivalent to the adventitious carbon wetting behaviour, as can be seen in Figure 5.5-34 below.
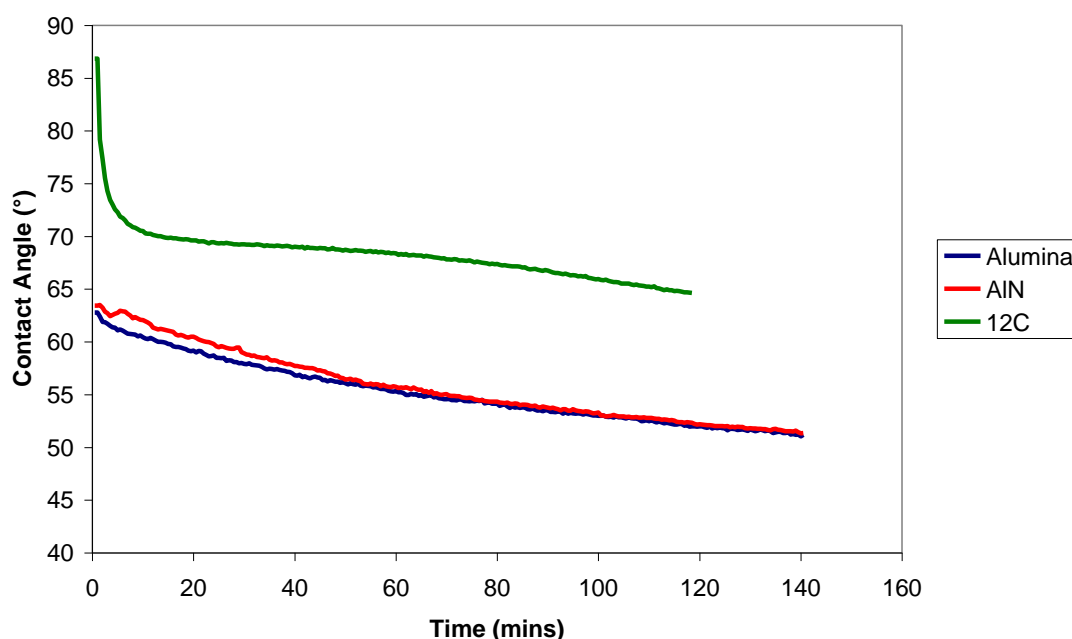
Figure 5.5-34 Wetting of the curing agent solution on adventitious carbon contaminated aluminium oxide and aluminium nitride samples. Included for comparison is the wetting behaviour of BN epoxy on perfluorododecanoic acid (12 carbon chain) coated AlN.

5.5.6 Analysis of Interaction of Curing Agent with SAM Coated Surfaces

5.5.6.1 Experimental Procedures

A number of different experiments were devised to investigate mechanisms of removal or the penetration of SAMs by the curing agent. Firstly a test was done to verify that the SAMs were chemisorbed onto the ceramic surfaces and not physisorbed. The test consisted of contact angle measurements made after exposure of SAM coated surfaces to ultrasonics in 60°C deionised water for 2 minutes followed by 5 minutes of rinsing with 60°C deionised water. As is described in *Section 4.6 FCOOH Coating*, deionised water at this temperature is the solvent used for application of the monolayers and would therefore be expected to dissolve the monolayer, should it be only weakly attached to the ceramic surface, upon agitation with ultrasonics. One would expect the molecules to diffuse to equalise the concentrations of the surface and the solvent. This is desorption which is the reverse of adsorption. At equilibrium physisorption the processes occur at equivalent rates. By putting

the samples in a system which is not in equilibrium (in a solvent of adsorbate concentration of zero) some desorption should be seen should physisorption be the adsorption process.

The second experiment was devised to test for the removal of the SAMs by the adhesives. Ceramic samples were treated as usual, *Section 4.6 FCOOH Coating*, to coat them with fatty acid SAMs. They were then exposed to both the home made and commercial adhesives for 18 hours. After this exposure the samples were thoroughly cleaned with acetone for 5 minutes each to remove all traces of adhesive and dried in a room temperature air flow for 5 minutes. Following this XPS analysis was performed. There were 5 samples: sample 1 was a control sample to ensure the acetone clean did not remove the coating (rinsed with acetone following coating only). Sample 2 was perfluorooctadecanoic acid (18 C chain) treated aluminium nitride exposed to the home made adhesive. Sample 3 was perfluorooctadecanoic acid (18 C chain) treated aluminium nitride exposed to silver filled adhesive. Sample 4 was perfluorooctadecanoic acid (18 C chain) treated aluminium nitride exposed to boron nitride filled adhesive and sample 5 was perfluorododecanoic acid (12 C chain) coated aluminium nitride exposed to the silver filled adhesive.

Finally XPS analysis of the adhesive curing agent (2-ethyl-4-methylimidazole) was performed along with analysis of a lab prepared ceramic sample which had been exposed to the compound for 24 hours.

5.5.6.2 Results and Discussion

The contact angle measurements following the physisorption test treatment are given in Table 5.5-9. It can be seen that the contact angles measured are not decreased by the treatment but are consistent with previous results, Table 5.5-2. Hence it can be concluded that the coatings are indeed chemisorbed.

SAM	Material	Water CA	Diiodomethane CA	SE
12	Al_2O_3	111.5	101.3	8.77
12	AlN	107.3	107.2	9.06
18	Al_2O_3	123.1	111.5	4.37
18	AlN	129.7	119.6	3.27

Table 5.5-9 Contact angle and surface energy measurements for perfluorododecanoic acid and perfluorooctadecanoic acid coated AlN and Al_2O_3 surfaces following thorough wash with

DI water at 60°C for 5 minutes. Where CA is contact angle in ° and SE is surface energy in mJ/m$^{2.}$

Sample	C	O	F	Al	B	N	S	Na	Si
1	23.2	11.9	25	19.3	1.1	19.7	0	0	0
2	40.5	24	1.2	15.2	3.1	16	0	0	0
3	66.1	15.3	2.3	5.8	0	5.6	1.4	1.1	2.4
4	36.3	18	3.8	21.6	2	18.3	0	0	0
5	52.7	20.4	5	11.4	0	7.2	1.3	2	0

Table 5.5-10 Relative atomic compositions of aluminium nitride surfaces from XPS following adhesive exposure for 18h.

Table 5.5-10 shows the relative atomic compositions for the elements found on the treated surfaces after the adhesive had been removed. The key measurement in this study was the abundance of fluorine. Presence of fluorine on the samples in high percentages indicates that the fatty acid monolayer is still present. Sample 1 (control) shows similar atomic percentages of fluorine and carbon. Analysis of the carbon peak revealed that the bond type ratio of C1s and CF$_2$ was approximately 50:50, Figure 5.5-35, as seen in previous analysis of good quality coatings, Figure 5.5-3. A proportion of the signal is also attributable to the underlying bulk material, showing ~20% of aluminium and nitrogen from the aluminium nitride. This shows that the 25% reading for fluorine does not represent a 25% surface coverage, just 25% of the signal from the three dimensional area sampled by the beam.
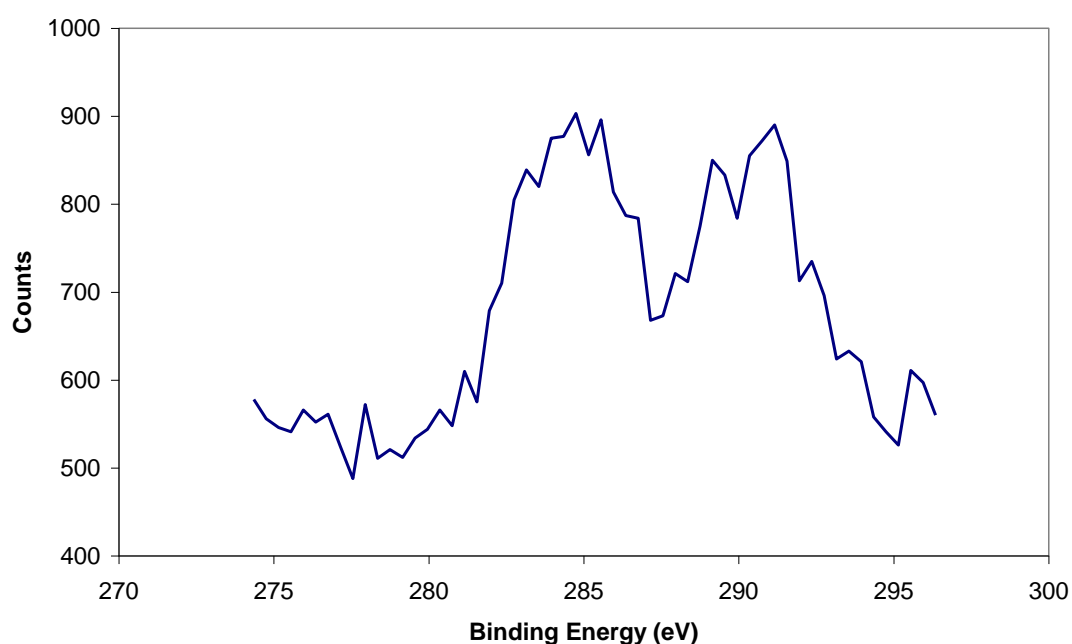
Figure 5.5-35 Carbon peak area for perfluorooctadecanoic acid treated aluminium nitride before cleaning with acetone to test for removal

Sample 2 (perfluorooctadecanoic acid) shows an increase in the carbon and oxygen signals, and large reduction of the fluorine signal (25% → 1%) due to the adhesive treatment. The occurrence of aluminium and nitrogen in the spectra confirms that the bulk material is still contributing some signal, which means any residual adhesive remaining on the surface is not simply masking the fluorine signal. Analysis of the carbon peak area, Figure 5.5-36, shows the disappearance of the CF_2 peak and broadening of the C1s peak. Three peaks can be seen in the spectrum in the same positions as seen with the adhesive analysis, *Section 5.3 Identification and Removal of Contamination*, C1s, C-O-C and epoxide. This suggests that there is some residual adhesive on the surface, which is not unexpected due to the affinity of the adhesive groups for a hydroxylated surface[32]. Similar results are obtained with the other adhesive/SAM combinations Figure 5.5-37, Figure 5.5-38 and Figure 5.5-39.
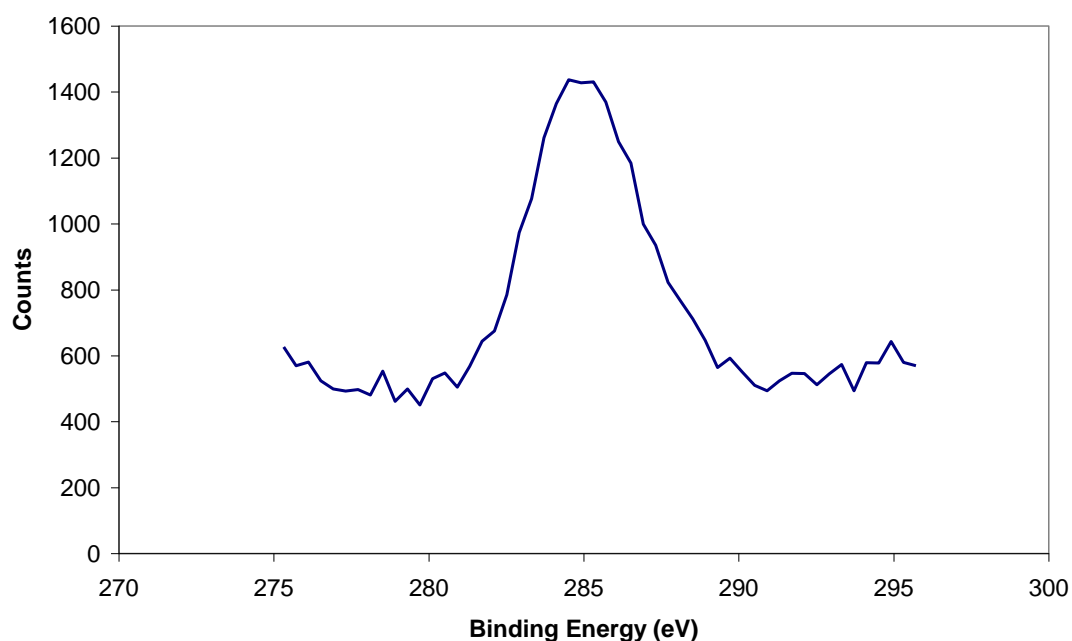
Figure 5.5-36 Carbon peak area for perfluorooctadecanoic acid treated aluminium nitride after coating with home made adhesive for 18h to test for removal
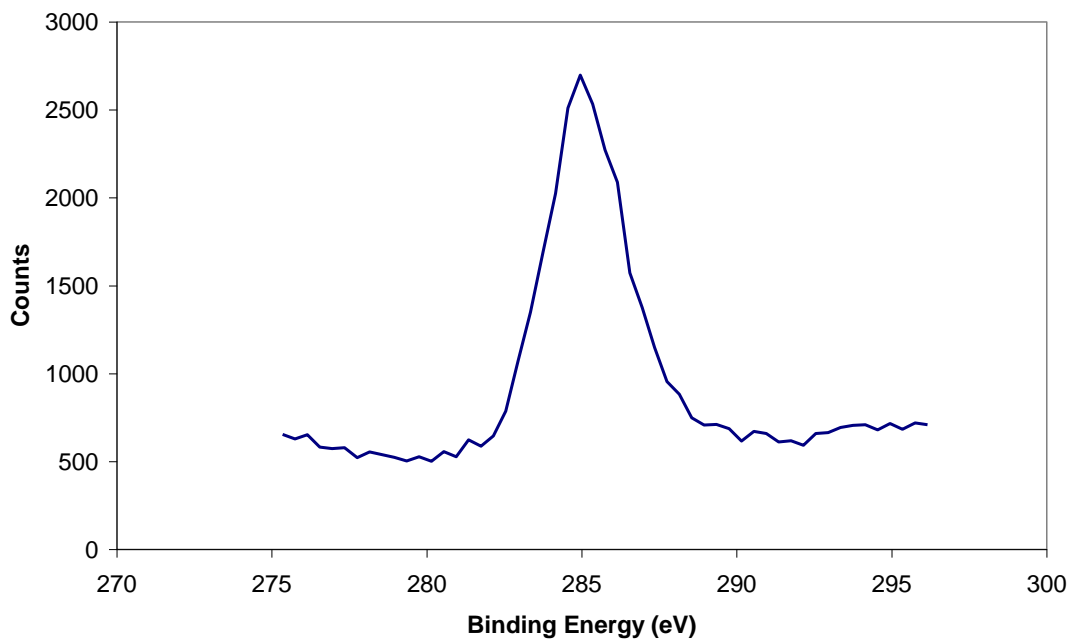
Figure 5.5-37 Carbon peak area for perfluorooctadecanoic acid treated aluminium nitride after coating with silver filled adhesive for 24h to test for removal.
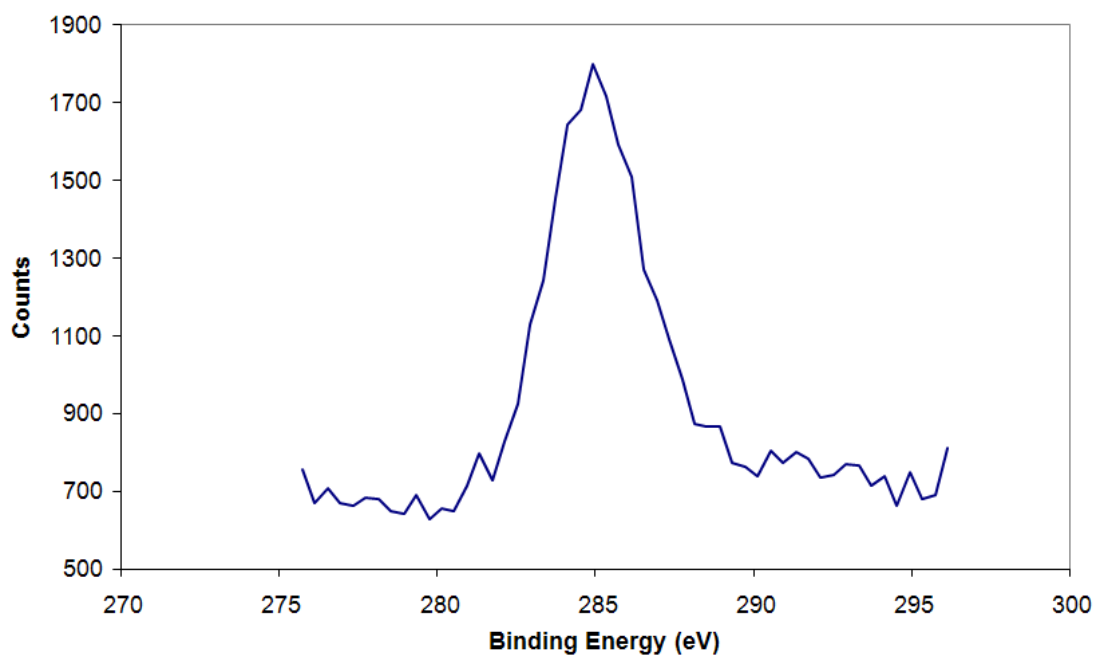
Figure 5.5-38 Carbon peak area for perfluorooctadecanoic acid treated aluminium nitride after coating with boron nitride filled adhesive for 24h to test for removal
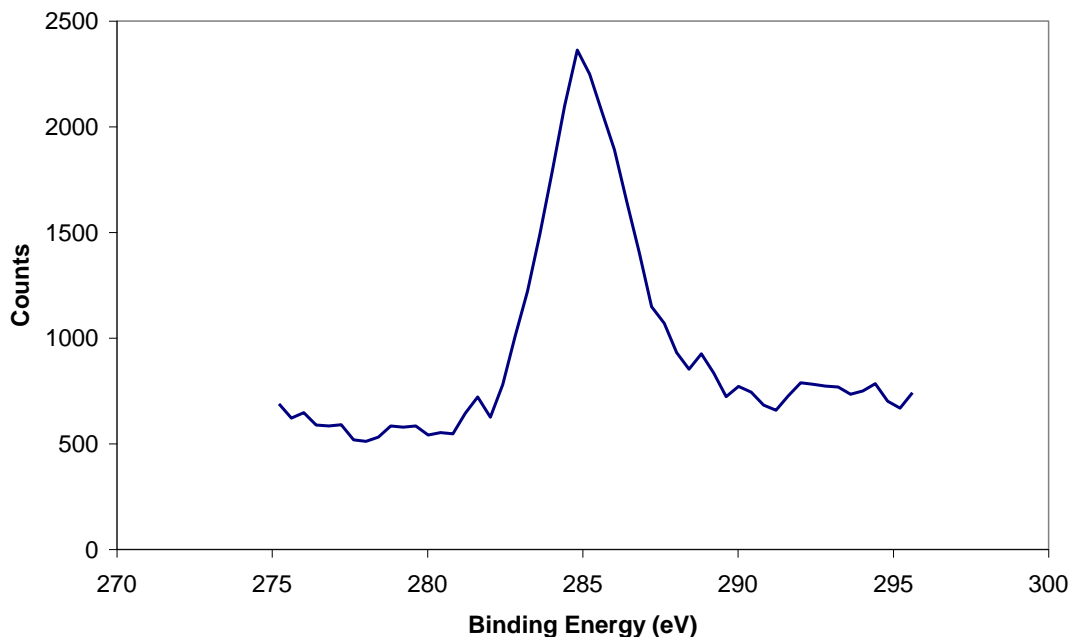
Figure 5.5-39 Carbon peak area for perfluorododecanoic acid treated aluminium nitride after coating with silver filled adhesive for 24h to test for removal.

It can be concluded form these results that the fluorinated fatty acid coatings are indeed being stripped off by the adhesive curing agents.

When attempting to obtain bulk XPS spectra for the curing agent so that it could be seen if the curing agent was bonded to the surfaces in place of the fluorinated fatty acids, the 2-ethyl-4-methylimidazole proved to be too volatile to allow this and evaporated in the XPS chamber. As an alternative a sample which had been exposed to the curing agent solution for a number of hours was analysed. However, the narrow scan spectrum was too noisy to allow detection of peak shape changes due to nitrogen mediated bonding to the surface, Figure 5.5-40.
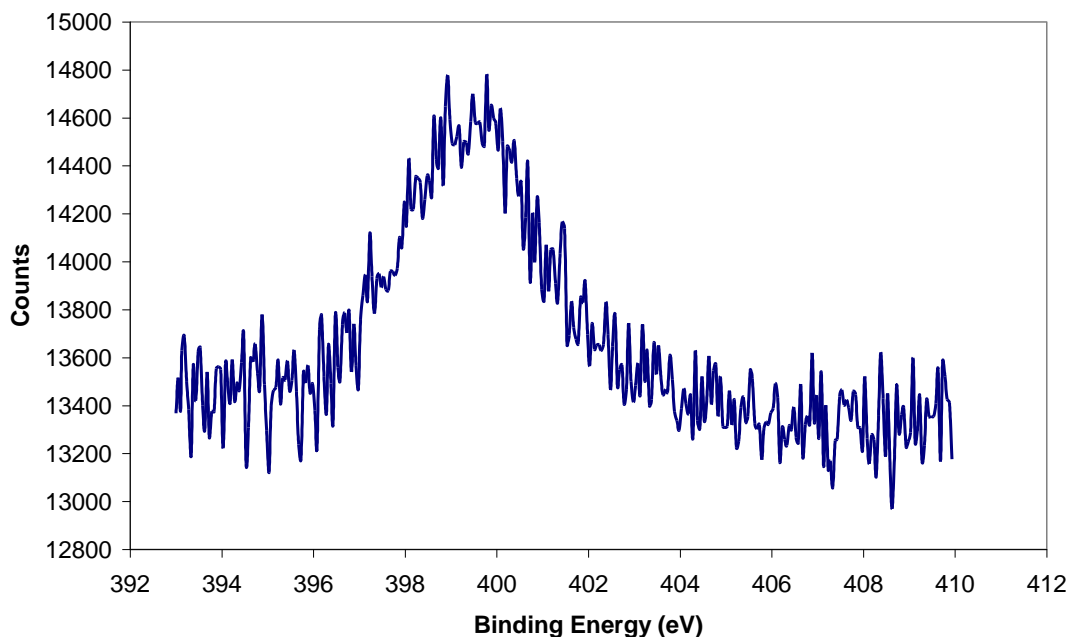
Figure 5.5-40 Nitrogen peak area for aluminium oxide exposed to 2-ethyl-4-methylimidazole dissolved in 1,2-propanediol for 2 hours.

5.5.7 Effects of SAMs on Electrical Conductivity

It has been proposed in this work that thiol SAMs be used beneath adhesives on copper and gold surfaces to stop adhesive bleeding. An investigation was carried out to determine the magnitude of any series resistance introduced by the coatings to conductive adhesive joints. Three mechanisms whereby an increase of resistance could be created were identified and the experiment was designed to test these.
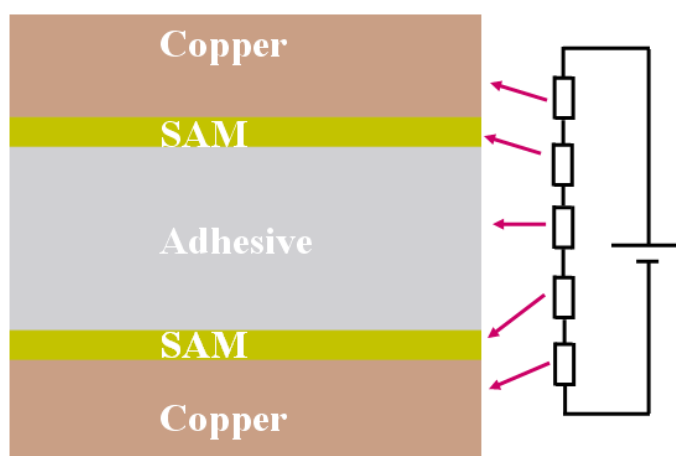
Figure 5.5-41 Equivalent circuit model for test electrical joint showing series resistances potentially introduced due to inclusion of an intermediate layer between adhesive and adherend.

The total resistance through an electrical joint would be the sum of the track resistance, the adhesive resistance and the interfacial resistances at the adhesive/adherend interface, as shown in Figure 5.5-41. The interfacial resistances may include some contribution due to the presence of the SAM organic layer. In addition reduction of wetting due to this low energy organic layer could have a further effect on the bond conductance by inhibiting intimate contact between adhesive and adherend. The third potential source of resistance was hypothesised to be reduction of contacts between the silver particles filling the adhesive and the adherend surface due to surface roughness, see Figure 5.5-42. Previous work, *Section 5.1.4.2 AFM Surface Texture Characterisation,* has shown that the silver particle size exceeds the surface texture feature size, which makes lack of contact a real possibility.
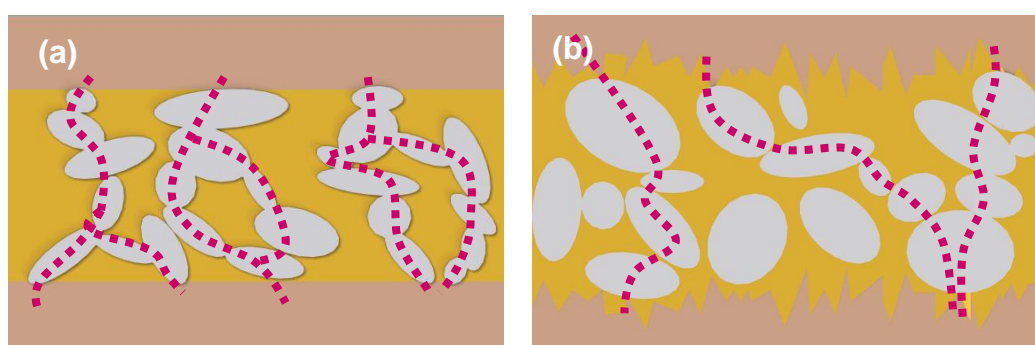
Figure 5.5-42 Conceptual model of conductive pathways of a silver filled adhesive on (a) a polished surface, (b) on a rough surface.

Rough copper surfaces with a granular surface texture were prepared by aggressive ferric chloride etching, *Section 4.2.5 Ferric Chloride Etching*. The roughness achieved is given in Table 5.5-11. The roughness of an as-received copper coupon subjected only to an oxide removal HCl etch is also included.

Etch	Ra (µm)	Wenzel Roughness Factor	Texture
$FeCl_3$	0.2873	1.2835	Granular
HCl	0.0489	1.0442	Polished

Table 5.5-11 Mean AFM surface texture data for HCl and $FeCl_3$ etched copper surfaces.

Conductive bonds between the prepared surfaces were prepared as described in *Section 4.9 Electrical Testing*. The SAM used was

octadecanethiol. A four point probe test was used to measure joint resistances. Table 5.5-12 shows the resistances measured.

Treatment	Rough Copper	Polished Copper	Rough SAM	Polished SAM
Resistance (mΩ)	1.55	1.61	3.59	3.92
Standard Deviation	0.72	0.78	2.83	2.95

Table 5.5-12 Mean electrical resistance values of 4mm^2 40µm thick conductive adhesive bonds formed between copper samples of the given surface preparations (10 prepared of each).

The quoted resistivity of the H20E silver filled adhesive is a maximum of 0.0004Ωcm[33].

$$R = \rho \frac{l}{A}$$

Equation 5.5-1 Formula for the calculation of resistance given resistivity, ρ, of the conductor is known, the length, l is known and the cross sectional area A is known.

Using Equation 5.5-1 the calculation of the expected resistance of the conduction path through the conductive adhesive is therefore 400 mohm. This is significantly higher than the measured results. This is possibly due to the conductive pathways being composed of almost entirely silver with little inclusion of epoxy, made possible by the small bond line thickness on the same order of magnitude as the silver flakes.

The effect of roughness on the conductivity is the reverse of the expected affect. It is seen to slightly decrease the interfacial resistance of the bond, presumably increasing the number of flake to surface contacts due to the increased surface area of the etched sample. The effect of the SAM is to approximately double the mean interfacial resistance of the adhesive bonds. However, there is large overlap in the ranges of the sets of measurements. It can be therefore be concluded that effect of the octadecanethiol intermediate layer on the resistance of the adhesive bonds is not significant.

5.5.8 Multi Stage Coating of Ceramic/Metal Heterogeneous surface

The efficacy of the concept for multistage coating of heterogeneous surfaces, as described in the introductory section was tested.

5.5.8.1 Sample Preparation

Full details of the preparation methods for the samples are given in *Section 4 Experimental Procedures*. In summary, samples were plasma cleaned, half coated with 20nm of copper by evaporation, and then treated with octadecanethiol by full immersion, washed and treated with either perfluorododecanoic acid fatty acid or perfluorooctadecanoic acid fatty acid by full immersion. The test sample configuration and desired result of coating is shown in Figure 5.5-43.
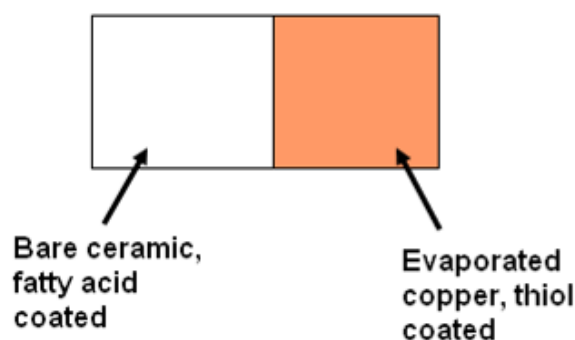
Figure 5.5-43 Test sample configuration and desired result of multistage coating method.

5.5.8.2 Initial Tests

Samples were first tested for selectivity of the coatings. A sample was fully immersed in thiol to show that it bonded only to the copper. It was found that the ceramic maintained its high surface energy of $>60mJ/m^2$ while the copper surface energy was reduced to the level expected for a thiol coated surface. Next a different sample was fully immersed in the fatty acid. The copper showed a small decrease in surface energy probably due to oxidation of the surface and adsorption of some fatty acid monolayer. However, the resultant surface energy change of the copper was much lower than seen on the ceramic, showing that the fatty acid coating was sporadic and not structured and homogenous on the copper as it was on the hydroxylated aluminium oxide.

5.5.8.3 Multi – Stage Coating Tests

The results of contact angle measurements on multi-stage coated samples are shown in Table 5.5-13. Spatially uniform surface energies and contact angles were achieved. Epoxy bleed measurements also demonstrated that

the combined coatings were equally as effective at resisting bleed as seen previously with each of the fatty acids on ceramic only surfaces.

Material/Treatment	Water CA	Diiodomethane CA	SE
AlN 12C	114.5	108.9	6.79
AlN Cu 18C	119.7	114.1	5.12
Al2O3 12C	103.1	111.5	11.08
Al3O3 Cu 18C	94.8	111.9	16.74

Table 5.5-13 Contact angle and surface energy data for samples which had undergone fatty acid coating on the ceramic end and thiol coating on the copper coated end. Where CA is contact angle in ° and SE is apparent surface energy in mJ/m^2. 12C represents a perfluorododecanoic acid coating. 18C represents a perfluorooctadecanoic acid coating.

5.5.8.4 XPS Analysis of Multi-stage Coated Surfaces

Sample	Treatment	Material
1	Untreated Cu end	Al_2O_3
2	Untreated Ceramic end	Al_2O_3
3	Untreated Cu end	AlN
4	Untreated Ceramic end	AlN
5	ODT Only Cu	Al_2O_3
6	ODT Only Ceramic	Al_2O_3
7	FA Only Cu	Al_2O_3
8	FA Only Ceramic	Al_2O_3
9	FA+ODT Cu	Al_2O_3
10	FA+ODT Ceramic	Al_2O_3
11	FA+ODT Cu	AlN
12	FA+ODT Ceramic	AlN

Table 5.5-14 Sample preparations for multi stage coating experiment. Where FA denotes perfluorooctadecanoic acid treatment and ODT denotes octadecanethiol treatment. Cu denotes analysis of the of the copper coated end, ceramic denotes analysis of the ceramic end of the sample.

Sample	Ceramic	Analysis	C	O	Cu	Al	Si	F	Na	Ca	N	B	Mg
1	Al_2O_3	Cu	43.6	33.8	22.6	0.0	0.0	0.0	0.0	0.0	0.0	0.0	0.0
2	Al_2O_3	Ceramic	30.9	34.2	0.5	23.9	4.3	5.7	0.7	0.0	0.0	0.0	0.0
3	AlN	Cu	45.8	34.0	20.2	0.0	0.0	0.0	0.0	0.0	0.0	0.0	0.0
4	AlN	Ceramic	18.6	36.1	0.5	22.4	4.8	7.9	1.2	0.5	5.9	2.0	0.0
5	Al_2O_3	Cu	68.6	15.7	15.8	0.0	0.0	0.0	0.0	0.0	0.0	0.0	0.0
6	Al_2O_3	Ceramic	39.1	32.4	0.5	21.2	4.6	2.2	0.0	0.0	0.0	0.0	0.0
7	Al_2O_3	Cu	43.2	16.4	7.9	0.0	0.0	42.5	0.0	0.0	0.0	0.0	0.0
8	Al_2O_3	Ceramic	23.6	31.1	0.0	21.1	0.0	23.4	0.0	0.0	0.0	0.0	0.8
9	Al_2O_3	Cu	47.2	12.3	10.3	0.0	0.0	30.3	0.0	0.0	0.0	0.0	0.0
10	Al_2O_3	Ceramic	17.7	31.4	0.0	22.6	1.9	26.4	0.0	0.0	0.0	0.0	0.0
11	AlN	Cu	46.9	8.0	7.0	0.0	0.0	38.0	0.0	0.0	0.0	0.0	0.0
12	AlN	Ceramic	28.7	9.8	0.2	15.9	0.0	30.5	0.0	0.0	13.0	1.9	0.0

Table 5.5-15 Relative atomic percentage compositions obtained from XPS for samples treated as shown in **Table 5.5-14**.

The XPS results shown in Table 5.5-15 confirm the presence of both monolayer types simultaneously present bonded to their respective ends of the samples with samples 5-8. It can be seen, however, that a high presence of fluorine is seen on samples 7, 9 and 11 which suggests that the fatty acid monolayer has bonded to the copper metallisation. Although fatty acid monolayers are known to bond to hydroxylated copper oxide surfaces, it was expected that the copper surface would be oxide free due to the preparation method which in the literature is reported to remove oxide from copper foils and protect from re-oxidation[4]. Deposition with an imperfect vacuum could result in an amount of copper oxide included in the bulk copper. The presence of CF_2 peaks on a copper analysis area is shown in Figure 5.5-44.
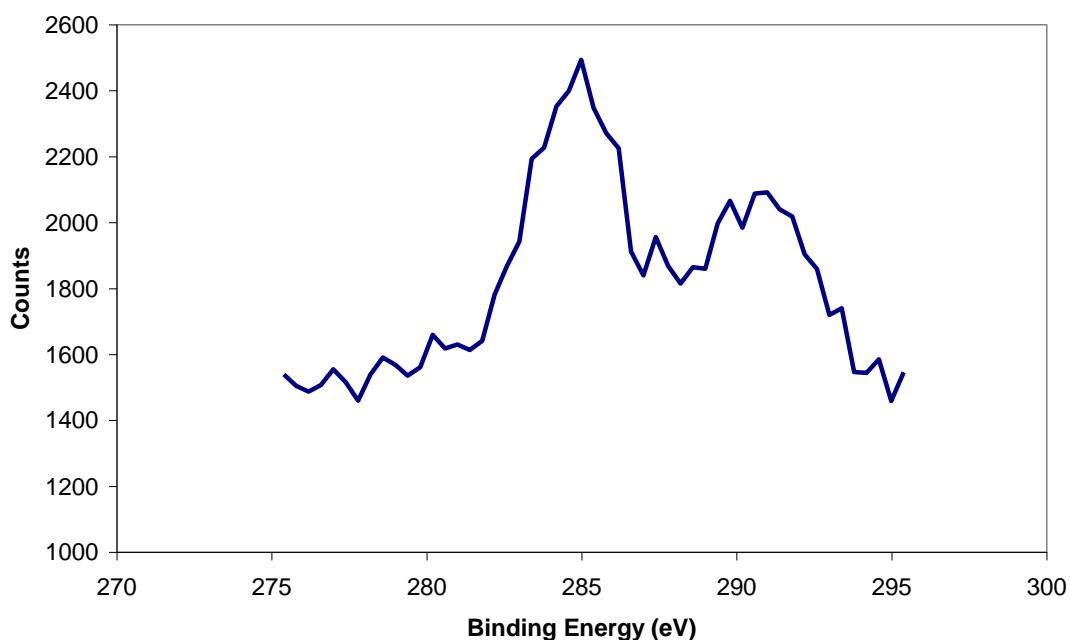
Figure 5.5-44 Carbon peak for ceramic/copper hybrid surface coated with perfluorooctadecanoic acid only, sample 7 copper end. Peaks visible are C1s and CF_2.
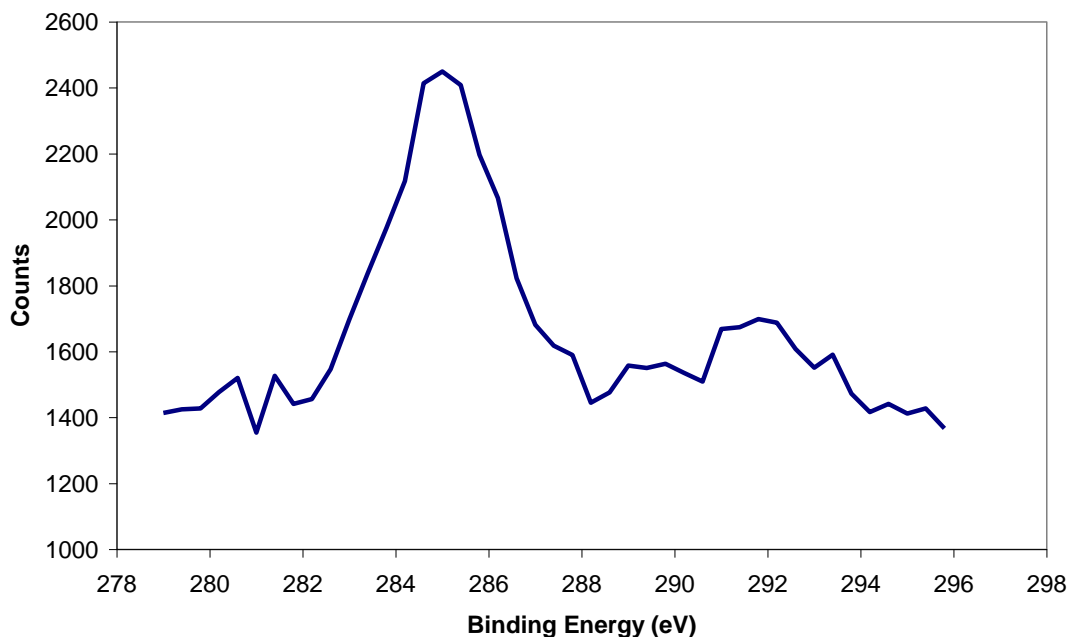
Figure 5.5-45 Carbon peaks of copper area on sample subjected to octadecanethiol treatment only, sample 5.

Figure 5.5-45 shows an XPS scan carbon peak area for octadecanethiol coated copper, sample 5. Interestingly from the broad scan spectra of sample 5 a 15% copper oxide signal can be seen, suggesting defects in the monolayer, again possibly due to the copper deposition method.. This would also explain the appearance of fatty acid monolayers in regions which have been coated with octadecanethiol, since fatty acid molecules will bond to copper oxide, but a thiol molecule will only bond to copper metal. In principle perfluorooctadecanoic acid should not adhere to the thiol.

That the fatty acid is detected means implies that the multi-stage method is highly defect tolerant, as any defects in the octadecanethiol monolayer will be filled with perfluorooctadecanoic molecules. This suggested mechanism is possible because the solvent used to apply the fatty acid is water, which would readily hydroxylate any exposed copper oxide. Figure 5.5-46 supports this suggested mechanism as it can be seen that the carbon peak area heavily favours C-H C-C bonds which are abundant in an octadecanethiol monolayer. That expected from a quality fatty acid is a ratio between the peaks for C-H/C-C and CF_2 of 50:50, as has been seen consistently in this work and which is seen again in Figure 5.5-47.

242
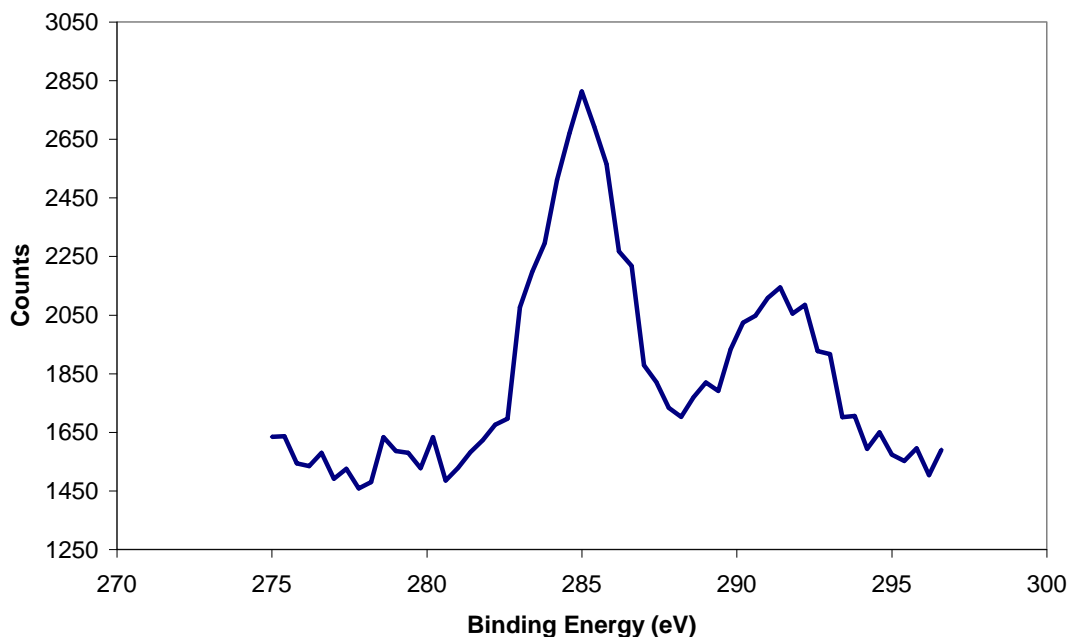
Figure 5.5-46 XPS carbon peaks of copper area on AlN sample which has been double treated with ODT and FA.
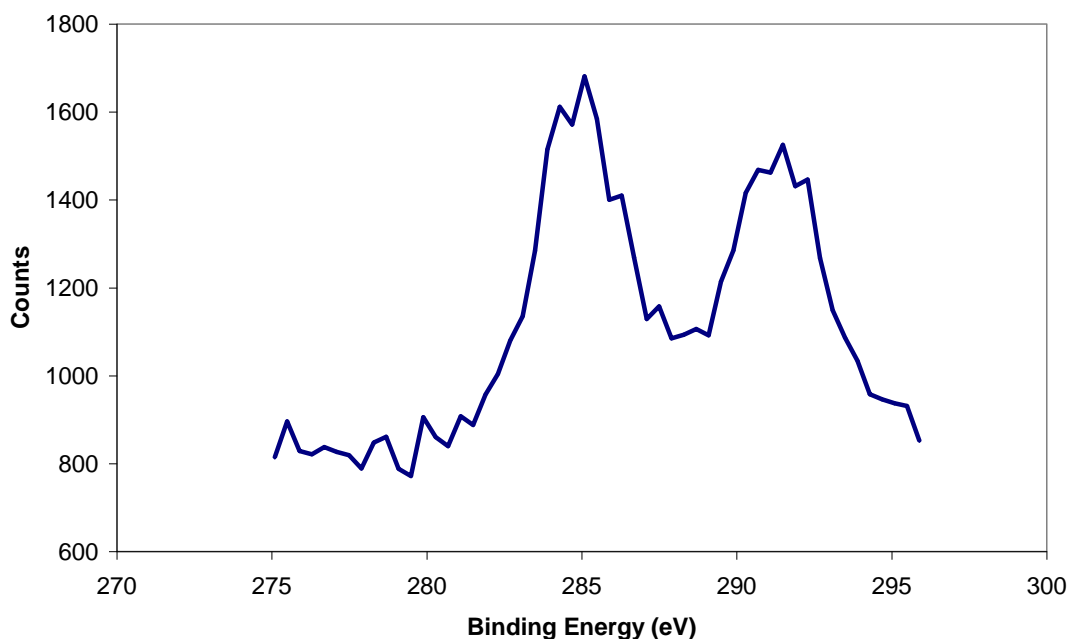
Figure 5.5-47 XPS carbon peaks of aluminium nitride which has been double treated with ODT and FA.

5.5.9 Patterning of OTS for Adhesive Spreading Control

Due to the resilience of octadecyltrichlorosilane as a coating and its observed resistance to removal by the curing agent, it was investigated briefly for use as an adhesive wetting barrier. Additive patterning of monolayers has been investigated in some depth previously by the author[34], and be the method micro contact printing, ink jet printing or another, the coating quality was found

to be inferior to that achieved by dip coating or by dip coatings followed by selective removal. For this reason the patterning method chosen was selective removal of octadecyltrichlorosilane with an oxygen plasma clean. The monolayer was applied, half of it was masked and then the plasma removal performed. Adhesives were then applied to the surfaces and cured, and their wetting behaviour observed with SEM and optical microscopy.

Figure 5.5-48 shows an optical microscope image (x50) of one single spot of boron nitride filled adhesive on a sample half coated in octadecyltrichlorosilane (coating on the right). It is clear epoxy and bleed material do not wet the coated area, as seen in Figure 5.5-48 and Figure 5.5-49. The investigation was not pursued further because it was considered that the integration of the plasma patterning method into the optoelectronics assembly line would be prohibitively complex and expensive.
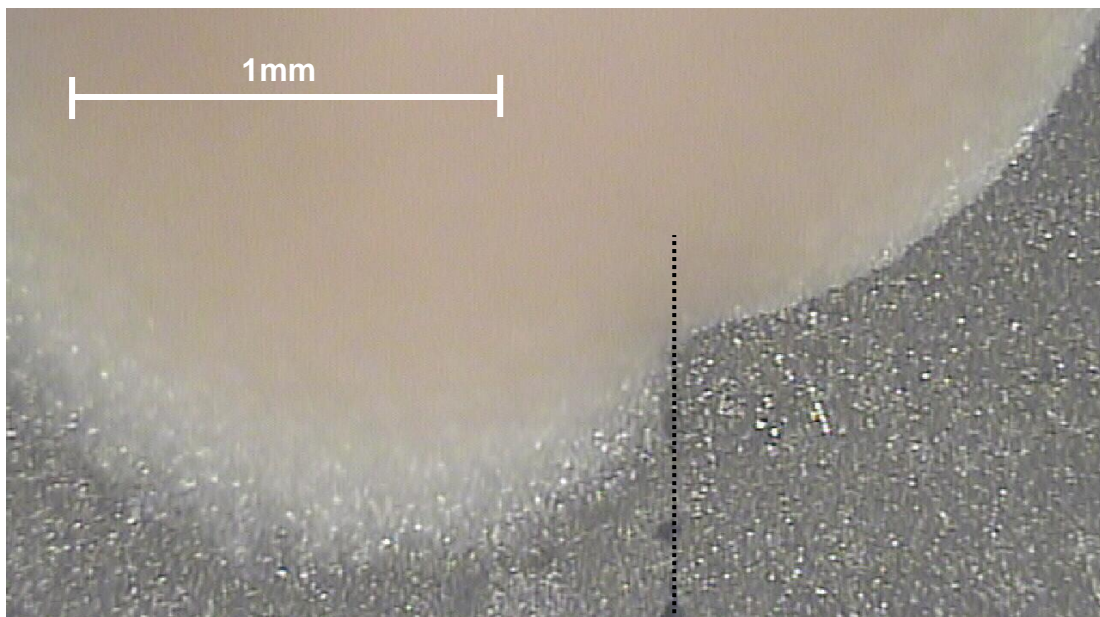
Figure 5.5-48 Change in wetting behaviour on an octadecyltrichlorosilane patterned AlN surface. Optical microscope image x50. Dashed line shows the interface between the uncoated area (left hand side) and coated area.

```
EHT= 5.00 kV        WD=  32 mm        Mag=    100    X
100µm  ⊢━┥          Photo No.=314     Detector= SE1        ▪
```
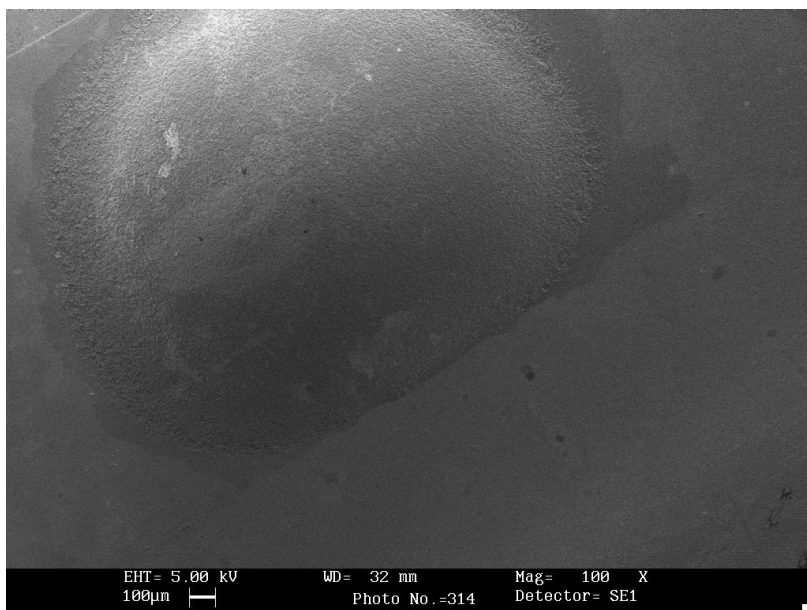
Figure 5.5-49 Octadecyltrichlorosilane as a wetting barrier on aluminium oxide, with boron nitride filled 930-4 epoxy adhesive. The straight edge to the bottom part of the adhesive spot indicates the edge of the uncoated region.

5.5.10   Conclusions

It has been shown that self assembled monolayers successfully control epoxy bleed, due to their reducing the surface energy of the substrate materials, especially the dispersive component of surface energy. Roughness was not seen to interfere with the use of self assembled monolayers as a solution to the epoxy bleed issue.

The self assembled monolayers were all shown to be stable over time, with possible increased ordering of fatty acid monolayers over the two days after application. Fatty acid, thiol and silane monolayers all showed resistance to the elevated temperatures witnessed in adhesive cure schedules.

The fatty acid self assembled monolayers used were seen to be stripped off the surface slowly by the adhesive, which meant that there was no reduction in adhesion strength of the systems studied. This was an important result for this study as it was shown that epoxy bleed could be controlled with no detrimental effect on the bond strength. For the same reason epoxy bleed was also not reduced to zero, but was reduced to an acceptably short distance. The curing agent of the adhesive was seen to be responsible for the stripping of the fatty acid monolayers, with a currently unknown mechanism.

The curing agent of the adhesives was also seen to strip thiol and silane monolayers, but at a much slower rate than the fatty acid SAMs. A positive correlation was seen between the free energy of adsorption of the different monolayers on the given surfaces, and the speed at which the curing agent stripped off the molecules. This relationship extended to adhesion strength, i.e. a positive correlation between rate of wetting of the curing agent and breaking stress of lap shear samples. The curing agent was also seen to wet across an adventitious carbon contaminated sample, explaining the unusual adhesion strength seen in *Section 5.2.4.2 Bond Strength Analysis*.

Octadecanethiol monolayers increase the interfacial electrical resistance of bonds formed with conductive adhesives by a negligible amount. Thus thiol monolayers may be considered as suitable for use in coating electrical contacts in optoelectronic assemblies.

A method for coating heterogeneous metal/ceramic surfaces was successfully developed. It was shown that a heterogeneous surface could be homogenised in terms of surface energy, making the whole substrate epoxy bleed resistant. The method consisted of two subsequent coatings of a thiol targeted at coating the metallisations and a fatty acid monolayer which coated the hydroxylated ceramic surfaces. The method was found to tolerant to pinhole defects in metal layers. Although demonstrated with copper metallisations, the process is predicted to also work with gold metallisations. In fact copper is notoriously more difficult to work with, in terms of self assembled monolayers, than gold.

OTS patterning across ceramic substrates by plasma treatment has been demonstrated, along with its ability to act as a wetting barrier.

5.5.11 References

[1] Tan N.X. Lim K.H.H. Bourdillon A.J. Analysis of coatings which inhibit epoxy bleeding in electronic packaging, Journal of Materials Science: Materials in Electronics, Volume 8, Number 2, 1997 , pp. 73-77(5)

[2] Burmeister, M. Elimination of epoxy resin bleed through thin film plasma deposition. Proceedings of SPIE--the international society for optical engineering 2003Vol. 5288pp 780-785

[3] Lee, N. Choi,S. Kang, S. Self-assembled monolayer as an antiadhesion layer on a nickel nanostamper in the nanoreplication process for optoelectronic applications, Appl. Phys. Lett. 88, 073101 (2006)

[4] Hutt, D.A. Liu, C. Oxidation protection of copper surfaces using self-assembled monolayers of octadecanethiol, Applied Surface Science, Volume 252, Issue 2, 15 October 2005, Pages 400-411

[5] Liu; C. Hutt, D.A, Fluxless Soldering of Copper Substrates Using Self-Assembled Monolayers for Preservation, Components and Packaging Technologies, IEEE Transactions on, Vol 29 , Iss 3 2006

[6] USPTO application no 61/266,611; Filed 04 December 2009. Surface treatments and coatings to reduce adhesive spread, Inventors: O. Williams, C.Liu, D.P.Webb, P.Firth. Assignee: Oclaro Technology plc

[7] Sah, A. Castricum, H.L. Bliek, A. Blank, D.H. Elshof, A.J.E. Hydrophobic modification of [gamma]-alumina membranes with organochlorosilanes, Journal of Membrane Science, Volume 243, Issues 1-2, 1 November 2004, Pages 125-132,

[8] Khatri, O.P. Biswas, S.K. Thermal stability of octadecyltrichlorosilane self-assembled on a polycrystalline aluminium surface, Surface Science, Volume 572, Issues 2-3, 20 November 2004, Pages 228-238,

[9] Tanoglu, M. McKnight, S.H. Palmese, G.R. Gillespie, J.R. Use of silane coupling agents to enhance the performance of adhesively bonded alumina to resin hybrid composites, International Journal of Adhesion and Adhesives, Volume 18, Issue 6, 1998, Pages 431-434

[10] Leger, C. Lira, H.D.L. Paterson, R. Preparation and properties of surface modified ceramic membranes. Part III. Gas permeation of 5 nm alumina membranes modified by trichloro-octadecylsilane, Journal of Membrane Science, Volume 120, Issue 2, 13 November 1996, Pages 187-195

[11] Lim, M.S., et al Adsorption and Desorption of Stearic Acid Self-Assembled Monolayers on Aluminum Oxide, Langmuir 2007 23 (5), 2444-2452

[12] Karaman, M.E. Antelmi, D.A. Pashley, R.M. The production of stable hydrophobic surfaces by the adsorption of hydrocarbon and fluorocarbon carboxylic acids onto alumina substrates, Colloids and Surfaces A: Physicochemical and Engineering Aspects, Volume 182, Issues 1-3, 30 June 2001, Pages 285-298

[13] Ullman, A., Formation and Structure of Self-Assembled Monolayers, Chemical Reviews 1996 96 (4), 1533-1554

[14] Foster, T.T. Alexander, M.R. Leggett, G.J. McAlpine, E. Friction Force Microscopy of Alkylphosphonic Acid and Carboxylic Acids Adsorbed on the Native Oxide of Aluminum, Langmuir 2006 22 (22), 9254-9259

[15] Steiner, G. Sablinskas, V. Savchuk, O. Bariseviciute, R. Jahne, E. Adler, H.J. Salzer, R. Characterization of self assembly layers of octadecanephosphonic acid by polarisation modulation FT-IRRA spectroscopy mapping, Journal of Molecular Structure, Volumes 661-662, Raman Spectroscopy and Molecular Structure, 16 December 2003, Pages 429-435

[16] Ulman, A. 1946- An introduction to ultrathin organic films : from Langmuir-Blodgett to self-assembly / London : Academic, 1991

[17] Taranets, N.Y. Jones, H. The influence of surface roughness and pre-oxidation state on the wettability of aluminium nitride by commercial brazes, Journal of Materials Science VL 39, IS 18, 2004/09/01/

[18] Thompson, W.R. Pemberton, J.E. Characterization of Octadecylsilane and Stearic Acid Layers on Al2O3 Surfaces by Raman Spectroscopy, Langmuir 1995 11 (5), 1720-1725

[19] Ulman, A. 1946- Characterization of organic thin films / Boston, Mass. ; London : Butterworth-Heinemann, c1995

[20] Laibinis, P.E. Whitesides, G.M. Allara, D.L. Tao, Y.T. Parikh, A.N. Nuzzo, R.G. Comparison of the structures and wetting properties of self-assembled monolayers of n-alkanethiols on the coinage metal surfaces, copper, silver, and gold, Journal of the American Chemical Society 1991 113 (19), 7152-7167

[21] Sandroff, C.J. Herschbach, D.R. Surface-enhanced Raman study of organic sulfides adsorbed on silver: facile cleavage of sulfur-sulfur and carbon-sulfur bonds, The Journal of Physical Chemistry 1982 86 (17), 3277-3279

[22] Jennings, G.K. Laibinis, P.E. Self-assembled monolayers of alkanethiols on copper provide corrosion resistance in aqueous environments, Colloids and Surfaces A: Physicochemical and Engineering Aspects, Volume 116, Issues 1-2, A collection of papers presented at the Wetting and Interfacial Phenomena Symposium at the 69th Annual Colloid and Surface Science Symposium, 16 September 1996, Pages 105-114

[23] Abel, E.W. Pollard, F.W. Uden P.C. Nickless. G.D. A New Liquid Chromatographic phase, Chromatogr. 22 (1966), p. 23

[24] Cohen, S.R. Naaman, R. Sagiv, J. Thermally induced disorder in organized organic monolayers on solid substrates, The Journal of Physical Chemistry 1986 90 (14), 3054-3056

[25] Matthias Geissler,, Heinz Schmid,, Alexander Bietsch,, Bruno Michel, and, Emmanuel Delamarche, Defect-Tolerant and Directional Wet-Etch Systems for Using Monolayers as Resists, Langmuir 2002 18 (6), 2374-2377

[26] Briggs, D. 1948- Practical surface analysis / Chichester : Wiley, 1990

[27] Hutt, D.A. Leggett, G.J. Functionalization of Hydroxyl and Carboxylic Acid Terminated Self-Assembled Monolayers, Langmuir 1997 13 (10), 2740-2748

[28] Graham, L. Bain, C.D. Biebuyck, H.A. Laibinis, P.E. Whitesides, G.M. "Damage to Trifluoroacetamido-Terminated Organic Self-Assembled Monolayers (SAMs) on Aluminum, Titanium, Copper and Gold by Aluminum Ka X-rays is Due Principally to Electrons" Journal of Physical Chemistry 1993, 97, 9456–9464.

[29] Schulze, M. Bolwin, K. Gülzow, E. Schnurnberger, W. XPS analysis of PTFE decomposition due to ionizing radiation, Fresenius' Journal of Analytical Chemistry, volume 353, Issue 5, pg 778-784.

[30] Brewis, D. M. Industrial adhesion problems / New York : Wiley, 1985

[31] Lee, L.H. 1924- Fundamentals of adhesion / New York ; London : Plenum Press, 1991

[32] Zhou, T. Wang, X. Mingyuan, G.U. Liu, X Study of the thermal conduction mechanism of nano-SiC/DGEBA/EMI-2,4 composites, Polymer, Volume 49, Issue 21, 6 October 2008, Pages 4666-4672, ISSN 0032-3861, DOI: 10.1016/j.polymer.2008.08.023.

[33] http://www.epotek.com/SSCDocs/datasheets/H20E.PDF Supplied with adhesive order and accessed 17-02-10

[34] Ebbens, S.J. Hutt, D.A. Liu, C. Williams, O. Surface Micro-patterning with Self-assembled Monolayers Selectively Deposited on Copper Substrates by Ink-jet Printing, Proceedings of the 57th Electronic Components and Technology Conference, 2007 pp.1362-1367

5.6 Laser Micromachining

5.6.1 Introduction

Laser technology is rapidly expanding in the manufacturing sector. Where previously the technology was limited to crude cutting and welding applications, advances have allowed the applications to expand to microelectronics manufacturing and laser micromachining. Due to the exemplary control of a modern laser system, the diversity of applications is impressive. However, the parameter range for the various applications such as cutting, drilling, micromachining and surface modification can be quite narrow. While lasers can be used in the manufacture of optoelectronic modules for the dicing and drilling of ceramics, these are delicate operations because of the properties of the materials. This difficulty has lead to the industry relying on more robust methods, such as diamond saw cutting and milling, to cut and shape the ceramic tiles. The limitations of such conventional machining methods are their inability to produce complex three dimensional structures. Much like the capabilities of a bench saw, only a two dimensional extruded profile is possible. This limitation can be seen in the design of the optoelectronic sleds, in which the substrate carries no surface geometries which can aid in locating components.

Components in optoelectronic circuits are frequently actively aligned in the assembly process and have inherent variation in their dimensions. This means that some components must be shaped or ground to match steps in the substrate material, and that all assemblies must undergo a time consuming active alignment process. Laser machining could offer a solution to both substrate shaping and the active alignment issues in the design and assembly of optoelectronic packages. A further limitation of optoelectronic manufacture is the epoxy bleed phenomenon, i.e. the separation of adhesive components and their wetting across a substrate onto sensitive areas. Laser machining could offer a solution to this issue by the creation of barriers to the spread, or selectively polishing areas to make epoxy bleed less favourable[1].

Examples of 3D surface geometric features which could machined into ceramic surfaces to improve the optoelectronic assembly process are shown in Figure 5.6-1. These are: the machining of bleed control features, three dimensional structuring of the sleds for presenting components at the correct height for beam paths, and machining of passive alignment features for a reduction in the active alignment process time. The work reported here focussed on the problem of epoxy bleed, however the feasibility of three dimensional structuring and passive alignment features production is considered briefly in the discussion below.

As shown in the figure bleed control/lens alignment features could simultaneously offer passive alignment and bleed control properties. These could be recesses which position ball lenses in two dimensions and prevent the spread of lens mounting adhesive due to near vertical side walls. Other passive alignment features can be machined to match dimensional variation in component parts[5], such as the planar material removal area which allows alignment of the laser diode with the ball lens. V-grooves laser machined into the optoelectronic substrate could be implemented for passive alignment, reducing the passive alignment time required.
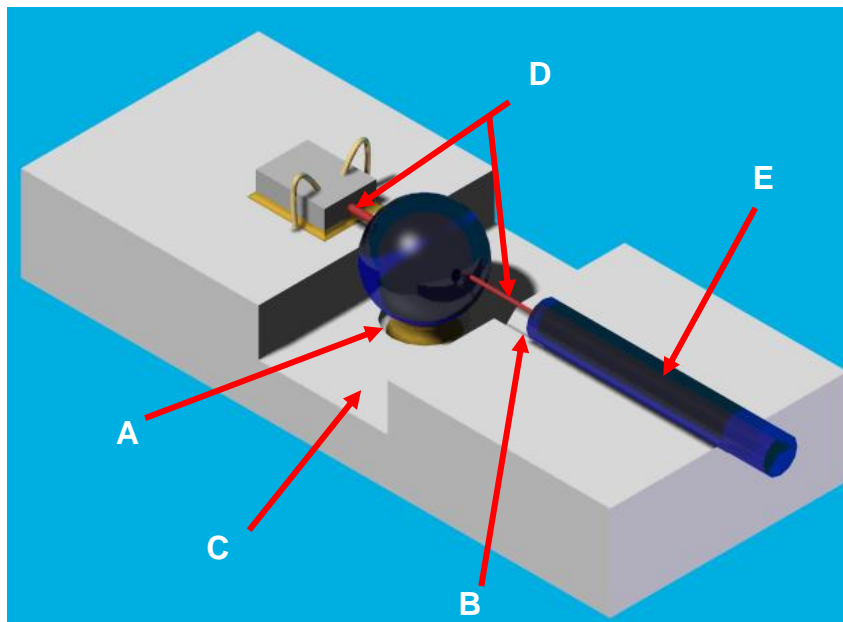
Figure 5.6-1 Applications of laser machining in optoelectronics' manufacturing. (a) laser machined lens alignment and bleed control circular recess with vertical side walls, (b) laser

---

[5] Communication from Paul Firth of Oclaro plc. Lenses have an inherent variability in their dimensions which must be accounted for in the assembly process.

machined v-groove for optical fibre passive alignment, (c) laser machined planar material removal for dimensional variation tolerance or bleed control, (d) laser beam, (e) optical fibre.
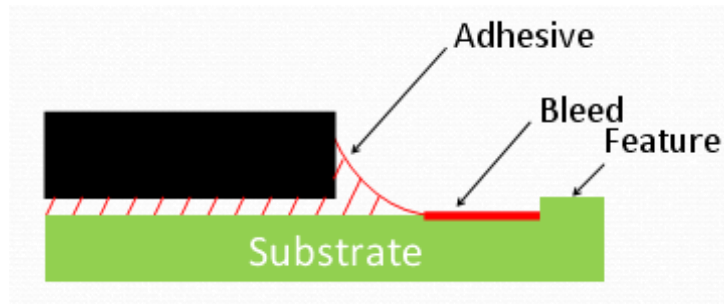
Figure 5.6-2 Epoxy bleed control by a laser machined barrier.

Figure 5.6-2 shows in more detail the concept of laser machined flow stops for epoxy bleed control. The high spreading tendency of epoxy bleed would be counteracted by a vertical wall which would act as a flow stop since it is thermodynamically unfavourable for the liquid to climb the wall.

Laser surface modification is a further method which could be employed, primarily for features to control epoxy bleed. It differs from laser machining insofar as the objective is to induce chemical, physical or crystallographic changes rather than the manufacture of physical artefacts. Both increase of roughness and polishing can be achieved with the correct parameters. The work reported in *Section 5.2* showed that high quality polishing of surfaces reduced the tendency for epoxy bleed to spread a large distance. Although it was not inhibited entirely its occurrence was controlled to a distance consistently <50µm.

The literature survey produced few examples of laser machining ceramics with CO_2 lasers. The work undertaken began with a preliminary study focussed upon finding the optimum parameters for CO_2 laser induced material removal. Firstly, single tracks were machined and characterised quantitatively and physically with an SEM and a Talysurf machine. The most effective laser parameters were then applied to create more complex machined areas through multiple overlapping laser passes. The usefulness of some of these features for epoxy bleed control, and passive alignment processes was considered. Bulk material changes induced by the laser processing were explored with X-ray diffraction (XRD) and nanoindentation.

Excimer laser processing of ceramics is widely reported in the literature, however, the range of parameters quoted for effective machining of aluminium oxide and aluminium nitride is wide. This range of parameters was investigated on the polycrystalline substrates used throughout this work. Features were machined with passive alignment and epoxy bleed functionality in mind, which differed from the objectives of the work published in the literature. Features were characterised quantitatively and physically with an InfiniteFocus surface texture measurement machine and an SEM.

It was found that near vertical walled features could block the flow of epoxy bleed. However, the machined areas produced were not of adequate dimensional accuracy for direct usage as passive alignment features for sub micron component placement.

5.6.2 Background

Lasers offer a non contact process capable of delivering specified amounts of photon energy to a highly localised area. The interaction between laser and target is dependent on the properties of the target material and the beam properties. Power, frequency, duty cycle and target area are all controllable to some degree with modern lasers, although changing the wavelength of the laser usually involves changing the type of laser being used. For the purpose of this investigation a CO_2 laser and excimer laser were used, each offering different material removal mechanisms and greatly different wavelengths.

CO_2 laser processing is an example of a thermal process where thermal energy is used to melt and vaporise material. Alternatively the laser material removal mechanism can be ablation – the breaking of chemical bonds and resultant vaporisation of the material. Excimer laser processing is an example of this.

Al_2O_3 and AlN are notoriously difficult to machine using conventional laser machining methods. This is largely the result of their brittle nature and high hardness which leads to fractures in the event of localised heating[2]. There is little evidence of efforts made to micromachine these materials using CO_2 lasers with the aim of 3D structuring of the surfaces. However drilling and cutting using a CO_2 laser is well documented for green Al_2O_3[3] and sintered

AlN[4]. Excimer lasers have the advantage that only a small amount of heat is transferred to the substrate in the machining process. The disadvantage of an excimer laser is the material removal rate. The process is a precision one making it unsuitable for large scale machining. Although Increasing excimer laser fluence is seen to increase ablation rate, a threshold value is then reached above which the ablation rate decreases[5]. A maximum ablation rate of 0.2µm/pulse is reported for AlN. Excimer laser machining has been successfully used for the surface treatment of Al_2O_3 to both reduce and increase surface roughness[6]. Increase of surface roughness as an effect of excimer laser machining of AlN is well documented[7]. Close to vertical side walls for excimer machined features have also been reported in literature[8], which are desirable for this application.

5.6.2.1 The CO2 Laser

A CO_2 laser is typically of 9.4-10.6µm wavelength, lying in the infrared part of the electromagnetic spectrum. CO_2 lasers can be used in continuous wave mode or pulsed mode. For this work a pulsed CO_2 laser was used to limit the energy input into the sample, as shown schematically in Figure 5.6-3.
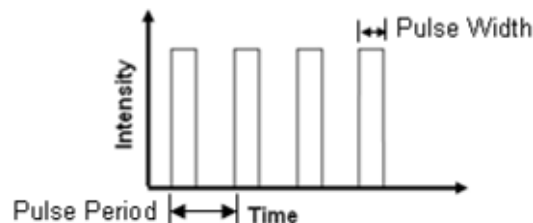
Figure 5.6-3 Energy intensity over time for a pulsed CO_2 laser.

The generated infrared beam of a CO_2 laser produces a Gaussian intensity distribution across the diameter of the spot incident on a surface, which can be described by:

$$I_{(r)} = I_o e^{\left(\frac{-r^2}{d^2}\right)}$$

Equation 5.6-1 Energy intensity from a CO_2 laser. Where I_o is the intensity in the centre of the spot, d is the Gaussian beam radius and r is the radial distance from the centre of the spot.

The energy intensity can also be considered in terms of depth into the material z:

$$I_{(z)} = I_o e^{\left[\left(\frac{4\pi}{\lambda}k'n\right)z\right]}$$

Equation 5.6-2 Beam intensity for a given depth into a material. Where I_o is the laser beam intensity at the surface (z=0), λ is the wavelength of the laser, k' is the material extinction coefficient and n is the material refractive index.

In Equation 5.6-2 the term $\frac{4\pi}{\lambda}k'n$ is the absorption coefficient (α) for the material considered, where the skin depth, or depth to which the laser affects the material is given by $1/\alpha$.

For the CO_2 laser the primary mechanism of material/laser interaction is Fresnel absorption. This is when the photons of the laser beam interact with the electrons of the material inducing vibrations, and because of this, heat. Infrared lasers have a comparatively long wavelength (10.6µm for a CO_2 laser compared to 248nm for a KrF excimer laser) which means that the photons are of low energy, so that more are needed to be absorbed by the material in order to remove it. For a laser of low photon energy, heating, melting, boiling and vaporisation all occur as the cumulative amount of energy delivered to the material increases. This makes CO_2 laser machining a photo-thermal process.

5.6.2.2 The Excimer Laser

The excimer laser, due to the wavelength being similar to the excitation energy of the material bonds, has the ability to break bonds directly without having to rely on the same heating→ melting→ boiling→ vapourisation mechanisms of a thermal process such as the CO_2 laser. The mechanism is known as scission and is a photo-chemical process which ablates small areas of material with each pulse accompanied by relatively small thermal energy input into the bulk material. In excimer laser processing attenuators (electro-optical circuits), are used to vary the throughput of laser energy to the optics without changing the temporal or spatial beam profile[11].

The threshold in fluence seen in excimer ablation rate occurs because of the formation of a plasma above the surface which absorbs some of the incident

energy, and because of the re-ablation of deposited debris left by previous pulses[5]. The debris deposited on the surface can also make accurate measurement of the processing depth difficult.

Higher energy densities can also lead to thermal affects effects such as increased melt phases, increased deposits in adjacent regions to the irradiated area and an increase in breakouts in the structure all of which can hinder the creation of smaller features[9]. From the results presented later in this chapter it appears that these thermal effects limit the ideal processing fluence, or energy density, for creating high quality structures to about $10J/cm^2$.

The fluence can be used to control the sidewall angle of the features. Lower fluences often cause a reduction in effective feature size with increasing depth, resulting in an angle >90°. Higher fluences are prone to causing undercut and producing a sidewall angle <0°. Fluence must therefore be optimised to produce side walls of the usually desired 0° angle.

Ablation rates up to 0.2 μm/pulse have been achieved when laser machining AlN with a KrF excimer laser with a fluence of $30J/cm^{2}$[10]. However, this was performed in a vacuum and a fluence about 50% higher than one would expect in air.

Excimer lasers which produce shorter wavelength laser light offer the best processing capabilities in terms of removal rate. In processing a variety of ceramics, including Al_2O_3, it has been shown that the threshold fluence is lower when processing with shorter wavelength lasers[11]. This is due to the shorter wavelength giving more effective excitation of the molecular bonds and so faster ablation.

It has been shown[12] that a decrease in pulse width also leads to an increased ablation rate of alumina and other ceramics. This is due to a higher intensity impulse favouring localised material excitation and vaporisation over thermal transmission. Due to this excimer laser machining with shorter pulse widths reduces the threshold fluence for a material.

An initial linear correlation exists between the number of pulses and the depth of the machined area. This relationship has been demonstrated in several

works[13]. However, previous work[5] has shown that the ablation rate can remain constant with depth only to a few microns into the material. One reason is the aforementioned plasma formation interfering with subsequent pulses. A second is that the material surface may move out of the focal plane of the laser. For this reason movement of the sample during processing to maintain focal plane alignment with the surface may be necessary.

It is shown in previous work[9] that the ablation rate (μm/pulse) of Al_2O_3 is affected by the size (and possibly shape) of the laser profile on the substrate surface. The reason for this is the escape mechanism of the plasma formed upon irradiation, i.e., a large feature allows plasma to expand unimpeded. A smaller feature can create a higher pressure due to the limited space for the plasma to expand into, resulting in the plasma leaving the surface parallel to the laser path.

It has also been shown that the surface roughness of the irradiated area can affect the ablation rate. A rougher surface has a greater tendency to absorb laser energy[11].

Some workers have reported[9] that when machining Al_2O_3 the ablation rate decreases with increasing pulse repetition frequency, possibly due to the escape of plasma impeding ablation at high frequencies. This is disputed by other authors[5] who have suggested that repetition rate has little influence on the processing of ceramic material. This seems more probable as the laser/material interaction period for a typical nanosecond laser is so short compared to the inter pulse spacing that each individual pulse and its interaction with the surface can be considered separate events.

Previous reports have shown that surface texture of the excimer laser irradiated area which remains following ablation is affected by the fluence and number of pulses. It is possible to use the excimer laser radiation to control surface roughness to desired amounts. This has been demonstrated[14] on Al2O3 where the effect of a fluence slightly above the threshold for the material yielded a large increase in roughness. Reduction in the surface roughness is believed to occur from the melting and re-solidification of the surface material during irradiation[15] . In the work reported here it was found

that increasing the number of pulses above 50 has the effect of increasing roughness, after an initial reduction in roughness for less than 50 pulses.

Other work[16] which studied the effect of fluence on the surface texture has shown that for a constant number of pulses, low enough fluences will merely clean the surface and will not affect the topography of the ceramic material. It has been reported that excimer laser machining of Al_2O_3 by fluences of 150mJ/cm^2 and 300mJ/cm^2 produced no measureable change to the physical surface properties. Increasing the fluence to 500mJ/cm^2 led to reduction of the surface texture profile depth (peak to valley height, R_t value), which was attributed to the melt and solidification mechanism previously described. For fluences of 1.5J/cm^2 and above ablation and not just surface modification occurred. These trends are seen consistently in similar work[17].

Work has been carried out to establish the capability of the excimer laser for physical surface modification rather than micromachining[13]. This work identified a limit of around 0.15µm in R_a to the polishing capability of an excimer laser.

Previous work[5] has shown that ablated material redeposits on the substrate surface regardless of processing parameters. The work also highlighted that redeposited material is easily removed with a solvent clean, or with ultrasonics.

Work has been carried out to assess the effects of excimer radiation on the bulk material properties of Al_2O_3[18]. The fracture toughness of pure polycrystalline sintered ceramics is generally poor but it can be improved by laser polishing as this removes areas of high stress concentration which act as crack initiators. Increased fracture toughness seen in excimer laser irradiated Al_2O_3 is also due to the formation of γ-Al_2O_3. This introduces a compressive stress in the surface which increases the fracture toughness due to any externally applied force having first to overcome the counteracting compressive residual stress to cause failure. The new phase was detected using X-ray Diffraction (XRD), where a peak which corresponded to γ-Al_2O_3 was reported at 2θ = 45.70°. The combined effects of the modified surface texture and crystal orientation resulted in a 40% increase in fracture

toughness. Further XRD studies of excimer laser processed Al_2O_3 ($7J/cm^2$ 100 pulses) showed peaks corresponding to α-Al_2O_3, θ-Al_2O_3 and γ-Al_2O_3. Spectra of the unprocessed materials exhibited peaks for only the α and θ phases[6]. This is consistently reported throughout the literature[16].

5.6.3 Methodology

The aim of the work in this chapter was to determine the feasibility of 3D functionality into the optoelectronic ceramic substrate materials using lasers. For CO_2 laser machining, relevant literature was limited. With regards to excimer laser machining, dimensional accuracy, repeatability and machining features for a specific application were not found to be tackled in the literature.

Firstly, preliminary studies were performed with the CO_2 laser to find the optimum parameters for material removal. Then machining of defined features was attempted. The goal was vertical, i.e. 0° side walls as defined in Figure 5.6-4, and roughness comparable to the unprocessed ceramics of $\leq$0.25μm R_a value. These were desired due to the effect of roughness on epoxy bleed, *Section 5.2 Surface Parameter Effects on Epoxy Bleed,* the increase of geometric inaccuracy with increasing roughness, and the assumption that a near vertical sidewall would stop the spreading of the bleed material.
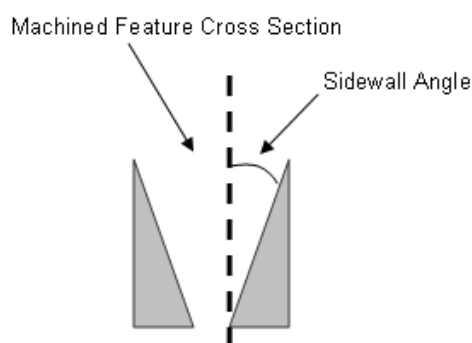
Figure 5.6-4 A diagram depicting a cross sectional view to define the sidewall angle of a machined feature. The grey area is the bulk material.

Excimer laser machining was performed with the intention of increasing the dimensional accuracy of CO_2 laser machined areas, and reducing their roughness. The KrF laser was also implemented as a single process with the same aims as the CO_2 laser method.

Characterisation was carried out to assess the machined artefacts for effectiveness in the applications indentified in *Section 5.6.1 Introduction.*

Methods implemented included qualitative: SEM, surface profiling, and stereo microscopy, and quantitative: surface profiling, XRD and nanoindentation. XRD and nanoindentation were performed to investigate bulk material changes which could detrimentally affect the substrate materials' functionality.

5.6.4 Experimental setup

The materials tested were 99.6% Al_2O_3 and 99% AlN which were supplied as 75mm square tiles 1mm thick, as used for the work described in *Section 5.3 Identification and Removal of Contamination*. The tiles were processed similarly to *Section 5.3 Identification and Removal of Contamination*, being diced using a CO_2 laser and thoroughly cleaned before processing, as described in *Section 4.1 Ceramic Sample Preparation*. Initial characterisation revealed the samples to have a granular surface finish with R_a values between 0.2-0.25µm.

All CO_2 laser machining was done with a 150W 10.6µm infra red laser produced by Coherent with a fixed, nominal beam width of 300µm. Pulse width, traverse speed and pulse period were all controllable manually. For the experiments The pulse width (interval between laser energisations) was fixed at 500µs and the pulse period (duration of the laser energisation) was varied from 1µs to 250µs. The duty cycle, the percentage duration of the pulse period with respect to the pulse width (i.e. 50% duty cycle = 500µs pulse width and 250µs pulse period), is the variable quoted in the results section. The laser spot position was fixed and the sample was placed on an x-y table to provide the lateral machining movements. The traverse speed used was in the region of 100mm/s to 400mm/s, due to cracking occurring at slower speeds, and separation of melt pools at higher speeds, as reported below. The laser operation and x-y table movements were controlled by CNC instructions.

Excimer laser machining was carried out by mask projection processing using a KrF 248nm laser source. The mask sizes and shapes used were a 1mm diameter circular hole, a 5mm on a side square and a 15mm on a side square. The optics were fixed at 10x reduction giving a machined area 1/10 of the mask size. Samples were kept stationary during irradiation. The pulse

energy at the mask was fixed at 250mJ/pulse and the repetition rate at 15Hz unless otherwise stated. The fluence incident on the sample was adjusted via an attenuator. The position of the attenuator is quoted in this work as fluence measurement equipment was not available. A higher attenuator number corresponds to a lower attenuation, i.e. higher fluence.

5.6.4.1 Evaluation and Analysis

SEM

Due to the insulative properties of the ceramics all samples had to be given a metallic coating prior to SEM analysis. This was done via vacuum coating of gold.

Surface metrology

The Talysurf CLS 2000 was used for non-contact profiling of machined features. Features were analysed in a number of areas with multiple profiles measured for each to show heterogeneity of the geometries. Features were also analysed using the InfiniteFocus 3D surface measurement equipment which allows the imaging and measurement of vertical features. For more details see the experimental methods chapter, *Section 4 Experimental Procedures.*

X-ray diffraction

X-ray diffraction (XRD) was performed with a Bruker D8 X-ray diffractometer on CO_2 laser processed samples to identify any crystallographic changes. Al_2O_3 was analysed from 15-80° and AlN from 20-90°. The samples analysed had undergone planar material removal for a 10mm wide section across their surface using the CO_2 laser. The machining was done with a beam offset of 90μm, a duty cycle of 10% and a traverse speed of 100mm/s. The area analysed was the surface which underwent the laser treatment.

Nanoindentation

Nanoindentation was performed on cross sections of CO_2 laser machined ceramics in order to gauge changes in the mechanical properties of the bulk material as a result of laser machining. At least 6 indentations were performed on each section, which had been previously mounted and polished to expose

the crystal structure. Al_2O_3 was indented at 3mN/s to a maximum load of 200mN, with a dwell time set at 90s before unloading at 3mN/s. AlN was indented at 2mN/s to a peak load of 50mN. The dwell time was again set at 90s and the unloading rate was equivalent to the loading rate. All indentations were performed with a pyramidal Berkovich indenter.

5.6.5 Results

5.6.5.1 CO2 Laser Machining

The optimal settings for surface machining to achieve planar material removal were found experimentally, as no data had been located in the literature . The variables considered were traverse speed and duty cycle. Figure 5.6-5 below shows the effect of traverse speed on the machined channel topography. 100mm/s was judged to be the best result and was adopted for all future machining.
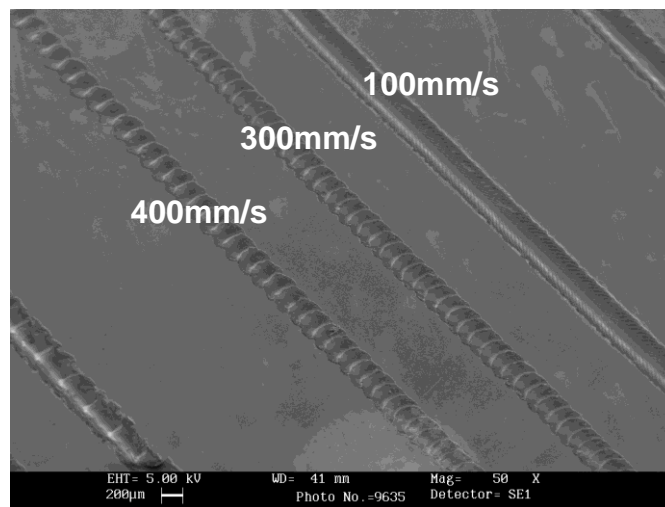
Figure 5.6-5 Traverse speed effect upon machining Al_2O_3. 400mm/s, 300mm/s and 100mm/s shown at 50x magnification, machined with a 10% duty cycle.

The offset between traverses for rastering was next optimised. At a traverse speed of 100mm/s the machined channel width produced is 150µm. The optimised offset was found to be a large fraction of this at 90µm. A shorter offset was found to create excessively deep and inconsistent channels whilst a longer offset left ridges of unaffected material in areas at the edge of the

channel, where the energy density of the beam was too low to induce effective removal.

The SEM image in Figure 5.6-6 illustrates the effectiveness of the CO_2 laser for planar material removal on Al_2O_3 using the identified parameters. The feature widths are 1mm, 1.25mm and 1.4mm. A crust was formed on the Al_2O_3 during machining which was loosely attached to the machined area beneath. This is shown in more detail in Figure 5.6-7.
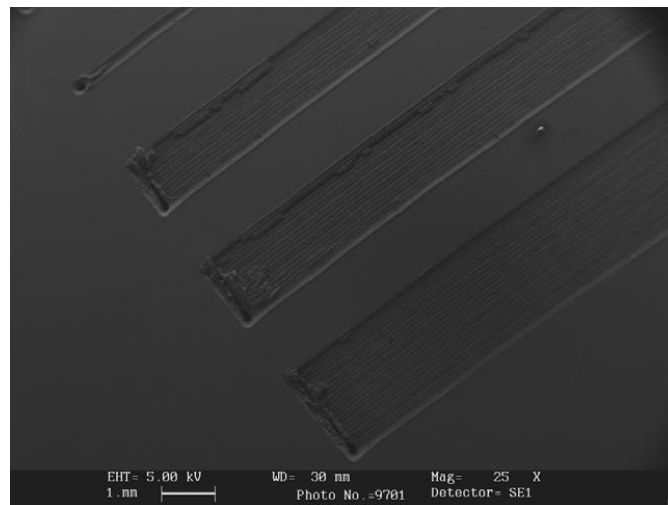
Figure 5.6-6 SEM image of planar material removal with a CO_2 laser on Al_2O_3. 90µm spacing between laser tracks, 25x magnification.
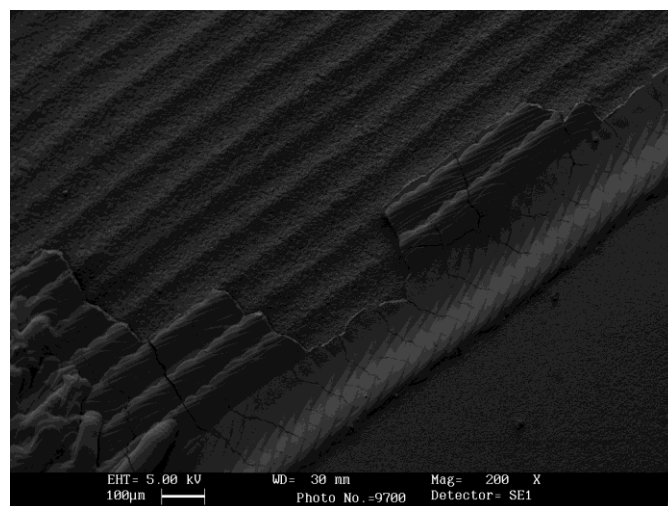
Figure 5.6-7 SEM image of the crust formed on Al_2O_3 during CO_2 laser machining.

Planar material removal on AlN was also achieved with the same parameters, producing features similar in quality and roughness to Al_2O_3. The depth of machining for a single pass process was 60µm for AlN and 40µm for Al_2O_3 (once the machined material was removed). Multi pass (i.e.; repeat rasters over previously treated material) areas were also machined for both AlN and Al_2O_3, which saw an increase of depth proportional to the number of passes as expected.

The same parameters were used to machine discrete, limited area features. Different laser paths were tested and are shown in Figure 5.6-8.
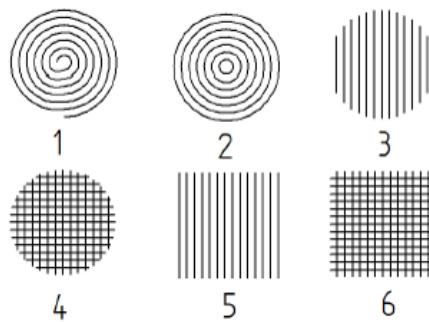
Figure 5.6-8 Laser machining paths used for CO_2 machining discreet areas of AlN and Al_2O_3. All laser tracks have a 90µm offset.

Excessive energy input into small areas of the ceramic materials was seen to induce fracture during the machining process, especially on Al_2O_3 for patterns 1, 4 and 6 shown in Figure 5.6-8. Of the different spot movement patterns used to machine a discreet circular feature, a series of parallel lines, method 3 in Figure 5.6-8, consistently produced the best results. Figure 5.6-9 shows a 1.25mm diameter laser machined circle using pattern 3 in an Al_2O_3 surface. The same weakly adhered crust is seen with this feature as with the planar material removal. Figure 5.6-10 shows the same feature/pattern machined into an AlN surface with the CO_2 laser.
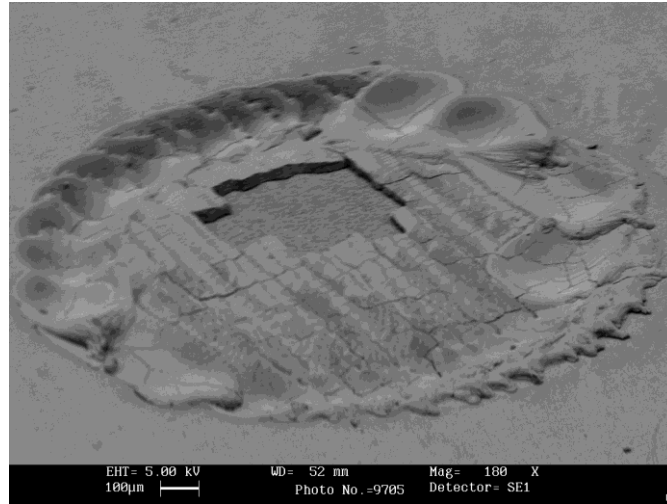
Figure 5.6-9 SEM image of a CO_2 laser machined 1.25mm diameter circle in an Al_2O_3 surface.
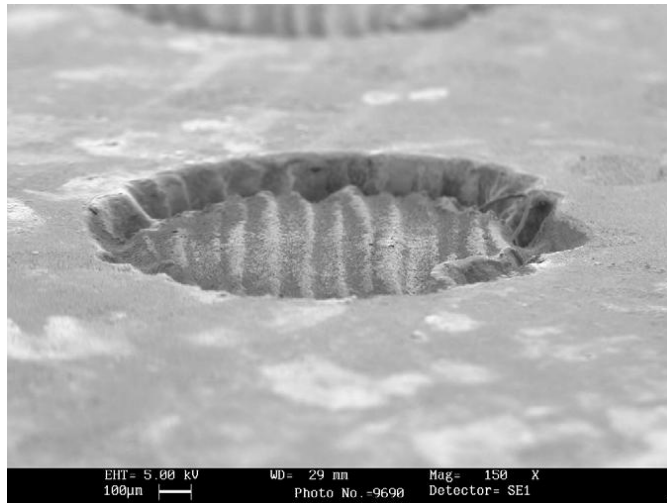
Figure 5.6-10 SEM image of a CO_2 laser machined 1.25mm diameter circle in an AlN surface.

The depths of machined features were consistent with the large area treatments (40 and 60µm), as was the roughness of the laser affected area. The laser processing was seen to increase the roughness by a large amount, as measured with the Talysurf. The unprocessed materials had a maximum roughness of 0.25µm R_a, and the laser machined areas 4.5µm R_a.

Nanoindentation measurements were used to measure changes in the material properties due to the effect of the infrared energy input, see Table 5.6-1. These were done on cross sections of the material due to the excessive roughness of the planar surface.

Material	Al_2O_3	AlN
Hardness (GPa)	17.29±0.78	11.25±1.73
Reduced Modulus (GPa)	196.32±6.87	186.70±23.37
Plastic Depth (nm)	860.68±17.57	407.38±29.27
Material	Laser Al_2O_3	Laser AlN
Hardness (GPa)	15.21±1.32	7.86±2.23
Reduced Modulus (GPa)	188.22±8.36	173.27±41.2
Plastic Depth (nm)	715.15±33.17	505.54±85.54

Table 5.6-1 Nanoindentation results for unprocessed and laser processed ceramic cross sections.

The X-ray diffraction spectra of unprocessed CO_2 laser processed AlN and Al_2O_3 are shown in Figure 5.6-11 and Figure 5.6-12.
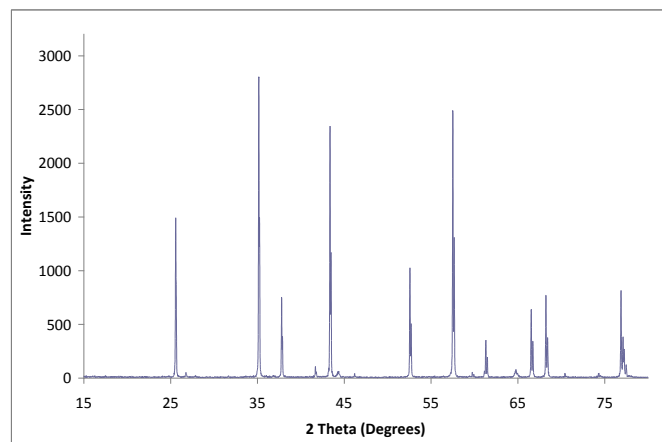
Figure 5.6-11 XRD spectra of unprocessed Al_2O_3
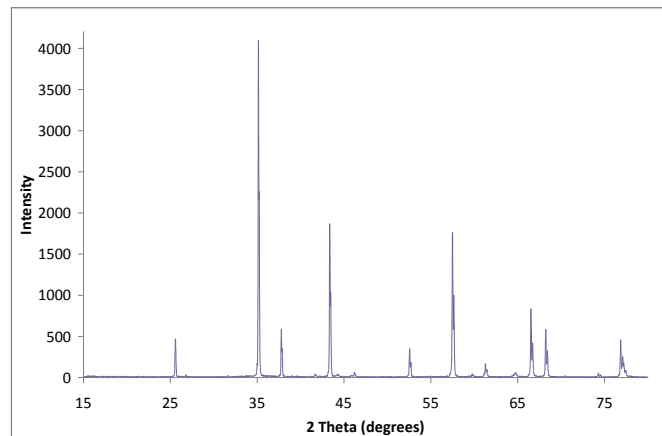
Figure 5.6-12 XRD spectra of CO_2 laser processed Al_2O_3 (10% duty cycle, 100mm/s traverse speed)

Figure 5.6-11 and Figure 5.6-12 show a change in peak ratios following laser processing. The AlN spectra showed a decrease in the peak intensity at a diffraction angle of 27° following laser processing, but also the appearance of small peaks at 31.9°, 36.9° and 38.5°. These peaks increased in intensity with increased laser power used for machining, Figure 5.6-13.
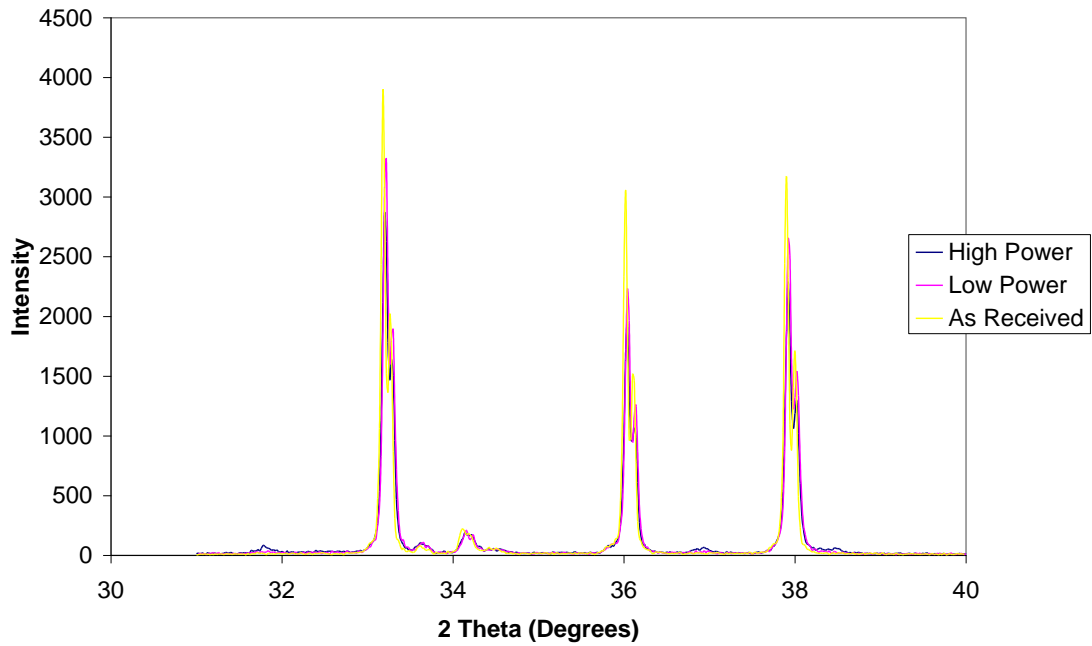
Figure 5.6-13 XRD spectra for 21-40° area showing small peaks for an AlN sample processed at high power at 31.9°, 36.9° and 38.5°.

Epo-Tek 930-4 and H20E adhesives were applied to 1.4 mm width linear laser machined areas on Al_2O_3. Bleed was seen along the direction of the laser path, but the side walls of the features stopped bleed perpendicular to the laser path, Figure 5.6-14.
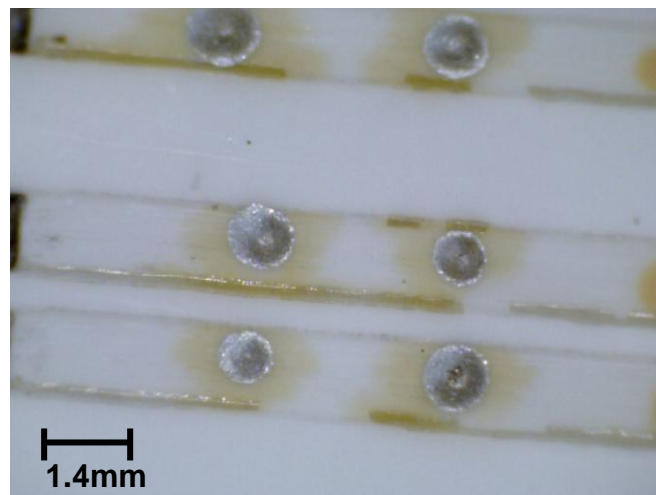
Figure 5.6-14 Epoxy bleed control from a silver filled epoxy adhesive on an Al_2O_3 surface machined by CO_2 laser. 1.4mm width planar material removal with 90μm beam path spacing and 10% duty cycle.

5.6.5.2 Excimer Laser Machining

Excimer laser machining was undertaken with the aim of producing localised polishing of surfaces and machining of repeatable features. Columnar topographies were seen to be created at fluences just above the threshold fluence of the materials. This is consistent with findings reported in the literature[6]. The attenuator setting corresponding to the threshold fluence of the materials was 0.4 for Al_2O_3 and 0.5 for AlN. Below these no visible effects on the materials due to laser irradiation was apparent. Figure 5.6-15 shows an area of an Al_2O_3 sample which was excimer laser machined with the aim of polishing the surface with minimal material removal. It was prepared with 30 pulses at 10Hz with an attenuator setting of 0.7. The machined feature had an average depth of 4µm as measured with the InfiniteFocus. The polishing effect (considered to be a measured decrease in R_a value) was seen consistently on Al_2O_3 surfaces with 30 pulses and AlN surfaces with 180 pulses. Varying the fluence over attenuator settings of 0.4-0.7 did not change the surface texture, but the machined depth increased with increasing fluence. The roughness of the machined area decreased with increasing depth, until the processing depth went beyond the depth of the roughness profile, as for example in Figure 5.6-15.
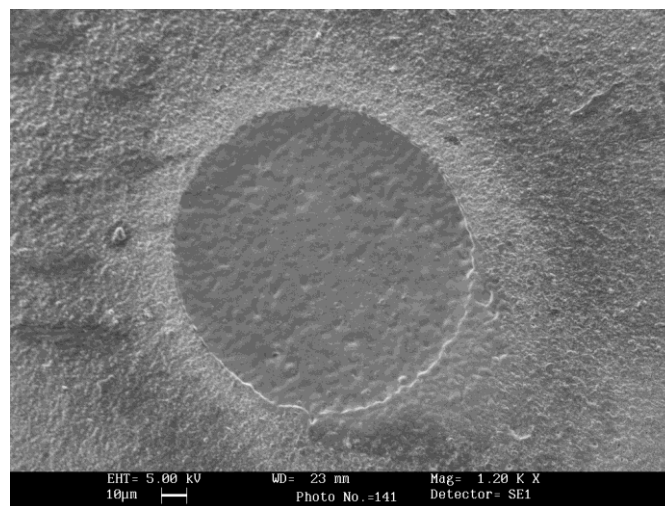
Figure 5.6-15 Excimer laser polished area of an Al_2O_3 surface, diameter 100µm.

It was found not possible to use AFM to assess the surface roughness of the machined area, because of debris on and around the surface of the machined areas interfered with the measurements.
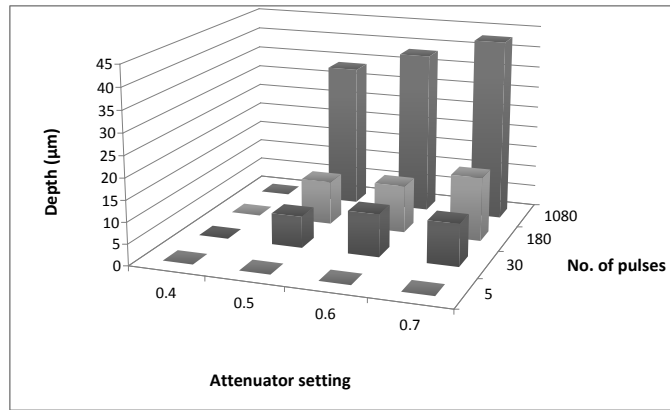
Figure 5.6-16 Depth of machined features compared to processing parameters.
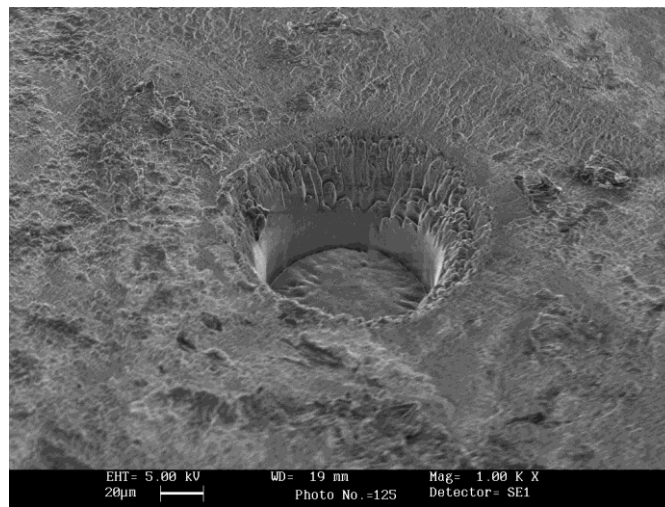
Figure 5.6-17 Excimer laser machined circular hole machined into Al_2O_3. 1080 pulses with attenuator setting of 0.7.

Figure 5.6-16 shows the machined feature depth as measured with the InfiniteFocus, compared to the attenuator setting and the number of pulses. The relationship among the variables is consistent with the literature. Figure 5.6-17 and Figure 5.6-18 show excimer laser machining of AlN. The features created are very similar in depth and topography to the Al_2O_3 features.
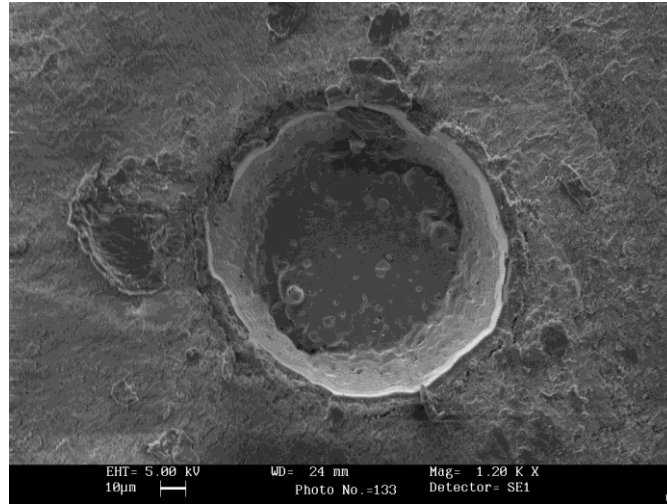
Figure 5.6-18 Excimer laser machined circular hole machined into AlN, 1080 pulses, attenuator setting 0.7.

5.6.5.3 Combined Laser Machining

The excimer laser was used on CO_2 laser processed samples to attempt to simultaneously exploit the high material removal rate of the CO_2 laser and the precision and polishing properties of the excimer laser. Figure 5.6-19 shows the results of differing amounts of excimer laser polishing on a CO_2 laser processed rough area.
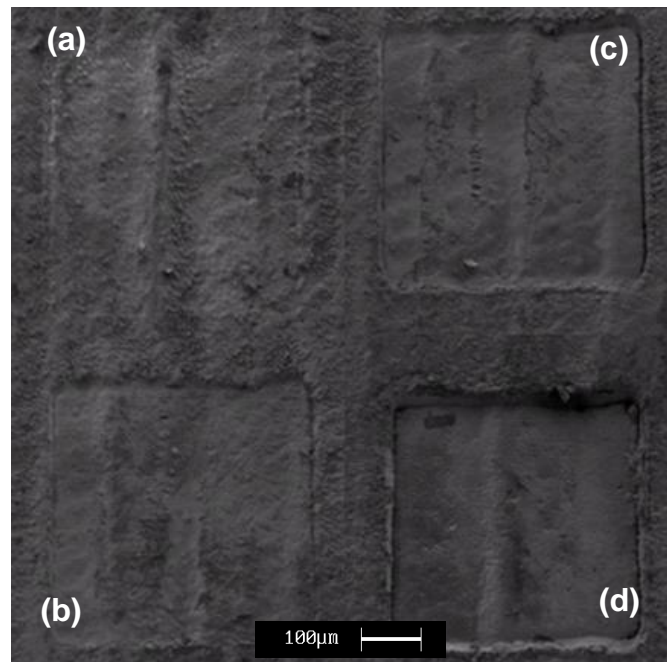
Figure 5.6-19 Polishing of a CO_2 laser produced rough surface by excimer laser machining, (a) 50 pulses (b) 150 pulses (c) 300 pulses (d) 1000 pulses. Attenuator 0.6.

Much data was gathered on the repeatability of the machining processes. There was found to be less than 5% variation in the machining depth for excimer laser machining. It was found not possible to obtain a figure for the repeatability of the CO_2 laser processing due to the excessive roughness.

5.6.6 Discussion

As might be expected clear correlations were seen between the energy delivered into the sample and the amount of material removed with both lasers. The lower the traverse speed and the higher the duty cycle the higher rate of material removal.

The CO_2 laser material removal mechanisms were clearly different between AlN and Al_2O_3. The Al_2O_3 appeared to melt upon irradiation and migrate to form ridges at the edge of the melt pools. The resolidified ceramic was then loosely attached to the underlying material and easily broke off. Figure 5.6-7 shows the remnants of this crust, and the cracks in it. This crust became an issue when machining smaller features such as in Figure 5.6-9. Here the crust was not easily removed leaving the machined feature uncompleted. The formation of this crust is probably due to the high vaporisation energy of the material. The heat due to the laser irradiation was sufficient only to melt the material and not to 'burn' it away. This crust if not removed could be detrimental to the reliability and functionability of optoelectronic modules. For example poor adhesion of the crust could induce failure of adhesive bonds due to the delamination of the underlying material. Discontinuity in the bulk material could also affect the thermal conductivity due to the inclusion of a thin layer of air under the melted crust. Figure 5.6-9 shows this layer of air to be a number of microns thick, below a crust of 35µm thickness. No crust was seen to form during the machining of AlN, suggesting the material had vaporised. However some redeposition over the surface was seen. It may be that masking the surface prior to machining would be beneficial. Using the CO_2 laser it was possible to achieve high speed planar material removal on both of the ceramics. However the Al_2O_3 does require post processing to remove the crust which formed.

Numerous attempts were made to modify the CO_2 machining parameters and movement patterns to improve the machined surface quality, but all were unsuccessful. This is due to the gaussian profile produced by each laser pass in the material surface, so that even with multiple passes a minimum R_a value of 4.5µm was produced. This is too great for optical assemblies which require sub-micron height accuracy. The R_t value (maximum peak to height distance) for all CO_2 laser machined surfaces was ~30µm, showing a large amount of variability created in the surfaces by the machining. It therefore seems unlikely that any further improvement in machined surface quality could be achieved with the CO_2 laser process, at least with the equipment used

The XRD results, Figure 5.6-11 and Figure 5.6-12, show changes in the peak intensity ratios following laser machining of the Al_2O_3. Although this suggests some reorientation of some of the crystals, because all of the peaks correspond to α-Al_2O_3 both before and after laser machining, there is no evidence that major crystallographic changes have taken place, in contrast to previous reports[6]. The results for AlN show additional small peaks following CO_2 laser machining at 31.9°, 36.9° and 38.5°. The 31.9° and 38.5° peak correspond to (220) and (111) FCC aluminium nitride crystals, where all other peaks correspond to hexagonal crystal structure. However, the peak heights are so small, Figure 5.6-13, that any effects on the properties of the bulk material are highly unlikely. The peak appearing at 36.9° does not appear for aluminium nitride in the XRD database[19] and is of unknown origin.

The nanoindentation results shown in Table 5.6-1 show a reduction in the hardness and reduced modulus of both of the ceramics after CO_2 laser machining. This suggests damage extending deeper into the bulk than the directly laser machined regions.

The effect of excimer laser machining of AlN was consistent with that reported in the literature[5,8]. Similar ablation rates were achieved and feature geometries created, along with the formation of an aluminium metal film over all irradiated surfaces (assumed to be this as it is seen in the literature[5]) on the machined areas. Polishing of small areas up to 0.5mm diameter was achieved with good repeatability. However, processing of larger areas >1mm diameter was not achieved as a single process with a large mask size. It was

seen that with a large mask size the process produced features of poor machined depth homogeneity, possibly due to the lack of a beam homogeniser on the setup used. Al_2O_3 was consistently machined at a higher ablation rate than AlN at lower fluence and pulse number, possibly due to the higher thermal conductivity of the material. At higher fluences and pulse number the ablation rate was seen to be similar for both materials, suggesting that with deeper features the machining is limited by feature geometry rather than material properties. The depth of machined featured after 1080 pulses at an attenuator setting of 0.7 was 43µm for both materials, Figure 5.6-17 shows that the ablation rate reduces with increased number of pulses, probably due to the mechanisms associated with increased escape depth described in the background section. Tapered side walls are also seen in Figure 5.6-16 and Figure 5.6-18. This is probably due to the focal plane of the laser being fixed at the original surface of the ceramics. Thus as the ablation depth increases the laser spot becomes less focused, decreasing its effectiveness. This side wall taper angle was seen to remain unchanged when the machining area was increased. Both 100µm and 0.5mm diameter features resulted in a sidewall angle of 25° on AlN. When the machined area was increased on Al_2O_3 a columnar topography was formed, which was not seen for the same machining parameters for 100µm diameter features. This indicates that different parameters are needed when increasing the machined area on Al_2O_3. The columnar topography was seen to grow with increasing numbers of laser pulses. Small features were seen of a diameter of ~10µm at 180 pulses (attenuator 0.5 and 0.7) which grew to ~50µm after 1080 pulses. Although these features are undesirable for the applications considered here, their formation is very consistent. Thus it would seem to be feasible to reliably remove them using an appropriate process.

Figure 5.6-19 shows the result of excimer laser post-machining on an AlN surface which had previously been machined with a CO_2 laser. The step-wise evolution of a smooth surface from one which was previously extremely rough is apparent in the figure. In principle a smooth surface is only achievable once the ablation depth has exceeded the peak to valley depth of the roughness profile. This was measured to be ~30µm using the Talysurf. Figure 5.6-19

shows that the peaks of the roughness profile are affected by the excimer laser before the troughs. This is because the peaks lay within the laser's focal plane giving more effective machining. Consequently the roughness can be machined away effectively with the excimer laser. The same post-machining approach was repeated on Al_2O_3 whilst the crust was still present. The results were much the same as with the AlN but columnar topographies were formed once the crust was penetrated by the machining and the bulk Al_2O_3 was reached. In addition the excimer laser machining was seen to induce flaking of the crust, highlighting the importance of the removal of this crust prior to further processing.

5.6.7 Conclusions

Planar material removal using an infrared 10.6µm CO_2 laser was achieved on both AlN and Al_2O_3 ceramics. However, the usefulness of the process for optoelectronic application is likely to be limited by the extreme surface roughness created by the machining. XRD and nanoindentation results show some machining induced changes to the bulk material properties for both materials. Epoxy bleed was successfully controlled using laser CO_2 laser machined features. A depth of 50µm and close to vertical side walls were found to be a requirement for successful control.

Excimer laser machining was shown to be a repeatable process with the capabilities of machining controlled, precise geometries and surface roughnesses. However in this work attempts to machine large areas >1mm diameter were unsuccessful. This problem would limit the usefulness of the technique for optoelectronic application, if not overcome.

Combining the material removal speed of CO_2 laser processing, with the precision of excimer laser post-processing produced some promising results. Excimer laser machining was seen to remove the excessive roughness caused by CO_2 laser processing.

The geometries created in this work were not of adequate quality for use in the manufacture of optoelectronics, largely due to the redeposition of material following ablation. However, there is clearly scope for process improvements and high quality features would seem to be achievable. For example while this

work was limited to static sample processing with an excimer laser, dynamic processing (i.e. moving the laser spot) could be used to improve feature geometry, and masking and post-processing could be used to remove redeposited material.

5.6.8 References

[1]. Williams, O. Liu, C. Webb, D.P. Firth, P. Epoxy adhesion strength to ceramic surfaces in commercial optoelectronic assemblies. Electronic Components and Technology Conference, 2008. ECTC 2008. 58th , vol., no., pp.1673-1678, 27-30 May 2008

[2]. Pereles-Santiago, V. Washington, M. Brugan, P. Cai, G. Akarapu, R. Pulford, S. Segall, A.E. Faster and damage-reduced laser cutting of thick ceramics using a simultaneous prescore approach, J. Laser Appl. 17, 219 (2005), DOI:10.2351/1.2080547

[3]. Imen, K. Allen, S.D. Pulse CO_2 laser drilling of green alumina ceramic, Advanced Packaging, IEEE Transactions on , vol.22, no.4, pp.620-623, Nov 1999

[4]. Leonard R. Migliore and Arzu Ozkan, Laser cutting of aluminum nitride, Proc. SPIE 5063, 505 (2003)

[5]. Lumpp, J.K. Allen, I. Susan, D, Excimer laser ablation of aluminum nitride, Journal of Materials Research. Vol. 12, no. 1, pp. 218-225. Jan. 1997

[6]. Oliveira, V.Conde, O. Vilar, R. UV Laser Micromachining of Ceramic Materials: Formation of Columnar Topographies, Advanced Engineering Materials, Vol 3, Iss1-2, Pg 75-81, 2001

[7]. Yaghdjian, L. Vacquier, G. Fabre, A. Autric, M.L. Excimer laser surface processing of Si_3N_4 and AlN Proc. SPIE 4070, 226 (2000)

[8]. Lumpp, J.K. Excimer laser machining and metallization of vias in aluminium nitride, Materials Science and Engineering B, Volume 45, Issues 1-3, March 1997, Pages 208-212

[9] Goller, M. Lutz, N. Geiger, M. Micromachining of ceramics with excimer laser radiation, Journal of the European Ceramic Society, Volume 12, Issue 4, 1993, Pages 315-321

[10] Lumpp, J.K. Coretsopoulos, N. Allen, D. Fluence Dependence of Excimer Laser Ablation of AlN, Materials Research Society, 1994.

[11] Ihlemann, J. Scholl, A. Schmidt, H. Wolff-Rottke, B. Nanosecond and femtosecond excimer-laser ablation of oxide ceramics. Applied Physics A: Materials Science & Processing. Volume 60 Issue - 4. 411 - 417

[12] Ihlemann, J. Wolff-Rottke, B. Excimer laser micro machining of inorganic dielectrics, Applied Surface Science, Volume 106, Proceedings of the Second International Conference on Photo-Excited Processes and Applications, 2 October 1996, Pages 282-286

[13] Sciti, D. Melandri, C. Bellosi, A. Excimer laser-induced microstructural changes of alumina and silicon carbide, Journal of Materials Science, Volume 35 Issue - 15, 3799 - 3810

[14] Thomas, D.W. Williams, C.F. Rumbsby, P.T. Gower, M.C. Surface modification of polymers and ceramics induced by excimer laser radiation. In: Laser Ablation of Electronics Materials Basic Mechanisms and Applications Elsevier (1992).

[15] Oliveira, V. Conde, O. Vilar, R. UV Laser Micromachining of Ceramic Materials: Formation of Columnar Topographies. Advanced Engineering Materials. Vol 3 Iss 1-2 Pg75-81

[16] Laude, L.D. Kolev, K. Brunel, M. Deleter, P. Surface properties of excimer-laser-irradiated sintered alumina, Applied Surface Science, Volume 86, Issues 1-4, February 1995, Pages 368-381

[17] Tonshoff, H.K. Hesse, D. Mommsen, J. Micromachining Using Excimer Lasers, CIRP Annals - Manufacturing Technology, Volume 42, Issue 1, 1993, Pages 247-251

[18] Wu, Y. Feng, Z. Liang, J.. Surface modification of ceramic materials using excimer laser. Journal of Materials Science and Technology. 2000 Vol. 16 (04): 401-40

[19] Powder diffraction file 2009 Swarthmore : JCPDS International Centre for Diffraction Data.

6 Evaluation

This work has shown the effects of surface properties on epoxy bleed and examined methods of preventing or inhibiting it on metallised and unmetallised ceramic materials used in optoelectronic manufacture. The chemistry of the surfaces has been seen to be the principal factor determining the occurrence of epoxy bleed through the effect it has on surface energy. It has been seen that roughness exacerbates the problem on surfaces which are chemically similar. A highly polished surface was seen to inhibit the spreading of epoxy material. This was thought to be due to capillary action being the mechanism of spreading on a rough surface.

Standard models for wetting of rough (Wenzel) and chemically inhomogeneous (Cassie) surfaces do not correctly predict observed variation of contact angle due to roughness and degrees of surface contamination. An extension to the Cassie model for chemically inhomogeneous surfaces was proposed to allow calculation of contact angle on a mixed completely wetting/partially wetting surface.

Adsorption of adventitious carbon from the atmosphere was shown to produce marginal results when the aim was inhibiting epoxy bleed. The extended periods of time (~28 days) required to reach this time rendered this as an industrial solution to the problem unfavourable. However, it seemed that the seemingly random occurrence of epoxy bleed reported by an optoelectronics manufacturer was due to the time between manufacture of substrate materials and when they were used in the assembly line. The primary source of this contamination was found to be the industry standard storage method of polymer waffle packs containing protective lint free paper and polyethylene inserts.

The first successful and industrially feasible solution for inhibiting epoxy bleed found was the use of self assembled monolayers to modify the surface energy of the ceramic and metallisation materials. Adhesion strength was maintained using a fluorinated carboxylic acid monolayer on the ceramic materials due to the curing agent of the adhesive stripping off the SAM molecules. A multistage SAM coating method was developed and tested in the laboratory

for treating industrial optoelectronic substrates consisting of both ceramic and metal surfaces, and is currently being tested on the assembly line at Oclaro plc.

The control of epoxy bleed has also shown to be possible with the use of laser machined features on the ceramic surfaces. Although laser machining of ceramic is covered in the literature, a novel feature of this work was to attempt to combine the high removal rates of thermal CO_2 laser processing ,with the fine feature and low damage ablation machining of slower excimer laser processing. Although the machining process was shown to damage the bulk of the ceramic materials, the results show promise for extension of laser machining to other potential applications in the assembly/manufacture of optoelectronic substrates. These include the machining of passive alignment features and replacing conventional machining methods in the structuring of ceramic substrate surfaces.

6.1 Further work

Surface texture of ceramics was studied in depth in this work. It was also demonstrated that a polished copper surface can inhibit epoxy bleed as well as a polished ceramic surface. Further work could focus upon the deposition of metallisation patterns of very low roughness so adhesives which are applied do not have the tendency to bleed.

The method proposed for the multi-stage coating of heterogeneous surfaces was shown to work as a lab process. Much further work could be done to turn this into a viable large scale industrial process. Aspects which have not been considered in this work are the resilience of the coating to the many processes undergone in the assembly line, the optimum point in the assembly process for application, and whether multiple applications could be necessary.

The applications of laser machining to the optoelectronic assembly process do not end at epoxy bleed control. The potential for machined features to be used as active alignment features was studied briefly in this work. So far the features have not been machined to acceptable accuracy for this purpose. However this is an area of follow up research thorough an MSc research project, which aims to determine the feasibility of incorporating laser

machined features into the optoelectronic substrate assembly process as passive alignment features.

7 Acknowledgements

8 Publications

Epoxy adhesion strength to ceramic surfaces in commercial optoelectronic assemblies

Williams, O. Liu, C. Webb, D.P. Firth, P.

Electronic Components and Technology Conference, 2008. ECTC 2008. 58th

27-30 May 2008 Pages:1673 – 1678

Laser micromachining of polycrystalline alumina and aluminium nitride to enable compact optoelectronic interconnects

Williams, Owain; Williams, Martin; Liu, Changqing; Webb, Patrick; Firth, Paul;

Electronics Packaging Technology Conference, 2009. EPTC '09. 11th

Digital Object Identifier: 10.1109/EPTC.2009.5416413

Adsorbed contamination on ceramic surfaces stored in industrial ambient conditions and its effect on epoxy bleed

Williams, O.; Liu, C.; Webb, D.P.; Firth, P.;

Electronics Packaging Technology Conference, 2009. EPTC '09. 11th

Digital Object Identifier: 10.1109/EPTC.2009.5416497

Epoxy adhesive behaviour on ceramic surfaces in commercial optoelectronic assemblies

O. Williams, C. Liu, D.P. Webb, P. Firth,

International Journal of Adhesion and Adhesives,

Surface treatments and coatings to reduce adhesive spread

USPTO application no 61/266,611; Filed 04 December 2009. Inventors: O. Williams, C.Liu, D.P.Webb, P.Firth. Assignee: Oclaro Technology plc

9 Appendices

9.1 Appendix 1 – Journal Paper

Epoxy adhesive behaviour on ceramic surfaces in commercial optoelectronic assemblies

O. Williams [a,*], C. Liu [a], D.P. Webb [a], P. Firth [b]

[a] Mechanical and Manufacturing Engineering, Loughborough University, Loughborough LE11 3TU, UK
[b] Bookham Technology PLC, Brixham Road, Paignton, Devon TQ4 7BE, UK

ARTICLE INFO

ABSTRACT

Chemical and physical variability in the as-received state of aluminium oxide and aluminium nitride ceramic substrate materials used in optoelectronic modules currently leads to a process yield less than 100% when adhesives are used for assembly and interconnection. The phenomenon of epoxy bleed is a contributing factor to this yield and steps are not yet taken in the industry to control or inhibit the undesirable wetting.

Standard surface texture measurement techniques, XPS and contact angle measurements were implemented to characterise and compare commercial as-received samples. The quality controls currently in place are assessed and additional analysis methods in the QC stage are suggested for increasing yield. Commercially available conductive and thermally conductive adhesives, also used in optoelectronic module manufacture, were studied along with the surfaces.

In this work the surface property measurements, wetting observations and shear failure modes are compared and discussed. It was found that varying as-received surface properties did not affect adhesion strength between the adhesives and ceramics enough to induce an undesirable failure mode, although epoxy bleed distance varies dramatically with varying surface conditions.

1. Introduction

The components in many modern optoelectronic modules are assembled using adhesives at greater spacing than optically necessary. Given the current trend towards miniaturisation in the optoelectronics industry [1], it is desirable to reduce the component spacing to allow for further reduction in the size of the module. This issue extends to many microelectronic applications in which adhesives are used for component assembly. One of the factors limiting reduction in component spacing is lack of control of the surface wetting behaviour of the epoxy adhesives on the ceramic sleds used as the optical bench. Good wetting is usually considered desirable to ensure strong and reliable adhesive joints. However, good wetting also increases the area of the joint fillet and hence reduces the potential to pack components more closely together. A further problem is variability in wetting behaviour and hence fillet size from batch to batch of the ceramic sleds. In extreme cases epoxy bleed occurs, where one or more adhesive components separate out before curing and spread widely across the ceramic surface, interfering with wire bonding processes and the application of subsequent adhesives.

The aims of the investigation described in this paper were firstly to understand the origin of the variability in adhesive wetting on ceramic sleds observed on the production line, and then to suggest cost-effective methods of reducing or eliminating it, particularly bleed. A subsidiary aim was to scope the possibility of reducing adhesive joint fillet sizes, without affecting the reliability of the optoelectronic modules. To achieve these aims the study was carried out on a representative range of different types of ceramic sled obtained from the optoelectronic industry supply chain, in the condition in which they would be received by an optoelectronic module assembly plant. The results of surface characterisation of the as-received samples, of bleed measurements with epoxy adhesives used in optoelectronic assembly on as-received and plasma cleaned samples, and of adhesion strength tests with the epoxies and ceramics, are reported here. Conclusions are drawn as to the alternatives for reducing variability in wetting behaviour and eliminating bleed.

2. Background

Aluminium oxide and aluminium nitride are popular substrate materials used in optoelectronic modules. Their low thermal expansion, dimensional stability and relatively high thermal conductivity make them ideal for use in high power applications. The similarity between the coefficient of thermal expansion (CTE)

* Corresponding author. Tel.: +44 01509 227677.
  E-mail address: O.Williams@lboro.ac.uk (O. Williams).

of Al_2O_3 ($9.5e^{-6}$/K), AlN ($5.6e^{-6}$/K), and silicon ($2.6e^{-6}$/K) means they are compatible materials with little reduction in reliability due to CTE mismatch. The CTE and thermal conductivity of the ceramics makes them suitable for use as substrate materials for laser transmitter modules where the laser diode requires good thermal draining. If the laser diode sees excessive temperature then the wavelength of the laser can be affected, jeopardising the functionality of the transmitter. An intermediate material is required for bonding the optoelectronic components to the ceramic substrate material, including the laser diode. Filled epoxy adhesives are used for this purpose. Epoxies are electrically and thermally insulative (thermal conductivity 0.2 W/m/K), and so the adhesives used in the assembly line are filled either with silver, for electrical conduction, or boron nitride for thermal conduction. The use of adhesives in the assembly of optoelectronic modules leads to a less than 100% process yield. One of the contributors to module failure is the uncontrolled spread of epoxy adhesive material over the substrate and interconnection features. However, optoelectronics manufacturers can only specify dimensions, tolerances and surface finish when purchasing ceramic substrate materials, not wetting properties. Different surface preparation methods are used by the ceramic manufacturers to achieve a specified R_a value. These include lapping, polishing, chemical etching and no surface preparation after sintering (as-fired). The different surface preparations are used in the optoelectronics assembly line with little understanding of the effects of the treatments on the adhesive wetting and the bond strengths.

The manufacture of the substrates is done in two stages, typically by different companies. Ceramic tiles are produced from slurry and sintered into a polycrystalline solid with a grain size dependant on the application and manufacturer. The same company typically performs the surface treatment of the ceramics also. A second company dices the ceramic tiles and is the direct supplier to the optoelectronic manufacturer. A number of cleaning processes are included in the cutting process before a final firing at $\sim$850 °C in air. Substrates are typically shipped and stored in polymer waffle packs.

The surface chemical as-received state of the ceramic materials is not characterised by the optoelectronics manufacturer, and is uncontrolled in the assembly process, as substrates may or may not be subjected to further cleaning. It is therefore a source of variation in the behaviour of adhesives on the ceramics, and in the quality of the adhesive joints formed.

The surface preparations used in the industry are usually quantified with R_a, R_t and R_z roughness parameters. However, for the purpose of this study a roughness factor was needed, which could be directly related to wetting and adhesion. The Wenzel roughness factor was chosen as it makes frequent appearances in the literature as a roughness parameter which can be linked directly to wetting and adhesion [2]. The Wenzel roughness factor is the ratio of the actual surface area to the planar surface area, i.e., a dimensionless parameter where a value of exactly one constitutes an ideal, perfectly flat surface with no deviation from the plane, and values greater than one correspond to real surfaces.

The relationship between roughness and contact angle is given by the Wenzel model to be

$$r \cos \theta = \cos \phi \qquad (1)$$

where ϕ is the apparent (measured) contact angle, θ is the ideal contact angle on a perfectly flat surface and r is the Wenzel roughness factor. This relationship predicts that for an intrinsic contact angle above 90° roughness will give an apparent increase in contact angle, and reduction in wetting. Whereas for a true contact angle below 90° roughness will act to decrease the contact angle and increase wetting. This relationship suggests that epoxy bleed could be affected by the roughness of the substrate

material. Where it occurs the degree of epoxy adhesive bleed has also been linked to substrate composition, contamination and surface energy [3,4].

Theories of wetting and adhesion suggest resin bleed could be controlled by surface texture alone [5], produced by mechanical processes which are already used in the production of the ceramic sleds that form the component substrates in optoelectronic modules. Surface texture or roughness on the nanometre scale is one of the most important factors determining the strength achieved by an adhesive bond. This can be because of mechanical interlock effects, but also because increased roughness can increase the area of intimate contact available for inter-material physical or chemical bonds [6]. By changing the surface texture of the substrates the actual bond area will change [7], whilst the apparent bond area remains constant. However it should be noted that attempts to control the epoxy resin bleed by means of surface texture could render the bond strength unacceptably weak [5]. Poor wetting of the adhesive on the substrate, and a high adhesive viscosity, could result in formation of air pockets at the interface [8] and a reduction in the actual bond area. A scientific approach to engineering surface wetting of the adhesive therefore requires separation out of the surface energy and surface texture effects of surface treatments.

3. Methodology

The ceramic sleds used in the study had undergone a variety of surface texture modifying treatments typically applied by suppliers to meet the R_a specified by the customer. The surfaces of the sleds were characterised for surface texture, chemistry and wetting properties, in the as-received state. Several different methods of measuring surface texture were compared to identify the one most suited to the samples. Two different kinds of commercial epoxy-based adhesive that are also used for optoelectronic assembly were obtained and used in shear tests with the sleds. The degree of bleed of the epoxies on the ceramic surfaces was also measured. To separate out the relative influences of surface texture and surface texture, bleed measurements were also made on sleds which had been cleaned in oxygen plasma.

4. Experimental details

Sets of rectangular alumina and aluminium nitride ceramic sleds, of area 5.5 × 16 mm and thickness 1 mm, were bought from a commercial supplier to the optoelectronics industry. The surface preparations of the sleds were polished, lapped, as-fired, polishing followed by light etching, and polishing followed by heavy etching, as listed in Table 1. The R_a and R_T values given by the

Table 1
Measured surface properties of as-received materials.

Sample number	Material	Preparation	R_a (µm)	R_t (µm)
1	AlN	Polish+light etch	0.06	1.3
2	AlN	Polish+heavy etch	0.08	2.7
3	AlN	Polished	0.04	1.9
4	AlN	As-fired	0.17	2.1
5	AlN	As-fired	0.61	409
6	AlN	As-fired	0.85	7.2
7	AlNl	Lapped	0.75	8.2
8	Al_2O_3	As-fired	0.05	0.5
9	Al_2O_3	Polished	0.02	0.4
10	Al_2O_3	Lapped	0.45	4.0

supplier for the samples had been obtained using a Mitotoyo Surftest SJ-400 surface contact probe with a 5 μm tip radius.

The surface textures were subsequently characterised at Loughborough University using atomic force microscopy (AFM) measurements in tapping mode. The Wenzel roughness factor r and R_a were calculated from the data. White light interferometry (WLI) was also used to obtain values for R_a.

The chemical composition of the surfaces was measured using X-ray photoelectron spectroscopy (XPS), and the wetting characteristics by water and diiodomethane equilibrium sessile drop contact angle measurements on a contact angle goniometer. Surface energies were calculated from the contact angle measurements using the Owens Wendt Kaeble method. At least nine contact angles were recorded for each liquid on each surface from three samples. The Owens Wendt Kaeble method was chosen due to the expectation of a wide range of surface energies.

Application of adhesive spots to the sleds for bleed measurements and tensile tests was by dispensing from a syringe using a cylindrical needle 0.56 mm in diameter. Tensile test pieces were prepared in a single lap joint configuration using commercial silver filled (H20E) and boron nitride loaded (930-4) epoxy adhesives, manufactured by Epo-Tek. The mating sled was mounted on to the adhesive spot using a jig that aligned the sleds and maintained a bond thickness of 30 μm. All adhesives were handled, prepared and cured according to the manufacturer's instructions. The H20E adhesive components were combined in a 1:1 ratio by weight and the 930-4 adhesive components were combined in a ratio of 100:3.3 resin to curing agent ratio by weight, each measured to an accuracy of 0.01 g. The adhesives were mixed thoroughly for 5 min. It was ensured that the adhesives were used within their pot lives of 24 h, usually within 30 min of mixing. The adhesives were cured in an oven at 150 °C for 30 min. The joints created varied in diameter from 1.8 to 4.3 mm, so the diameters were measured after failure in an SEM as described below. Some joints were subjected to thermal cycling from −40 to +80 °C, with a 20 min transition and 10 min dwell time, for 2 days. The adhesive joints were tested to the point of failure under shear loading using the compression function of an Instron microtensile test machine. The compressive extension was controlled at a constant rate of 0.001 mm/s whilst the applied load and extension were recorded. The fracture surfaces were examined by scanning electron microscopy (SEM) and profiled with an optical surface metrology system; Talysurf CLS 2000, to determine the failure mode. The joint areas for the shear stress calculation were taken to be the apparent areas of the fracture surfaces from the SEM images. A reference artefact was used to calibrate the measurements. For measurement of bleed from AFM images the bleed distance was taken to be the maximum perpendicular distance from a tangent to the adhesive spot that the material spread.

Plasma cleaning for removal of surface contamination consisted of 1 min of treatment in a 300 W oxygen RF (13.56 MHz) plasma at a flow rate of 100 sccm. Removal of surface contamination was confirmed using diiodomethane and water contact angles, within 1 h of treatment, to calculate a figure for apparent surface energy. AFM profiling before and after treatment confirmed that there was no observable effect on the surface topology.

5. Results

5.1. Surface texture analysis

From Table 1 it can be seen that as-fired samples (4–6 and 8) show a large range of roughness ($0.05\,\mu m \leq R_a \leq 0.85\,\mu m$), probably due to variation in the grain size of the ceramic in the green state prior to sintering. The granular texture of the as-fired surfaces can be seen in the 3D AFM plot in Fig. 1 for sample 8 (A_2O_3 as-fired, R_a 0.05 μm). The large variation in as-fired surface textures is one reason for a manufacturer to specify a mechanical or mechanical chemical surface preparation to the sleds to reduce manufacturing variations due to surface texture variation. To attempt to determine whether R_a gives sufficient information to allow this source of manufacturing variation to be controlled, white light interferometry and an AFM were also used to


```
Digital Instruments NanoScope
Scan size          10.00 μm
Scan rate          1.001 Hz
Number of samples     256
Image Data         Height
Data scale         1.000 um
Engage X Pos      -19783.4 um
Engage Y Pos      -42151.3 um
```

view angle
light angle

X 2.000 μm/div
Z 1000.000 nm/div
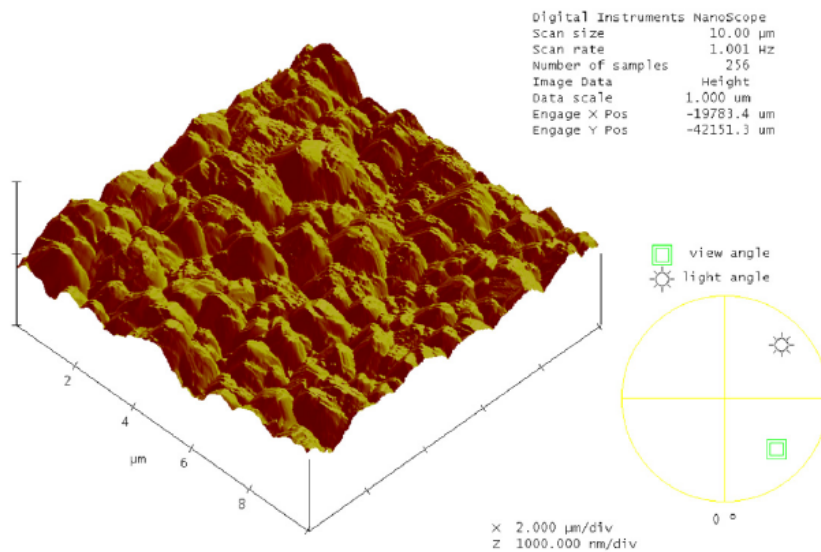
Fig. 1. AFM 3D morphology representation of sample 8 R_t value 0.791 μm.
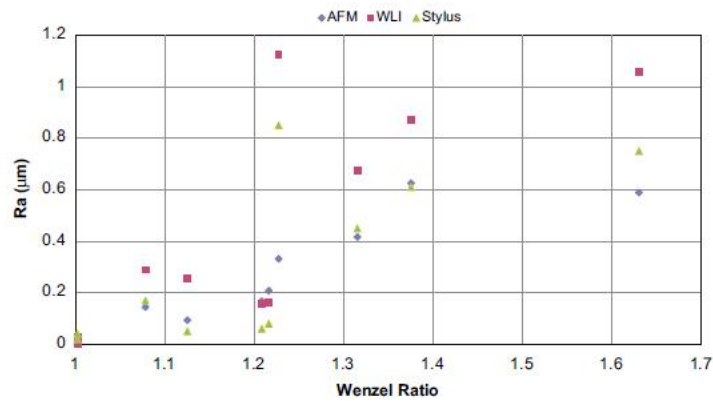
Fig. 2. Comparison of R_a roughness values produced by AFM, WLI and stylus profiling to the Wenzel ratio produced by AFM.
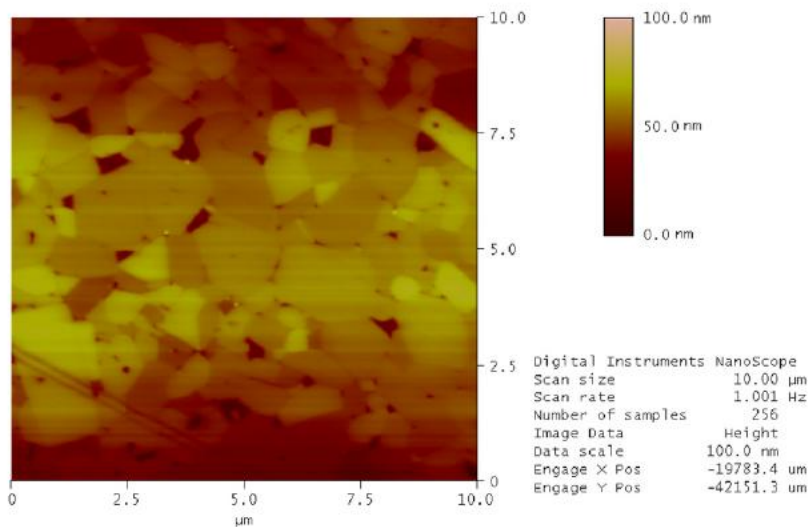
Fig. 3. AFM 2D representation of 3D morphology of sample 9.

characterise the surface textures. The AFM gives the additional capability of producing a value for the Wenzel roughness ratio r. A comparison of R_a measured by the different methods plotted versus r is given in Fig. 2.

On average (mean of the ratios) R_a by WLI is twice that by AFM. This is probably due to measurement artefacts in the WLI data. The 3D surface plots show multiple steep sided fissures which are not visible in AFM. The artefacts are probably caused by multiple reflections from the surface features which increase the length of the light path. Evidence for this suggestion is provided by the high frequency of the occurrence of the fissures in the profiles and their equal depth. In addition there is a high frequency of missing data in the profiles, probably due to the incident light angles being such that the light is not returned to the sensor. These issues have been documented in the literature [9].

The mean ratio of R_a by the stylus instrument (Surftest SJ-400) to that by AFM is around 1.3 (single anomalous data point at very low R_a ignored, stylus: AFM value of 25 at $r=1.002$). Since both methods are surface contact the closer correlation is unsurprising. However there are reasons to prefer the AFM measurements. In Fig. 2 it can be seen that R_a by any method is not strongly correlated with r until $R_a > 0.2\ \mu m$. This shows that the AFM is picking up structure relevant to wetting in the surface texture at low R_a that is not reflected by that index. The major limitation of the AFM for assessing surface texture application is its inability to analyse large areas, and so properties such as flatness cannot be determined. However for adhesive flow micro- and nanoscale roughness is likely to be more important. Other reasons for preferring the AFM are that profiles are measured along an outwards and a return stroke along the same line of travel. This gives added reliability to the measurements because the tracking

of the two directions can be compared. The AFM used in tapping mode allows precise control of the pressure the tip exerts on the surface.

A potential reason for the anomalous R_a ratio obtained with the stylus instrument at low roughness (stylus: AFM value of 25 at $r=1.002$) is the nature of the situations in which the measurement methods are performed. The AFM is insulated against vibration and air flow whilst the portable stylus instrument has no means of filtering background vibration and atmospheric effects. The vulnerability of the stylus instrument to vibration could define its measurement limit, the point at which the effect of the surface upon the stylus is exceeded by the effect of noise.

An interesting result obtained with the AFM can be seen in Fig. 3 for a polished Al_2O_3 surface (sample 9), which shows a 2D height plot. Despite the polishing a grain structure is still apparent. This is probably due to different hardnesses of the material across the surface. Intergranular material and grains with different crystalline orientations have been removed differing extents. This implies sharp height boundaries which may provide good keying features for adhesive joint formation.

5.2. Sample surface chemical and contact angle characterisation

Surface chemical characterisation of the sleds was carried out by XPS, while the wetting characteristics were determined by contact angle measurement. The XPS elemental quantifications from broad scans are listed in Table 2. The major constituents of the AlN surface signal after aluminium and nitrogen were primarily carbon and oxygen, suggesting the presence of organic molecules, probably atmospheric or other contamination. High energy, clean surfaces such as the ceramics studied have a tendency to adsorb organic films upon exposure to air [5], the composition of which is determined by the atmosphere the surfaces are subjected to. The spectra of the Al_2O_3 indicated the presence of trace amounts of group 1 and 2 metals (calcium, sodium, magnesium) along with up to 14% silicon. The silicon is present on the surface regardless of surface preparation method, while the "as-fired" samples exhibit a comparable surface composition of trace elements to those which have undergone further processing. It is difficult to determine the origin of these elements due to the commercial nature of the samples. The magnitude of the signal from the group 1 and 2 metals is closely related to the purity of the samples as reported by the suppliers; those which were over 99% pure have only trace amounts of these elements present, whilst those 96% pure showed presence of up to 3%. The correlation with purity and insensitivity to surface treatment suggests that the trace elements form part of the material composition.

Fig. 4 shows a plot of surface carbon percentage against r, showing that there is evidently no correlation. The two very high carbon percentage data points are for the etched AlN sleds, suggesting that either the chemical etch provides a clean high energy surface for the adsorption of higher levels of organic contamination, or that it leaves behind residues on the substrate surface after drying. There is also no evident correlation between the surface energy calculated from the contact angle measurements and r, as can be seen in Fig. 5. The very high energy AlN surface (72 mJ/m^2) in Fig. 5 is the lapped sample (number 7). The surface carbon content of this sample is not particularly low at 21.1%, so the low contact angles seen may be due to the high roughness (r of 1.63).

The lack of correlation between the surface energy calculated by wetting measurements and surface roughness is surprising in view of the well known effects of roughness on contact angles [2]. However, there is a clear correlation between surface energy and surface carbon visible in Fig. 6, with surface energy decreasing with increasing carbon content for both AlN and

Table 2
Relative atomic percentages of the elements present on the ceramic substrates, measured using XPS.

Sample	Relative atomic percentage							
	Al	O	N	C	Si	Mg	Ca	Na
1	23.5	37	4	35.6	0	0	0	0
2	28.6	25.3	13.7	32.5	0	0	0	0
3	31.7	39.2	9	20.1	0	0	0	0
4	28.9	42.4	6.2	22.6	0	0	0	0
5	30.4	42.5	5.5	21.6	0	0	0	0
6	33.4	44.6	5.2	16.8	0	0	0	0
7	30.1	42.8	6	21.1	0	0	0	0
8	23.1	44	0	18.2	12.3	0.9	0.5	1
9	28	40.2	0	21.2	8.8	1.2	0	0.6
10	20.1	39.4	0	21	14.2	3.2	2.2	0
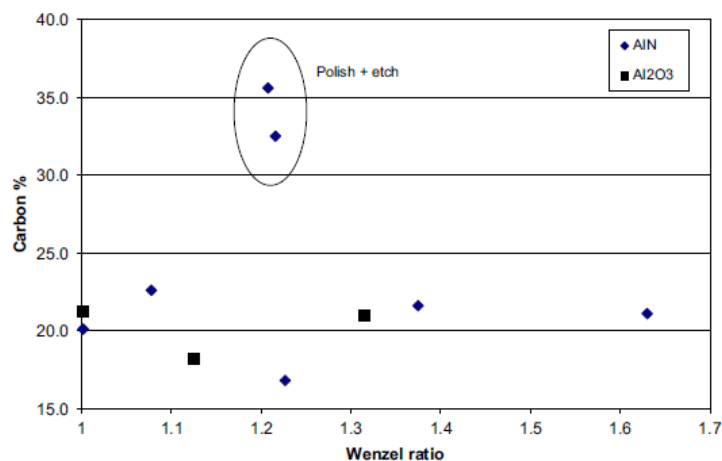
Fig. 4. Comparison of Wenzel ratio to relative carbon percentage as measured with XPS.
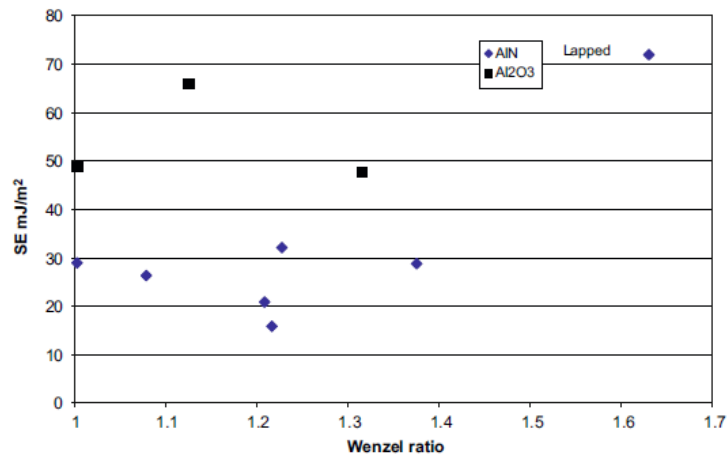
Fig. 5. Plot of apparent surface energy (according to Owens-Wendt) against the Wenzel ratio.
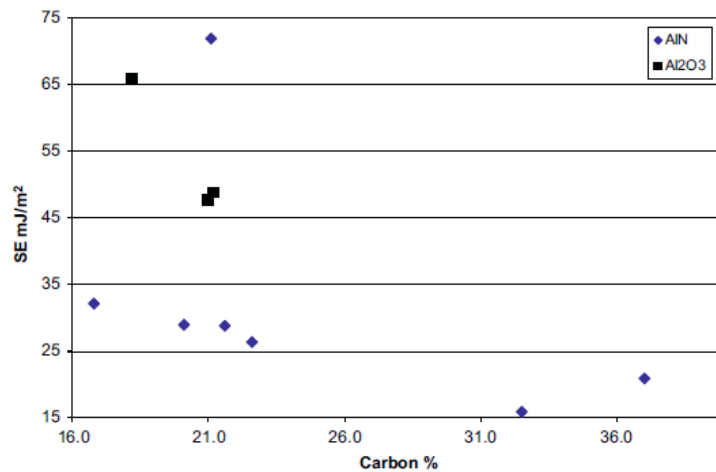
Fig. 6. Plot of surface energy (according to Owens-Wendt) against relative atomic carbon percentage as by XPS.

Al_2O_3, apart from the anomalous result for sample 7 already noted, as seen in other work [4]. Since in principle both roughness and surface contamination affect wetting, it would therefore appear that the variation in carbon content is large enough to mask any effect of roughness on the contact angles in Fig. 5 apart from the very rough lapped AlN (sample 7), while the roughness variation is not large enough to disturb the trend seen with carbon percentage in Fig. 6, again excepting sample 7. It is worth noting that the R_a value given by the supplier of 0.75 μm for sample 7 was not the highest in the sample set, while the value of r determined by AFM was the highest by some margin (next highest sample 5, r 1.35, R_a 0.61 μm; highest R_a value sample 6 at 0.85 μm but r only 1.23). Wenzel's parameter r is therefore a better predictor of wetting than R_a with this sample set.

5.3. Bond strength analysis

Cohesive failure is the failure of a bond through the adhesive and is considered the failure mode which occurs in an ideal bond for it constitutes evidence that the adhesive has adhered to the adherend [6]. The indicator of cohesive failure in this case is that there are equal amounts of adhesive remaining on both the adherend surfaces. Fig. 7 shows that equal amounts of adhesive remained on each surface of both rough and polished samples following shear failure (failed boron nitride filled adhesive spot, measured with a Talysurf CLI 2000).

Measurements were made on all failed joints and it was seen that all bonds underwent cohesive failure in the adhesive, and that therefore no inferences can be drawn as to the effects of the surface energies and textures on bond strength.
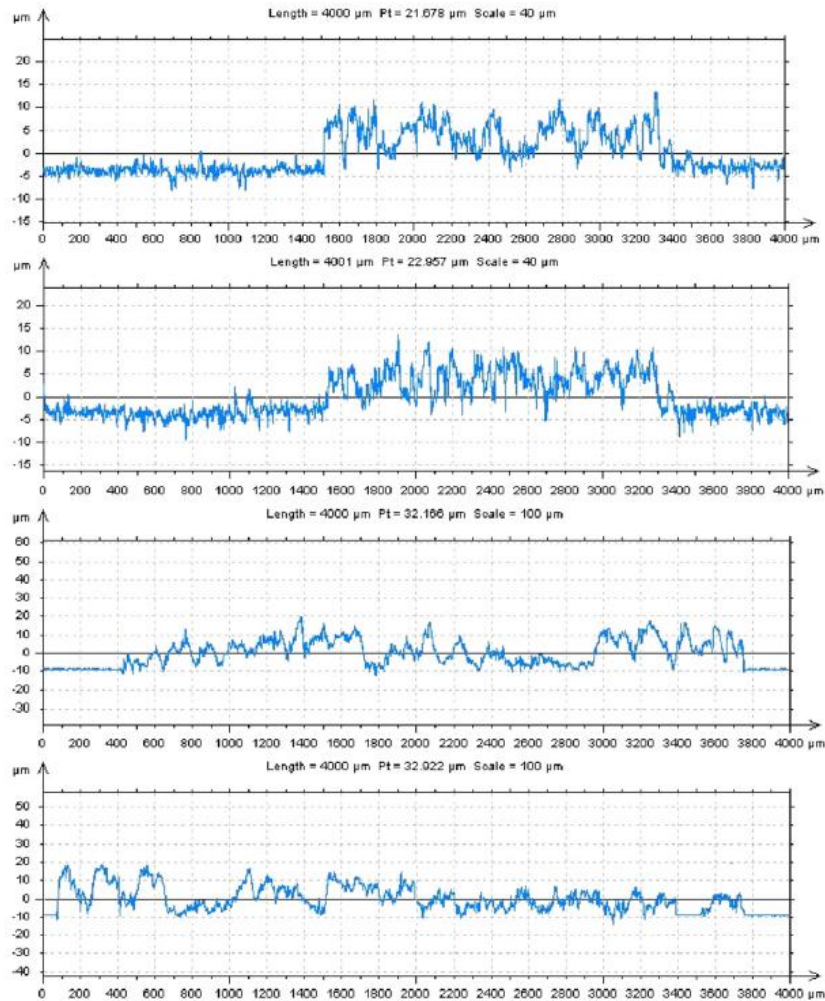
Fig. 7. Talysurf profile of a failed adhesive spot on alumina surface, sample 10 top and sample 9 bottom.

Further evidence for cohesive failure comes from the proportional relationship observed between the measured shear strength and measured bond area. In Fig. 8, it can be seen that the constant of proportionality is dependent on the choice of adhesive, and independent of surface type or treatment.

The near constant slope and instantaneous failure seen in the load vs extension curves for the tensile testing suggests the joint underwent elastic deformation followed by brittle fracture. SEM images of the failed adhesive surfaces supported this, for they showed no signs of plastic deformation and the topography of the adhesive consists of sharp jagged profiles typical of brittle failure. The jagged nature of the surface topography in the SEM images is consistent with the Talysurf profiles in Fig. 7. The SEM images of the failed bonds also show failure occurred entirely though the adhesive.

The bond strengths were not detrimentally affected by thermal cycling, Fig. 9 shows the same correlation between shear force and bond area as seen with the samples which were not cycled, along with comparable shear force values. The failure modes are comparable to those of the bonds which were not cycled. Fig. 8 also shows the silver filled adhesive has become stronger after thermal cycling; a possible reason for this is that the adhesive continued to cure at the elevated temperatures in the cycles. Manufacturer's data gives 80 °C cure time of 90 min for the silver filled epoxy and 6 h for the boron nitride filled epoxy, supporting this theory.

Higher magnification SEM images of the failed silver filled epoxy bonds showed the failure occurred along the boundaries between the epoxy adhesive polymer and the silver flakes. The images suggested that the weak interface is that between the
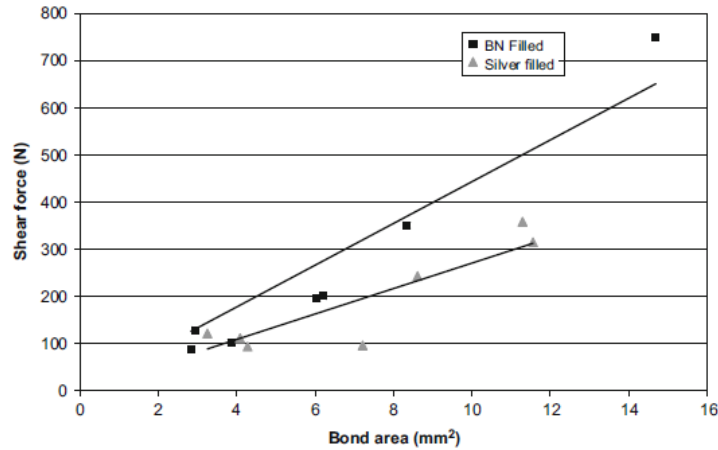
Fig. 8. Comparison of bond area to shear force lines are least-squares best fits with 0 intercept.
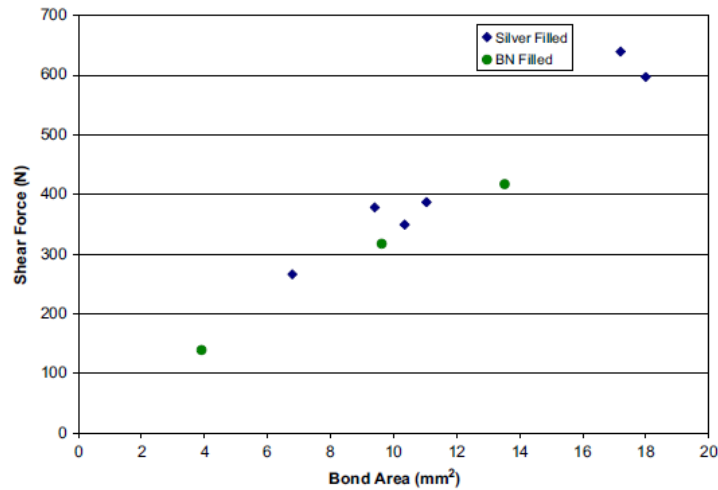
Fig. 9. Comparison of bond area to shear force for thermally cycled samples.

components of the adhesives, and as the other evidence supports, not between the adhesive and the ceramic surfaces.

5.4. Epoxy bleed

The resin bleed phenomenon appears not to be exclusively related to the contaminants found to be present. Fig. 10 shows examples of minimal and pronounced bleed, respectively, on surfaces which were found to have an equal degree (21%) of carbon contamination. The pronounced bleed occurs on the lapped surface (r 1.63), rather than the polished surface (r 1.00). It was therefore hypothesised that the bleed materials wetting performance might be sensitive to both topography and composition. For the most part the very thin bleed films were not highly visible optically, so a scanning electron microscope

(SEM) in secondary electron (SE) mode was used to measure their extent. An example of minimal bleed is shown in Fig. 11(a). The bleed is visible as a dark band surrounding the bulk adhesive with high contrast to the surrounding area and with reduced filler content compared to the bulk. Fig. 11(b) shows pronounced bleed at a much reduced scale. The bleed can still be distinguished as a dark area around the central sessile drop. The topic of contrast in SE images is a complex one. However it seems likely the contrast between the bleed and bulk is due to the higher atomic number of the filler in the bulk increasing the secondary electron yield from that region. See for example Sakai et al. [10]. Of the samples listed in Table 1, pronounced epoxy bleed was witnessed on 2 samples both of which had comparatively low carbon contamination and comparatively high surface roughness, samples 5 and 7 (r=1.37, 1.63, respectively, bleed distance 1.1, 2.2 mm, respectively). Minimal or no bleed was observed on samples 1–4 and 8–10,
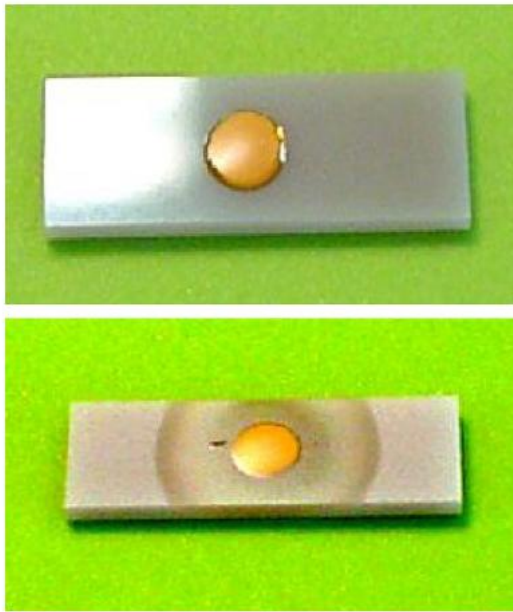
Fig. 10. Top: minimal epoxy bleed on an AlN polished surface with 20.1% carbon contamination, sample 3. Bottom: pronounced epoxy bleed on an AlN lapped surface with 21.1% carbon contamination, sample 7. Sled lengths are 16 mm. Adhesives are boron nitride filled in both cases.

Fig. 11. (a) SEM image of limited epoxy bleed on a polished Al_2O_3 surface with 21.2% carbon, sample 9. (b) SEM image of maximum bleed seen with the silver filled adhesive on AlN surface with 21.1% carbon, sample 7.

samples 3 and 12, both of which were polished ($r = 1.0024$, 1.0021, respectively), showed no bleed from the silver filled adhesive, and $< 10\mu m$ of bleed from the boron nitride filled adhesive.

In order to separate out unambiguously the influences of surface roughness from that of surface contamination/surface energy, the samples were cleaned using oxygen plasma to reduce the variation in surface contamination among samples. Oxygen plasma was chosen for its effectiveness in reacting with carbon-based molecules and its slow etching rate for the ceramics of interest. Contact angle measurements on all samples which underwent this treatment gave apparent surface energies in excess of 70 mN/m. This suggests removal of the majority of contamination, although the apparent surface energy is not high enough to denote complete removal [11]. The upper measurement limit of the surface energy is defined by the surface tensions of the liquids used, if the surface energy exceeds the surface tension of the test liquid then a stable contact angle is not formed and the surface energy cannot be estimated with the contact angle method. Low contact angles $< 10°$ were witnessed with water following plasma treatment, this indicated highly polar surfaces which are very near the useful limit of water as a test liquid.

The dispersive component of the surface energy was unchanged by the plasma treatment, whilst the polar component increased to 50 mN/m (standard deviation 1.03), for all samples. This supports the suggestion that the main effect of the plasma exposure is to remove carbon-based contamination, thus reduced the hydrophobicity of the surfaces. While the contact angle technique may not be capable of resolving any remaining differences in total surface energy among samples, XPS analysis of the plasma cleaned samples showed a relative carbon percentage of 12% on all samples. It therefore seems justifiable
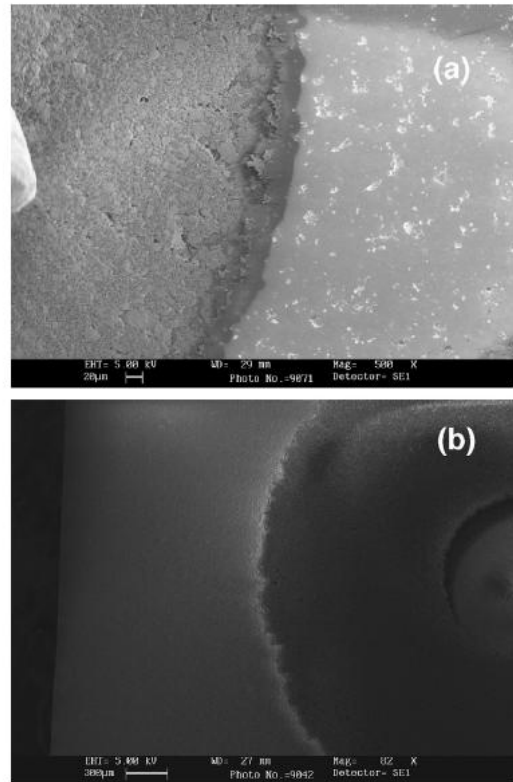
to consider the surfaces to have been chemically homogenised, allowing the differences in bleed behaviour described below to be attributed solely to differences in surface roughness.

Following the plasma clean the adhesives were applied as sessile drops to the sample surfaces within 1 h of cleaning and cured as before. Removal of contamination results in all surface/adhesive combinations exhibiting bleed visible to the naked eye, except the polished surface 9 with the silver filled adhesive and the polished surface 3 with both adhesives. Fig. 12 shows bleed distance plotted versus the AFM measured Wenzel ratio value for both substrate and adhesive materials and a roughly linear correlation can be seen. The alumina data points show more scatter about the linear trend line. It can also be seen that the boron nitride filled adhesive consistently bleeds further at each roughness value for both ceramic types than the silver filled adhesive. This shows that the bleed distance is partly affected by the adhesive formulation, probably because different adhesive additives or the filler properties either inhibit or encourage epoxy bleed. Further investigation of the effects of adhesive composition was beyond the scope of this work, partly because the commercial nature of the adhesives used meaning that the ingredients were not identified. However the influence of the ceramic surface on the bleed distance, is far stronger than that of the adhesive type. The result is possibly due to capillary action, which is known to extend to liquid spreading over surfaces [12].
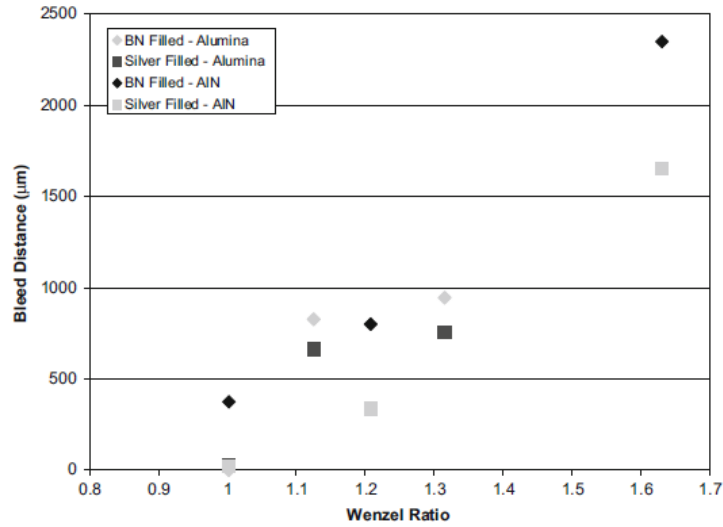
Fig. 12. Graph showing the relationship between epoxy bleed distance and Wenzel ratio for plasma cleaned AlN and Alumina with the boron nitride filled and silver filled adhesives.
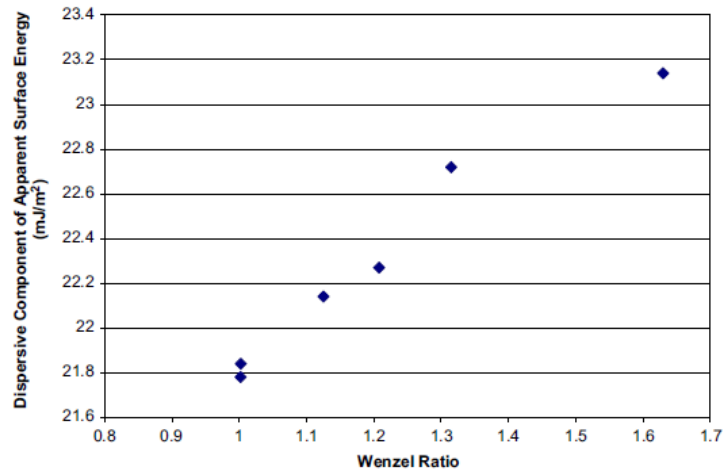
Fig. 13. A graph to show the relationship between Wenzel ratio and the dispersive component of apparent surface energy.

It can be seen in Fig. 13 that the dispersive component of the apparent surface energy is strongly linearly correlated to the roughness, irrespective of surface material. However the total variation in the dispersive component of surface energy (2%) is much smaller than the observed total variation in bleed distance (68%). It therefore seems likely that the effect is due to the influence of roughness on the contact angles measured using the test liquids, from which the surface energy is calculated, and hence that the bleed distances are indeed being determined solely by the ceramic surface texture after plasma cleaning, for each epoxy type.

6. Conclusions

Both adhesives exhibited unacceptable bleed distances on most of the plasma cleaned ceramic surfaces, but on only two of the uncleaned surfaces. Adventitious surface contamination is therefore an integral part of the product quality of optoelectronic module assemblies. It is undesirable that such an important parameter is completely uncontrolled by either part specifications or goods inwards checks. A simple qualitative wetting test with a suitable liquid could probably be made the basis of the necessary control if considered along with the

roughness measurements which are currently supplied with the ceramics.

For the adhesive/adherend systems investigated all joints failed cohesively, so that the mechanical surface preparation and surface chemistry had no influence on measured bond strength. This means that there is scope for engineering the surfaces in the study to reduce bleed without affecting bond strength or thermal fatigue resistance. This engineering will be the subject of further work.

The level of carbon-based contamination was found to be a much stronger influence on wetting of the ceramics than surface texture with as-received samples. However, once the contamination was removed it was clear that the surface texture, quantified as the Wenzel roughness factor, has a large effect upon the promotion or resistance to epoxy bleed.

Apparent surface energy alone is thus not sufficient information to determine the degree of epoxy bleed on a surface. This work has highlighted that surfaces of very low roughness and high surface energy can still resist epoxy bleed, and that surfaces of equal apparent surface energy but different roughnesses show different bleed behaviour. If the components of apparent surface energy are considered separately a clear linear correlation can be seen between the dispersive component and the bleed distance. The bleed distance is also linearly correlated with the AFM Wenzel ratio (r) value, indicating that the surface texture is directly linked to the measured dispersive component of surface energy. It can therefore be concluded that surface texture does have a direct effect upon the bleed distance, once contamination is removed. This gives rise to the possibility of varying surface texture as a means of epoxy bleed control.

Portable hand-held surface roughness measuring machines are not, in this case, particularly suited to giving an accurate representation of a ceramic surface, due to the feature size being such that it is not penetrable by the probe. For a smooth surface this is especially apparent as the surface has been machined to give the smallest feature size possible.

Light-based methods of surface measurement are also not suitable for these ceramic samples, for the crystal angles and steep angles of the topography create missing data points due to the incident angle being such that the light is not returned to the sensor. Steep fissures also appear to be present using this method,

but their nature and absence with other analysis methods suggest this is a phenomenon of the method and not an actual surface feature. The limited effectiveness of these surface analysis methods suggests that manufacturers should adopt high resolution stylus profiling methods, such as AFM, for quantifying the roughness of ceramics.

Acknowledgment

References

[1] Hall J, Edge C, Randle F, Pope S, Fraser J, Loosley J, et al. Integrated tunable transmitters for 10Gb/s long-haul DWDM applications. In: 53rd electronic components and technology conference, New Orleans, 27–30 May 2003, p. 796–800.

[2] Wenzel Robert N. Surface roughness and contact angle. Journal of Physical Chemistry 1949;53(9):1466–7, doi:10.1021/j150474a015.

[3] Hsiung JC, Pearson RA, Lloyd TB. A surface energy approach for analyzing die attach adhesive resin bleed. Journal of Adhesion Science and Technology 2003;17(1):1–14.

[4] Burmeister M. Elimination of epoxy resin bleed through thin film plasma deposition. Proceedings of SPIE—The International Society for Optical Engineering 2003;5288:780–5.

[5] Brewis DM. London: Applied Science; 1982.

[6] Pocius Alphonsus V. Adhesion and adhesives technology: an introduction. Cincinnati, OH: Hanser Gardner; 2002.

[7] Lawrence J (Jonathan), Li L (Lin). Laser modification of the wettability characteristics of engineering materials. London: Professional Engineering; 2001.

[8] Cassie ABD, Baxter S. Wettability of porous surfaces. Transactions of the Faraday Society 1944;40:546–51.

[9] Pavliček P, Hýbl O. White-light interferometry on rough surfaces—measurement uncertainty caused by surface roughness. Applied Optics 2008;47(16): 2941–2949.

[10] Sakai Y, Yamada T, Suzuki T, Ichinokawa T. Contrast mechanisms of secondary electron images in scanning electron and ion microscopy. Applied Surface Science 1999;144–145:96–100.

[11] Guzman-Castillo ML, Bokhimi X, Rodriguez-Hernandez A, Toledo-Antonio A, Hernandez-Beltran F, Fripiat JJ. The surface energy of quasi-amorphous [gamma] alumina calculated from the temperature of the [gamma]—> [alpha] transition. Journal of Non-Crystalline Solids 2003;329(1–3):53–6.

[12] Starov VM, Velarde, Manuel G (Manuel García). Wetting and spreading dynamics. Boca Raton, FL, London: CRC/Taylor & Francis; 2007.

9.2 Appendix 2 – Patent Application

PROVISIONAL PATENT SPECIFICATION

Surface treatments and coatings to reduce adhesive spread

Abstract
Treatments and coatings are disclosed that reduce the spread of liquid adhesive on ceramic and metal surfaces during the period before curing of the adhesive. The treatments and coatings are particularly suitable for mixed ceramic and metal surfaces to which epoxy adhesive is applied during the manufacture of electronic and optoelectronic components.

Background
This invention is in the field of the manufacturing of electronic and optoelectronic device where liquid adhesive is used. Such an adhesive is typically an epoxy adhesive which may be cured using UV light or thermally.

Liquid adhesives are widely used in the manufacture of electronic and optoelectronic components. Epoxy adhesives are commonly used because they are strong and have long life-times in harsh or otherwise demanding environments. As components have become smaller, adhesive management has become more important. The control of the flow of adhesive can be achieved by control of parameters such as viscosity, temperature and cure time. The less adhesive spreads from the area of the joint between the materials to be joined, the less adhesive is used and the less interference will there be between one affixed component and the adjacent items in the product. One known way to affect the spreading of a liquid over a surface is the modification of the surface energy of the surface and one way to do this is to treat the surface so that a layer or coating is placed upon the surface in order to alter its surface energy.

Materials that are commonly used in electronics and optoelectronics are ceramics (such as alumina and aluminium nitride (AlN)) and metals (such as copper and gold). The surfaces of such materials may differ from the bulk composition of the material. For example, copper and AlN my have oxide surface coatings through aerial oxidation. Thus any treatments used to modify the surface properties of the ceramics or metals need to take account of the surface compositions of materials as used in industry.

The wetting properties of metallised ceramic substrates for use in optoelectronic assemblies are not specified or controlled by suppliers or optoelectronic module manufacturer customers. The wetting properties of aluminium oxide and aluminium nitride substrate materials in the as received state have been shown to vary widely. Variation has also been shown to

depend on storage and handling procedures implemented by the suppliers and customers. Variation in the composition of the surfaces leads to poor process control of material interactions in assembly processes, such as the adhesion of metal tracks and the flow behaviour of adhesives for interconnections[1]. Ceramics and metals have intrinsic high surface energies which favour low equilibrium contact angles for epoxy adhesives used for component mounting and interconnection. In extreme cases separation of epoxy components and bleed across the surface occurs, interfering with nearby components and contaminating sensitive areas such as wire bonding pads. Surface contamination of ceramic substrates tends to restrict spreading due to wetting by reducing the effective surface energy. However, the variability of surface contamination levels of as-received surfaces has so far made this an unreliable solution.

A self assembled monolayer is a single molecule thick chemical layer which forms spontaneously on a given surface, the surface properties change from those of the bulk material to those of the SAM chemical following coating. Molecules of an amphiphilic substance (molecules having a hydrophilic head and a hydrophobic tail) are chemisorbed on a suitable solid surface, the hydrophilic end typically to the solid surface, leaving a hydrophobic tail exposed as a new surface. The exposure of the hydrophobic tail groups as a new surface and the uniform coverage of the solid surface reduces the apparent surface energy of a hydrophilic solid surface. The surface energy is an effect of the chemical and physical properties of the surface of the solid, the region where liquid/solid interactions take place. The reduction of this surface energy can increase the contact angle of liquids on the surface and thus reduce wetting. A well-known SAM is made from silane – for example treatment of a surface with trimethylchlorosilane. The treatment is sometimes known a silanisation.

An important practical point is that surfaces to be prepared for bonding are frequently composed of more than one material. For example, a surface may be made up of a ceramic with an embedded copper track and epoxy bonding may be required to both the ceramic and the metal surfaces.

There is thus a need for means and methods of preparing the complex surfaces of materials to be bonded in the manufacture of optoelectronic devices so that adhesive bleed is reduced and minimised. Preferably the whole complex surface composed of a variety of materials must be homogenised in surface energy so that the whole surface gives minimal adhesive bleed.

Description of the invention

A material made up of at least one ceramic material is treated with a solution of an alkanoic acid, a phosphonic acid or silane, preferably a fluoroalkanoic acid. After washing and drying a component or device is bonded to the surface using an adhesive, preferably an epoxy adhesive. The bleed of adhesive is thus greatly reduced with no significant effect of the bond strength achieved between the component or device and the ceramic substrate, in the

case of the alkanoic acid. Silane and phosphonic acid monolayers can be used where bond strength is not imperative.

In a further embodiment of the invention, a material made up of at least one ceramic and at least one metal, having a surface with exposed ceramic and exposed metal is treated with an alkanethiol, followed by one of the ceramic treatments mentioned above to reduce the surface energy across the surface so that the spread of uncured and curing adhesive is reduced.

Preferably, a longer chain length SAM chemical will reduce bleed more effectively than a shorter one. Any chain length can be used providing it can be dissolved in a solvent which does not interfere with the chemisorption process.

Technique for coating ceramic with alkanoic acid:
1. Dissolve $CA_3(CB_2)_nCOOH^*$ in deionised water or another suitable solvent, typically at 60°C to make an approximately 0.01M solution
2. Expose the ceramic (typically Al_2O_3 or AlN) to the solution. The exposure is at approximately 60°C for up to approximately one hour but other conditions may be suitable depending upon the solid substrate and the alkanoic acid.
3. Remove the ceramics from the treatment solution and wash with thoroughly with deionised water.
4. Dry.

*Where A and B are hydrogen, chlorine or fluorine, n is an integer from 1-21. Aqueous solution may not be suitable for all, tested for A=F, B=F, n = 1-16.

Technique for coating metal (or a surface containing a metal and a ceramic)*:
1. Dissolve organosulphide into isopropylalcohol (propan-2-ol, or another suitable solvent, typically a hydroxylic solvent) for a concentration of 10mM
2. Preparation of surfaces for SAM treatment: For copper only, etch with dilute (~5%) HCl for 10 minutes to remove oxide layer. The SAM solution is preferably acidified with 40ml/l of acetic acid. Gold needs no preparative treatment.
3. Add metal surface to the coating solution (from 1 or as modified for copper). Leave the surface exposed to the solution for a period up to approximately one hour. This operation is typically effected at room temperature.
4. Remove metal from treatment solution and wash thoroughly with solvent (typically isopropylalcohol).
5. Dry
6. Where the surface also contains a ceramic requiring reduced bleed characteristics, the alkanoic acid treatment is the applied as above, or the silane and phosphonic acid treatment as below.

* SAM substances suited to this are those with the chemical formulas HS-R or R-S-S-A where R and A are alkyl or aryl chains which could be partially or totally fluorinated or chlorinated. The hydrocarbon chains will terminate in a methyl, ethylene, fluorinated methyl or chlorinated methyl tail group.

Technique for coating ceramic with silane[*] or phosphonic[#] acid SAMs

1. Prepare a solution of phosphonic acid or silane to a concentration of 0.01M, solvents preferred are ethanol for phosphonic acid and cyclohexane for silanes.
2. Expose the ceramic (typically Al_2O_3 or AlN) to the solution. The exposure is at approximately 20°C for up to approximately one hour but other conditions may be suitable depending upon the solid substrate and the SAM substance used.
3. Remove the ceramics from the treatment solution and wash with thoroughly with their respective solvent.
4. Dry.

* SAM substances suited to this are those with a silane group and general formula $R-SiA_3$ where A can be hydrogen, chlorine or fluorine and R is a linear or branched alkyl or aryl chain of length 1-21 carbon atoms which could be partially or totally chlorinated of fluorinated.
# SAM substances suited to this are those with a phosphoric acid group of the form $C-PO(OR)_2$ where R is an alkyl or aryl chain which could be partially or totally chlorinated of fluorinated.

The performance of the treatments is assessed by measuring the distance the adhesive spreads away from the base of the item to be adhered to the test surface. For an untreated surface in ceramic the spread is typically 2mm. For an untreated metal it is typically 1mm. After treatments described above the bleed is reduced to approximately 30μm for ceramic or metal using the thiol and alkanoic acid treatments.

The SAM treatments produce monolayers, and such monolayers are resistant to removal by solvent cleaning processes. The presence of SAM monolayers on ceramics and metals treated as above has been confirmed with XPS both before and after solvent cleaning. The protection of the metal from alkanoic acid by the alkanethiol monolayer has also been shown with XPS.

The adhesives used in the tests were 1) Epo-Tek 930-4 (boron nitride loaded thermally conductive/electrically insulative), 2) H20E (silver loaded electrically conductive) and 3) a home made one prepared from 2-ethyl-4-methylimidazole (curing agent dissolved in 1,2-propanediol) and poly((phenyl glycidyl ether)-co-formaldehyde).

Surprisingly, the shear strength of epoxy bonds to the ceramics was not affected by the coatings, with joints failing cohesively for both coated and uncoated samples. The SAMs were shown to be thermally stable, being unaffected by heat soaking at 150 °C for 12 hours, augmenting their suitability as a solution to the problem of bleed.

The measured shear strengths of the commercial adhesives (on the ceramics) were 34.6N/mm2 and 23.9N/mm2 respectively, both before and after the ceramics were treated. The adhesives always underwent cohesive failure, showing that there was no strength reduction at the interface. This has been done repeatedly with 4 lengths of fluorinated carboxylic acid, with all 3 epoxies. Using a silane SAM (stronger bond) the shear strength is reduced to almost zero and the failure mode changes to adhesive failure (in fact these

bonds are so weak that the adhesive spots can be pushed off with a gentle prod of a finger), the surface energy is however higher than the fluorinated carboxylic acid SAM coated surfaces.

Using well-known SAMs such as silanes a large drop in strength due to the reduction in surface energy (lower less Van Der Waals forces, less wetting, less contact between adherend/adhesive).   It is believed that the reason this does not occur in the present invention is that the carboxylic acid SAM molecules are displaced by the reactive curing agent in the adhesive and this has been shown to occur by XPS data. This displacement happens sufficiently slowly that bleed does not occur significantly at the three phase line (the line between the adhesive the SAM and the solid surface) but bond strength is regained at the interface under the adhesive bulk. This is the reason the bleed distance is not zero.

Description of figures

Figure 1 illustrates bleed on a ceramic material as received from the manufacturer and having a measured surface energy of 70mN/m.
Figure 2 shows the bleed on the same ceramic after treatment with perfluorooctanoic acid giving a measured surface energy of 30mM/m.
Figure 3 give the relationship between the bleed distance and carbon chain length for a ceramic treated with linear fluoroalkanoic acids.
Figure 4 gives the relationship between the surface energy of a ceramic surface treated with fluoroalkanoic acid and the carbon chain length for linear fluoroalkanoic acids.

Figures

Figure 1

15

1,5 Bleed

Ø 1,5 Epoxy

5
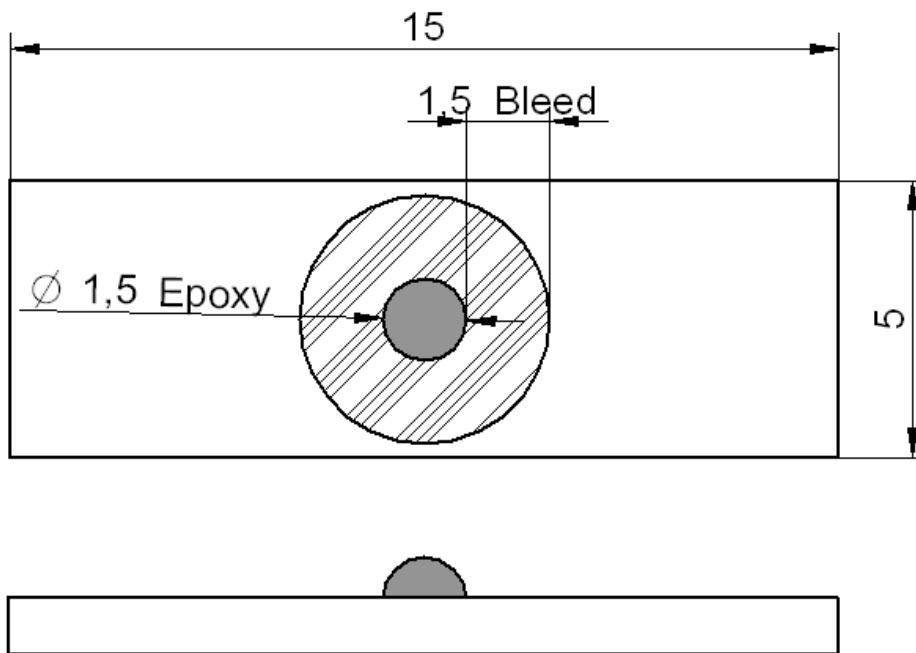
Worst case bleed at 70mN/m as
received ceramic

Figure 2

15

0,1 Bleed

Ø 1,5 Epoxy

5
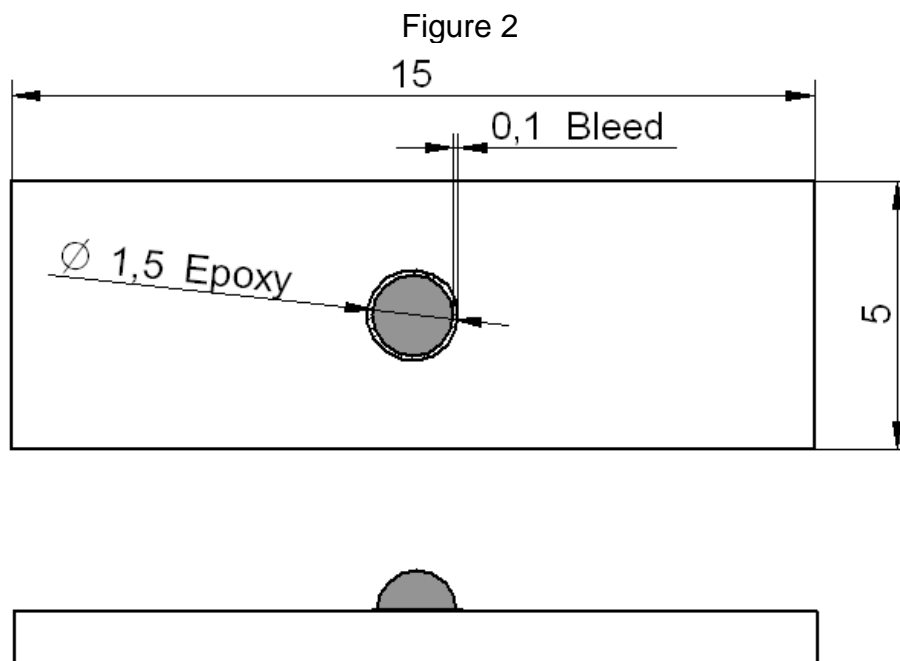
Acceptable bleed at 30mN/m on a
fluorinated carboxylic acid coated surface
(perfluorooctanoic acid)

Figure 3

Bleed distance vs fluorinated carboxylic acid SAM chain length

Figure 4

Surface energy vs fluoroalkanoic acid SAM chain length
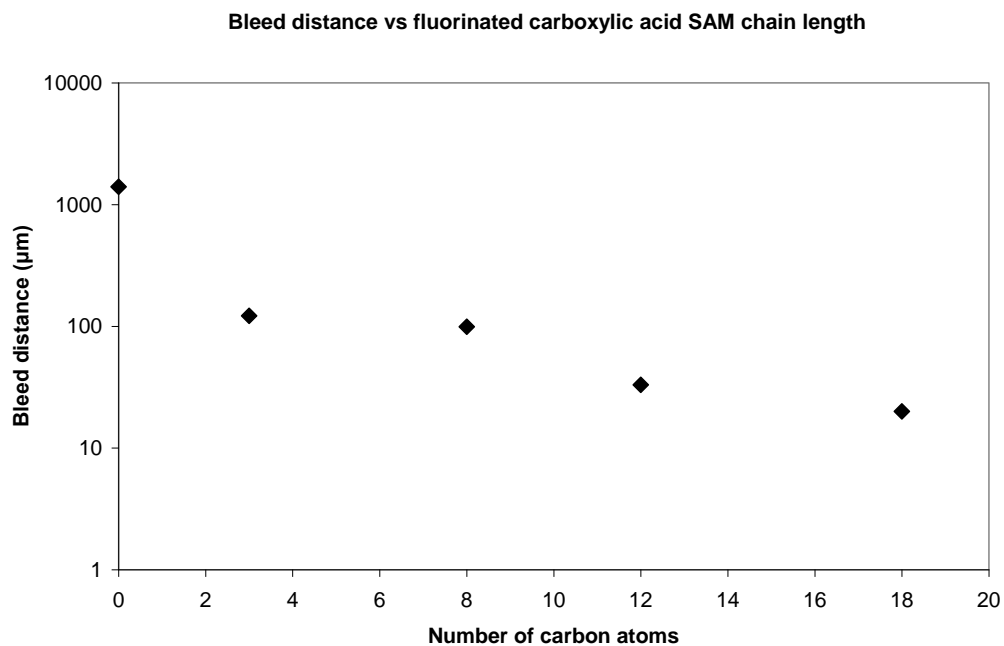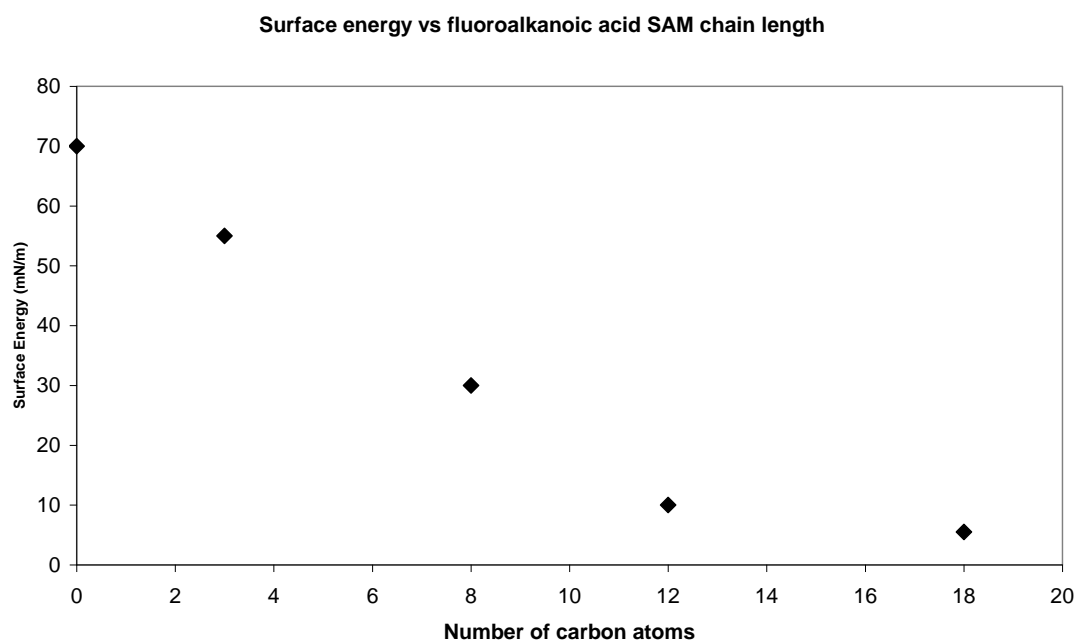
Claims.

1) A treatment for a ceramic surface to be bonded with adhesive, the treatment consisting of a solution of an alkanoic acid.

2) A treatment of claim 1 in which the surface energy is reduced by 50Newtons per cm.

3) A treatment as in claim 1 where the alkanoic acid has a linear carbon chain.

4) A treatment as in claim 1 where the alkanoic acid has a branched carbon chain.

5) A treatment as in claim 1 where the alkanoic acid has the formula $C_nH_{(2n+1)}COOH$.

6) A treatment as in claim 1 where the alkanoic acid is a fluoroalkanoic acid of the formula $C_nF_{(2n+1)}COOH$.

7) A treatment for a surface consisting of ceramic and metal areas, the treatment consisting of at least one alkane thiol for the metal and at least one alkanoic acid for the ceramic.

8) A treatment as in claim 7 where the alkane thiol has a branched chain.

9) A treatment as in claim 7 where the alkane thiol has the formula $C_nH_{(2n+1)}SH$.

10) A surface coating of an electronic or optoelectronic ceramic substrate consisting of at least one alkanoic acid

11) A surface coating of an electronic or optoelectronic surface containing ceramic and metallic areas, the treatment consisting of at least one alkanoic acid and at least one alkane thiol.

12) A treatment to homogenise to a low level the surface energy of a solid surface comprised of a mixture of ceramic and metal areas.

13) Treatments and coatings of the preceding claims where the alkanoic acid preferable has 8 to 21 carbon atoms.

14) Treatments and coatings of the proceeding claims where the alkane thiol has 5 to 21 carbon atoms and more preferably 5 to 12 carbon atoms.

9.3 Appendix 3 – Evaluation of Surface Energy Estimation Methods

9.3.1 Introduction

There are a range of methods for estimating the surface energy of a solid, as covered in *Section 2.4 Wetting, Contact angle and Surface energy*. One of the simplest ways is indirectly by measuring the contact angle formed by a liquid of known properties, on a surface of unknown properties. This can be done with one (Fowkes method) or more liquids and the contact angles are manipulated mathematically along with the surface tensions of the liquids, to yield an estimation of surface energy for the solid. The first to link contact angle to interfacial tensions was Young[1] whose work is the area is usually summarised by citing the Young equation:

$$\gamma_{lv} \cos\theta + \gamma_{sl} = \gamma_{sv}$$

Equation 9.3-1

Where γ_{lv} is the liquid/gas interfacial tension, γ_{sl} the solid/liquid interfacial tension, γ_{sv} the solid/gas interfacial tension and θ is the contact angle at the solid/liquid/gas interface.

However this equation is difficult to use in practice due to the difficulty of measuring the values of γ_{sl} and γ_{sv}. It is only practical to measure γ_{lv} and $\cos\theta$[2]. Therefore, starting with the work of Fowkes[3], many expressions have been derived to link the contact angle and liquid surface tensions to the polar and dispersive energies of solid surfaces.

Owens and Wendt introduced a method for calculating both the polar and dispersive fractions of surface energy from wetting data, in an expression especially suited to low energy solids[4]. A further method was described by Wu[6] which reportedly gives more accurate data at higher surface energies. Due to these methods being effective at opposite ends of the surface energy scale, they are both used in this work for surface energy estimations.

In this appendix the surface energies calculated with the Owens Wendt and Wu methods are compared. This was done to aid in the interpretation of

experimental data from previous chapters. In particular the sensitivity of the calculated surface energies to changes of contact angle was studied.

9.3.2 The Owens Wendt Method

Owens and Wendt theorised that the polar and hydrogen bonding contributions to surface tension can be considered together and so the surface tension and surface energy could be written as the sum of the dispersive and polar components[4]:

$$\gamma_l = \gamma_l^P + \gamma_l^D$$

Equation 9.3-2 The surface tension of a liquid as the sum of the polar and dispersive components.

And:

$$\gamma_s = \gamma_s^P + \gamma_s^D$$

Equation 9.3-3 The surface energy of a solid as the sum of the polar and dispersive components.

Where γ_l is the surface tension of a liquid with P and D denoting polar and dispersive components, and γ_s is the surface energy of a solid with P and D denoting polar and dispersive components.

Owens and Wendt hypothesised that the interfacial liquid/solid term in the Young equation, Equation 2.3-6, can be calculated from the polar and dispersive components of the interacting pair as follows:

$$\gamma_{sl} = \gamma_s + \gamma_l - 2\left(\sqrt{\gamma_s^D \cdot \gamma_l^D} + \sqrt{\gamma_s^P \cdot \gamma_l^P}\right)$$

Equation 9.3-4

Note that the two interaction terms on the right hand side are the geometric means of the dispersive (polar) components of the interaction pair. Inserting 5.4-4 into the Young equation they obtained:

$$1 + \cos\theta = 2\sqrt{\gamma_s^D}\left(\frac{\sqrt{\gamma_l^D}}{\gamma_{lv}}\right) + 2\sqrt{\gamma_s^P}\left(\frac{\sqrt{\gamma_l^P}}{\gamma_{lv}}\right)$$

Equation 9.3-5 The Owens Wendt equation as derived from the Fowkes equation to include both polar and dispersive forces.

Equation 9.3-5 may be rewritten in the format of the equation for a straight line:

$$\frac{(1+\cos\theta)\cdot\gamma_l}{2\sqrt{\gamma_l^D}} = \sqrt{\gamma_s^P}\cdot\sqrt{\frac{\gamma_l^P}{\gamma_l^D}} + \sqrt{\gamma_s^D}$$

Equation 9.3-6 The Owens Wendt equation in the form of the equation of a straight line, Y=MX+C, following contributions by Kaelble[5] and Rabel.

Equation 9.3-6 can be used as the basis of a method for measuring the surface energy of a solid. Two liquids are needed which contribute two points which define a straight line. The gradient of the line is then the square root of the polar component of the solid surface energy, while the Y-intercept is the square root of the dispersive component of the surface energy of the solid.

To evaluate the Owens Wendt equations for a range of contact angles a Matlab program was written and is shown in *Section 9.4 Appendix 4 – Matlab Programs.*

The surface energies for the corresponding contact angles were calculated first by using diiodomethane as a fixed value and plotting values of surface energy for contact angles of water 0-150°. A plot for equal water and diiodomethane contact angles is also shown in Figure 9.3-1. Contact angles were calculated for the following values for the dispersive and polar components of surface tension. Water total: 72.8mJ/m^2 polar: 46.8mJ/m^2 and dispersive: 26mJ/m^2. Diiodomethane total: 50mJ/m^2 polar: 2.6mJ/m^2 and dispersive: 47.4mJ/m^2.
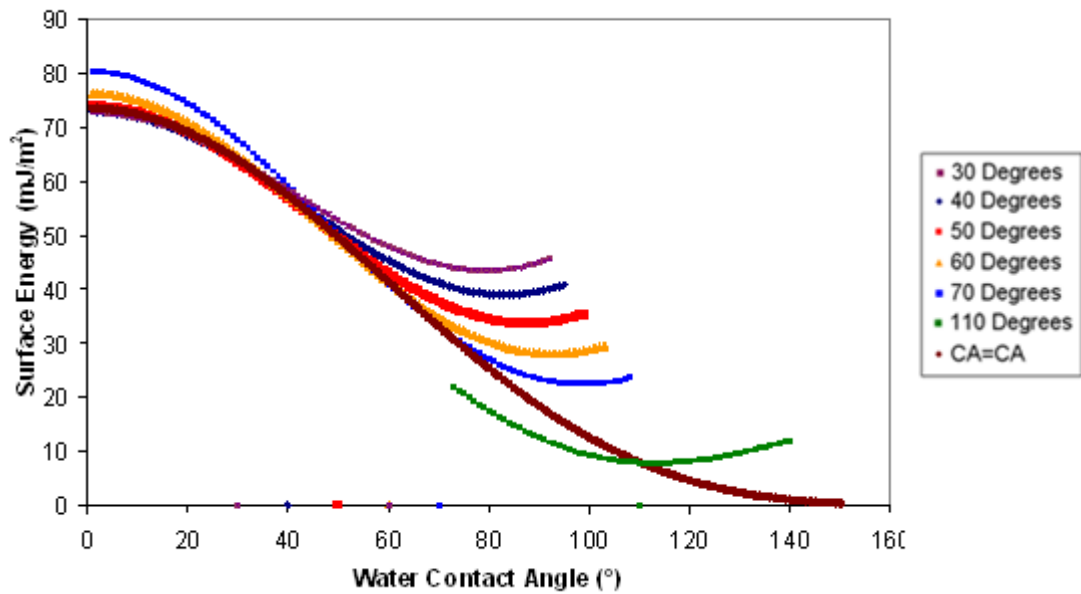
Figure 9.3-1 The affect of varying water contact angle on the total surface energy for fixed values of diiodomethane contact angle (see legend). CA=CA represents a plot for equal values of water and diiodomethane contact angles.

It can be seen from the CA=CA plot in Figure 9.3-1 that the total surface energy for equal contact angles for water and diiodomethane is not a linear plot. This is an interesting result as it shows that the resolution of the calculated surface energy value can be expected to change with the measured contact angles. The steepest gradient in the equal contact angles line is seen from 40° to 80° which means that small deviations in contact angle will produce larger deviations in surface energy than if the contact angles were outside of this range. From Figure 9.3-1 it can also be seen that for each fixed value of diiodomethane contact angle, there is a value of water contact angle for continued increase of water contact angle produces an increase in calculated surface energy. The reason for this is that the dispersive component is increasing due to a low dispersive liquid (diiodomethane) contact angle, and a high polar liquid (water) contact angle. However, for water contact angles much beyond this point the solutions to the expression are not real, i.e. no longer physical. As one would expect this happens at a higher water contact angle as the diiodomethane contact angle is increased. Thus if measured contact angles are seen to fall into this range of values (low polar component of surface energy and high dispersive component of surface energy) then any surface energy measurements which

302

are produced by contact angle goniometer software should be treated as questionable. A similar effect is seen when the water contact angle is fixed and the diiodomethane contact angle is varied, Figure 9.3-2. Here the surface energy values rise implausibly high. It can also be seen from Figure 9.3-2 that the sensitivity of the surface energy to diiodomethane contact angle is small compared to water, probably due to the higher surface tension of water which is composed of both polar and dispersive components whereas diiodomethane is almost entirely dispersive. Thus even a change in diiodomethane contact angle of ±10° makes a very small difference to the total surface energy.

However closer inspection reveals a transition point of a change in the nature of the solid surface from predominantly dispersive to polar, without affecting the total surface energy beyond experimental error. For example for water contact angle of 60° and diiodomethane of 50° the polar and dispersive components of the surface are 18.34 mJ/m^2 and 24.62 mJ/m^2 respectively, giving a total of 42.96 mJ/m^2, whereas for water 60° and diiodomethane 70° the polar and dispersive components are 27.76 mJ/m^2 and 13.24mJ/m^2 giving a total of 41.00 mJ/m^2. This result strongly highlights the limited value of a surface energy estimation alone, without considering its respective components. This is particularly relevant to this work because an adhesive system can be highly non-polar and changes to the distribution of surface energies between the two components could mean the difference between epoxy bleed occurring, and not occurring.
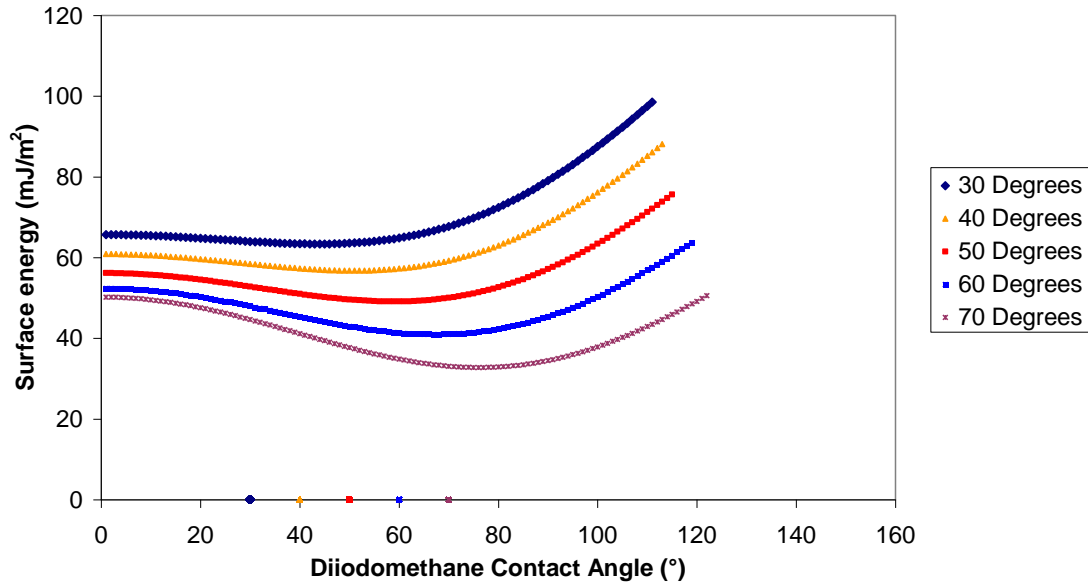
Figure 9.3-2 Plots of the affect of varying diiodomethane contact angles for fixed values of water contact angle (see legend).

9.3.3 The Method According to Wu

Wu followed Owens and Wendt but calculated the interaction terms between liquid and solid using the harmonic mean of the surface tension/energy components rather than the geometric mean[6] yielding first order non-linear equations of the form:

$$\left(b_1 + c_1 - a_1\right)\sigma_s^D \sigma_s^P + c_1\left(b_1 - a_1\right)\sigma_s^D + b_1\left(c_1 - a_1\right)\sigma_s^P - \left(a_1 b_1 c_1\right) = 0$$

Equation 9.3-7 Wu Equation 1 where sigma represents surface energies of liquids (l) and solids (s) as defined by the subscript letters l and s.

$$\left(b_2 + c_2 - a_2\right)\sigma_s^D \sigma_s^P + c_2\left(b_2 - a_2\right)\sigma_s^D + b_2\left(c_2 - a_2\right)\sigma_s^P - \left(a_2 b_2 c_2\right) = 0$$

Equation 9.3-8

Where:

$$a_1 = \tfrac{1}{4}\sigma_{l1}\left(\cos\theta_1 + 1\right)$$

$$b_1 = \sigma_{l1}^D$$

$$c_1 = \sigma_{l1}^P$$

Equation 9.3-9 Wu identities for Equation 9.3-7

$$a_2 = \tfrac{1}{4}\sigma_{l2}\left(\cos\theta_2 + 1\right)$$

$$b_2 = \sigma_{l2}^D$$

$$c_2 = \sigma_{l2}^P$$

Equation 9.3-10 Wu identities for Equation 9.3-8

Equations 9 and 10 are first order non-linear equations of the form:

$$Axy + Bx + Cy + D = 0$$

Equation 9.3-11 General form of Equation 9.3-7 and Equation 9.3-8

Where:

$$x = \sigma_s^D$$

$$y = \sigma_s^P$$

Equation 9.3-12 Source of the values of the dispersive component of surface energy and the polar component of surface energy from the Wu equations.

Each equation has two unknowns and there are two equations so the system must be solved simultaneously. This was done with a Matlab program which can be found in *Section 9.4 Appendix 4 – Matlab Programs*.

Solutions to the Wu equation were plotted as with the Owens Wendt equation. The expressions gave less real answers to contact angle combinations than the Owens Wendt equation, but was simultaneously less useful for low energy surfaces. The Wu equations produce two sets of values for dispersive and polar components of surface energy. The physical solution is usually readily apparent as one set of solutions is frequently negative or has imaginary parts (however in some instances small negative answers may simply reflect experimental measurement error). Occasionally however both sets are of similar magnitude and apparently equally valid. Interestingly some real surface energy component solutions to the Wu equations were returned by the Dataphysics OCA20 contact angle machine software, for pairs of angles yielding imaginary solutions when the maths was processed with Matlab. The algorithm used by the Dataphysics software to find solutions to the equations therefore appears to be different to that implemented for this work. The Wu

equation was found to be sensitive to contact angles which were widely different, i.e. for a surface which is highly polar or highly non-polar, frequently returning no valid answers when inputted with contact angles greater than or equal to 20° apart.
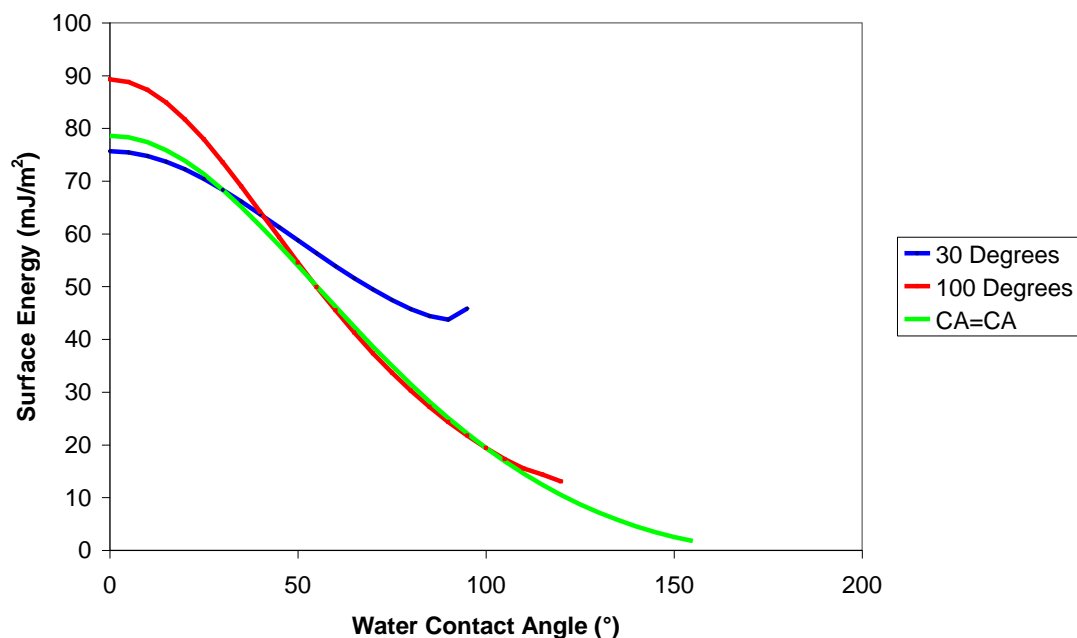

Figure 9.3-3 Plot of the varying surface energy for changing water contact angle against constant diiodomethane contact angles as calculated with the Wu method. CA=CA represents equal contact angles.

Figure 9.3-3 shows surface energy plots for varying water contact angles with diiodomethane angles fixed at 30° and 100°. The equal contact angle line CA=CA is also shown where water contact angles are equal to diiodomethane contact angles. The high angle limits to the lines are those beyond which no physical solutions are obtained, e.g. for 30° contact angle with diiodomethane there are no water contact angles higher than 95° giving a physical solution. The lines are of similar shape to those of the Owens Wendt fixed water contact angle plot, Figure 9.3-1, which suggests that the Wu equation has a similar sensitivity to the varying contact angles of water and diiodomethane.

Figure 9.3-4 shows the total surface energy variation with diiodomethane contact angle with fixed water contact angles at 30° and 100°. The same insensitivity of the surface energy to the diiodomethane contact angle is seen as with the Owens Wendt method. Interestingly the Wu method shows an inability to return surface energy estimations for diiodomethane contact angles

below 55° when the water contact angle is 100°. This suggests that the method is not suitable for surfaces with low polar components and high dispersive components of surface energy. The same implausible high diiodomethane contact angle rise in surface energy seen for the 30° water plot as with the Owens Wendt plots.
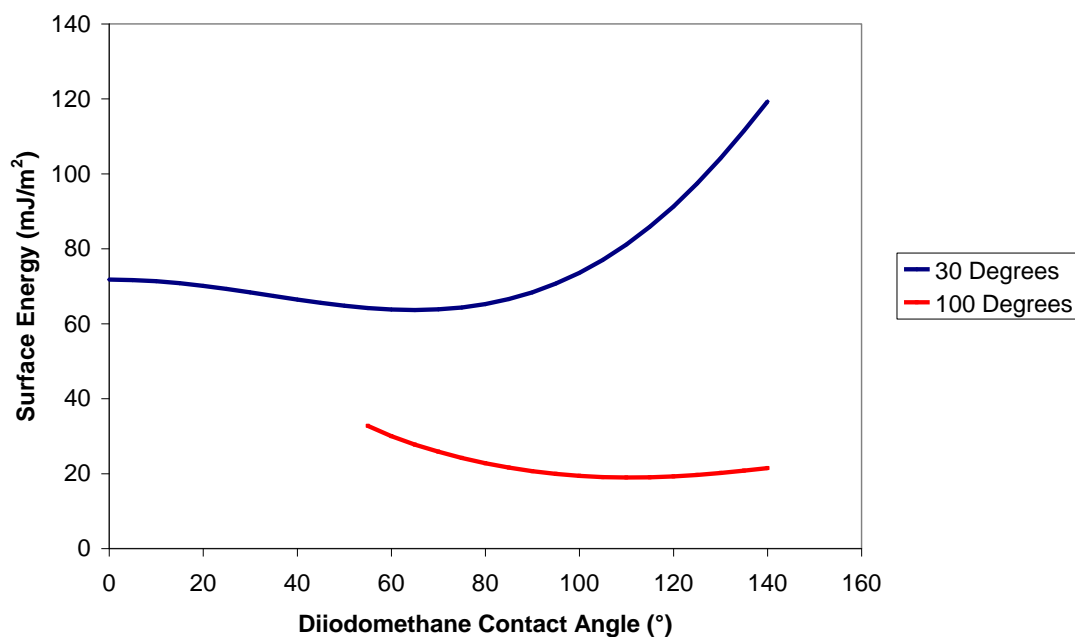

Figure 9.3-4 Plot of varying surface energy for steady water contact angles and varying diiodomethane contact angles as calculated with the Wu method.

The insensitivity of the surface energy to the varying diiodomethane contact angle was explored by plotting the total surface energy along with its polar and dispersive components, Figure 9.3-5. The transition between predominantly dispersive and predominantly polar surface character and relative stability of the total surface energy can be seen. A minimum in the total surface energy is seen near where the lines of the component plots cross. This figure shows that it is only the total surface energy that is insensitive to change in the diiodomethane contact angle.
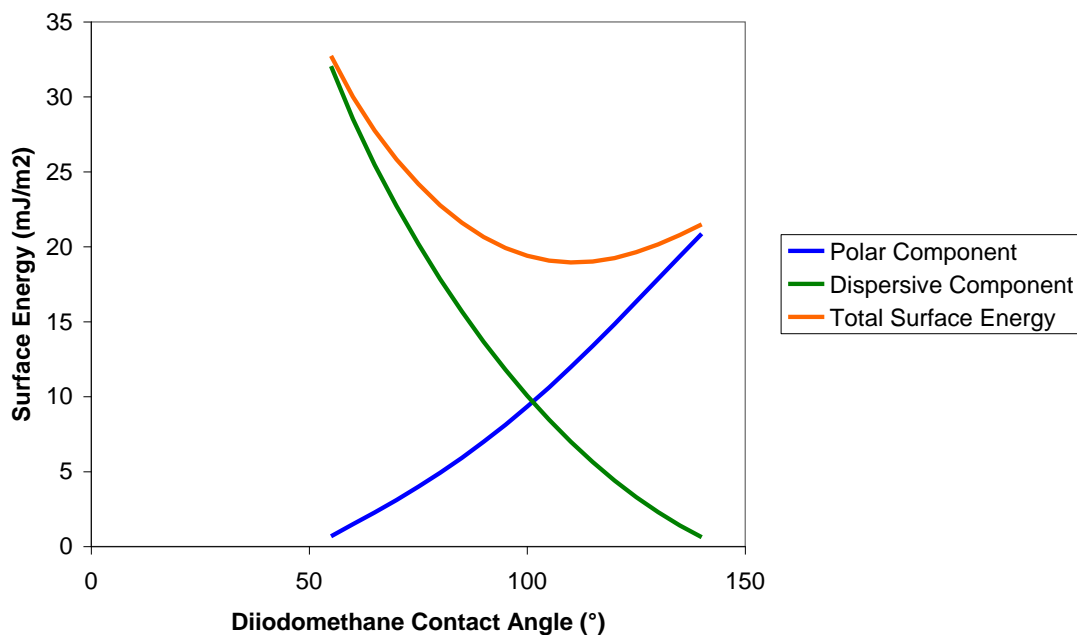
Figure 9.3-5 The changing contributions of the polar and dispersive components of surface energy for a fixed water contact angle at 100° and diiodomethane contact angle varying from 55-145°.

Finally, the surface energy calculated for equal contact angles using both the Owens Wendt method and the Wu method were plotted together and are shown in Figure 9.3-6. It can be seen that the models return very similar results, however the Owens Wendt values are consistently lower than the Wu Values.

It is clear from the data that the estimation of surface energy from contact angles is not a simple task. It is quite apparent that contact angles, components of surface energy, surface energy totals and knowledge of the sensitivity and suitability of the two methods is needed for the full interpretation of data.
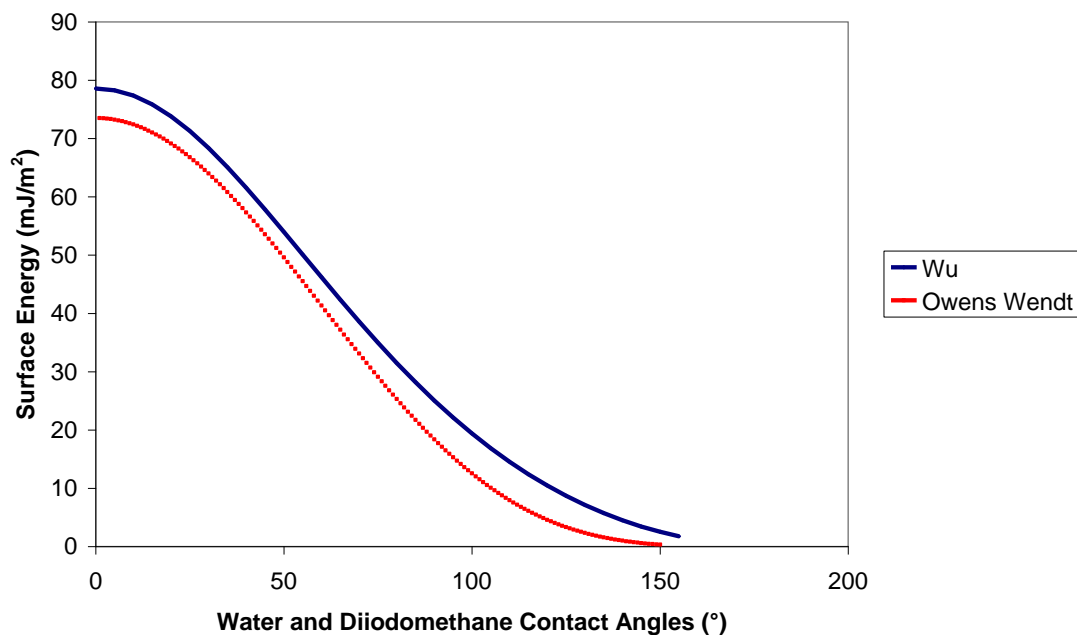
Figure 9.3-6 Comparison of the Owens Wendt and Wu methods for equivalent contact angles for water and diiodomethane.

9.3.4 Conclusions

The total surface energies produced by the Owens Wendt and Wu equations must be considered along with their respective components, the contact angles of the liquids and also the charts in this chapter for accurate interpretation to be made. It has been seen with both methods that the surface energies calculated have varying sensitivity to changes in contact angle.

[1] Young, T. "An Essay on the Cohesion of Fluids". *Phil. Trans. R. Soc. Lond.* 95: 65–87 1805

[2] Adamson, Arthur W. (Arthur Wilson)   Gast, Alice P. (Alice Petry), 1958- Physical chemistry of surfaces /   New York ; Chichester : Wiley, c1997

[3] Frederick M. Fowkes. ATTRACTIVE FORCES AT INTERFACES, Industrial & Engineering Chemistry 1964 56 (12), 40-52

[4] D. K. Owens, R. C. Wendt, Estimation of the surface free energy of polymers, Journal of Applied Polymer Science, Volume 13, Issue 8, 1969, Pages 1741-1747.

[5] D. H. Kaelble, Dispersion-Polar Surface Tension Properties of Organic Solids, The Journal of Adhesion, Volume 2, Issue 2 April 1970 , pages 66 - 81

[6] Souheng Wu, Kenneth J. Brzozowski, Surface free energy and polarity of organic pigments, Journal of Colloid and Interface Science, Volume 37, Issue 4, December 1971, Pages 686-690,

9.4 Appendix 4 – Matlab Programs

9.4.1 Wu Programs

First program to output solutions to the equations:

```
Theta2 = input('Diiodomethane Contact Angle?'); %user input contact
angle values
Theta1 = input('Water Contact Angle?');
Theta1 = Theta1*(pi/180);
Theta2 = Theta2*(pi/180);
sigma_l_disp_1 = 26; % sets values of the components of surface
tension
sigma_l_disp_2 = 47.4 ;% 1 = water, 2 = diiodomethane
sigma_l_pol_1 = 46.8;
sigma_l_pol_2 = 2.6;
a1 = 0.25*(sigma_l_disp_1 + sigma_l_pol_1)*(cos (Theta1) +1); %
introduces WU variables
b1 = sigma_l_disp_1;
c1 = sigma_l_pol_1;
a2 = 0.25*(sigma_l_disp_2 + sigma_l_pol_2)*(cos (Theta2) +1); %
introduces second set of WU variables
b2 = sigma_l_disp_2;
c2 = sigma_l_pol_2;
A1 = b1+c1-a1;
B1 = (c1*(b1-a1));
C1 = (b1*(c1-a1));
D1 = a1*b1*c1;
A2 = b2+c2-a2;
B2 = (c2*(b2-a2));
C2 = (b2*(c2-a2));
D2 = a2*b2*c2;
eqs = '((A1 * x * y) + (B1 * x) + (C1 * y) - D1), ((A2 * x * y) + (B2
* x) + (C2 * y) - D2)';
[x,y] = solve (eqs);
y
x
```

Second program to solve the equations:

```
Theta2 = input('Diiodomethane Contact Angle?'); %user input contact
angle values
Theta1 = input('Water Contact Angle?');
Theta1 = Theta1*(pi/180);
Theta2 = Theta2*(pi/180);
sigma_l_disp_1 = 26; % sets values of the components of surface
tension
sigma_l_disp_2 = 47.4 ;% 1 = water, 2 = diiodomethane
sigma_l_pol_1 = 46.8;
sigma_l_pol_2 = 2.6;
a1 = 0.25*(sigma_l_disp_1 + sigma_l_pol_1)*(cos (Theta1) +1); %
introduces WU variables
b1 = sigma_l_disp_1;
c1 = sigma_l_pol_1;
a2 = 0.25*(sigma_l_disp_2 + sigma_l_pol_2)*(cos (Theta2) +1); %
introduces second set of WU variables
b2 = sigma_l_disp_2;
c2 = sigma_l_pol_2;
A1 = b1+c1-a1;
B1 = (c1*(b1-a1));
```

```matlab
C1 = (b1*(c1-a1));
D1 = a1*b1*c1;
A2 = b2+c2-a2;
B2 = (c2*(b2-a2));
C2 = (b2*(c2-a2));
D2 = a2*b2*c2;
Y1 = 1/2/(A1*C2-C1*A2)*(A1*D2-B1*C2+C1*B2-
D1*A2+(A1^2*D2^2+2*A1*D2*B1*C2+2*A1*D2*C1*B2-2*A1*D2*D1*A2+B1^2*C2^2-
2*B1*C2*C1*B2+2*B1*C2*D1*A2+C1^2*B2^2+2*C1*B2*D1*A2+D1^2*A2^2-
4*A1*C2*D1*B2-4*C1*A2*B1*D2)^(1/2));
Y2 = 1/2/(A1*C2-C1*A2)*(A1*D2-B1*C2+C1*B2-D1*A2-
(A1^2*D2^2+2*A1*D2*B1*C2+2*A1*D2*C1*B2-2*A1*D2*D1*A2+B1^2*C2^2-
2*B1*C2*C1*B2+2*B1*C2*D1*A2+C1^2*B2^2+2*C1*B2*D1*A2+D1^2*A2^2-
4*A1*C2*D1*B2-4*C1*A2*B1*D2)^(1/2));
X1 = -(1/2*C2/(A1*C2-C1*A2)*(A1*D2-B1*C2+C1*B2-
D1*A2+(A1^2*D2^2+2*A1*D2*B1*C2+2*A1*D2*C1*B2-2*A1*D2*D1*A2+B1^2*C2^2-
2*B1*C2*C1*B2+2*B1*C2*D1*A2+C1^2*B2^2+2*C1*B2*D1*A2+D1^2*A2^2-
4*A1*C2*D1*B2-4*C1*A2*B1*D2)^(1/2))-D2)/(1/2*A2/(A1*C2-C1*A2)*(A1*D2-
B1*C2+C1*B2-D1*A2+(A1^2*D2^2+2*A1*D2*B1*C2+2*A1*D2*C1*B2-
2*A1*D2*D1*A2+B1^2*C2^2-
2*B1*C2*C1*B2+2*B1*C2*D1*A2+C1^2*B2^2+2*C1*B2*D1*A2+D1^2*A2^2-
4*A1*C2*D1*B2-4*C1*A2*B1*D2)^(1/2))+B2);
X2 = -(1/2*C2/(A1*C2-C1*A2)*(A1*D2-B1*C2+C1*B2-D1*A2-
(A1^2*D2^2+2*A1*D2*B1*C2+2*A1*D2*C1*B2-2*A1*D2*D1*A2+B1^2*C2^2-
2*B1*C2*C1*B2+2*B1*C2*D1*A2+C1^2*B2^2+2*C1*B2*D1*A2+D1^2*A2^2-
4*A1*C2*D1*B2-4*C1*A2*B1*D2)^(1/2))-D2)/(1/2*A2/(A1*C2-C1*A2)*(A1*D2-
B1*C2+C1*B2-D1*A2-(A1^2*D2^2+2*A1*D2*B1*C2+2*A1*D2*C1*B2-
2*A1*D2*D1*A2+B1^2*C2^2-
2*B1*C2*C1*B2+2*B1*C2*D1*A2+C1^2*B2^2+2*C1*B2*D1*A2+D1^2*A2^2-
4*A1*C2*D1*B2-4*C1*A2*B1*D2)^(1/2))+B2);
```

9.4.2 Owens Wendt Program

```matlab
Theta1 = input('Water Contact Angle?'); %user input contact angle
values
Theta2 = input('Diiodomethane Contact Angle?');
Theta1 = Theta1*(pi/180);
Theta2 = Theta2*(pi/180);
sigma_l_disp_w = 26; % sets values of the components of surface
tension
sigma_l_disp_d = 47.4 ;% 1 = water, 2 = diiodomethane
sigma_l_pol_w = 46.8;
sigma_l_pol_d = 2.6;
sigma_l_w = 72.8;
sigma_l_d = 50;
Y1 = (((1+ cos (Theta1)) * sigma_l_w)/(2*(sqrt (sigma_l_disp_w))));
X1 = (sqrt (sigma_l_pol_w / sigma_l_disp_w));
Y2 = (((1+ cos (Theta2)) * sigma_l_d)/(2*(sqrt (sigma_l_disp_d))));
X2 = (sqrt (sigma_l_pol_d / sigma_l_disp_d));
M = (Y2 - Y1)/(X2 - X1);
C = Y1 - (M * X1);
sigma_s_pol = M^2;
sigma_s_disp = C^2;
sigma_s_pol = sigma_s_pol
sigma_s_disp = sigma_s_disp
```